Monitoring seawater intrusion into the fractured UK Chalk aquifer using measurements of self-potential (SP)

Donald John MacAllister

March 2016

Supervised by

Prof. Matthew D. Jackson, Dr Adrian P. Butler and Dr. Jan Vinogradov

A dissertation submitted in fulfilment of the requirements for the degree of Doctor of Philosophy in Earth Science and Engineering and the Diploma of Imperial College London.

Declaration of originality

The work reported in this thesis is entirely my own and was conducted under the supervision of Prof. Matthew Jackson, Dr. Adrian Butler and Dr. Jan Vinogradov. The research was carried out in the Department of Earth Science and Engineering at Imperial College London. All other source material has been cited and referenced as appropriate. None of the work reported here has been previously submitted to Imperial College London or any other academic institution for a degree or diploma, or any other qualification.

Donald John MacAllister

PhD student

Department of Earth Science and Engineering

Imperial College London

Copyright declaration

Abstract

Using laboratory, numerical and field experiments this study investigated whether borehole measurements of self-potential (SP) can be used to monitor seawater intrusion into the fractured UK Chalk aquifer. The SP, a natural voltage, arises in water saturated fractured porous media due to gradients in pressure (electrokinetic (EK) potential) and concentration (exclusion-diffusion (EED) potential), both features of seawater intrusion. An electrode array was installed in a monitoring borehole c.1.7 km from the coast, in Saltdean, East Sussex, and c.1.3 km from an active abstraction borehole. Head fluctuations in the monitoring borehole were controlled by tidal processes and seasonal changes in inland head.

SP monitoring over 1.5 years revealed tidal SP signals. The fluctuations (c.600 μV) were two orders of magnitude larger than those observed at an inland site in the same aquifer, near Reading in Berkshire. Numerical simulation, supported by laboratory measurements, of the coupled hydrodynamic and electrical processes in the coastal aquifer suggested that the EK potential generated by tidal processes was one order of magnitude too small to be responsible for the tidal SP fluctuations. Instead, SP was caused by the EED potential that arose due to the concentration gradient between groundwater and seawater across the saline front (i.e. the 1000 mg/l isoline) some distance from the borehole. The saline front moved through a fracture at the base of the borehole in response to tides.

A vertical SP gradient (c.0.22 mV/m), only present in the coastal borehole, was also observed. Modelling suggested that the gradient was due to the close proximity of the saline front (c.4 m) below the borehole and was caused by the EED potential. In August 2013 and 2014, tides and a decline in inland head caused saline water to enter the borehole. Fluid electrical conductivity logging showed that entry was via the fracture. Prior to each occurrence of saline breakthrough, an increase in the SP of c.300 μV was observed, commencing c.7 days before saline water was detected in the borehole.

Although this study focused on a monitoring borehole, SP arrays could be installed in abstraction boreholes. The results suggest that SP monitoring may be used to provide early warning of saline water breakthrough, allowing for improved management of groundwater resources in coastal aquifers.

Acknowledgements

The Natural Environment Research Council is gratefully acknowledged for funding this project through the award of a CASE studentship in partnership with Atkins and Southern Water. TOTAL are thanked for supporting the Reservoir Physics Laboratory in which the laboratory work was conducted.

Thank you to my supervisors Prof. Matthew Jackson, Dr. Adrian Butler and Dr. Jan Vinogradov, whose enthusiasm, patience, support and guidance throughout the research process has been invaluable. Thanks also to Graham Nash who supported the laboratory work. Thanks to my examiners Prof. Denis Peach and Prof. Joanna Morgan for their improvements to the original manuscript.

Thank you to Mike Packman, John Moore and Simon Cook at Southern Water. Southern Water provided access to the Saltdean monitoring borehole, and the field element of this study would not have been possible without their support and enthusiasm. Thank you also to my industrial supervisor Douglas Hunt and Jamie Tomlin and Lesley McWilliam at Atkins. Atkins provided additional financial support and equipment and played a vital role in helping me gain access to the Saltdean borehole. I would also like to acknowledge Tim Power at AMEC who shared monitoring data from the Saltdean borehole that was crucial to identifying this as a suitable SP monitoring location. Thank you also to Prof. Rory Mortimore who provided the chalk cores for the laboratory experiments.

Thank you to my colleagues in the Smart Wells and Reservoir monitoring group at Imperial College London. Particular thanks to Amadi Ijioma for sharing the forward modelling SP code he developed which was used in the numerical investigations reported. Thank you also to Malcolm Graham for sharing his vast hydrogeological experience particularly with regards to the hydrodynamic modelling.

The support of my parents and siblings has been hugely appreciated throughout; they have all kept me going with their love and humour. Thanks to all my friends who have provided endless incentives to work hard over the last four years. Last, but by certainly no means least, thank you to my beautiful wife Kripa without whose patience, love and support this thesis would simply not have been possible.

"You care for the land and water it; you enrich it abundantly. The streams of God are filled with water to provide the people with grain, for so you have ordained it." Psalm 65:9-13

Conference presentations

MacAllister, DJ., Jackson, M., Butler, A. & Vinogradov, J., 2012. Laboratory measurements of the electrokinetic and electrochemical potential in chalk, with application to monitoring of saline intrusion in the UK Chalk aquifer. AGU Fall Meeting, 17 - 21 December 2012 San Francisco, USA.

MacAllister, DJ., Jackson, M., Butler, A. & Vinogradov, J., 2013. Laboratory and field measurements of the self-potential (SP) in Chalk, with application to monitoring of saline intrusion. AGU Fall Meeting, 16 - 20 December 2013 San Francisco, USA.

MacAllister, DJ., Jackson, M., Butler, A. & Vinogradov, J., 2014. Self-potential (SP) response to seawater intrusion in coastal aquifers. 23rd Salt Water Intrusion Meeting, 16-20 June 2014 Husum, Germany, pg. 239 - 242.

MacAllister, DJ., Jackson, M., Butler, A. & Vinogradov, J., 2014. Evidence for the application of self-potential (SP) monitoring to the management of abstraction in coastal aquifers. AGU Fall Meeting, 15 - 19 December 2014 San Francisco, USA.

MacAllister, DJ., Jackson, M., Butler, A. & Vinogradov, J., 2015. Monitoring seawater intrusion using self-potential. Geolsoc Instrumenting Groundwater Meeting, 21 April 2015 Birmingham, UK.

MacAllister, DJ., Jackson, M., Butler, A., Vinogradov, J. & Ijioma, A. A., 2015. Monitoring seawater intrusion into a fractured coastal aquifer using measurements of self-potential (SP). AGU Fall Meeting, 14-18 December 2015 San Francisco, USA.

Contents

List of Figures

List of Tables

Nomenclature

Symbol	Description	Units
a	Ionic activity	N/A
C_{cc}	SP coupling coefficient	N/A
C_{EED}	Exclusion-diffusion coupling coefficient	mV/M
C_{EK}	Electrokinetic coupling coefficient	mV/mH_2O
C_M	Molar concentration	M
C_{rEED}	Relative exclusion-diffusion potential scaling factor	N/A
C_{rEK}	Relative electrokinetic coupling coefficient	N/A
C_{scale}	Exclusion-diffusion potential scaling factor	N/A
C_{TDS}	Mass concentration	kg/m^3
D	Diffusion coefficient	m^2/s
d	Saturated thickness	m
e	Electron charge	C
F	Formation factor	N/A
g	Acceleration due to gravity	m/s^2
h_f	Water table elevation	m
j	Current density	A/m^2
j_d	Concentration flux	M.m/s
j_s	Heat flux	W/m^2
K	Hydraulic conductivity	m/d
k	Permeability	m^2
k_b	Boltzman constant	$m^2kgs^{-2}K^{-1}$
L	Length	m
L_{EED}	Exclusion diffusion cross coupling term	$A.S/m.m^{-1}$
L_{EK}	Electrokinetic cross coupling term	$A.mH_2O^{-2}m^{-2}$
L_{TE}	Thermoelectric cross coupling term	$A.Km^{-1}$
m	Cementation exponent	N/A
n	Saturation exponent	N/A
N_A	Avogadro's number	M^{-1}
P	Pressure	mH_2O
Q	Flow per unit length	m^3/m
q	Volumetric flow rate	m/s
R	Resistance	Ohm
r	Radius	m
S	Specific storativity	N/A
S_w	Water saturation	N/A
t	Time	s
T	Temperature	K
$T_{\pm}$	Macroscpoic Hittorf transport numbers	N/A

$t_{\pm}$	Ionic transport numbers	N/A
U	Effective velocity	m/s
V	Electric potential	mV
V_{AC}	Apparent column electric potential	mV
V_{AP}	Apparent plug electric potential	mV
V_C	Concentration dependant electrode potential	mV
V_{ED}	Diffusion potential	mV
V_{EE}	Exclusion potential	mV
V_{EED}	Exclusion-diffusion potential	mV
V_{EK}	Electrokinetic potential	mV
x	Distance in x direction	m
X	Reactance	Ohm
y	Distance in y direction	m
z	Ionic valence	N/A
Z	Impedance	Ohm
α	Dispersion coefficient	m^3/m
β	Ionic mobility	$m^2s^{-1}V^{-1}$
γ	Activity coefficient	N/A
ε_f	Dielectric permittivity	F/m
ζ	Zeta potential	mV
η	Exclusion efficiency	N/A
κ	Thermal conductivity	W/m.K
λ	Debye length	m
ρ_f	Density of freshwater	kgm^{-3}
ρ_s	Density of seawater	kgm^{-3}
ρ_w	Density of water	kgm^{-3}
σ_-	Anion contribution to conductivity	S/m
σ_+	Cation contribution to conductivity	S/m
σ_{fec}	Fluid conductivity	S/m
σ_{fspec}	Specific fluid electrical conductivity	S/m
σ_{gw}	Conductivity of groundwater	S/m
σ_{rec}	Saturated rock electrical conductivity	S/m
σ_{sw}	Conductivity of seawater	S/m
τ	Transmissivity	m^2/d
ϵ	Error	N/A
ϕ	Porosity	N/A
μ_w	Dynamic viscosity of water	Pa.s

Abbreviation	Description
AOD	Above ordnance datum
ASP	Azimuthal self-potential
CEC	Cation exchange capacity
DFT	Discrete Fourier transform
DI	Deionised water
EA	Environment Agency
EDL	Electrical double layer
EED	Exclusion-diffusion potential
EK	Electrokinetic potential
EPM	Equivalent porous medium
ERT	Electrical resistivity tomography
EU	European Union
FEC	Fluid electrical conductivity
FEC/T/P	Fluid electrical conductivity, temperature and pressure multi-parameter probe
FFT	Fast Fourier transform
GW	Groundwater
I	Ionic strength
IC	Ion chromatography
ICP-AES	Inductively coupled plasma atomic emission spectroscopy
IEP	Isoelectric point
IHP	Inner Helmholtz plane
MINRES	Minimum residual method
OBH	Observation borehole
OHP	Outer Helmholtz plane
P	Pressure
PDI	Potential determining ions
PSD	Power spectral density
SG	Savitsky Golay filter
SP	Self-potential
SW	Seawater
T	Temperature
TDM	Time domain electromagnetic
TDS	Total dissolved solids
TE	Thermoelectric potential
TER	Travelling electrode reference
TZ	Transition zone
VES	Vertical electric sounding
WHO	World Health Organisation
WT	Water table
ZPC	Zero point of charge

Chapter 1

Introduction

1.1 Overview

Seawater intrusion is a global phenomenon occurring in many coastal aquifers (van Weert et al., 2009, Werner et al., 2013). Approximately half of the world's population, including eight out of ten of the world's largest cities, are located in coastal areas (UN Atlas of the Oceans, cited in Post (2005)). Therefore, coastal aquifers are an extremely important water resource and a significant source of potable water for coastal populations. Recent studies suggest that excessive consumption of saline water (total dissolved solids > 2000 mg/l) over a period of time has significant negative health effects (Khan et al., 2011). It is estimated that up to 187 million people could be affected by seawater intrusion globally (van Weert et al., 2009). The problem of seawater intrusion as a result of overexploitation of coastal aquifers remains a significant scientific challenge (Post, 2005). Thus, the management of coastal aquifers is of particular concern to water planners, scientists and engineers.

Hydraulic connections between the sea and coastal aquifers result in a lateral intrusion of a landward thinning saltwater wedge (Goswami and Clement, 2007, van Weert et al., 2009). Reduction in recharge to aquifers and/or the abstraction of groundwater decreases the freshwater hydraulic head and can result in the saline front, defined here as the point at which groundwater transitions to brackish water (i.e. the 1000 mg/l isoline), advancing towards abstraction boreholes (van Weert et al., 2009). In the UK, seawater intrusion is considered one of the main risks to the Chalk aquifer groundwater resource in the South Downs, the focus area of this study, on the south-coast of the UK (Jones and Robins, 1999). The complexity of the Chalk aquifer in this area influences the extent of seawater intrusion and complicates the management of the aquifer.

The Chalk aquifer is a very important water resource as it contributes as much as 60% of groundwater use and 20% of total water use in England and Wales (MacDonald and Allen, 2001). The Chalk is a dual permeability aquifer, meaning that flow occurs both within the matrix and the fractures. Without

fractures the Chalk would not be a productive water resource, and it is the movement and storage of water in the fractures that makes the Chalk a productive aquifer. However, there is evidence to suggest that in the South Downs these fracture networks are also critical in controlling the extent of seawater intrusion (Jones and Robins, 1999, Robins and Dance, 2003). The dense fracture networks of the Chalk can provide highly permeable pathways for the rapid intrusion of seawater into the coastal aquifer, endangering public water supply. Thus, high resolution monitoring methods that provide both spatial and temporal information on the movement of the saline front are required in order to assess and monitor the risk of seawater intrusion into the aquifer in this area. Existing methods such as conductivity monitoring or resistivity surveying do not provide the spatial or temporal resolution required (de Franco et al., 2009, Ikard et al., 2012, Werner et al., 2013). However, one method that may facilitate continuous and dense spatial and temporal monitoring is self-potential (SP) monitoring.

SP arises in order to maintain overall electrical neutrality when a separation of charge occurs due to gradients in pressure (electrokinetic or streaming potential), concentration (electrochemical or exclusion-diffusion potential) and temperature (thermoelectric potential) (Revil, 1999a). Concentration gradients are a characteristic feature of seawater intrusion and may give rise to a measureable exclusion-diffusion potential (EED). In addition, the electrokinetic potential (EK) will arise during abstraction for public water supply. Furthermore, tides will alter both the pressure and concentration gradients within the coastal aquifer giving rise to a periodic SP signal. The hypothesis of this work is that the fluctuating and intruding saline front could potentially be detected and monitored continuously using a permanent array of borehole SP electrodes, providing dense monitoring in space and time. SP logging has been conducted for a wide variety of sub-surface applications for many years; however, this study focusses on long-term SP monitoring measurements from a permanently installed electrode array in a coastal borehole near Brighton in the South Downs.

The SP log is one of the oldest borehole logging tools and has been used in the oil and gas and mining industries for over 60 years (Wylie, 1949, Kirsch, 2006), although many of the original interpretations were thermodynamically untenable (Wylie, 1949, Wylie, 1951). More recently the SP monitoring method has been applied to geothermal applications (Anderson and Johnson, 1973, Corwin and

Hoover, 1979) and has even received interest as an earthquake precursor (Corwin and Morrison, 1977). More importantly, the application of SP monitoring to hydrogeological problems has been widely investigated in recent years (Jouniaux et al., 2009, Revil and Jardani., 2013, Jackson, 2015).

Most of the SP work applied to hydrogeology is fairly recent but covers many common hydrogeological problems. For example, SP monitoring has been applied to pumping tests (Rizzo et al., 2004, Maineult et al., 2008a, Jackson et al., 2012a) or the flow of groundwater under natural conditions in a buried paleochannel (Revil, 2005), in a sinkhole (Jardani et al., 2006) or in geothermal fields (Jardani et al., 2008). Other applications reported in the literature include monitoring sub-surface glacial flows (Kulessa, 2003) and redox fronts in contaminant transport problems (Arora et al., 2007, Revil et al., 2009). Jackson et al. (2012a) recently conducted SP monitoring experiments in the Chalk aquifer in response to a pumping test and measured a c.60 μV electrokinetic response to pressure drawdown. They concluded that SP monitoring may be a useful tool for in-situ characterisation of the Chalk aquifer. Furthermore, there are a few early examples of SP logging being used to characterise hydrogeochemical parameters in coastal aquifers (Radhakrishna and Gangahara, 1990, Nativ, 1994, Radhakrishna, 2001) and groundwater salinity threats to potable water supplies as a result of oil drilling (McConnel, 1983).

However, no previous work has focussed on the application of long-term SP monitoring to seawater intrusion, although there are some studies that have looked at the SP response to saline tracers in field experiments. These studies focussed on using saline tracers to characterise potential leakage zones in earth embankment dams (Bolève et al., 2011, Boleve et al., 2012, Ikard et al., 2012) and the SP response to tracer movement in the unsaturated zone (Jougnot et al., 2015). Recent work has also focussed on the SP response to movement of seawater through sea dykes (Kang et al., 2014). However, there are significant differences between these works and the work reported here. For example, Kang et al. (2014), studied dykes directly parallel to the coast and some of the methods they used for data acquisition and analysis are questionable, including ignoring the exclusion-diffusion component of the SP signal. The work was also conducted in a very different hydrogeological setting and; thus, cannot be directly related to the work described here. However, their work does suggest that

SP of sufficient magnitude arises in coastal areas and may yield useful information on the flow processes occurring in coastal aquifers.

Much of the motivation for the present study is derived from numerical studies of SP in oil reservoirs during water flooding for enhanced oil recovery (Saunders et al., 2012, Gulamali et al., 2011, Jackson et al., 2012b) a situation that has strong parallels with seawater intrusion. The injection of low salinity water into a reservoir containing oil and high salinity connate water introduces large gradients in temperature, pressure, concentration and saturation. Similarly natural seawater intrusion is associated with dynamic pressure and concentration gradients induced by the movement of seawater into the coastal aquifer. Abstraction for public water supply can enhance the pressure gradients and draw the salinity front closer to the abstraction borehole. Likewise, during water flooding, pumping at an oil abstraction borehole draws the saturation front towards the well and water breakthrough is undesirable. Similarly breakthrough of saline water at a fresh water abstraction borehole is a major problem for the water supplier and must be avoided at all costs. Furthermore, the recovery of the aquifer in the area adjacent to an abstraction borehole can take considerable time (Zhou et al., 2005). SP monitoring may provide the means to proactively manage coastal abstractions and assist in avoiding the risks of saline breakthrough in the first place.

In the numerical experiments conducted by Jackson et al. (2012b) the SP recorded at an oil abstraction borehole responded to the movement of the injected water hundreds of metres away. The change in SP contained information about the geometry of the intruding water front, and spatial and temporal information on the position of the front relative to the abstraction borehole where SP was monitored. Therefore, SP measurements were indicative of the movement of the water front towards the abstraction borehole. Most significantly, SP measurements provided early warning of the imminent breakthrough of the water front at the abstraction borehole. The parallels with seawater intrusion are striking and provide the basis for this study which aimed to assess the potential of using borehole SP measurements, from a permanently installed array of electrodes, for monitoring and early warning of seawater intrusion.

1.2 Aims and objectives

This study aimed to determine if measurement of self-potential could be used to monitor seawater intrusion into the fractured Chalk aquifer. The key research questions addressed were: (i) do tidal effects induce a measureable SP response within the borehole (chapter 5)? (ii) What are the main source mechanisms for the tidal SP and what is the relative contribution of the EK and EED potential (chapter 5)? (iii) Does SP respond to declining inland head and the consequent movement of the saline front towards the monitoring borehole (chapter 6)? Or, in other words, can SP measurements provide a precursor to saline breakthrough at a monitoring borehole? To address these questions three phases of work were conducted, the objectives were:

1. Laboratory Experiments (chapter 3): Measure EK and EED potential in the laboratory on chalk samples saturated with seawater and groundwater and in the presence of isolated pressure and concentration gradients. These measurements supported interpretation of the field monitoring measurements, allowed first order estimates of the magnitudes of EK and EED potentials generated in the coastal aquifer by natural gradients in pressure and concentration respectively and provided the basis for the electrodynamic models of the coastal aquifer.

2. Field experiments (chapter 4 – 6): Instrument a coastal borehole in the South Downs Chalk aquifer at risk of seawater intrusion to investigate whether SP responds to coastal hydrodynamic processes. An inland borehole was also instrumented in order to compare the SP results to the coastal site and to identify features of the SP that were unique to the coastal borehole.

3. Numerical Modelling (chapter 4 – 6): Construct coupled hydrodynamic and electrodynamic numerical models to investigate the possible hydrodynamic processes leading to the generation of SP signals in a Chalk coastal aquifer and assess, to first order, the relative contribution of the EK and EED potential to the SP signals observed.

1.3 Thesis outline

To begin, chapter 2 provides the basis for the laboratory, field and numerical investigations by reviewing the literature to understand flow processes occurring within the Chalk aquifer in the South Downs and the impact this has on the dynamics of seawater intrusion in the area. The literature review

was important in order to begin to identify the likely range of pressure and concentration gradients present and how they may affect the measured SP. The various theories regarding the physical mechanisms leading to the generation of SP in carbonates are then reviewed along with the mathematical description of the SP mechanisms. Then previous applications of SP in fractured and saline aquifers are examined along with the design of long-term SP monitoring experiments.

Chapter 3 describes the laboratory experiments designed to characterise the SP properties of the chalk. The laboratory method is presented and the results are discussed in the context of the potential implications for the long-term seawater intrusion monitoring, which is reported subsequently.

Chapter 4 introduces the two field sites. The chapter begins by describing the inland site near Reading in Berkshire. Then the coastal site, at Saltdean in East Sussex in the South Downs, is described and the history of seawater intrusion in the area is briefly discussed. The acquisition of the field SP data is described, and the modelling methodology adopted to simulate the coastal aquifer is presented.

Chapter 5 presents the analysis of the SP data acquired in the coastal aquifer and compares it to the SP data obtained at the inland site. The analysis focused on the tidal periodicity of the SP signals observed and aimed to determine whether any periodicity that was observed in the coastal aquifer could be directly attributed to tidal hydrodynamic process active at the coast but absent inland. Numerical modelling was also used to identify the relative contribution of the EK and EED potential to the total SP in the coastal aquifer.

In chapter 6 the long-term coastal hydrodynamic and SP monitoring results are examined in order to determine whether they provide any evidence of the temporal or spatial location or extent of the saline front relative to the monitoring borehole. The analysis was supported by numerical modelling and where appropriate comparison to the inland site.

Finally, in chapter 7, the results are summarised and conclusion are drawn on the use of the SP monitoring method for seawater intrusion in the fractured UK Chalk aquifer.

Chapter 2

Seawater intrusion and the application of long-term self-potential (SP) monitoring

2.1 Introduction

The threat to global coastal water resources from seawater intrusion is significant. Consequently, there is a need to develop new measurement, monitoring and management strategies (Post, 2005, Werner et al., 2013). The challenge of seawater intrusion and the possibility for using SP as a new monitoring approach is reviewed in this chapter. The chapter begins by providing a definition of saline intrusion, and reviews the chemical and physical dynamics of the problem more generally. The problem of seawater intrusion in the UK Chalk is then reviewed. Next, the existing seawater intrusion monitoring methods and their strengths and weaknesses are discussed, setting the context for the possibility of using SP monitoring as a new technique. The second part of the review begins by introducing the SP and the fundamental principles and theory of the main SP source mechanisms. The broader application of SP in hydrogeological studies is next discussed before reviewing previous work that hints at the possibility of applying SP monitoring to seawater intrusion in fractured coastal aquifers such as the chalk.

2.2 Saline intrusion

Saline groundwater can be classified into four main groups (van Weert et al., 2009). These are saline groundwater of; (i) marine origin, (ii) natural terrestrial origin, (iii) anthropogenic terrestrial origin and (iv) mixed origin. Saline water of marine origin includes connate water deposited along with the rock matrix, or through ancient marine transgressions and seawater flooding (van Weert et al., 2009). Natural terrestrial effects include evaporation linked to shallow water tables and limited flushing of accumulated salts. Another natural effect is dissolution, salts are dissolved while flowing through soluble porous media; this is often a problem in carbonates such as chalk (van Weert et al., 2009). Anthropogenic effects include irrigation, which creates a situation where evapotranspiration of the high salinity irrigation water deposits salt residue which can percolate into the upper sections of an

aquifer (van Weert et al., 2009). This work considers modern saline intrusion of marine origin, i.e. seawater intrusion.

2.2.1 Definition of saline water

2.2.1.1 Seawater

Seawater contains traces of all the natural elements, but 99.8% of the mass of the total dissolved solids in the ocean is dominated by a few major ions (Angelis, 2005) (Table 2.1). Major ions are defined as dissolved species having a concentration in seawater greater than 1 mg/l. The chemical composition of seawater is almost globally constant (Angelis, 2005), with notable exceptions such as in the polar regions.

Major Ion	% by wt.	Concentration (mg/l) at salinity of 35,000ppm	Molar Concentration (M/l)
Chloride, Cl^-	55.30	19353	0.54588
Sodium, Na^+	30.77	10781	0.46895
Sulphate, SO_4^{2-}	7.75	2712	0.00084
Magnesium, Mg^{2+}	3.69	1284	0.05283
Calcium, Ca^{2+}	1.18	411.9	0.01028
Potassium, K^+	1.14	399	0.01021
Bicarbonate,	0.41	126	0.00207
Bromide, Br^-	0.19	67.3	0.00084
Strontium, Sr^{2+}	0.023	23	0.00026
Fluoride, F^+	0.0037	1.3	0.00007
Total TDS	35158.5	**Total Ionic Strength (M)**	0.69721

Table 2.1 - Major ions in seawater. Note that Na^+ and Cl^- comprise about 86% of total dissolved solids in seawater (Angelis, 2005).

Note that throughout this work concentration is reported as mass concentration (mg/l) and molarity (M/l). Total dissolved solids (TDS) and ionic strength (I) will also be used to refer to the overall salinity. TDS is simply the sum of the mass concentration of all of the ions in solution. The relationship between ionic strength and molarity is (McNaught, 2005):

$$I = \frac{1}{2}\sum_{i=1}^{n} C_{Mi} z_i^2 \qquad \textbf{Equation 2.1}$$

Here C_{Mi} is the molarity of ion i and z_i is the charge number of ion i.

The fluid electrical conductivity (FEC) is the most common method used in seawater intrusion investigations (FAO, 1997). Table 2.2 shows the variation of FEC of seawater in response to temperature and salinity (Bullard, 2011).

	Salinity (mg/l)				
	20,000	25,000	30,000	35,000	40,000
Temperature (°C)	**Electrical Conductivity (µS/cm)**				
0	17,450	21,370	25,230	29,060	32,850
5	20,150	24,660	29,090	33,460	37,780
15	25,950	31,700	37,350	42,900	48,370
20	29,010	35,420	41,710	47,880	53,970
25	32,170	39,260	46,210	53,020	59,740

Table 2.2 - FEC of seawater at various temperatures and salinities (Bullard, 2011).

2.2.1.2 Saline groundwater

Definitions of saline groundwater are provided by Reilly and Goodman (1985) and van Weert et al. (2009) (Table 2.3(a)). Table 2.3(b) shows the limits recommended by the WHO and the EU for salt content in drinking water. Loaiciga et al. (2012) in their study on the effects of climate change on seawater intrusion, used 10,000 mg/l to define the landward advance of the saline front. Citing the US Environmental Protection Agency (1976), they state that this is the maximum limit for potable water. In their analysis of the global occurrence of saline water, van Weert et al. (2009) define saline water as TDS > 1000 mg/l. However, based on the definition in Table 2.3(b) it would seem more reasonable to define the limit for potable water at about 1750 mg/l or 2500 µS/cm (Table 2.3(b), i.e. brackish water from the definitions in Table 2.3(a)) based on the EU-directive cited in Kirsch (2006).

(a)

Class name	TDS (mg/l)	FEC (µS/cm)
Fresh water	< 1,000	< 1,430
Brackish water	1,000 – 10,000	1,430 – 14,300
Saline water	10,000 – 100,000	14,300 – 143,000
Brine	> 100,000	> 143,000

(b)

Indicator	WHO	EU-directive on water quality
FEC (µS/cm)	2850*	2500
TDS (mg/l)	2000	1750*
	Defined by acceptability to taste	**Defined as upper limit in drinking water**

Table 2.3 – (a) Class limits for the main parameters used for measuring salt content adapted from Van Weert et al. (2009). (b) Upper limits for drinking water taken from Khan et al. (2011) and Kirsch (2006). * FEC is calculated from approximate conversions given in van Weert et al. (2009) where FEC = TDS/0.7.

2.2.2 Seawater intrusion dynamics

This section deals with the basic principles of seawater intrusion in porous media; the nature of seawater intrusion in the Chalk aquifer is dealt with in section 2.2.3.

2.2.2.1 Saline interface dynamics and properties

Seawater intrusion is controlled by the local geology, the flow regime in the aquifer, the density contrast between fresh and saline water, and hydrodynamic dispersion (Bear et al., 1999). Hydrodynamic dispersion includes the effects of molecular diffusion and mechanical dispersion (Fetter, 2001). These multiple controlling factors make seawater intrusion a complex phenomenon. Many conceptual models and analytical solutions have been developed to represent the behaviour of the saline interface in coastal aquifers. Although these models only approximate real-world situations, they are useful tools for analysis and serve as good benchmark problems for numerical algorithms. Note that the terms saline interface and saline front are used interchangeably. The saline front, between the seawater and groundwater end members, is defined in this thesis as the point at which the coastal groundwater transitions from freshwater to brackish water (i.e. the 1,000 mg/l or 1,430 µS/cm isoline, see Table 2.3). The terms saline front or interface, as defined here, do not refer to a sharp interface between freshwater and seawater, unless otherwise stated, and include the possibility of the existence of dynamic and miscible interface between the seawater and groundwater end members.

The earliest attempt to describe the seawater wedge was developed independently by Badon-Ghyben and Herzberg (Reilly and Goodman, 1985, Bear et al., 1999). The Ghyben-Herzberg relation is still widely used today and relates the elevation of the water table (above mean sea level) in an unconfined aquifer to the depth of the saline-freshwater interface (below mean sea level):

$$z = \frac{\rho_f}{\rho_s - \rho_f} h_f = \frac{1}{\gamma} h_f \approx 40 h_f \qquad \textbf{Equation 2.2}$$

Here $\gamma = \frac{\rho_s - \rho_f}{\rho_f}$, where ρ_f = 1000 kgm^{-3} is the density of freshwater and ρ_s = 1025 kgm^{-3} is the density of seawater, z is the depth below sea level (m) to a point on the interface and h_f is the water table elevation above that point (m) (Figure 2.1)

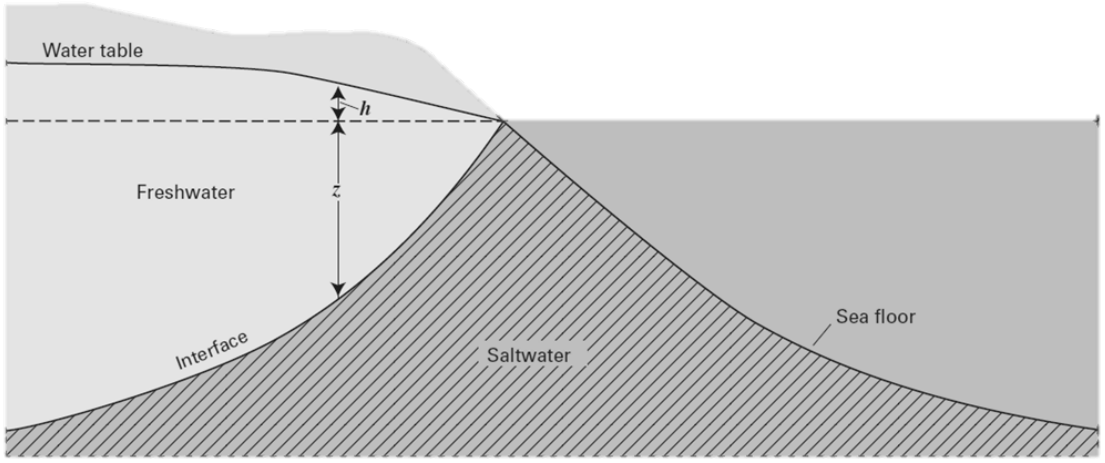

Figure 2.1 - The Ghyben-Herzberg relationship between fresh and saline groundwater in a coastal aquifer. The position of the interface between the fresh and saline groundwater is related to the difference in density of the two waters. The depth of the interface below sea level is about 40 times the height of freshwater above sea level, so z=40h_f (Barlow, 2003).

The Ghyben-Herzberg relation makes several assumptions and simplifications. The first of these is that the groundwater head at the water table is the same as the head of the freshwater interface, which implies that there is no vertical head gradient (this is also known as the Dupuit assumption) (Reilly and Goodman, 1985). Therefore, the freshwater head is zero at the shore so there cannot be any freshwater discharge. The second assumption is that the boundary between the seawater and freshwater is a sharp, immiscible interface. In natural systems, neither of these assumptions hold true.

The Glover solution improved on the Ghyben-Herzberg relation by explicitly dealing with the first of these assumptions (Reilly and Goodman, 1985). A sharp interface is also assumed. The solution allowed for the movement and discharge of freshwater at the coast:

$$\gamma^2 - \frac{2Q}{\gamma K}x - \frac{Q^2}{\gamma^2 K^2} = 0 \qquad \textbf{Equation 2.3}$$

Here Q is the freshwater flow per unit length of shore (m^3/m), K is hydraulic conductivity of the medium (m/d) and x is the distance from the shore (m).

Cooper et al. (1964), investigating the relatively homogeneous coastal aquifer of Pearl Harbour, Hawaii, and the Biscayne aquifer of Miami, Florida, suggested that there exists a zone of mixing, known as the zone of diffusion or dispersion between the freshwater and the seawater. As a

consequence seawater circulates in the aquifer (Figure 2.2). This conceptual model was based on observations of salt water discharge near the freshwater discharge zone.

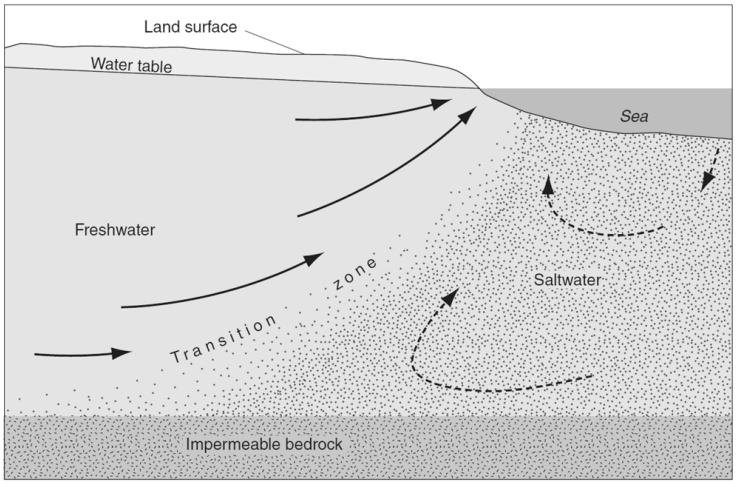

Figure 2.2 - The zone of mixing and the flow patterns that lead to seawater circulation during seawater intrusion (Barlow, 2003).

The theory was confirmed by Kohout (in Cooper et al. (1964)) in a detailed field investigation of the Biscayne aquifer, which showed that the landward advance of the seawater wedge was much less than that predicted by the Ghyben-Herzberg relation. Kohout attributed this to seawater circulation, which he explained by dispersion produced by the reciprocating motion of tides. The transition zone was found to be about 11 m thick; small relative to the lateral extent of the aquifer, but large relative to the thickness of the aquifer (30 m). Cooper et al. (1964), found a large transition (304 m thick) in the Pearl Harbour aquifer using chloride content measurements from a deep test borehole (427 m deep).

Kohout (in Cooper et al. (1964)) hypothesised that two mechanisms lead to the existence of a transition zone. These are advection and molecular diffusion, although the latter was mistakenly considered to be a type of convection. Advection is the transport of the solute with the flowing groundwater. Molecular diffusion ensures the micro-scale mixing of the fluids due to the concentration gradient and subsequent migration of solute from a region of higher concentration to lower concentration (Fetter, 1999). Mechanical dispersion also influences the transition zone by controlling mixing (Abarca et al., 2007, Kerrou and Renard, 2010). Longitudinal dispersion acts parallel to the flow path due to the variation in velocity of the water containing the solute because of

variations in pore size and path length. Transverse dispersion acts normal to the flow path due to divergence of the water containing the solute at the pore scale (Fetter, 1999).

Heterogeneity intensifies dispersion and creates locally reduced concentration gradients and density contrasts. These effects are commonly studied using numerical modelling. For example, Kerrou and Renard (2010), suggest that increasing heterogeneity leads to less significant inland penetration of the saline wedge and a thicker mixing zone. Abarca et al. (2007) investigated the contribution of transverse and longitudinal dispersion to the thickness of the transition zone and found that transverse dispersion was the main factor controlling mixing. Increased transverse dispersion contributed to a general broadening of the concentration profile (Figure 2.3(a)). However, longitudinal dispersion was found to cause seaward displacement of the high isoconcentration lines (Figure 2.3(b)), which meant that vertical concentration profiles in the mixing zone still displayed significant increases in concentration but only the base of the saline wedge had seawater concentrations (Abarca et al., 2007) .

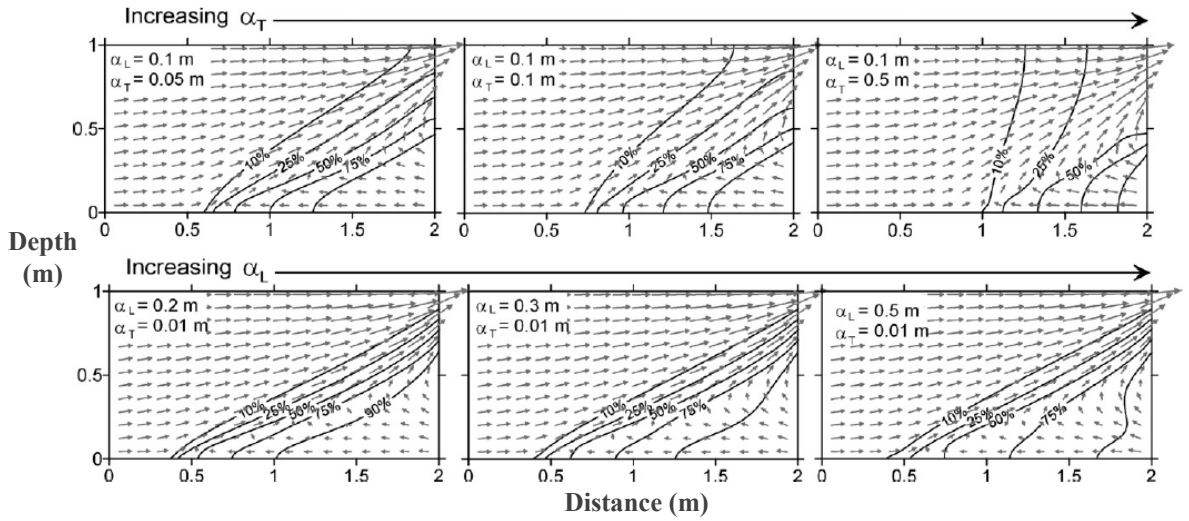

Figure 2.3 - Concentration distribution showing the effects of longitudinal and transverse dispersion on the properties of the saline wedge. α_T is the transverse dispersion coefficient and α_L is the longitudinal dispersion coefficient (Abarca et al., 2007).

The studies mentioned above investigated the problem in an equivalent porous medium, however the impact of large variations in permeability also have an effect on the development of the mixing zone. Lu et al. (2009) investigated the effects of kinematic mass transfer using a dual domain transport model. They also applied periodic and temporal transient boundary conditions, i.e. tides and seasonal fluctuations in freshwater discharge (Michael et al., 2005). They suggest the larger the matrix

porosity, which is relatively immobile over the timescales considered, with respect to the fractures or other low permeability zones, i.e. the more mobile porosity, the greater the extent of the mixing zone. This is important for the present study as the Chalk aquifer has a large relatively immobile matrix porosity (Jones and Robins, 1999). The maximum width of the mixing zone may be reached when the mean retention time in the matrix and the period of water level fluctuations are comparable (Lu et al., 2009). Despite the challenges in investigating the mixing zone it appears that dispersion is the primary control on the width of the zone (Abarca et al., 2007, Kerrou and Renard, 2010).

Understanding the impact of fractures on the seawater intrusion process is challenging due to the difficulty of adequately representing fractures in numerical models. Field studies indicate that fractures have a significant effect on the inland extent of the saline water movement (Park et al., 2012), and pose particular problems for management of fractured coastal aquifers, similar to the UK Chalk aquifer. Thus, the ability to model and simulate such systems is important. Despite this, Simmons et al. (2010) suggest the treatment of fractures in models has been simplistic to date, but note that fractures are likely to play a very important role in the variable density flow process and emphasise the need to understand their influence on macroscopic dispersion. In their study Dokou and Karatzas (2012) superimposed field observations of fracture locations, in a karst limestone aquifer, on a homogenous porous medium model. They then added further fractures to calibrate the model to observed salinity patterns. They found that the fracture orientation resulted in asymmetric movement of the saline front inland, and also demonstrated the importance of groundwater abstractions on the development of the front in the fractured aquifer. A more detailed study of the effects of fractures, by Graf and Therrien (2005), also found that fracture orientation played a significant role in the development of the saline front, and that the presence of fractures resulted in barriers to convective flow in the aquifer.

Henry (in Cooper et al. (1964)) was the first to account for the transition zone by applying the advection-dispersion equation describing miscible fluids to the seawater intrusion problem. There are many algorithms available to solve the advection-dispersion equation described in detail by Bear et al. (1999). However, the governing equations are the mass balance equation (Equation 2.4), Darcy's flux

(Equation 2.5) and the solute transport equation (Equation 2.6). These are coupled by the equations of state, which give the fluid density and viscosity as a function of concentration (Ackerer et al., 1999, Ackerer et al., 2004):

$$\rho S \frac{\partial P}{\partial t} + \phi \frac{d\rho}{dC_{TDS}} \frac{\partial C_{TDS}}{\partial t} + \nabla \cdot (\rho q) = \rho Q_s \quad \textbf{Equation 2.4}$$

$$q = -\frac{k}{\mu_w} \cdot (\nabla P + \rho g \nabla z) \quad \textbf{Equation 2.5}$$

$$\phi \frac{\partial C_{TDS}}{\partial t} + q \cdot \nabla C_{TDS} - \nabla \cdot (\alpha \cdot \nabla C_{TDS}) = Q_s (C_{sTDS} - C_{TDS}) \quad \textbf{Equation 2.6}$$

Here C_{TDS} is the concentration of salt in mass per unit volume (kgm^{-3}), C_{sTDS} is the concentration at source (kgm^{-3}), S is the specific storativity of the porous medium, α is the hydrodynamic dispersion tensor, g is gravitational acceleration (ms^{-2}), k is the intrinsic permeability (m^2), ϕ is the porosity, P is the pressure (kgm^{-1}s^{-2}), q is specific discharge (m/s), Q_s is the source/sink term, ρ is fluid density (kgm^{-3}) and μ_w is dynamic viscosity (kgm^{-1}s^{-1}).

2.2.2.2 Tidal processes in coastal aquifers

Tides are important in this study because of their likely impact on the pressure and concentration gradients in the coastal aquifer. In fact, chapter 5 deals specifically with the impacts of tides on the observed SP in the South Downs. Tidal fluctuations in boreholes are indicative of regional changes in pressure gradients over the tidal cycle. Tidally driven fluctuations in hydraulic head are common in coastal boreholes (Nielsen, 1990, Wang and Tsay, 2001, Carey et al., 2009). Some authors suggest that these signals can be used to characterise the hydraulic properties of the aquifer (Chen et al., 2011, Cutillo and Bredehoeft, 2011) including hydraulic conductivity. However, Earth tides can also cause tidal responses in boreholes, away from the coast (Hsieh et al., 1988, Rojstaczer and Riley, 1990); in fact, some authors even use the Earth tide response in boreholes to characterise fracture distribution and properties (Bower, 1983, Burbey, 2010).

In the near-coastal zone tidal fluctuations are a major driver for the advection of the seawater-freshwater interface; however, the effect of tides on seawater intrusion is still not well understood (Kuan et al., 2012). Most studies of tidal effects have used numerical models, with some authors reporting that tides reduce the landward advance of the seawater wedge (Kuan et al., 2012) and others

reporting an increased landward advance (Ataie-Ashtiani et al., 1999). Xin et al. (2010) investigated tide and wave effects on a near-shore subterranean estuary and found that the wave effects are important in the area immediately adjacent to the coast, and that the waves induced a higher than average seawater level which could affect the regional pressure gradients. They found that these effects created an upper saline plume in the near shore area but that the effects were negligible over larger distances. Furthermore, tidal effects increase the thickness of the saline transition zone (Ataie-Ashtiani et al., 1999, Robinson et al., 2007, Lu et al., 2009) possibly due to increased hydrodynamic dispersion as a result of tidal fluctuations and heterogeneity which creates non-uniform advection (Lu et al., 2009). It appears likely however that tides will influence both the long-term and shorter-term position of the saline front. Thus, tidal effects will alter the mixing zone seasonally, over the diurnal and semi-diurnal tidal cycles and over the fortnightly spring/neap cycle.

2.2.2.3 Impact of pumping on seawater intrusion

Saltwater up-coning occurs when the natural equilibrium of the saltwater interface is disturbed by pumping an abstraction borehole in the freshwater zone causing the interface to move towards the abstraction borehole (Reilly and Goodman, 1985). Whether or not the cone intersects the borehole depends on the discharge rate, the duration of pumping and the local hydrogeological conditions (Reilly, 1986). There is a certain critical discharge above which the borehole will become saline (Reilly, 1986). Neglecting all other forcing mechanisms for the moment, including tides and seasonal heads, below this critical rate the cone will stabilise, with the apex of the cone below the base of the pumping borehole. If the pumping rate is kept constant a new equilibrium condition occurs and potable water can continue to be pumped (Reilly, 1986). However, with increased pumping rates the cone will gradually move towards the borehole. At the critical pumping rate the cone is still below the borehole but the cone is at the highest position at which it can remain stable (Figure 2.4).

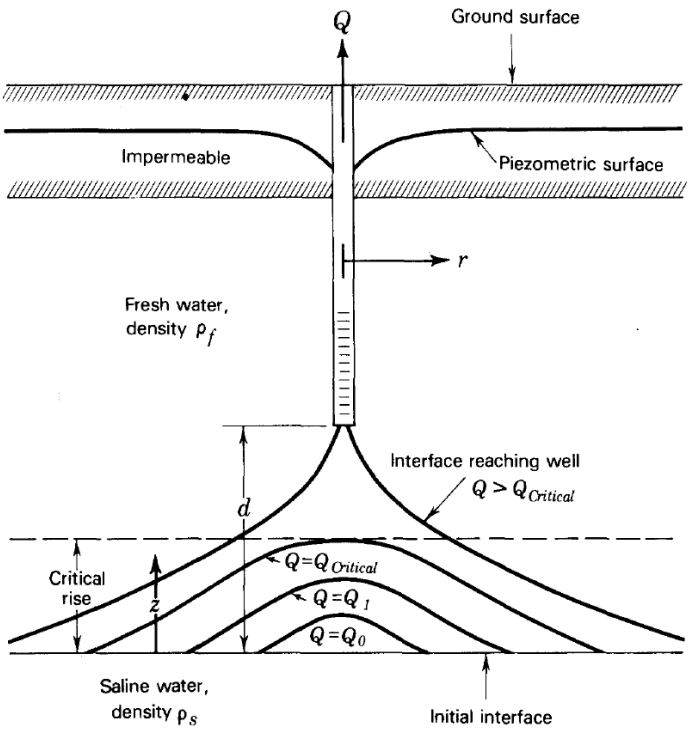

Figure 2.4 – Saltwater up-coning beneath a pumping well illustrating the critical pumping rate above which the abstraction borehole will start to discharge saline water (Reilly, 1986). Q is the discharge rate, Q_0 is the initial discharge rate, Q_1 represents a higher discharge rate, and $Q_{critical}$ is the highest pumping rate above which the saline water will move into the borehole.

Most studies of up-coning rely on analytical methods (Muskat and Wycokoff, 1935, Wang, 1965), numerical modelling (Reilly, 1986, Zhou et al., 2005), laboratory studies (Oswald and Kinzelbach, 2004, Werner et al., 2009) or a combination (Johannsen et al., 2002, Oswald and Kinzelbach, 2004). It is difficult to investigate up-coning in the field, because it is a highly localised phenomenon.

Zhou et al. (2005) investigated saltwater up-coning and decay using a finite element method to solve the advection-dispersion equation. They looked specifically at the effects of dispersion, density and the decay of the cone after pumping terminated. They found that the decay process is very lengthy. Therefore, it is essential to avoid contamination of the area adjacent to an abstraction borehole. Monitoring methods that provide information on the proximity of the saline interface relative to an abstraction or monitoring borehole could assist in avoiding contamination during abstraction, a hypothesis that provided much of the motivation for this study.

In some cases, where wide transition zones have developed, hydrodynamic dispersion may result in a long-term change to the position of the transition zone and, as a result, a decline in water quality in the vicinity of the borehole (Zhou et al., 2005). They found that after only 4 years the borehole could

become saline, but decay could take longer than 50 years. They attributed this to the absence of regional flow in their model and the effect of transverse dispersivity. Another reason may be due to the circular velocity field that arose as a result of gravity imbalance after the pump was shut down changing the natural flow field under ambient conditions, which was also used to explain the widening of the cone. Transverse dispersivity was found to be the critical factor and led to a wider transition zone, a flatter salinity mound, a need for earlier shut down of the pump and a longer decay period. The early shut-off was attributed to the wider transition zone and a shorter distance for salt particles to travel to the borehole. Werner et al. (2009) examined up-coning in a homogeneous sand tank and came to similar conclusions. Dispersion effects were found to be important in the early stages of the experiment, diluting the salt plume as it rose towards the pumping borehole. Once the cone intercepted the borehole, dispersion effects decreased and the cone continued to widen.

2.2.2.4 Geochemical processes during seawater intrusion

Geochemical processes occurring in the aquifer during seawater intrusion will affect the measured SP signal, primarily by changing the chalk surface charge (section 2.3.2) The main processes occurring during seawater intrusion are mixing, calcite dissolution and oxidative degradation of organic matter (Andersen et al., 2005, Russak and Sivan, 2010, Panteleit et al., 2011). Andersen et al. (2005) analysed the geochemical properties of groundwater, seawater and intermediate water in the transition zone in a shallow coastal aquifer in Zealand, Denmark. The aquifer consists mainly of sand and gravel deposits and layers of peat. They found that the water in the transition zone was of intermediate salinity, as expected, but that it was also enriched in sulphide and alkalinity and had a higher pH than either the groundwater or seawater. Degradation of organic matter in the aquifer produced HCO_3^{2-} and CO_2 and affected the $CaCO_3$ equilibrium and pH. These, in turn, influenced ion exchange processes which were dominated by methanogenesis in the freshwater zone and sulphate reduction in the seawater zone. Therefore, organic matter was considered to be the main ion exchanger. Ion exchange and calcite dissolution also appeared to be coupled. The increased uptake of Ca^{2+} from freshwater on the marine organic ion exchanger and its subsequent loss from solution during freshening events leads to a lowered calcite saturation state and may stimulate increased calcite dissolution and, consequently, acid consumption by the calcite carbonate ions, which also explains the zone of high pH. This was

further supported by the fact that Na^+ enrichment occurred in the high pH zone due to the cation exchange between Ca^{2+} and Na^+. Calcite dissolution appears to be most important in areas with less than 50% seawater particularly in the case of aquifer freshening as it flushes out marine ions, Na^+ and Mg^{2+}, from the aquifer (Panteleit et al., 2011). Calcite dissolution may be further increased by the degradation of organic matter, or the partial pressure of atmospheric CO_2 in unconfined aquifers in equilibrium with CO_2.

2.2.3 Chalk hydrogeology and seawater intrusion

Chalk is a very pure limestone consisting almost entirely (96%) of calcium carbonate (Hancock, 1975). The Chalk aquifer is often described as a dual porosity aquifer (Price, 1987). Chalk is formed from the deposition of cocoliths, which results in a high porosity in the inter-granular space within the matrix (Price, 1987, MacDonald and Allen, 2001). In a classic dual porosity system, the storage is provided by the inter-granular matrix porosity (MacDonald and Allen, 2001). The porosity of the Chalk matrix is estimated at between 35% and 47% (Hancock, 1975). Much of this porosity, however, is effectively inaccessible (from a hydrodynamic perspective) as the matrix porosity in the chalk is not readily drained due to a very small pore throat radius (MacDonald and Allen, 2001) (typically 0.1 to 1 μm, (Price, 1987)). The fractures act as the primary permeable pathways for fluid flow in the Chalk aquifer (Price, 1987). Therefore, much of the useful storage is in the fractures or the larger pores (MacDonald and Allen, 2001). The extensive fracture network that is found in the Chalk aquifer increases the bulk permeability by as much as three orders of magnitude (Price, 1987). Without this fracture network, the chalk would not be considered an aquifer (Price, 1987, MacDonald and Allen, 2001). However, Price (1987) suggests that even the original fracture permeability is relatively low. Therefore, fracture permeability must be enhanced through a secondary process. Dissolution enlargement of the fractures is considered the main process that enhances Chalk permeability (Price, 1987). It is this final process that gives the Chalk aquifer its high transmissivity and ensures its usefulness as a water resource (Price, 1987). MacDonald and Allen (2001) collated 2100 pumping tests conducted in the Chalk and found that the median transmissivity was 540 m^2/d, with a maximum value of 1800 m^2/d in the Yorkshire Chalk. Most of the flow in the aquifer occurs within 50 metres of

the water table, due to the aforementioned dissolution process and the reduced overburden (Jones and Robins, 1999, Williams et al., 2006, Butler et al., 2012).

Transmissivity and storage are known to mirror the topography throughout the Chalk aquifer. In the valleys transmissivity is generally higher than on the interfluves due to better developed fracture systems (Jones and Robins, 1999, MacDonald and Allen, 2001, Robins and Dance, 2003). The favourable aquifer properties found in the valleys results in a higher number of boreholes drilled in these areas (MacDonald and Allen, 2001). There are a number of reasons for the development of enhanced transmissivity in valleys (Jones and Robins, 1999). For example, valleys commonly follow lines of structural weakness and erosion in valleys reduces the effective stress resulting in opening of horizontal fractures. Preferential flow to valleys, which are zones of discharge, is believed to result in enhanced dissolution possibly due to mixing of waters with different chemical compositions. Periglaciation is also believed to have contributed towards enhanced permeability due to repeated freezing and thawing opening up fractures at depths of as much as 30 m in the valleys. Finally, there is evidence that the main fracture systems were developed during the Pleistocene when sea levels were lower, resulting in greater hydraulic gradients and groundwater flux leading to more dissolution.

Another important factor in the development of enhanced aquifer permeability in the Chalk is the presence of hardgrounds, marls and flint beds (Jones and Robins, 1999). Hardgrounds fracture more cleanly than softer chalk and have a higher permeability. Low permeability marl bands, although thin (typically only a few millimetres), can be laterally extensive (100s of kilometres) and can result in enhanced dissolution due to concentration of groundwater flow at the surface of the marl band. Similar processes can occur at flint beds. Marl bands can also act to reduce the vertical permeability of the Chalk. However, there is evidence that dissolution enhancement of vertical fractures also occurs (Maurice et al., 2012), and some key horizons, such as the Seaford Chalk, lack the marl bands present in other areas of the Chalk aquifer resulting in a more isotropic permeability field.

As a result of the Chalks very high permeability, the water table can remain relatively flat over large areas. Furthermore, the undulating topography common in Chalk areas results in an unsaturated zone tens of metres thick (Price et al., 2000). Recharge process are controlled by the dual permeability

nature of the aquifer (Ireson et al., 2009). During the summer months, the reduction in pressure due to falling water tables leads to drainage of the fractures; however, due to the high air entry pressure, estimated at 30 m based on a pore radius of 1 μm (Price, 1987), the Chalk matrix above the water table remains saturated.

2.2.3.1 Influence of Chalk hydrogeology on seawater intrusion

Clearly the properties described above will have a significant impact on flow and will consequently exert a controlling influence on seawater intrusion in the Chalk aquifer. Butler et al. (2009) analysed flow behaviour at a borehole cluster located in the Berkshire Chalk under both pumped and ambient conditions and found that different flow processes occurred under the two regimes. Under pumped conditions, they found that flow was confined to a series of discrete horizons, whereas, under ambient conditions, flow entered the boreholes over a much wider region. Flow in the discrete horizons was activated by pumping, which suggests that the fractured nature of the Chalk aquifer could significantly increase the risk of borehole salinization under pumped conditions, depending on the orientation and connectivity of the fracture networks and recharge of the aquifer. Such networks are a common feature of carbonate aquifers (Worthington and Ford, 2009).

Barker and Foster (1981) proposed that solute transport in fractured porous rock in the unsaturated zone is controlled mainly by fracture flow but that solute exchange occurs between the more mobile fracture water and the matrix water. Mathias et al. (2006) suggested that some flow must occur in the matrix in order to explain distributions of solutes that are observed in the field. Price (1987) suggests that exchange of solutes between the matrix and fractures also occurs within the saturated zone. Fracture water may elute solute from the saline matrix nearer the coast into regions of lower concentration inland. In the Chalk aquifer, diffusive exchange between the matrix and the fractures may result in a wide mixing zone because the greater the ratio of immobile to mobile porosity, the larger the extent of the transition zone (Lu et al., 2009). As saline water is carried through the fractures, with the decline in inland head over the summer, diffusion of ions from the fracture into the relatively fresher matrix may occur. As inland head begins to recover during the winter months, this process will reverse as the saline water retreats back towards the coast through the fractures, resulting

in the more saline matrix diffusing back into the fractures. In areas where the transmissivity is low solute exchange between the fractures and the matrix may be very important and lead to a relatively saline matrix over time. However, over a tidal cycle or in large fractures, the rapid flow velocities found in the aquifer may limit the effectiveness of this mechanism (Jones and Robins, 1999), and the matrix may remain relatively fresh. Clearly these micro-scale interactions will have an effect on the measured SP, but because the impact these processes may have is not known and is hard to quantify, these micro-scale affects are neglected in the preliminary modelling study, the method for which is described in section 4.3.1. Hydrodynamic dispersion will also play an important role in the Chalk aquifer (Jones and Robins, 1999). For example, dilution may occur as the saline water flows through the complex network of orthogonal fractures. It is likely that the longitudinal dispersivity will be greater than the transverse dispersivity, due to the presence of marls bands in some Chalk units restricting the vertical permeability. Therefore, this permeability anisotropy may result in a horizontally extensive, but vertically limited, transition zone (Abarca et al., 2007) within the Chalk aquifer in the study area, which is described in the following section.

2.2.3.2 Hydrogeology and seawater intrusion on the South Coast of the UK

The South Downs is made up of Lower Cretaceous to Palaeogene units (Figure 2.5). The Upper Cretaceous Chalk group is the major aquifer in the region, supplying groundwater to approximately 700,000 people, predominantly in the towns of Brighton, Worthing, Eastbourne, and Portsmouth in the coastal region (Jones and Robins, 1999). The Chalk group was previously divided into three main units; the bottom 60-70 m is classified as Lower Chalk, about 80 m is Middle Chalk and the upper 320 m is Upper Chalk. The sequence is interrupted by marls, flints and hardgrounds at regular intervals. The Lower Chalk contains a significant amount of detrital content and marls and so is much less permeable overall than the other two Chalk units. Calcareous clay marls also occur in the Middle and Upper Chalk. The marls are about 0.1 m thick and are laterally extensive; they have low permeability and can cause local perching of groundwater during periods of high recharge. The Chalk is separated from the overlying Palaeogene and the underlying Lower Cretaceous by two major unconformities (Figure 2.6). A new classification of the Chalk was developed by Bristow et al. (1997) who subdivided the traditional units into sub-divisions based on their lithology and topographic

expression. The Seaford Chalk, a sub-division of the Upper Chalk, is considered the major water bearing unit of the South Downs aquifer (Jones and Robins, 1999). In the valleys, the water table can range from 0 to 20 m, in the interfluves it can be deeper than 100 m (Jones and Robins, 1999).

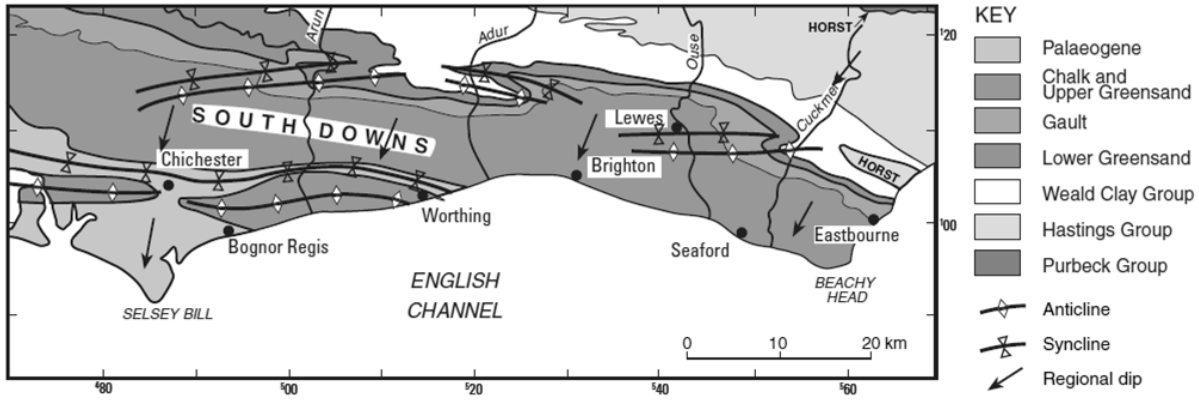

Figure 2.5 - A simplified geological map of the South Downs showing the major bedrock and highlighting the extent of the Chalk aquifer in the area (Jones and Robins, 1999).

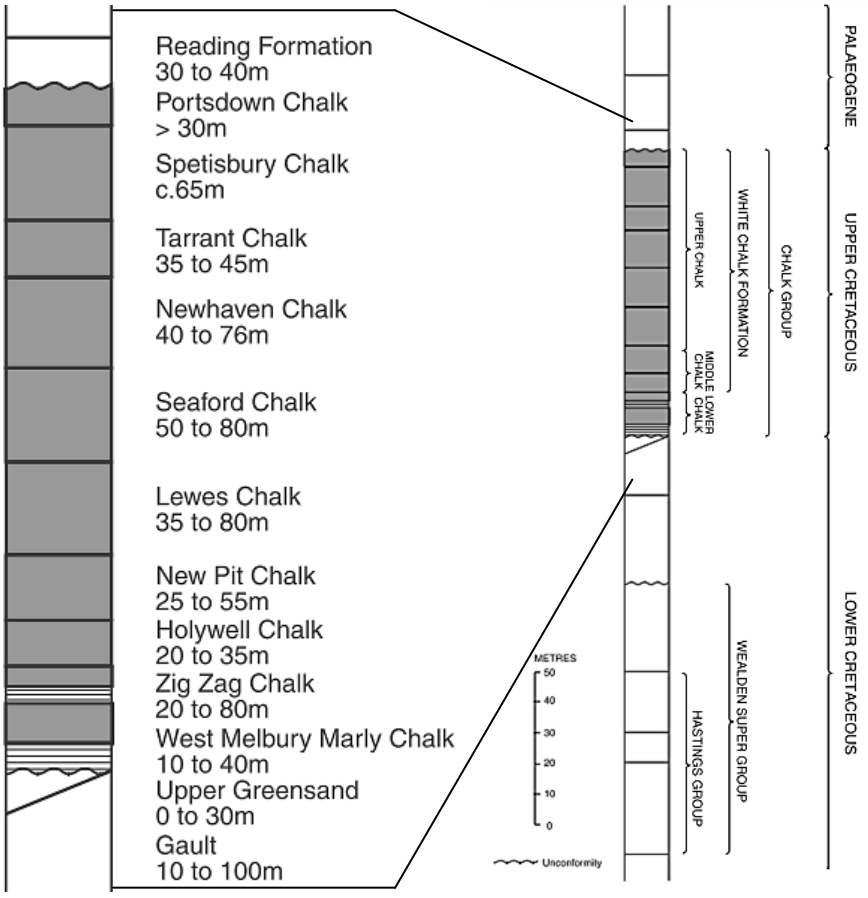

Figure 2.6 - A simplified stratigraphic column showing the main rock types, their thickness and depth. The two main unconformities found on the South Downs are also illustrated. The chalk group is the major aquifer in this area, this is highlighted in grey (Jones and Robins, 1999).

In general, groundwater flow is controlled by the regional dip of the aquifer and flows from North to South, towards the sea. Seawater intrusion is considered one of the main risks to the groundwater resource in the South Downs (Jones and Robins, 1999). Figure 2.7 shows a conceptual model of groundwater in the South Downs, illustrating the influence of fractures on seawater intrusion.

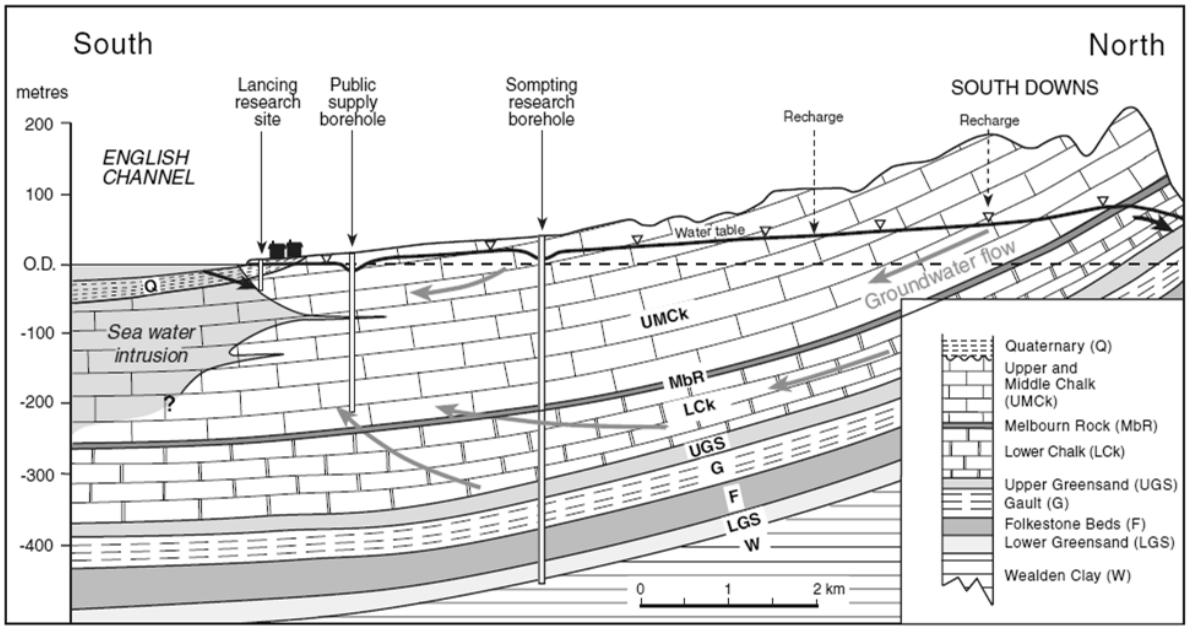

Figure 2.7 – The groundwater flow conceptual model for the South Downs area at Lancing near Brighton, from Jones and Robins (1999).

According to Monkhouse and Fleet (1975), the abstraction borehole most at risk is the Balsdean source Located 2.5 km from the coast the Balsdean abstraction borehole is a major source of drinking water for Brighton (see Figure 2.5 and Figure 4.3). There are very few published attempts at modelling seawater intrusion into the Chalk aquifer on the South Coast of the UK. However, one study conducted by Nutbrown et al. (1975) found that in order to model to observed water level fluctuations in the Balsdean area, they had to increase transmissivity values to over 2500 m^2/d. Some authors argue that due to these very high transmissivity values there are areas of the Chalk that can be described as karst (Jones and Robins, 1999, Robins and Dance, 2003), including the Balsdean area.

Monkhouse and Fleet (1975) and Fleet et al. (1977) emphasised the important role of fractures in the flow regime in the South Downs and hint at their controlling influence on seawater intrusion in the area. They noted that pressure differences created by tides and seasonal changes in inland water

pressures will create piezometric head differences between different fracture systems. If there is a connection between these systems, i.e. a vertical fracture or a borehole, then flow will occur through this vertical conduit between the two fracture systems. One implication of this is that conductivities measured in boreholes may not represent the salinity profile in the Chalk matrix, although Fleet et al. (1977) pointed out that their resistivity logs suggested that saline water had diffused into the matrix over time. Thus, the process of drilling a borehole creates a risk of allowing saline water to move further inland through fracture systems which may not previously have been connected to the sea.

Geophysical investigations of the Balsdean abstraction borehole conducted by Monkhouse and Fleet (1975) suggested that there may be a system of interconnected fractures that connect the abstraction borehole to the sea, and high rates of pumping could lead to a sharp rise in salinity after only a few hours under certain circumstances such as a very low inland heads, and during a spring tide. Monkhouse and Fleet (1975) suggested that as the tide rises, the flow of freshwater towards the sea is reduced. Eventually the tidal head dominates the freshwater head and saline water moves further inland. As a consequence Balsdean was previously not pumped three hours either side of the high tide (Jones and Robins, 1999). Furthermore, Monkhouse and Fleet (1975) observed a steady increase in salinity in coastal boreholes in the Brighton area through the summer until around the autumn equinox. After this there was an unexpected decrease in most of the boreholes which they suggested was due to decreased abstraction rates, and they speculated that pumping stations as far as 6 km inland could affect the salinity patterns of the coastal boreholes. Therefore, the South Downs was an ideal area to investigate the possibility of using SP to monitor seawater intrusion. There are a number of monitoring and abstraction boreholes that experience elevated salinities due to tidal (see chapter 5) and seasonal processes (see chapter 6) that existing SP theory introduced in chapter 1, and discussed in more details below, suggests should create measureable SP responses. In particular SP monitoring experiments in the area allowed investigation of the possibility raised in chapter 1, that SP monitoring could provide early warning of saline breakthrough in coastal boreholes.

2.2.4 Seawater intrusion monitoring strategies

A variety of monitoring strategies that have been used in seawater intrusion assessments (Werner et al., 2013). These include geochemical (Capaccioni et al., 2004, Bear et al., 1999, Mondal et al., 2010) and geophysical methods (Werner et al., 2013). The most common method is down-hole measurements of the fluid electrical conductivity (FEC) (FAO, 1997, Werner et al., 2009). However, FEC monitoring has the disadvantage of only being able to detect saline water once it has arrived in the borehole. Werner et al. (2009) studied up-coning dynamics and suggest that often the values of FEC are relatively small in the initial stages of the front intercepting the borehole. The relatively small FEC change was attributed to the rise of a dilute salt spike, caused by dispersion, at early times. By implication borehole-saline interface interactions may actually be a widespread but relatively undetected phenomenon (Werner et al., 2009). Therefore, FEC monitoring does not facilitate proactive management of groundwater abstraction in coastal areas. In addition, virtually all techniques relying on borehole observations suffer limited spatial coverage. Observation wells in the vicinity of the abstraction well are often not located near enough to be able to detect the rise of the saline cone. Most existing monitoring techniques encourage reactive management strategies because they cannot provide any information on the location of the saline interface in relation to abstraction boreholes.

Water quality sampling and analysis play an important part in seawater intrusion investigations. Sample analysis can help determine the differing origins of saline water (Bear et al., 1999) and distinguish between salinization and freshening events (Russak and Sivan, 2010). It is important to understand the type of event occurring and the seasonal nature of freshening and salinization (Russak and Sivan, 2010) as this can help characterise the processes involved in seawater intrusion and is useful in understanding and characterising the mixing zone. The FAO (1997) recommend that major ion chemical analysis should take place up to twice a year. The analysis should focus on Cl^-, Na^+, SO_4^{2-}, Ca^{2+} and Mg^{2+}. An excess of Ca^{2+}, or $Ca^{2+} + Mg^{2+}$ relative to Cl^-, or an increase in the Cl^-/ SO_4^{2-} ratio towards that of seawater, is an early warning of saline intrusion (FAO, 1997). Usually, the Na^+/Cl^- ratio is also lower in intruding seawater than would be found in marine environments, which can also provide early indications of seawater intrusion (Bear et al., 1999). The studies of Mondal et al. (2010) and Capaccioni et al. (2004) are good examples of the application of water sample analysis

methods in seawater intrusion studies. However, these methods suffer from many of the same problems as FEC monitoring, including limited spatial coverage and the fact that the changes identified have already occurred within the borehole.

Post (2005) and Werner et al. (2013) described many of the techniques and challenges in seawater intrusion characterisation and monitoring, and hint at the benefits of using geophysical methods. Geophysical methods can provide important hydraulic, lithological and salinity information over much larger areas without the need for multiple observation boreholes. However, existing techniques, mainly geoelectric methods (FAO, 1997, Wilson et al., 2006), have limitations. For example, surface based vertical electric sounding (VES) suffers from interpretation problems when high resistivity contrasts occur (Kirsch, 2006).

de Franco et al. (2009) illustrated that time-lapse monitoring of seawater intrusion is possible using surface electrical resistivity tomography (ERT), while Comte and Banton (2007) use this method to cross-validate hydrogeological models of seawater intrusion. Unfortunately, ERT, as an active technique, cannot provide truly continuous monitoring (Ikard et al., 2012) because resistivity techniques involve generating a direct current at a current injection electrode and receiving it at a potential electrode (Lowrie, 1997). The electrode array is then sequenced to build up a picture of the subsurface. This can take time; de Franco et al. (2009) managed to generate 10 tomograms per day. Although this will still provide useful information, more rapid processes such as the saline interfaces response to the onset or termination of pumping, may be only partially captured using ERT. Furthermore, it is logistically difficult to lay out long-term surface monitoring arrays in densely populated areas, such as in the coastal areas of the South Downs. Borehole ERT is another option, but requires at least two boreholes in order to conduct cross-hole monitoring, increasing the cost and the risk to the aquifer associated with additional boreholes.

Other techniques, such as time domain electromagnetic (TDM) methods which measure subsurface conductivity, have also been applied to seawater intrusion studies and can be conducted to screen large areas to assess the risk of seawater intrusion (Werner et al., 2013). Melloul and Goldenberg (1997) suggest that electromagnetic methods are useful because they can eliminate the effect of near-

surface variations, which is a common problem in other geoelectric methods. TDM can also be conducted from the air but only at considerable cost (Werner et al., 2013). However, all of these methods provide information on the resistivity or conductivity of the saturated media, rather than providing information about the fluid itself.

An alternative, passive geoelectric method is SP monitoring. The potential advantage of SP monitoring is that SP arises as a direct result of concentration gradients and groundwater flow rather than to the resistivity of the media. It has been shown that SP signals caused by groundwater flow at depth can be detected by borehole SP measurements in the UK Chalk aquifer (Jackson et al., 2012a). It is the hypothesis of this thesis that borehole SP monitoring could be used to detect and characterise the proximity of the saline interface to an abstraction or monitoring borehole. If such a hypothesis is demonstrated, it follows that SP monitoring could be used to manage coastal abstraction because it has been suggested that the currents generated by the SP source mechanisms could be detected ahead of the sources, i.e. ahead of concentration or pressure gradients induced by a saline water moving towards a monitoring or abstraction borehole (Gulamali et al., 2011, Jackson et al., 2012b). Therefore, SP monitoring has the potential to be used as an early warning and continuous monitoring technique over large areas, with dense sampling in space and time. Consequently, SP appears to be well suited to seawater intrusion monitoring.

2.3 Self-potential

2.3.1 Fundamental principles

Self-potentials arise in order to maintain overall electrical neutrality when a separation of charge occurs due to gradients in pressure (electrokinetic or streaming potential), concentration (electrochemical or exclusion-diffusion potential) and temperature (thermoelectric potential) (Revil, 1999a). These electrical flow processes are coupled to primary flow processes such as hydraulic conduction and chemical diffusion. The coupled flows are described by the principles of steady-state thermodynamics (Marshall and Madden, 1959, Nourbehecht, 1963). The constituent equations describing charge, mass, heat and species are described as follows (Jackson et al., 2012b):

$$\begin{bmatrix} j \\ q \\ j_s \\ j_d \end{bmatrix} = -\begin{bmatrix} \sigma_{rec} & L_{EK}(C_M) & L_{TE}(C_M) & L_{EED}(C_M) \\ L_{EK} & \frac{k}{\mu_w} & L_{23} & L_{24} \\ L_{TE} & L_{32} & \kappa(C_M) & L_{34} \\ L_{EED} & L_{42} & L_{43} & D(C_M) \end{bmatrix} \begin{bmatrix} \nabla V \\ \nabla(P - \rho_w g z) \\ \nabla T \\ \nabla C_M \end{bmatrix} \quad \textbf{Equation 2.7}$$

Here j is the current density (A/m^2), σ_{rec} is the electrical conductivity of saturated porous media (S/m), ∇V is the electric potential gradient (V/m), q is the flow rate (m/s), k is the absolute permeability (m^2), μ_w is the dynamic viscosity (kgm^{-1}s^{-1}), $\nabla(P - \rho_w g z)$ is the pressure gradient above hydrostatic pressure (kgm^{-1}s^{-2}), j_s is heat flux (W/m^2), κ is thermal conductivity (W/m.K), ∇T is temperature gradient (K/m), j_d is concentration flux (M.m/s), D is the diffusion coefficient (m^2/s), ∇C_M is the molar concentration gradient (M/m) and these are a function of the molar concentration of the electrolyte (C_M). The terms L_{EK}, L_{TE} and L_{EED} are the electrokinetic, thermoelectric and exclusion-diffusion current coupling terms respectively. The on-diagonal terms represent the constitutive equations, Ohm's law, Darcy's law, Fourier's law and Fick's law. The non-zero off-diagonal terms describe the cross-coupling between the constituent equations arising as a result of charge separation (Jackson et al., 2012b). Neglecting interactions between fluxes other than those resulting from separation of charge, the terms $L_{23}, L_{24,}L_{32}, L_{34}, L_{42}$ and L_{43} are assumed negligible.

The cross coupling terms for each component of SP can be expressed in terms of the saturated rock electrical conductivity (σ_{rec}) and by a coupling coefficient (C_{cc}) (Jackson et al., 2012b, Jackson, 2015) when the other contributing effects are assumed negligible and the net current is zero:

$$L_x = \sigma_{rec} C_{cc} \quad \textbf{Equation 2.8}$$

Here cc represents the subscript EK, EED or TE. The coupling coefficients (C_{cc}) are key petrophysical properties that relate the magnitude of the SP signal to the associated gradient in pressure, concentration or temperature and can be measured in the laboratory (Vinogradov et al., 2010, Leinov and Jackson, 2014, Leinov et al., 2010), the methods and the results of which are reported and discussed in chapter 3.

Since large concentration gradients are present during saline intrusion, it is hypothesised that observable EED potentials are likely to be generated. As a result of tidal effects and abstraction, EK

potentials will also be generated. Understanding the nature of each of these components of the SP signal could allow the intruding saline front to be detected and monitored continuously. Both the EK potential, and the exclusion potential component of the EED potential, arise as a result of the electrical double layer which forms at the fluid – rock interface (Hunter, 2001).

2.3.2 The electrical double layer (EDL) and carbonate surface charge

The so called electrical double layer (EDL) consists of the Stern layer and the diffuse layer (Revil, 1999b, Lorne et al., 1999) (Figure 2.8). The surface of the mineral itself has an electrical potential V_s. The Stern layer, also known as the Helmholtz layer, consists of absorbed counter-ions (Revil, 1999b) with an electric potential V_β. The Stern layer is often split into two layers, the inner and outer Helmholtz plane (IHP and OHP respectively). The IHP consists of salt ions directly bound to the mineral surface, whereas the OHP consists of weakly bound hydrated ions (Lorne et al., 1999). The final component of the EDL is the diffuse layer. The ions in the diffuse layer are predominantly of the opposing polarity to the surface charge. The Boltzmann distribution is assumed to describe the ion distribution within the columbic field created by the ionisation of the surface sites. Relative motion between the mineral surface and the electrolyte results in shear within the diffuse layer. Ions within the diffuse layer are mobile beyond the shear plane and have an electrical potential V_d. The concentration of excess counter-ions decreases away from the mineral surface until the fluid is neutral. The neutral fluid is the bulk electrolyte with potential V_{bulk}, which is assumed to be zero.

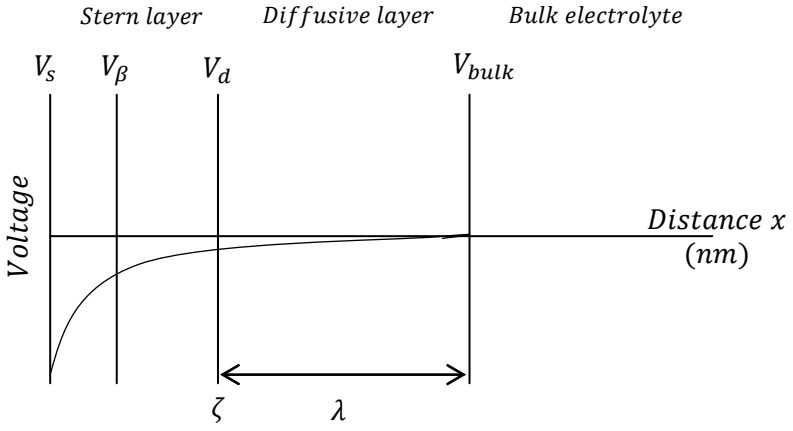

Figure 2.8 – The electrical double layer (EDL) that forms at the interface between an electrolyte and the surface of a mineral. The magnitude of the electrostatic potential decays through the EDL and away from the surface until it is zero in the bulk electrolyte. The zeta potential (ζ) is defined on the shear plane between the Stern layer and the diffusive layer. The shape of the voltage curve depends on the nature of the surface charge. Adapted from Hunter (1981), Revil (1999b) and Lorne et al. (1999).

Charge distribution in the diffuse layer is described by the Poisson-Boltzman equation (Lorne et al. 1999):

$$\frac{d^2V(x)}{dx^2} = \frac{N_A e}{\varepsilon_w}\sum z_i C_{Mi}^0 exp\left[-2z_i \frac{V(x)e}{2k_b T}\right] \quad \textbf{Equation 2.9}$$

Here $V(x)$ is the potential distribution within the diffuse layer, ε_w is the dielectric permittivity of the electrolyte in solution (F/m), k_b is the Boltzmann constant (1.3806488x10^{-23} m^{2}kgs^{-2}K^{-1}), T is the temperature (K), e is the electron charge (1.60217657x10^{-19}C), N_A is Avogadro's number (6.02214129x10^{23} mol^{-1}), z_i is the valence of ion i, and C_{Mi}^0 is the concentration of ion i when the potential is zero. Note that the Poisson-Boltzmann equation is not valid at high salinity (Vinogradov et al., 2010). The characteristic thickness of the diffuse layer is given by the Debye length (λ) (Revil, 1999b, Leinov and Jackson, 2014, Jackson, 2015), which is related to the total ionic strength (I) of the electrolyte (Equation 2.1):

$$\lambda = \left(\frac{\varepsilon_w k_B T}{2000 e^2 N_A I}\right)^{\frac{1}{2}} \quad \textbf{Equation 2.10}$$

The zeta potential (ζ), the potential on the shear plane between the Stern layer and the diffuse layer (Figure 2.8), is a very important component of the EDL model, as most studies of mineral surface use the zeta potential as a proxy for the surface charge because it is difficult to measure surface charge directly. Methods for determining zeta potential include electrophoresis (Sondi et al., 2009, Heberling et al., 2011) and electrokinetic potential (Somasundaran and Agar, 1967, Thompson and Pownall, 1988, Guichet et al., 2006, Eriksson et al., 2007, Eriksson et al., 2008). The shear plane is considered statistically at a distance x_ζ from the surface (Revil, 1999b) and the charge distribution within the diffuse layer is approximated by a simple exponential form:

$$\zeta = V_d(x) \approx V_d exp\left(\frac{-x_\zeta}{x_d}\right) \quad \textbf{Equation 2.11}$$

Equation 2.12 results from the solution of the Poisson-Boltzmann equation. Revil (1999b) assumed that the shear plane is located at the edge of the Stern layer, where $x_\zeta = 0$, then:

$$\zeta = V_d \quad \textbf{Equation 2.12}$$

Thus, it is assumed that the zeta potential is representative of the potential at the shear plane, between the Stern layer and the diffusive layer (Revil, 1999b) (Figure 2.8).

The Chalk aquifer consists of a very pure form of calcite ($CaCO_3$) (Hancock, 1975). The surface charge of calcite and the mechanisms for this charge are still poorly understood. The large variations in literature values of calcite zeta potential (Figure 2.9) are attributed to the source of the calcite, whether natural or synthetic (Vdovic and Biscan, 1998), whether in contact with atmospheric CO_2 (Thompson and Pownall, 1988) and the type of electrolyte used (Cicerone et al., 1992).

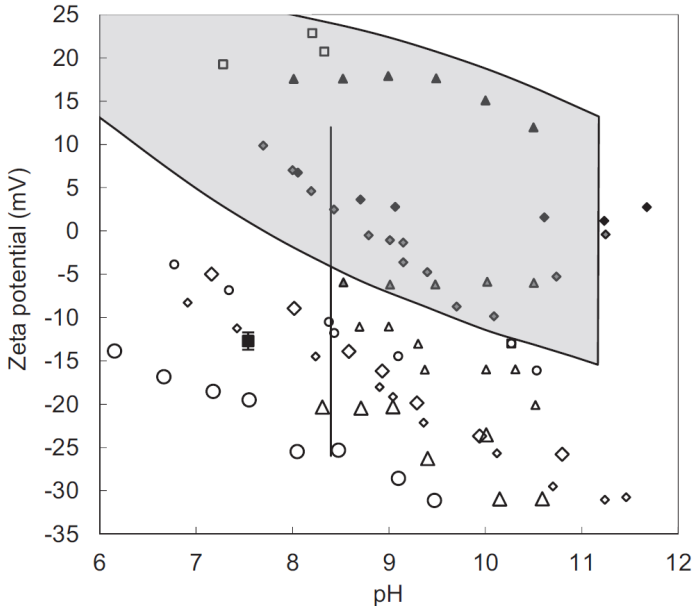

Figure 2.9 – The range of zeta potential values reported for calcite. The grey area indicates the values predicted by Guichet et al. (2006). Also shown, as a black square, is the result for Seaford Chalk saturated with natural groundwater published by Jackson et al. (2012a). This diagram is taken from that work. Open squares show data from natural carbonate samples in equilibrium with de-ionised water (Somasundaran and Agar, 1967). Circles show data from natural carbonate samples (small open circles, limestone; large open circles, lake sediment) in equilibrium with NaCl electrolyte (from Vdovic 2001). Diamonds show measurements on synthetic carbonate in equilibrium with different electrolytes (open diamonds, NaCl (5×10^{-3}M); large open diamonds, NaCl (5×10^{-3}M)/ $NaHCO_3$ (10^{-3}M); black diamonds, $CaCl_2$ (5×10^{-4}M); grey diamonds, NaCl (5×10^{-3}M)/$NaHCO_3$ (10^{-3}M); from Thompson & Pownall 1989). Triangles show measurements on natural (large open triangles) and artificial carbonates in equilibrium with KCl; (open triangles, artificial samples; grey triangles, with added $CaCl_2$ (10^{-3}M); black triangles, with added $CaCl_2$ (10^{-2}M); from Cicerone et al. 1992). Vertical line shows the spread of values measured on Stevns Klint Chalk in equilibrium with NaCl (0.573M), with added Ca, Mg and SO_4 ions (from Strand et al. 2006; Zhang & Austad 2006; Zhang et al. 2007).

Somasundaran and Agar (1967) investigated the properties of the calcite surface and suggested that the potential determining ions (PDI's), i.e. those ions whose concentration in aqueous solution control the polarity and density of electrical charge on the mineral surface, are Ca^{2+}, CO_3^{2-}, and HCO^{3-}. Cicerone et al. (1992) concluded that Mg^{2+} acts as a PDI under certain circumstances, controlled by the pH and the concentration of $MgOH_2$. At low pH (< 8), Mg^{2+} acts as an indifferent ion. Strand et al.

(2006) and Zhang et al. (2007) suggested that the surface charge of calcite is dictated by the relative contributions of two PDI's, Ca^{2+} and SO_4^{2-}, with SO_4^{2-} becoming more strongly absorbed at higher temperatures. H^+ and OH^-, the pH determining ions, play a secondary role through controlling the relative availability of the primary PDI's by hydroxylation and specific absorption and dissolution of the primary PDI's. At high pH, calcite approaches equilibrium with water and CO_3^{2-} is increasingly soluble (Somasundaran and Agar, 1967, Cicerone et al., 1992). Therefore, there is an excess of CO_3^{2-} which is specifically absorbed within the Stern layer and leads to a negative zeta potential (Somasundaran and Agar, 1967). At low pH, there is an excess of Ca^{2+} within the Stern plane, due to its increased solubility (Cicerone et al., 1992), leading to a positive surface charge (Figure 2.10). Thompson and Pownall (1988) and Cicerone et al. (1992) investigated the zeta potential of calcite in $CaCl_2$ solutions finding that the added availability of Ca^{2+} made the surface charge more positive. The additional Ca^{2+} was found to be the primary controlling factor for the surface charge and their results further emphasised the pH independence of the zeta potential for calcite (Cicerone et al., 1992). When the water is in equilibrium with atmospheric CO_2, such as is the case for chalk groundwater (Jones and Robins, 1999), the effect of excess Ca^{2+} is countered by the adsorption of CO_2 resulting in a more negative surface charge due to enhanced presence of CO_3^{2-} (Thompson and Pownall, 1988).

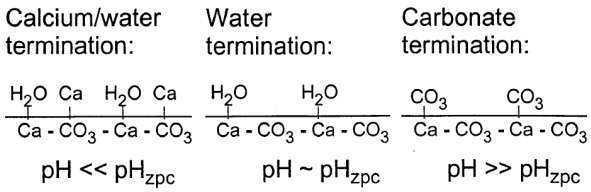

Figure 2.10 – The surface of carbonates and absorbed ions at different pH values (Fenter et al., 2000). The zero point of charge (ZPC) is the pH at which the surface is uncharged. The isoelectric point (IEP) depends on the specific adsorption of positive and negative ions at the surface. The IEP is the point of zero net charge on the shear plane as a consequence of charge balance within the EDL.

The processes that control the surface charge of calcite are complex; however, there are various models to represent the carbonate mineral-aqueous solution interface. The most widely used is the surface complexation model by Van Cappellen et al. (1993). The reactions shown in Figure 2.11(a) are thought to govern surface speciation. This model is considered to replicate well the ZPC, the insensitivity of surface charge to pH, and the dependence of dissolution kinetics of calcite in terms of surface speciation (Wolthers et al., 2008). A model of the EDL for calcite is shown in Figure 2.11(b).

(a)

$$>CO_3H^0 \Leftrightarrow >CO_3^- + H^+$$

$$>CO_3H^0 + Me^{2+} \Leftrightarrow >CO_3Me^+ + H^+$$

$$>MeOH_2^+ \Leftrightarrow >MeOH^0 + H^+$$

$$>MeOH^0 \Leftrightarrow >MeO^- + H^+$$

$$>MeOH^0 + CO_2 \Leftrightarrow >MeHCO_3^0$$

$$>MeOH^0 + CO_2 \Leftrightarrow >MeCO_3^- + H^+$$

(b)

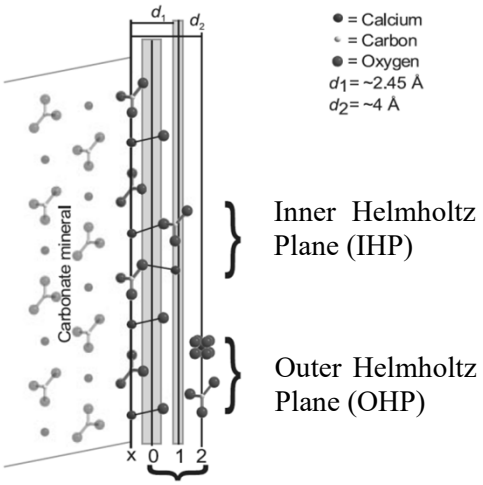

Figure 2.11 – The surface complexation model proposed by Van Cappellen et al. (1993), Me represents any divalent metal cation. b) The structure of the calcium carbonate EDL proposed by Wolthers et al. (2008).

Vinogradov et al. (2010) investigated the effects of increased salinity in sandstones and found that the zeta potential decreased with increased salinity. At salinities above c.0.4 M the zeta potential became independent of salinity; note that seawater has a salinity of c.0.7 M (Table 2.1). The shrinking of the diffuse layer until its thickness is about the same size as the hydrated counter-ions was suggested as the mechanisms responsible for this observation. A similar process is expected to occur in carbonates. Kosmulski et al. (2003) measured the zeta potential of calcium carbonate in artificial seawater and found a zeta potential of +1.91 mV. They stated that the high salt concentration in natural seawater decreases the value of the zeta potential, relative to freshwater, by a factor greater than 10.

The final determining factor of the calcite surface charge is the effect of impurities. Impurities include the presence of Mg^{2+} in natural calcite (Cicerone et al., 1992, Sondi et al., 2009), the presence of organic matter in biogenically formed calcite (Cicerone et al., 1992, Vdovic and Biscan, 1998, Vdovic, 2001) and the presence of organic matter in natural waters, such as seawater (Cicerone et al., 1992, Vdovic and Biscan, 1998, Vdovic and Kralji, 2000). Cicerone et al. (1992) investigated the influence of organic matter in biogenically formed calcite and in natural water and conclude that biogenic calcium carbonate has a more negative surface charge than synthetic calcite, which was attributed to the presence of organic matter in the calcite matrix. The more negative surface charge as a result of organic matter in the calcite was later confirmed by Vdovic and Biscan (1998) who found

natural calcite had a negative zeta potential in all experiments. They attributed this to deprotonation of an organic coating attached to the calcite surface. Organic coatings could include carboxylic acids such as fulvic acid. Later work by Vdovic and Kralji (2000) suggests that the presence of fulvic acid can actually reverse the surface charge of synthetic calcite from positive to negative. Yuan et al. (2008) observed a sign reversal of the positive calcite surface charge after introducing anti-scalants such as Calgon. Like fulvic acid, Calgon is a polyelectrolyte. They suggested the mechanism for this charge reversal involved the ring structure of the anti-scalant being adsorbed to the calcite surface, leaving a negatively charged surface. They further suggested that some of the functional groups determine the ability of the polyelectrolyte to be adsorbed to the calcite surface, while the rest act as PDI's. It seems reasonable to assume a similar mechanism for natural polyelectrolytes such as fulvic acid. Consequently, a negative zeta potential and surface charge is likely to be observed in the field where biogenically deposited chalk is in contact with natural seawater and groundwater.

2.3.3 Electrokinetic potential

The electrokinetic potential arises as a result of electrolyte flow due to the presence of an external pressure gradient (Hunter, 2001) (Figure 2.12). The flowing electrolyte drags some of the excess counter-ions in the diffuse layer along with it. This leads to movement of a net electric charge carried by the counter-ions; thus, a streaming current is generated (Hunter, 1981). To maintain the overall electrical neutrality, an electrokinetic potential drives an Ohmic conduction current. Divergence of the streaming current density leads to a streaming or electrokinetic potential (Hunter, 2001).

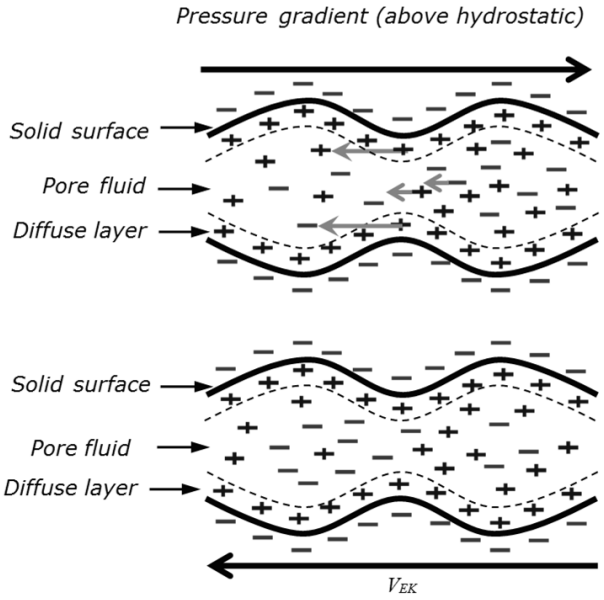

Figure 2.12 – The physical process leading to the EK potential. A pressure gradient causes the fluid to flow, this drags along the ions in the fluid. However co-ions are retarded within the Stern layer of the EDL and these in turn retard the counter-ions in the diffuse layer leading to a separation of charge (Jackson et al., 2012b).

From Equation 2.7 and Equation 2.8, under steady-state, one-dimensional flow in an electrically isolated medium, the EK coupling coefficient (C_{EK}) relates the fluid (dP) and electric potential (dV) gradients when the total current density (j) is zero (Vinogradov et al., 2010):

$$dV = C_{EK} dP|_{j=0}$$ **Equation 2.13**

dV and dP can be directly measured in the laboratory and Equation 2.13 forms the basis of the laboratory measurements of the electrokinetic potential. The magnitude of the coupling coefficient decreases as the salinity of the electrolyte increases (Revil et al., 2005, Jaafar et al., 2009, Vinogradov et al., 2010). The diffuse layer thickness is reduced as the ionic strength of the electrolyte increases because more of the counter-ions are packed into the immobile part of the EDL. As the diffuse layer collapses, less charge is transported down the pressure gradient, resulting in a smaller coupling coefficient. Vinogradov et al. (2010) approximated the relationship between salinity (C_M) and the coupling coefficient (C_{EK}) as follows, the coefficients m and n are less than zero:

$$C_{EK} = mC_M^n$$ **Equation 2.14**

The coupling coefficient can be related to the zeta potential (ζ) as follows (Jouniaux and Pozzi, 1995, Vinogradov et al., 2010):

$$C_{EK} = \frac{\varepsilon_w \zeta}{\mu_w \sigma_{rec} F}$$ **Equation 2.15**

Here σ_{rec} is the electrical conductivity of the saturated rock, ε_w is the dielectric permittivity and μ_w is the dynamic viscosity. F is the formation factor which is the ratio of the rock conductivity to the conductivity of the saturating electrolyte (σ_{fec}) and is measured when the surface electrical conductivity is negligible (Hunter, 2001, Vinogradov et al., 2010):

$$F = \frac{\sigma_{fec}}{\sigma_{rec}}$$ **Equation 2.16**

When σ_{rec} is negligible, Equation 2.15 simplifies to the Helmholtz-Smoluchowski equation:

$$C_{EK} = \frac{\varepsilon_w \zeta}{\mu_w \sigma_{fec}}$$ **Equation 2.17**

2.3.4 Exclusion-diffusion potential

The exclusion-diffusion potential has two source mechanisms illustrated in Figure 2.13. The first, known as the diffusion or liquid-junction potential, arises purely as a result of a separation of charge due to a concentration gradient and differences in ion mobility (Revil, 1999a, Leinov and Jackson, 2014). The second, known as the membrane or exclusion potential is influenced by the thickness of the EDL relative to the pore throat radius (Westermann-Clark and Christoforou, 1986, Leinov and Jackson, 2014) affecting the relative motion of the ions down the concentration gradient. If the thickness of the EDL is large relative to the pore throat radius then co-ions are excluded from the pore-space and a net excess of counter-ions migrate down the concentration gradient (Revil, 1999a, Leinov and Jackson, 2014). In natural environments, a combination of the two processes is likely to occur, i.e. neither pure exclusion nor diffusion potential will occur. In natural systems the exclusion and diffusion potential mechanisms compete for predominance, the relative contribution of the exclusion and diffusion processes depends on the mobility contrast between co-ions and counter-ions, the thickness of the EDL relative to the pore throat radius and the mineral surface charge. Although highly unlikely, in natural environments it is possible that the two mechanisms could cancel one another out. Given a certain ionic mobility ratio between anions and cations, a certain surface charge and EDL thickness, the competing mechanisms can have equal magnitude but opposite polarity resulting in an exclusion-diffusion potential equal to zero.

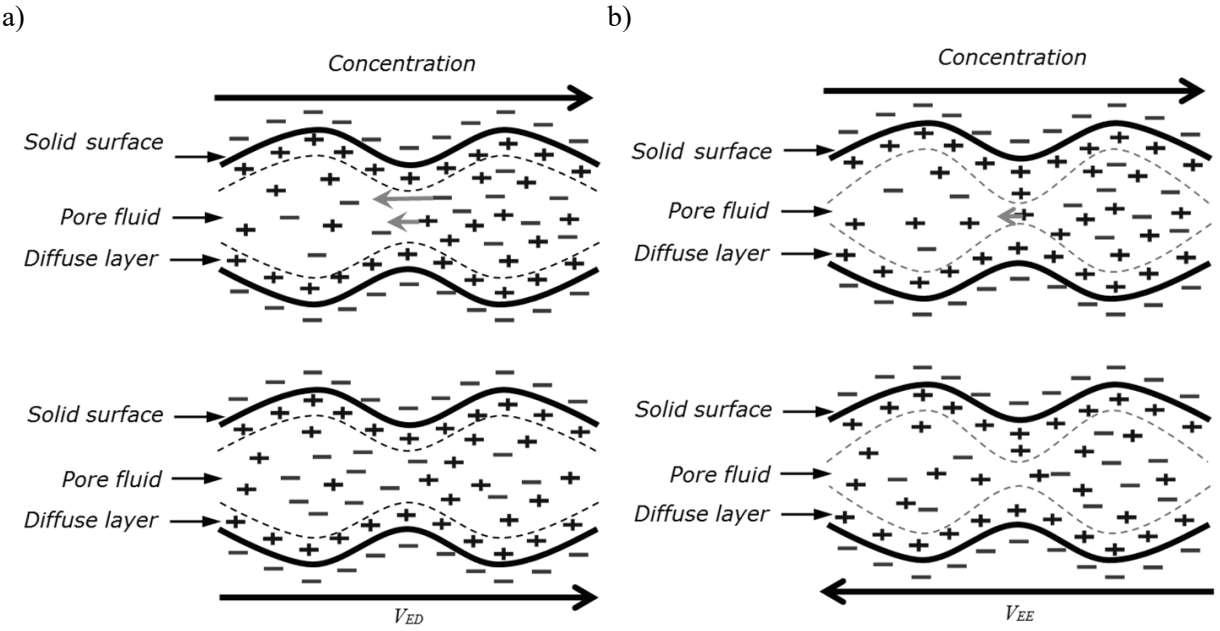

Figure 2.13 – The physical process leading to the exclusion-diffusion potential. (a) The diffusion potential. A concentration gradient forces the ions in the pore space to migrate to areas of lower concentration. Different ions have different mobilities which results in a separation of charge, known as the diffusion potential. (b) The exclusion potential. If the EDL occupies the whole pore space then the counter-ions will be unable to migrate down the concentration gradient. In natural environments a combination of both process will act together to generate an exclusion-diffusion potential (Jackson et al., 2012b).

The exclusion-diffusion potential for a 1:1 electrolyte is given by (Revil, 1999a):

$$\nabla V_{\mathrm{EED}} = -\frac{k_b T}{e}(2T_+ - 1)\nabla ln(a) \qquad \textbf{Equation 2.18}$$

Here $T_{\pm} = \frac{\sigma_+}{\sigma_+ + \sigma_-}$ is the macroscopic transport numbers of the cation or the anion and σ is the macroscopic electrical conductivity, where $\sigma = \sigma_+ + \sigma_-$ and $\sigma_{\mp}$ are the ionic contributions to σ. The electrolyte activity (a) is related to concentration (C_M) by an activity coefficient (γ) where $a = \gamma C_M$ (Braun and Weingartner, 1985). The limiting cases of pure diffusion and pure exclusion potentials are described below.

2.3.4.1 Diffusion potential

The diffusion potential arises as a result of separation of charge due to concentration gradients, under isobaric and isothermal conditions, and different ionic mobilities (Revil, 1999a, Leinov and Jackson, 2014). Sodium ions, for example, have a mobility at 25°C of about 70% that of chloride ions (Braun and Weingartner, 1985, Westermann-Clark and Christoforou, 1986). The resulting separation of charge is balanced by the diffusion potential to maintain overall electroneutrality (Revil, 1999a,

Leinov and Jackson, 2014). According to Revil (1999a) the gradient in diffusion potential (∇V_{ED}) is related to the gradient in electrolyte activity (a) by:

$$\nabla V_{ED} = -\frac{k_B T}{e}(t_+ - t_-)\nabla ln(a) \quad \textbf{Equation 2.19}$$

Here $t_\pm = \frac{\beta_\mp}{(\beta_+ + \beta_-)}$ are the ionic transport numbers of the cation and the anion respectively and β are the ionic mobilities of the cation and anion repectively. Note that $t_+ + t_- = 1$, so equation 19 can be written:

$$\nabla V_{ED} = -\frac{k_B T}{e}(2t_+ - 1)\nabla ln(a) \quad \textbf{Equation 2.20}$$

2.3.4.2 Exclusion potential

The higher the surface charge and the thicker EDL relative to the pore throat radius the more likely it is that the co-ion is expelled from the pore-space (Westermann-Clark and Christoforou, 1986). When all the co-ions are excluded from the pore-space the medium is termed a perfect membrane (Leinov and Jackson, 2014). The exclusion potential is also known as the membrane potential. The gradient of the exclusion potential (∇V_{EE}) can be expressed as (Revil, 1999a):

$$\nabla V_{EE} = -\frac{k_B T}{e}\nabla ln(a) \quad \textbf{Equation 2.21}$$

This relates the gradient in exclusion potential across a porous medium, in which all the co-ions have been excluded, to the gradient in electrolyte activity (Revil, 1999a, Leinov and Jackson, 2014). Integrating across a perfect membrane separating two electrolytes, with activities a_1 and a_2, gives:

$$V_{EE} = -\frac{k_B T}{e} ln(\frac{a_2}{a_1}) \quad \textbf{Equation 2.22}$$

2.3.5 Modelling SP

There are examples of both forward modelling (Sheffer and Oldenburg, 2007, Gulamali et al., 2011, Jackson et al., 2012b) and inversion (Revil et al., 2004, Straface et al., 2007, Jardani et al., 2008, Revil and Jardani, 2010) of SP data in the literature. In some cases, an SP post processor has been used in conjunction with an industry standard fluid flow model for forward modelling. The industry software

package is used to solve for the pressure, velocity and concentration and the post processor uses the calculated gradients to solve for the distribution and magnitude of the SP sources. For example, Sheffer and Oldenburg (2007) use MODFLOW, a common groundwater modelling tool, and Saunders et al. (2008), Gulamali et al. (2011) and Jackson et al. (2012b) use Eclipse 100, a reservoir simulator developed by Schlumberger. Note that chapter 4 reports the method for the hydrodynamic and electrodynamic models of the regional coastal aquifer.

Saunders et al. (2008), Gulamali et al. (2011) and Jackson et al. (2012b) developed a finite element method to solve the electrodynamic equations. The electrodynamic problem is related to the hydrodynamic problem via Equation 2.7. Therefore the constitutive equation used by these authors can be written as (Gulamali et al., 2011, Jackson, 2015):

$$\boldsymbol{j} = -\sigma_{rec}\nabla V + L_{EK}\nabla(P_w - \rho_w g z) + L_{EED}\nabla ln\,(C_M) \qquad \textbf{Equation 2.23}$$

Assuming that there are no external current sources or sinks, the net flow through the model is zero, i.e. charge is conserved throughout the model:

$$\nabla \cdot \boldsymbol{j} = 0 \qquad \textbf{Equation 2.24}$$

This results in:

$$\nabla \cdot \sigma_{rec}\nabla V = \nabla \cdot (L_{EK}\nabla(P_w - \rho_w g z) + L_{EED}\nabla\, ln(C_M)) \qquad \textbf{Equation 2.25}$$

2.3.6 Applications of SP monitoring

As highlighted in chapter 1 SP monitoring has a broad range of applications in hydrogeological investigations, from water flow in and around volcanoes to sub-glacial flow and application in dam leakage investigations and subsurface contamination. There are no existing studies of SP monitoring of seawater intrusion in fractured coastal aquifers. Thus, this section examines existing evidence, within the literature, for the application of SP for long-term seawater intrusion monitoring in fractured coastal aquifers.

2.3.6.1 SP survey design

Long-term SP monitoring studies can be conducted using down-hole electrode arrays, installed in the aquifer, and/or a multi-electrode surface array with a reference electrode placed outside the survey

area (Corwin, 1990). The SP recorded is the potential difference between each electrode and the reference electrode.

Noise, stability and electrode degradation are the key issues faced by SP monitoring (Corwin, 1990). Noise is a potential generated by a source other than that being investigated. Error is the irreproducible component of the signal associated with the acquisition process (Corwin, 1990). Petiau and Dupis (1980) defined noise as the peak-to-peak value (V_{pp}) for a constant relative bandwidth. Potential sources of noise include low frequency variations, such as those related to temperature and soil moisture changes (Ernstson and Scherer, 1986), or high frequency signals, related to percolation of rainfall through the unsaturated zone (Ernstson and Scherer, 1986, Perrier, 2000). Pinettes et al. (2001) highlight some of the challenges of detecting EK potentials generated at depth in fractured aquifers. A particular challenge is the possibility that shallower sources may generate SP anomalies masking the sources of interest. Natural telluric currents and anthropogenic sources such as buried electricity cables are additional sources of noise.

One of the most significant sources of noise when electrodes are in contact with the ground is related to electrochemical potentials generated in the vicinity of the electrodes. When a simple metal rod is in contact with an electrolyte, such as saturated soil, the potential between the rod and the soil can be hundreds of mV and is liable to change by hundreds of mV due to changes in soil humidity (Perrier et al., 1997). Non-polarising electrodes can reduce this problem by minimising the contact potentials with the electrode by introducing an intermediate medium where a metal/metal-ion couple, e.g. $Pb/PbCl_2$ or Ag/AgCl, is stabilised by a salt, e.g. NaCl or KCl, of the metal-ion (Petiau and Dupis, 1980, Perrier et al., 1997). The electrolyte used can be contained in a liquid reservoir or absorbed onto various different materials such as kaolinite or plaster. The reservoir or saturated material is then separated from the environment by a porous membrane, leaving only the liquid-junction potential across the membrane which is on the order of tens of mV (Perrier et al., 1997). Although the liquid-junction potential is essentially the same as the diffusion potential described above, the term liquid-junction potential is used when discussing the electrodes in order to distinguishes this electrode effect from naturally occurring diffusion potentials which maybe the target of a field study. Figure 2.14

shows the typical design of non-polarisable electrodes. Perrier et al. (1997) conducted a one year systematic study of different types of electrodes and concluded that silver/silver chloride (Junge, 1990) and lead/lead chloride (Petiau, 2000) electrodes are the most suitable type of electrode for conducting long-term monitoring experiments. Ideally the potential difference of polarisation between electrodes should be zero; if two electrodes were truly identical this would be the case.

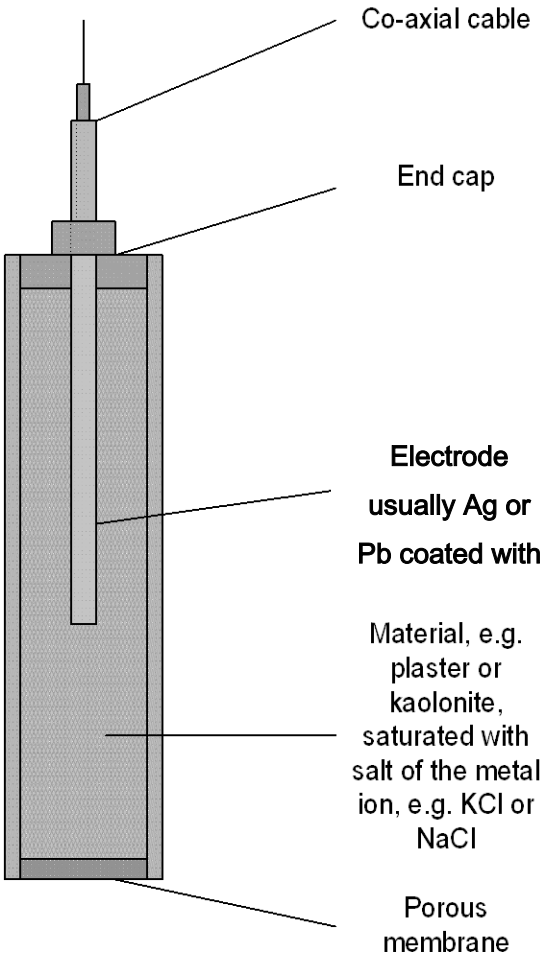

Figure 2.14 – Typical design of non-polarisable electrodes used in field based applications. Adapted from Junge (1990) and Petiau (2000).

SP surface monitoring or borehole measurements referenced at the surface are likely to be affected by temperature fluctuations due to the temperature sensitivity of electrodes. The temperature coefficient of a non-polarisable electrode depends on the equilibrium concentration of ions in the electrolyte solution. The equilibrium concentration is the point at which the temperature dependence of the electrode is minimised (Petiau and Dupis, 1980). The most suitable electrodes are those in which the salts can be brought as close as possible to their equilibrium concentration. Oversaturated solutions

allow the concentration to be kept constant ensuring the electrodes do not degrade over time. The temperature coefficient for lead/lead chloride electrodes at 25°C is -40 μV/°C and for silver/silver chloride electrodes it is -410 μV/°C (Petiau and Dupis, 1980).

Other important considerations in designing an SP survey include the equipment used and installation of the electrodes. The recording device should have high input impedance, so that it does not contribute to the noise (Petiau and Dupis, 1980, Corwin, 1990, Perrier et al., 1997). If possible natural telluric currents should also be monitored, as these are likely to have an impact on the recorded SP. Corwin (1990) suggested that thermocouples should be installed at each electrode, so that temperature effects can be assessed and removed if required at the data processing stage. However, the electrodes should be installed so as to ensure minimum exposure to diurnal temperature variations (Perrier et al., 1997, Corwin, 1990), which can be achieved by burying the electrodes at depth. Perrier et al. (1997) found that installing the electrodes in a plastic bucket filled with salted kaolinite significantly improved the quality of the data recorded from each electrode. It is likely that the use of the bucket minimised electrical potentials generated by water percolating to the water table through the unsaturated zone (Perrier, 2000). Trique et al. (2002) provided a good example of long-term SP surface monitoring survey design (Figure 2.15). They monitored groundwater level changes in response to lake level changes in the French Alps. They found an SP response of about 2.4 mV per metre of water level change, which corresponded to a total lake level fluctuation of about 50 m.

Downhole electrodes are not likely to suffer from as much noise and data quality issues as surface electrodes, mainly because the electrodes will be installed at depth in the aquifer with minimal exposure to temperature variations and no exposure to water percolating through the unsaturated zone. In addition, SP signals measured downhole could be larger than those measured at the surface as they will be in better electrical contact with the source. The long-term experimental design adopted at the coastal monitoring site is reported in chapter 4.

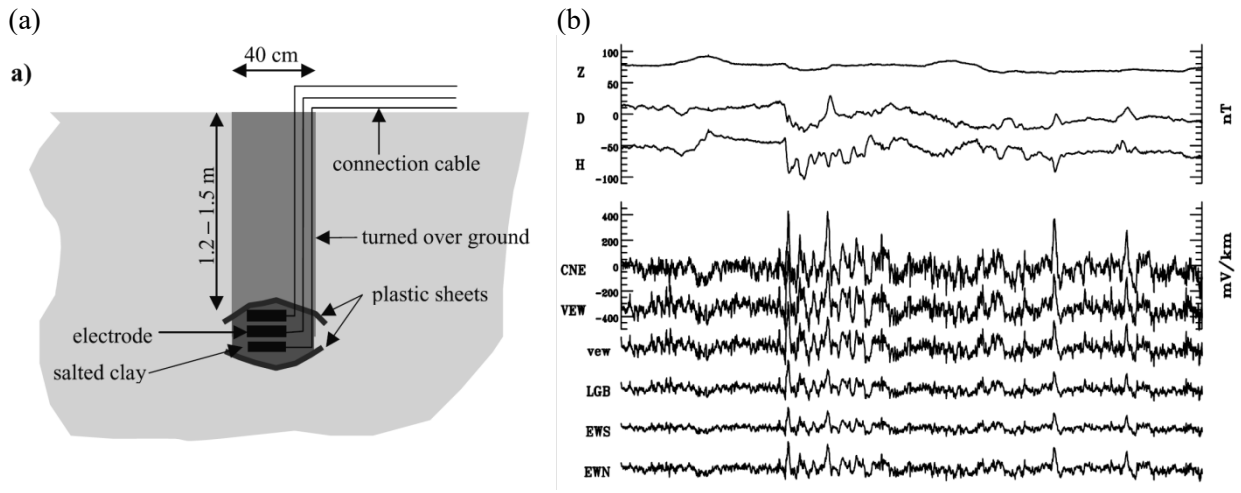

Figure 2.15 –The long-term experimental design used by Trique et al. (2002). a) The experimental set-up involved an array of 14 electrodes installed at a depth of 1.5m in salted kaolinite and arranged in 20 dipoles, a three component flux gate magnetometer to monitor telluric currents and a full meteorological station measuring air and soil temperatures and rainfall amongst other parameters. (b) The raw data from the experiment; notice the correlation between SP measured in mV/km and magnetotelluric effects on the top three lines of (b).

2.3.6.3 SP monitoring in fractured media

Several studies have examined SP in fractured media. For example, work by Zhou et al. (1999) in a karst aquifer in Indiana in the USA found SP anomalies, in a surface array, that correlated with vertical recharge. They related the negative SP anomalies to the presence of sinkholes. Hunt (2000) observed a relationship between EK potential and fracture aperture in a limestone aquifer in South Cumbria in the UK. They used a mechanical source to generate the flow of water in the fracture, and suggested that the observed SP signals were consistent with an EK source. More recently Suski et al. (2008) conducted SP, conductivity and calliper logging in a borehole in a karst aquifer in northern Germany. They found, qualitatively, that SP was correlated with the conductivity and calliper logs, and suggested that SP could be used to distinguish between hydraulically active and inactive fractures.

Furthermore, Wishart et al. (2008) conducted surface based azimuthal SP (ASP) surveys in a fractured crystalline basement aquifer, and suggested that SP was positively correlated with the number of fractures. The direction of the lobes of the azimuthal SP signal was believed to be indicative of the direction of flow within the fractures and was interpreted to be consistent with the EK potential. Wishart et al. (2009) subsequently examined the use of ASP surveys to characterise pneumatically fractured rocks in a laboratory study. They found that the ASP results from the laboratory were consistent with those from the field and argued that SP monitoring can be a powerful tool for studying

and characterising fractured aquifer systems. Similar conclusions were reached by Robert et al. (2011a) who observed SP anomalies in a fractured carbonate aquifer associated with areas of high borehole yield. They also found strong correlations with the hydraulic head gradient and attributed the observed SP to the EK potential. In another study in Switzerland, Maineult et al. (2013) attributed SP anomalies that appeared after drilling new boreholes to hydraulic reactivation of fractures. Similarly, Revil et al. (2015) observed SP anomalies in the laboratory associated with the development of new fractures after hydraulic fracturing, and found that the flow through the fractures could be remotely detected using SP. Finally, Bumpus and Kruse (2014) observed episodic SP anomalies in a surface array over the location of karstic conduits in a limestone aquifer. The anomalies were associated with changes in the conduit permeability caused by migration of clay, silt and sand through the conduits and ravelling which blocked the conduits. Positive SP anomalies were associated with high permeability conduits and negative SP anomalies with the blocked low permeability conduits.

It is clear that SP monitoring could be a very powerful tool for studying fluid dynamics in karst and fractured aquifers, and that both downhole (Hunt, 2000, Suski et al., 2008) and surface monitoring (Wishart et al., 2008, Robert et al., 2011b) can yield important information on fracture properties and groundwater flow directions within fractures. This has potential implications for SP monitoring in the highly fractured UK Chalk aquifer where fractures provide most of the aquifers transmissivity and storativity. However, the studies mentioned above all attributed the SP anomalies observed to the EK potential. None of the studies were conducted in fractured systems with significant concentration gradients. Thus, in the coastal Chalk aquifer the EED potential is likely to contribute significantly to the observed SP, complicating interpretation of the SP data.

2.3.6.4 Periodic SP signals

In coastal aquifers, periodic tidal process are likely to affect the pressure and concentration gradients (Kuan et al., 2012). Therefore, marine tides will lead to an EK response driven by periodic fluctuations in pressure. Tidal motion will also cause the saline front to fluctuate in the aquifer resulting in changes to the EED potential generated as a result of the concentration gradient between seawater and groundwater. Therefore, it is likely that SP monitoring data in coastal areas will have a

strong tidal periodicity. Table 2.4 shows the dominant tidal frequencies and their relative amplitudes, including the shorter period tides observed in the English Channel (Hamilton, 1978, Walters, 1987, Baptista et al., 1989). The short period tides are generated because of the limited width and depth of the English Channel (Hamilton, 1978, Walters, 1987, Baptista et al., 1989). Periodic signals, such as tides, if present in the SP data measured in South Downs coastal area of the UK, could be useful in helping to determine the primary SP source mechanisms, and could assist in the analysis and interpretation of SP data. Thus, in the remainder of this study natural tidal fluctuations are of significant interest to assessment of SP in the coastal Chalk aquifer. Chapter 5 focusses on the analysis of the periodic SP signal and attempts to determine its primary origin, i.e. EK or EED?

	Frequency (hrs)	Cycles per day (cpd)	Notation	Source	Amplitude relative to M_2
Diurnal	23.934	1.003	K_1	Principal Lunar-Solar	0.5842
	24.066	0.997	S_1	Principal Solar	0.1933
	25.819	0.929	O_1	Principal Lunar	0.4148
	26.868	0.893	Q_1	Elliptic Lunar	0.0795
Semi-diurnal	11.967	2.005	K_2	Lunar-Solar	0.1267
	12.000	2.000	S_2	Principal Solar	0.4656
	12.421	1.932	M_2	Principal Lunar	1.0000
	12.658	1.896	N_2	Lunar Elliptic	0.1915
Short period	6.301	3.809	MN_4	Shallow water components found in the English Channel	0.0297
	6.209	3.865	M_4		0.1000
	6.101	3.934	MS_4		0.0553
Long period	13.661 days	0.070	M_f	Fortnightly	0.1722

Table 2.4 - The main diurnal and semi-diurnal tidal components, their frequencies, notation, physical source and relative amplitudes. Adapted from Doodson (1921) and equilibrium tidal amplitudes from Apel (1987). Also shown are the shorter period tides that appear in the English Channel and are known as the shallow water components, the amplitudes of these components are estimated from (Hamilton, 1978, Walters, 1987, Baptista et al., 1989).

However, coastal abstraction will also contribute to the observed SP by, primarily, altering the local pressure gradients. Abstraction for public water supply is likely to follow a broadly periodic, albeit non-uniform, pattern. Furthermore, the deliberate introduction of periodicity into the system can, in some cases, assist interpretation of SP data. For example, Maineult et al. (2008b) conducted periodic pumping tests in a sandstone aquifer, in order to improve the signal-to-noise ratio of SP signals. Signal processing techniques were then used to differentiate the periodic pumping signal from background noise. However, to be clear, in this study tidally driven change in pressure and concentration gradients are the primary focuses for investigation of periodic SP in the coastal aquifer.

However, natural periodic SP signals have several possible source mechanisms other than marine tides. Several field studies have reported naturally occurring periodic SP signals, including effects related to diurnal spring discharge in Nepal (Perrier et al., 1999) and flow under glaciers in the French Alps driven by Earth tides (Kulessa, 2003). Bumpus and Kruse (2014) discussed the possible source mechanisms of some of the diurnal SP signals they observed and speculated that the most likely cause was evapotranspiration, where deep tree roots caused the water to flow upwards and past the surface electrode array as the vegetation at the surface transpired. Perrier et al. (1997) invoked a similar mechanism for diurnal SP observed in a long-term experiment in France.

Finally, diurnal and semi-diurnal fluctuations in SP could be driven by telluric currents due to the geomagnetic field. For example, Trique et al. (2002), observed the M_2 tidal component in their long-term SP experiment in the French Alps and attributed this to the geomagnetic field. The observation of tidal signatures in geomagnetic data is a global phenomenon (Cochrane and Srivastava, 1974, Lilley and Parker, 1976, Cueto et al., 2003, Maus and Kuvshinov, 2004, Love and Rigler, 2014); therefore, it has important implications for SP monitoring in coastal areas, as the diurnal and semi-diurnal periods found in the geomagnetic field are coincident with the periods of the ocean tides. Previous studies have shown that it is possible to observe tidally driven Earth electric fields across long (c. 200m) dipoles in coastal areas in the UK (Chapman and Kendall, 1970, Osgood et al., 1970, Brown and Woods, 1971, Hart et al., 1983a, Hart et al., 1983b). Such studies have generally attributed the movement of the ocean through the geomagnetic field to be the source of the measured electric field on land (Kendall and Chapman, 1970, Hewson-Browne, 1973), the so called oceanic dynamo (Rosser and Schlapp, 1990, Palshin et al., 1996, Palshin et al., 1997). Therefore, it is important to take account of these effects during long-term SP monitoring campaigns.

There are very few studies that report SP measurements in coastal aquifers. However, Gokhberg et al. (2009) observed tidal effects in 2 km long telephone cables and investigated the contribution of Earth tides to the observed signal using numerical models. They were unable to explain the observed magnitude of the signal by simply invoking the Earth tide response and suggested that ocean tides may also contribute to the signal as the measurements were made in a coastal area in Japan.

Furthermore, Kang et al. (2014) recently conducted an SP monitoring program at a sea dyke and observed periodic changes in SP which they attributed to marine tides. The tidal motion was thought to drive changes in the pressure gradient that in turn drove fluctuations in the EK potential across the tidal cycle. However, their method had significant problems. To begin with, they did not continually monitor SP; rather they made discreet measurements at 6 hour intervals. A 6 hour sampling rate is only just above the Nyquist frequency for the dominant tidal component (M_2); thus, aliasing effects are likely to have occurred in their analysis. Furthermore, the sampling rate would have resulted in a loss of resolution of the dominant tidal (M_2) component. Finally, it is impossible to extract higher frequency tidal components in the SP data using this sampling rate. Furthermore, both Gokhberg et al. (2009) and Kang et al. (2014) neglected the impact of the geomagnetic ocean dynamo which may have had a significant impact on the SP so close to the coast and on long monitoring arrays. Thus, it is difficult to clearly establish the true source mechanism for the periodic SP observed in both studies.

The challenge for monitoring SP in coastal aquifers is that the signals of interest, i.e. tidally driven changes in concentration and hydraulic gradients, will coincide with tidally driven changes in the SP created by the geomagnetic tidal dynamo, Earth tides and even changes in temperature. Therefore, the challenge is to extract the oceanic tidal EK and EED contribution to the overall observed SP.

2.3.6.5 Application of SP monitoring to seawater intrusion

There are no examples of long-term SP monitoring of seawater intrusion in the literature. However, there are examples of SP monitoring applied to measure the electrical response to concentration fronts or plumes in sand tanks (Maineult et al., 2004, Maineult et al., 2005, Martinez-Pagan et al., 2010, Revil and Jardani, 2010) and to monitor saline tracers in real aquifers (Bolève et al., 2011, Ikard et al., 2012). For example, Martinez-Pagan et al. (2010), observed an SP anomaly of a few tens of millivolts after a few minutes while monitoring a descending salt plume in a homogenous sand tank. They attributed a negative volumetric source current density to the salinity front moving down inside the sand tank and a positive volumetric source current density was associated with the position of the leak of the saline water into the freshwater saturated porous media. The electrical data obtained was used

to estimate the velocity of the sinking plume and inverted to reproduce the SP distribution in the sand tank (Figure 2.16(a)). The results were similar to predictions from a forward model (Figure 2.16(b)).

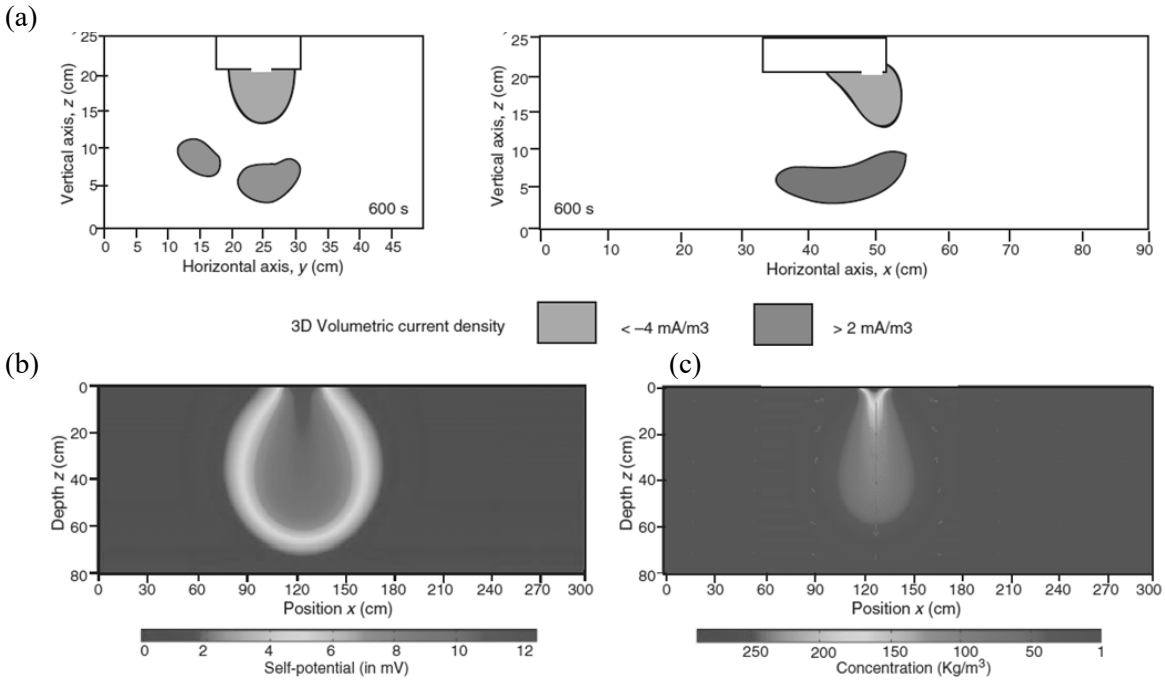

Figure 2.16 –(a) Three dimensional time-lapse tomography from the inversion of the SP data showing the volumetric current density in the sandbox after 600 seconds. Notice the SP anomalies at the front and rear of the sinking plume (b) Simulation of the SP signal after 600 seconds compared to the concentration in (c). (Martinez-Pagan et al., 2010).

Sandberg et al. (2002) reported results of a saline tracer test in an aquifer consisting of glacial deposits. They reported SP anomalies which they attributed to the movement of saline water passing their electrodes installed at the surface. They attributed the primary source mechanism to the EED potential and neglected the EK potential, although the passing of saline water would also cause a decrease in the EK potential due to the compression of the EDL. Furthermore, they did not collect any groundwater quality or FEC data to confirm the movement of the tracer. Similarly, Bolève et al. (2011), conducted a field experiment in which a saline tracer was injected into an embankment dam to detect and quantify leakage through the dam. Ikard et al. (2012) later attributed their measured SP anomalies to the reduction of the EK potential by the injection of the salt, and a contribution of the diffusion potential. They assumed there was no contribution to the EED potential from the EDL; therefore, they neglected any contribution from the exclusion potential. More recently, Jougnot et al. (2015) conducted a saline tracer experiment in the unsaturated zone at a site in Denmark and found that they could not explain the observed SP profile purely on the basis of the EK potential. Instead,

they suggested that the EED potential contributed significantly to the measured SP. Their numerical simulations reproduced the shape of the SP anomaly but could not reproduce the amplitude of the SP signal because they claimed that the EED potential was underestimated.

Pezard et al. (2009) reported the only other measurements of SP in a coastal borehole at risk of seawater intrusion. They reported SP measurements above a saline transition zone in the borehole, which was located in a limestone aquifer on Majorca in the Mediterranean. Their monitoring tool included apparatus for measurements of pressure, temperature, pH, conductivity, and SP. Therefore, they suggested the tool could be used to differentiate between different SP source mechanisms. In Figure 2.17, which shows their SP measurements, there appears to be a systematic decrease in SP beginning c.10 m above the saline transition zone. The decrease in SP may indicate the approach of the saline front as the tool was lowered down the borehole. If this is the case, by extension SP signals could provide information on the proximity of the saline front below the monitoring borehole.

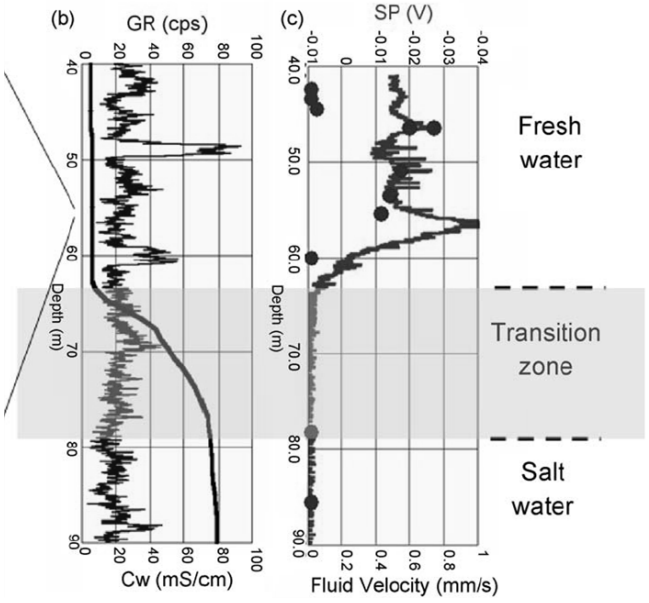

Figure 2.17 – FEC and natural gamma profile compared to SP and local heat-pulse flowmeter data (black dots).

The studies described above show that it is possible to monitor saline tracers in porous media using measurements of SP and demonstrate that SP monitoring in coastal aquifers may yield important information on the position of the saline front in relation to a monitoring borehole. However, much of the motivation for the current study derived from the work of Gulamali et al. (2011) and Jackson et al. (2012b) who investigated the relative contributions of the EED, EK and thermoelectric sources to the

SP measured in a borehole in an oil reservoir during water-flooding. They found that the SP signal, dominated by the EED and EK potentials prior to water breakthrough, can have a magnitude of hundreds of millivolts at the location of the moving water front, and that the signal decayed over tens to hundreds of metres ahead of the front. As a result, they suggested that the advancing water front could be detected and monitored before it arrived at the production borehole. In addition, the shape of the SP signal measured in the borehole reflected the geometry of the advancing water front. Jackson et al. (2012b) also suggested that larger signals would be observed in low permeability reservoirs and that the heterogeneity of the reservoir will significantly affect the SP signal (Figure 2.18). As mentioned in chapter 1, the parallels with seawater intrusion are striking. Therefore, their results strongly suggest that SP monitoring can be used to monitor the movement of a saline front towards monitoring or abstraction boreholes in coastal aquifers and predict the geometry of the advancing front. Thus, SP measurements could improve management of coastal water resources by assisting in avoiding breakthrough of saline water at abstraction boreholes. Chapter 6 focusses on the analysis of the long-term SP data, and aims to determine whether similar effects to those described above are observed in the coastal aquifer in the South Downs, and whether SP, does, in fact, provide spatial or temporal information on the movement of a salinity front towards a monitoring borehole.

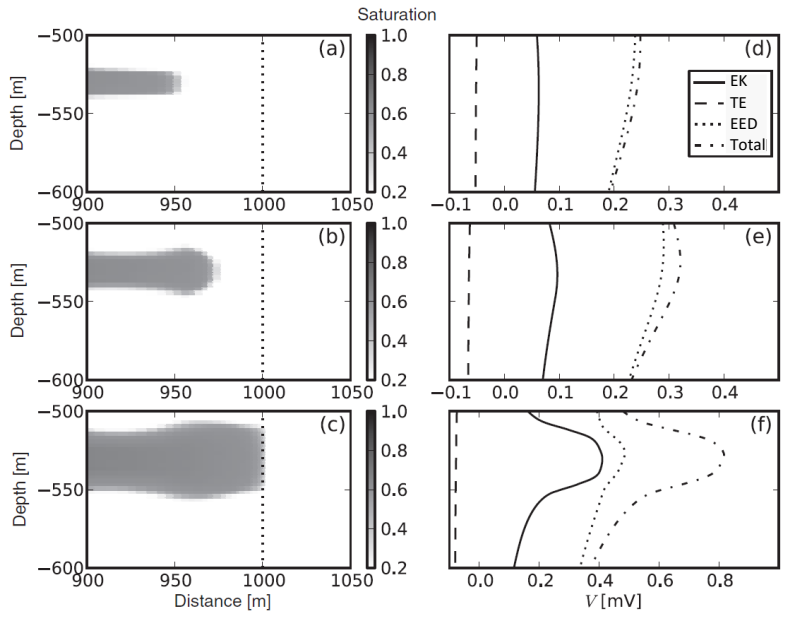

Figure 2.18 – Numerical results from a heterogeneous reservoir model with a single high permeability layer. (a), (b) and (c) show a cross-section through the 3D model and illustrate the water saturation front when it is 50 m and 25 m ahead of, and in the borehole respectively. The borehole is marked by the dashed line at 1000 m. (d), (e) and (f) show the corresponding SP signal and its components for each scenario along the borehole (Jackson et al., 2012b).

2.4. Conclusions: Applying SP monitoring to seawater intrusion

To date there is no evidence in the literature of long-term SP monitoring of seawater intrusion. Seawater intrusion is a complex phenomenon, and the fractured nature of the Chalk aquifer only enhances the monitoring and management challenge. However, recent studies suggest that SP may be a useful tool in detecting and monitoring the saline front in seawater intrusion problems. Furthermore, several authors illustrate its effective utility as a tool for long-term hydrogeological monitoring. SP has also been demonstrated to be a useful indicator of flow process occurring in aquifers, and may have particular application in studying fractured aquifers, such as the UK Chalk aquifer. Therefore, in theory, the nature of the physical mechanisms that led to the generation of SP make it an ideal method for monitoring seawater intrusion in fractured coastal aquifers. The coupling terms that are crucial for the interpretation of the SP data, in field and numerical monitoring experiments, can be measured in the laboratory (the results of these measurements are reported in chapter 3). Furthermore, recent field and numerical studies strongly suggest that long-term SP monitoring could be used to predict the influx of seawater into boreholes in the UK Chalk aquifer (the method for the monitoring experiment is reported in chapter 4). If SP does, as the evidence suggests, respond in this way to intruding salinity fronts, as a result of tidal processes (which are discussed further in chapter 5) or seasonal changes (which are discussed in chapter 6), then SP could facilitate more proactive management of groundwater resources and abstraction in coastal areas. Therefore, the overall aim of this work was to test this hypothesis and assess the possibility of using measurements of SP for long-term monitoring of seawater intrusion in the UK Chalk aquifer.

Chapter 3

Characterising the EK and EED self-potential mechanisms in chalk

3.1 Introduction

In this chapter the electrokinetic (EK) and exclusion-diffusion (EED) potential measurements that were conducted in order to characterise the SP properties of chalk are reported. The laboratory experiments allowed the pressure and concentration gradients, which are a characteristic feature of seawater intrusion, to be isolated from one another and from other effects that may lead to the generation of SP at the coast. Critically, measurements of the EK and EED potentials allowed determination of the coupling coefficients (Equation 2.8) that were necessary in order to determine the cross coupling terms (Equation 2.7) required in the electrodynamic models of the coastal aquifer (section 2.3.5). Thus, the experiments facilitated numerical investigation of the likely magnitude and polarity of the individual EK and EED potential components that manifest simultaneously in the total observed SP signal in the field experiments. The numerical modelling method is reported in chapter 4 and the results in chapter 5 and 6.

The aim of the laboratory work was to measure the EK and EED potentials likely to occur in the Chalk coastal aquifer. In order to achieve this, the objectives were; (i) measure, for the first time, the EED potential in natural brines by modifying and extending the method developed by Leinov and Jackson (2014), (ii) measure for the first time the EK coupling coefficient in chalk saturated with seawater, (iii) confirm previous measurements of the EK coupling coefficient measured in chalk saturated with groundwater, (iv) assess the role of variations in chalk properties on the magnitude of the EED and EK components, and finally (v) assess the effect of overburden and confining pressure on the EED potential likely to arise in the near-surface Chalk aquifer.

The EK potential laboratory work built upon that of Jaafar et al. (2009), Vinogradov et al. (2010) and Jackson et al. (2012a) who measured the EK potential in intact sandstone and chalk core samples.

Although previous measurements of the EK potential are available for chalk saturated with groundwater (Jackson et al., 2012a), no measurements of the EK potential in chalk saturated with seawater have previously been made. It is important to measure both end members in order to measure the respective EK coupling coefficients (e.g. Equation 2.13 and Equation 2.14). Knowledge of the coupling coefficients facilitated estimates of the magnitude of the EK potential component expected in both the groundwater and seawater regimes in the coastal Chalk aquifer.

The EED potential experiments built on the work of Leinov and Jackson (2014) who developed a method to measure the EED potential of intact core samples and allowed them to account explicitly for electrode effects. Electrode effects were found to dominate the apparent measured voltage when a concentration gradient was applied across the core samples. The EED potential has never previously been measured in chalk. Therefore, it was critically important to establish the approximate magnitude of the EED potential expected to exist across the saline front, between groundwater and seawater, in the Chalk coastal aquifer. Furthermore, all previous EED potential experiments used only 1:1 electrolytes such as NaCl (e.g. Equation 2.18). However, in the work described here natural electrolytes were used, as the presence of multiple ions may significantly affect the value of the EED potential in natural conditions. In order to achieve this the experimental method used by Leinov and Jackson (2014) was modified to ensure repeatable results using natural groundwater and seawater. The electrode design and configuration was found to be particularly important for measuring potentials in these natural systems; thus, the electrode design is described in detail in section 3.3.3.2.

3.2 Materials and methods

3.2.1 Sample characterisation and preparation

Both the EK and EED experiments were conducted using natural groundwater taken from the Balsdean abstraction borehole in the Chalk aquifer in East Sussex (see section 2.2.3.2) and seawater taken from the English Channel near Saltdean in East Sussex (see Figure 4.3, note that the marine origin of the intruding seawater is demonstrated in section 6.2). Prior to being used in the experiments the groundwater and seawater were filtered using 0.6 mm filter paper, and exposed to UV radiation, to remove suspended matter and bacteria or other micro-organisms present in the samples. After UV

treatment the samples were filtered once more before being used in the experiments. Sample aliquots were taken prior to some experiments and stored at 4°C prior to sample analysis. All aliquots were then analysed using ion chromatography (IC) (Jackson, 2000, Eith et al., 2001), titration for carbonate and bicarbonate analysis (Franson, 1998) and inductively coupled plasma atomic emission spectroscopy (ICP-AES) (Tatro and Amarasiriwardena, 2006, Alroudhan, 2015) for silica, strontium and barium. IC was conducted in the TOTAL Reservoir Physics laboratory at Imperial College London using a Metrohm 930 Compact IC Flex with a Metrosep A Supp 16 – 15/4.0 anion column and Metrosepp C4 250/4 cation column. Titration was conducted by Bangor University and ICP-AES was conducted by the Natural History Museum. Further details on the methods used for water quality analysis can be found in Appendix 2. The average ionic composition of the groundwater is shown in Table 3.1. Table 3.2 shows the composition of the seawater. The average conductivity and pH of the samples are also shown. Appendix 2 shows the data from which these values were obtained. The errors for the water quality analysis are determined based on the range of concentrations measured for each constituent ion. The average concentrations from the water quality analysis were used to calculate the diffusion potential. The error in the diffusion potential was based on the maximum and minimum concentrations from the water sample analysis. Note that samples were only used in the calculation for the EED potential if they had a charge balance error less than 5% (Appendix 2), a value which is widely used in charge balance analysis (Hounslow, 1995). The charge balance error (CBE) defines the electrical imbalance in the concentration data that arises as a result of analytical errors or unanalysed constituents. The CBE is calculated as follows:

$$CBE = \frac{\sum C_+ - |\sum C_-|}{\sum C_+ + |\sum C_-|} X100 \qquad \textbf{Equation 3.1}$$

Here C_+ and C_- are the concentrations of the cations and anions respectively, concentrations are in milliequivalents per litre (mEq/l). To convert from mg/l to mEq/L the following expression was used:

$$C_{(mEq/l)} = \frac{C_{(mg/l)} \cdot z}{m} \qquad \textbf{Equation 3.2}$$

Chemical species	Average concentration (mg/l)	Molarity (mM/l)	Milliequivalents (mEq/l)
Ba	0.01 ± 0.002	8.15e-5 ± 1.5e-5	0.0001 ± 3e-5
Ca	62.76 ± 13.29	1.57 ± 0.33	3.13 ± 0.66
K	1.88 ± 0.74	0.048 ± 0.019	0.048 ± 0.019
Mg	4.02 ± 1.11	0.16 ± 0.046	0.33 ± 0.09
Na	28.66 ± 5.60	1.25 ± 0.24	1.25 ± 0.24
Si	3.62 ± 0.27	0.13 ± 0.01	0.51 ± 0.038
Sr	0.20 ± 0.006	0.002 ± 0.00006	0.005 ± 0.0001
F	0.09 ± 0.026	0.005 ± 0.0014	0.005 ± 0.001
Cl	46.87 ± 8.85	1.32 ± 0.25	1.32 ± 0.25
Br	0.28 ± 0.1	0.0031 ± 0.0012	0.003 ± 0.001
NO_3	27.87 ± 4.108	0.45 ± 0.07	0.45 ± 0.07
SO_4	16.80 ± 2.82	0.17 ± 0.03	0.35 ± 0.059
HCO_3	158.18 ± 23.18	2.59 ± 0.40	2.59 ± 0.38
CO_3	24.71 ± 0.05	0.41 ± 0.0008	0.62 ± 0.002
TDS (mg/l)	**375.88 ± 60.15**		
Ionic Strength (mM)	**7.89 ± 1.37**		
Average pH	**7.79 ± 0.58**		
Average Conductivity (µS/cm)	**463.48 ± 90.48**		

Table 3.1 – Average concentrations for each ionic species for the groundwater used in the exclusion-diffusion and electrokinetic experiments. Samples were taken from the Balsdean abstraction borehole (Figure 4.3).

Chemical species	Average concentration (mg/l)	Molarity (mM/l)	Milliequivalents (mEq/l)
Ca	423.13 ± 43.07	10.78 ± 1.07	21.56 ± 2.15
K	453.39 ± 177.11	11.59 ± 4.53	11.59 ± 4.53
Mg	1227.90 ± 197.90	50.52 ± 8.14	101.04 ± 16.28
Na	10262.21 ± 529.39	446.38 ± 23.03	446.38 ± 23.03
Sr	8.27 ± 1.17	0.094 ± 0.013	0.18 ± 0.027
F	6.13 ± 1.44	0.32 ± 0.076	0.32 ± 0.076
Cl	19008.53 ± 1948.29	536.16 ± 54.95	536.16 ± 54.95
Br	107.00 ± 57.59	1.34 ± 0.72	1.34 ± 0.73
SO_4	2485.07 ± 502.70	25.87 ± 5.23	51.74 ± 10.47
HCO_3	131.60 ± 14.60	2.12 ± 0.23	2.16 ± 0.24
TDS (mg/l)	**34122.20 ± 3473.26**		
Ionic Strength (mM)	**673.49 ± 70.00**		
pH	**7.59 ± 0.60**		
Conductivity (mS/cm)	**50.34 ± 2.16**		

Table 3.2 - Average concentrations for each ionic species for the seawater used in the exclusion-diffusion and electrokinetic experiments. Samples were taken from the English Channel near Saltdean (Figure 4.3)

Table 3.3 shows the properties of the rock samples used in the experiments. The core samples were all English chalk, but were taken from different locations. Prior to each experiment the chalk samples were cleaned following standard core cleaning procedures (Byrne and Patey, 2004) using a soxhlet extractor and methanol. The methanol was heated in a boiling flask and allowed to evaporate. The vapour rises and was directed into a condensing chamber which sits above the core sample chamber. The condensed solvent was then allowed to run into the core sample chamber, and the sample was

slowly immersed in the methanol until the solvent reached an outlet at the top of the condensing chamber, which allowed it to run back into the boiling flask. The process was allowed to circulate for approximately 48 hours. The sample was then dried in an oven at 80^0C for approximately 48 hours. Finally, the core sample was saturated with groundwater in a vacuum chamber for about 24 hours.

The porosity and pore throat radius were measured by Aberdeen University using the mercury injection technique. Permeability was found during the EK experiments which are outlined below, the method for determining rock conductivity and formation factor is also outlined below. The error for the permeability was determined from the variation in the slope of the pressure versus the flow rate. Finally, the cementation factor is simply the ratio of the logarithm of the formation factor and the logarithm of the porosity.

The saturated rock conductivity was measured prior to conducting the experiments following the procedure outlined by Vinogradov et al. (2010). Two silver membranes of 1.5 inch diameter were clamped to each end of the chalk sample using an adjustable jig. A QuadTech 7600 Plus Precision LCR Meter was used to measure the conductivity over the frequency range of 10 Hz to 2 MHz, with an accuracy of 0.25% across this range. The conductivity meter measures frequency (f), impedance (Z) and resistance (R). The reactance (X) was then calculated using the following equation:

$$X = \sqrt{(Z^2 - R^2)} \qquad \textbf{Equation 3.3}$$

The value of the resistance at the minimum reactance was taken as the resistance of the sample. The conductivity of the saturated sample was then calculated:

$$\sigma_{rec} = \frac{L}{R\pi r^2} \qquad \textbf{Equation 3.4}$$

Here r is the radius of the sample and L is the length of the sample. The error in the rock conductivity was determined by repeating the measurement at least three times; the range of the measured conductivity values for each chalk core were then used to calculate the error in the formation and cementation factors.

The formation factor (Equation 2.16) is the ratio of brine conductivity to rock conductivity when the surface conductivity is assumed negligible (Jouniaux and Pozzi, 1995), i.e. when the electric double layer is thin (Vinogradov et al., 2010). The contribution of the surface conductivity to the effective conductivity of the rock decreases with increasing ionic strength and becomes negligible at > 0.2 M (Alroudhan et al., 2016). Thus, the formation factor was calculated as the ratio of the seawater conductivity to the rock conductivity saturated with seawater. The cementation exponent was then calculated using the following expression which was derived from Archie's Law:

$$F = \phi^{-m} \qquad \textbf{Equation 3.5}$$

#	Chalk type	Source	Length (mm)	Diameter (mm)	Porosity	Permeability (mD)
T1	Seaford	Berkshire	52.5 ± 0.05	37.4 ± 0.05	0.46	2.5 ± 0.10
S2	Seaford	Worthing	69.3 ± 0.05	36.8 ± 0.05	0.38	2.1 ± 0.11
S3	Seaford	London	77.1 ± 0.05	37.8 ± 0.05	0.37	N/A
S4	Lewes	Kent	76.1 ± 0.05	37.7 ± 0.05	0.41	N/A
X	Shale	Black shale				

#	Chalk type	Source	SW Conductivity (mS/cm)	GW Conductivity (mS/cm)	Formation factor	Cementation exponent m
T1	Seaford	Berkshire	6.69 ± 0.011	0.331 ± 0.0002	7.31 ± 0.11	2.58 ± 0.01
S2	Seaford	Worthing	5.05 ± 0.082	0.245 ± 0.0014	9.97 ± 1.73	2.36 ± 0.16
S3	Seaford	London	6.16 ± 0.025	0.301 ±0.0010	8.17 ± 0.32	2.12 ± 0.04
S4	Lewes	Kent	5.20 ± 0.004	0.250 ± 0.0004	9.68 ± 0.07	2.56 ± 0.01
X	Shale	Black shale				

Table 3.3 - Chalk sample number, chalk lithological classification, and the location from which the chalk was sourced, with the dimensions of the chalk core, the porosity and permeability and electrical properties of each sample. Note that Aberdeen University reported that the errors on the measurements of porosity were negligible (Healy, 2016), hence why no errors are shown in this column.

All experiments were conducted in the TOTAL Reservoir Physics Laboratory at Imperial College London with a controlled temperature of 22.5 ± 1^0C.

3.2.2 Electrokinetic potential experiments

3.2.2.1 Apparatus

The measurements of the EK potential followed the methodology of Jaafar et al. (2009) and Vinogradov et al. (2010). Section 2.3.3 provides a detailed explanation of the mechanisms that lead to the generation of the EK potential. Equation 2.13 provides the basis for the EK experiments, because dP and dV can be directly measured across intact chalk core samples; thus, allowing the coupling coefficient to be determined.

Figure 3.1 illustrates the experimental setup used. The chalk sample was placed in a stainless steel core holder, which was connected to earth and acted as a Faraday cage. A rubber sleeve was placed around the core, ensuring that the only pathway for the current was through the sample, and a confining pressure was applied by pumping gas through the purge opening. The confining pressure avoided any of the electrolyte flowing along the outer surface of the sample and ensured the sample was electrically isolated. The core holder was made from stainless steel and is shown in Figure 3.1(b). The confining pressure was kept several hundred kPa higher than the pressures used in the experiments. At the end of each core within the holder was a nylon mesh used as a flow disperser.

Two electrolyte reservoirs were placed at either side of the sample and the flow was driven by a column of Multipar-H synthetic oil using a GDS Advanced Pressure/Volume Controller syringe pump. The oil ensured that the electrolyte was entirely insulated. The oil also allowed air bubbles in the electrolyte to be captured at the top of the oil layer in each reservoir; it also prevented exposure of the electrolyte to air which can cause a change in pH and it eliminated the flow of electrical current through the electrolyte along a path parallel to the core sample. The synthetic oil also ensured that the stainless steel pump cylinder did not come into contact with the electrolyte and reduced corrosion of the pump. The pump maintained a constant flow rate to high accuracy (<0.25% of measured value for maximum rates). The pressure difference across the sample was measured using a pair of calibrated Druck PDCR 810 pressure transducers (accuracy 0.1% of measured value, resolution 70 Pa). The flow valves could be adjusted to reverse the flow (V_1 – V_6 in Figure 3.1(a)).

The EK potential across the chalk sample was measured using a pair of non-polarising Ag/AgCl electrodes (noise levels <20 μV). The electrodes were placed away from the core sample and offset from the main flow path to avoid electrode flow affects. The electrodes were located in a reservoir which was in electrical contact with the electrolyte via a low permeability ceramic disc (Figure 3.1(c)). The electrodes had an internal chloride concentration similar to the electrolyte investigated. Further discussion of electrodes can be found in section 3.3.3.2. The voltage measurements were made using an NI-9219 voltmeter with an internal impedance >1 GΩ, an accuracy of 0.18% of the full

scale measurement (1 V) and resolution of 50 nV. The voltage and pressure were measured with a 1 Hz sampling frequency.

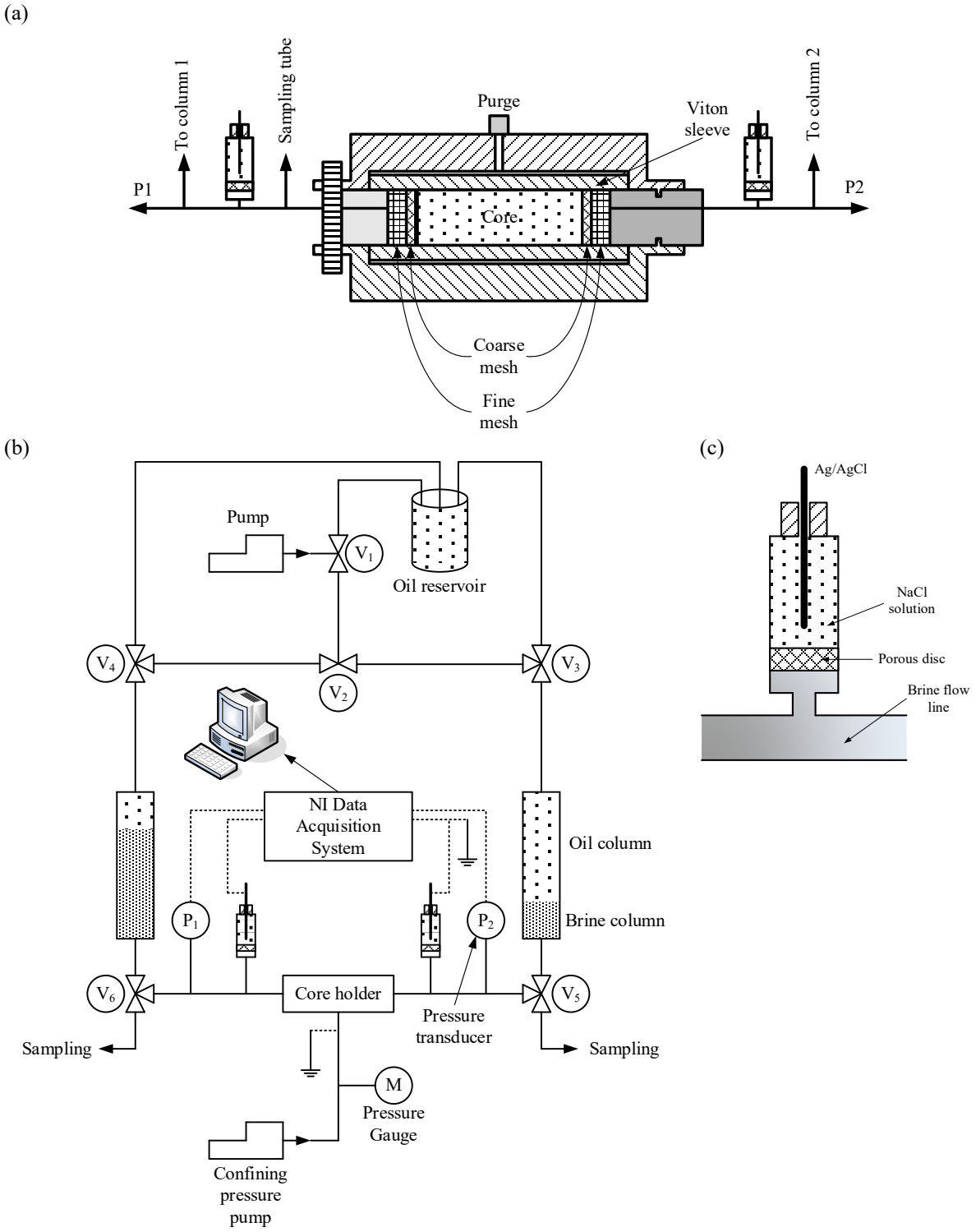

Figure 3.1 – The experimental set-up for measuring the electrokinetic potential coupling coefficient. (a) Cross-section through the core holder. (b) Pressure vessel, electrolyte reservoirs, pump, flow lines (solid lines) and electrical connections (dotted line). (c) Cross-section through the electrodes. Adapted from Jaafar et al. (2009).

3.3.2.2 Measurements of electrokinetic potential

Once the sample was ready it was installed into the pressure vessel. The same electrolyte that was used to saturate the chalk core was then pumped through the core in both directions until the pH and conductivity was stable to within a 10% tolerance. This ensured that the groundwater and seawater samples were equilibrated with the chalk core samples before beginning the experiments and that there were no further changes in pH or conductivity. Electrolyte samples were taken by opening the sampling lines using valves V_5 and V_6 in Figure 3.1(a). The conductivity of the electrolyte was measured using a Metrohm 712 conductometer with a resolution of 0.01 µS/cm and accuracy of 0.5% of the reading in the range from 2 µS/cm to 20 mS/cm and 0.8% in the range to 200 mS/cm. The pH of the electrolyte was measured using a Mettler Toledo FiveGo pH meter and LE438 electrode with an accuracy and resolution of 0.01 pH units over the full pH range. Both of these instruments were regularly calibrated.

Prior to inducing flow through the core the static voltage was measured. Once the static voltage was stable, a constant rate flow was induced across the sample; marking the beginning of the EK potential measurements. A stable static voltage and pressure were considered to be obtained when their temporal variations did not exceed <10 µV and <2 kPa respectively. Once the voltage stabilised, pumping was terminated, the system was allowed to relax and conductivity and pH were measured.

The flow direction was then reversed, but the flow rate was maintained, by adjusting valves V_1-V_6. Once the pressure and voltage were stable pumping was terminated and the conductivity and pH were measured. These paired experiments ensured that electrode polarization was negligible and eliminated the effects of temporal variations in static voltage. The procedure was repeated four times with different flow rates. The EK coupling coefficient was then estimated by plotting the stabilised voltage versus the stabilised pressure differences for four flow rates. The stabilised voltages were given by:

$$V_{m1} = V_{EK} + V_{static1} \quad \textbf{Equation 3.6}$$

$$V_{m2} = -V_{EK} + V_{static2} \quad \textbf{Equation 3.7}$$

Here V_{EK} is the EK potential. Assuming $V_{static1} \approx V_{static2}$ and subtracting the stabilised voltage and pressure differences measured in the two experiments, then:

$$V_{m1} - V_{m2} = 2V_{EK} \quad \textbf{Equation 3.7}$$

$$\Delta P_{m1} - \Delta P_{m2} = 2\Delta P \quad \textbf{Equation 3.8}$$

The EK coupling coefficient is the gradient of the linear regression of $(V_{m1} - V_{m2})/2$ against $(\Delta P_{m1} - \Delta P_{m2})/2$. The errors in the coupling coefficient were obtained by plotting the maximum and minimum slope of $(V_{m1} - V_{m2})/2$ against $(\Delta P_{m1} - \Delta P_{m2})/2$ based on the noise level and stability of the measured voltage. The zeta potential was obtained from the measured coupling coefficient by rearranging Equation 2.15.

The viscosity of the seawater was taken to be 1.08 mPa.s (Bullard, 2011) and groundwater, 1 mPa.s (Kestin et al., 1978). The dielectric permittivity as a function of total ionic strength (I) was calculated using the correlation suggested by Malmberg and Maryott (1956) where ε_w is in Fm^{-1} and I is in M.

$$\varepsilon = 8.85x10^{-12}(80 - 13I + 1.065I^2 - 0.03006I^3) \quad \textbf{Equation 3.9}$$

3.2.3 Exclusion-diffusion potential experiments

The exclusion and diffusion potential mechanisms leading to the generation of the EED potential are summarised in section 2.3.4. In the experiments described below, the electric potential induced by a concentration gradient across a saturated chalk plug was measured. There are several studies that have reported EED potentials in sandstones (Hill and Millburn, 1956, Nourbehecht, 1963, Ortiz Jr. et al., 1973, Smits, 1968, Thomas, 1976, Leinov and Jackson, 2014) and a study that measured EED potential in argillite (Revil et al., 2005), but none have been conducted on carbonate or chalk samples.

In section 2.3.4 the expression for calculating the diffusion potential in the presence of a 1:1 electrolyte was introduced (Equation 2.20). In these experiments the electrolytes used are natural and as such contain multiple ionic species. The diffusion potential for multi-ionic electrolytes can be calculated using the expression developed by Lanteri et al. (2009):

$$\Delta V_{ED} = -\frac{k_B T}{e}\left(\frac{\sum_i K_i D_i z_i (C_{Mi}^{\Delta x} - C_i^0)}{\sum_i K_i D_i z_i^2 (C_{Mi}^{\Delta x} - C_i^0)}\right) ln\left(\frac{\sum_i K_i D_i z_i^2 C_{Mi}^0}{\sum_i K_i D_i z_i^2 C_{Mi}^{\Delta x}}\right)$$ **Equation 3.10**

Here k_B is the Boltzmann constant, T is the absolute temperature, e is the electron charge, K_i is the hindrance diffusion coefficient which for the case of an infinite pore volume is 1, D_i is the diffusion coefficient (following Lanteri et al. (2009)) values of which are taken from Haynes and Lide (2012) for each ion, z_i is the charge number of ion i, C_{Mi}^0 is the concentration of the highest salinity solution and $C_{Mi}^{\Delta x}$ is the concentration of the lowest salinity solution. Leinov and Jackson (2014) assumed that transport numbers are constant for a simple NaCl solution; since transport numbers are related to the diffusion coefficients (i.e. section 2.3.4) it is assumed that the diffusion coefficients used in Equation 3.10 are also constant. Li and Gregory (1974) point out that this is a valid approximation when dealing with the diffusion coefficient of ions in seawater. Equation 3.10 is equivalent to the expression used by Leinov and Jackson (2014) in the case of a 1:1 electrolyte (Appendix 1).

In addition to EED potential measurements using groundwater and seawater, two other sets of experiments were conducted. These experiments were used to assess whether chalk was dominated by exclusion potentials. Previous measurements using a similar methodology but with sandstone samples recorded positive diffusion dominated potentials with a concentration ratio much larger than that produced by groundwater and seawater (Leinov and Jackson, 2014). Since chalk samples have a smaller pore throat radius, chalk was more likely to produce exclusion potentials.

The first set of experiments used a higher concentration contrast to investigate the exclusion efficiency of chalk (Leinov and Jackson, 2014); the second applied a confining pressure to the chalk to close micro-fractures and investigate whether this changed the polarity of the EED potential. As a benchmark a shale core was also tested to ensure that the experiments produced reliable results and that a negative EED potential could be measured. Shale was used because it has a micro-porous matrix and so should be dominated by the exclusion potential. Therefore, a total of three different sets of experiments were conducted, the first set of experiments used natural groundwater (Table 3.1) and seawater (Table 3.2) and are referred to as the GW/SW experiments. The second set of experiments used deionised water pre-equilibrated with chalk (Table 3.4) and 5 M NaCl also pre-equilibrated with

chalk (Table 3.5). These experiments are referred to as the pre-eq(DI/5M) experiments. Finally, the third set of experiments was designed to test whether the EED at depth is likely to be affected by the rock overburden, and to investigate whether micro-fractures within the chalk altered the EED potential. At the deepest parts of the active aquifer the overburden pressure can be tens of bars and may affect the surface area in contact with the electrolyte and the dynamics of the EDL. It may also change flow and diffusion pathways through the chalk.

3.3.3.1 Apparatus

The EED potential was measured across a chalk sample placed between a low and high salinity reservoir, creating a concentration gradient across the sample. The chalk was initially saturated with the low salinity electrolyte, for two reasons; the first was that this mimics the intrusion of seawater into a freshwater aquifer; the second was that the EDL is thickest when the saturating electrolyte is of low salinity (Vinogradov et al., 2010).

A two stage approach was taken to account explicitly for electrode effects in the EED potential experiments (Jougnot and Linde, 2013, Leinov and Jackson, 2014). The 'column' apparatus (Figure 3.2(b)) facilitated measurements of the diffusion potential (ED) across the salinity front without the porous media. The 'plug' experiment (Figure 3.2(a)) facilitated measurements of the EED potential across the chalk samples. The total electric potential measured in the 'plug' (Figure 3.2(a)) is termed the apparent 'plug' electric potential (ΔV_{AP}). It is made up of the EED potential (ΔV_{EED}) and a concentration dependent electrode potential (ΔV_C) (Leinov et al., 2010, Leinov and Jackson, 2014):

$$\Delta V_{AP} = \Delta V_{EED} + \Delta V_C \qquad \textbf{Equation 3.11}$$

The electrode potential was removed by conducting a second experiment using identical electrodes but without the chalk plug. Instead the two reservoirs (Figure 3.2(b)) were connected in a vertical column arrangement and the electric potential across the gravity stabilised salinity front was measured. The apparent 'column' electric potential (ΔV_{AC}) was made up of the diffusion potential (ΔV_{ED}) and a concentration dependent electrode effect (ΔV_C) which was assumed to be identical to the electrode effect in the plug experiment (Leinov and Jackson, 2014, Leinov et al., 2010):

$$\Delta V_{AC} = \Delta V_{ED} + \Delta V_C$$ **Equation 3.12**

Combining Equation 3.11 and Equation 3.12 gives an expression for the EED potential:

$$\Delta V_{EED} = \Delta V_{AP} - (\Delta V_{AC} - \Delta V_{ED})$$ **Equation 3.13**

The voltage measurements were taken using the same instrumentation as described in section 3.2.2. The electrical conductivity of the electrolytes was measured using Jenway 4520 conductivity meters (±0.5% accuracy and resolution of 0.01 μS/cm) and the temperature was measured using K-type isolated thermocouples (accuracy ±0.5°C). Voltage, temperature, and conductivity were recorded with a 1 Hz sampling frequency.

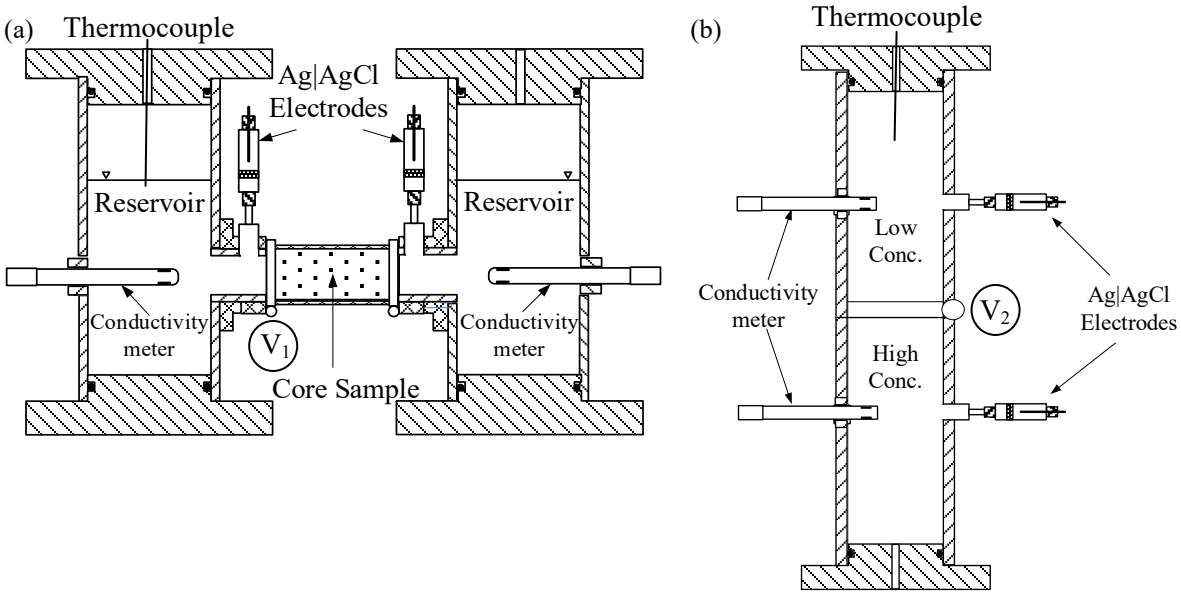

Figure 3.2 – (a) Configuration of the experiment for measuring the EED potential across a salinity front in the chalk samples. (b) Configuration of the experimental equipment for measuring the diffusion potential.

3.3.3.2 Electrodes

The method outlined here differs from that of Leinov and Jackson (2014) to account for the increased complexity of the natural electrolytes used. The electrodes used in these experiments were prepared identically for the plug and column apparatus and were similar to those used in the EK experiments. However, due to differences in ionic concentrations between the reservoirs and the electrolytes in the electrode casings it was important to minimise the liquid junction potential (see section 2.3.6.1) that existed across the electrode membranes (Barry and Diamond, 1970, Jougnot and Linde, 2013).

The chloride concentration within the electrode casing was kept as stable as possible throughout the experiments so that the electrode potential was stable and reproducible (Jougnot and Linde, 2013). For example, a lack of chloride ions in the electrode chamber can cause dissolution of the AgCl coating on the Ag electrode (Raynauld and Laviolette, 1987). Changes in the electrode coating alters the electrode behaviour and creates time-dependant and irreversible equilibrium contact potentials (Jougnot and Linde, 2013). The chloride content was kept stable by separating the electrode solutions from the electrolytes using a porous ceramic disc that limited exchange of ions and minimised convective mixing. Reproducibility was ensured by repeating the experiments multiple times.

However, as the electrolytes used were natural, they contained a significant amount of ionic species other than chloride that could have affected the stability of the electrodes (Snyder et al., 1999). The presence of these additional ions in solution created unwanted concentration gradients across the electrode membranes that are not present in the experiments which use only a 1:1 electrolyte. Mboh et al. (2012) dealt with this by using the same waters within the electrode casings as they used in the experiments. However, the presence of ions other than chlorine leads to additional contact potentials at the interface between the AgCl rod and the buffering electrolyte and causes problems with electrode stability and experimental repeatability.

To deal with stability and diffusion across the electrode membranes, the electrodes were prepared differently for the low and high salinity reservoirs. To do this, the conductivity of each reservoir fluid was measured and a NaCl electrolyte with slightly higher chloride content was prepared. The higher chloride content in the electrode casings buffered the effect of the concentration gradients across the membrane (Tallgren et al., 2005) and ensured that the chloride concentration in the electrode casings remained reasonably constant throughout the experiments.

To convert conductivity to concentration for the NaCl solutions used in the electrodes the approach developed by Vinogradov et al. (2010) was used. They related the conductivity of NaCl electrolyte to NaCl concentration using an empirical correlation (Worthington et al., 1990) and published data (Cicerone et al., 1992, William, 2011) at 23°C for lower conductivities (<1 S/m). They combined this

with a polynomial (Worthington et al., 1990) fitted to published data (Cicerone et al., 1992, William, 2011) for higher conductivities, where C_M is in M and σ_{fec} is in S/m:

$$C_M = 5.9738 \times 10^{-7}{\sigma_{fec}}^6 - 3.5136 \times 10^{-5}{\sigma_{fec}}^5 + 7.823 \times 10^{-4}{\sigma_{fec}}^4 - 8.0334 \times 10^{-3}{\sigma_{fec}}^3 + 4.0791 \times 10^{-2}{\sigma_{fec}}^2 + 3.4996 \times 10^{-2}\sigma_{fec} + 3.6104 \times 10^{-2} \quad \textbf{Equation 3.14}$$

It is impossible to completely eliminate diffusion across the electrode membrane and all of the ionic species within the natural electrolytes in the main reservoirs will diffuse into the electrode casing overtime. Despite this, the electrode design ensured that diffusion was minimised for the first few hours of the experiments. Once the electrodes started to drift, the experiment was terminated. At the start of each experiment a new set of electrodes was prepared for both the column and plug apparatus.

3.3.3.3 Measurements of exclusion-diffusion potential

In the column experiment the lower reservoir was filled with the high salinity electrolyte (Figure 3.2(b)). The two reservoirs were separated by a ball valve (V_2 in Figure 3.2(b)) with the same diameter as the column. The lower reservoir was filled just above the ball valve to ensure that no air was trapped and then the valve was closed. Any excess water was cleared from the compartment separating the two reservoirs and the upper reservoir was filled with the low salinity electrolyte. Therefore, the denser water was at the base of the column so there was no convective mixing and, due to gravity, the salinity front was stable once the ball valve was opened. The experiment started once the ball valve was opened and the two fluids came into contact with one another.

The electrolytes in the reservoirs were analysed for the ionic concentrations of their constituent components once the repeatability of the experiments was achieved. Aliquots were sampled from random experiments to ensure that there was no significant change in the ionic concentrations of the electrolytes that were used (i.e. >20% for major ionic constituents and >50% for minor ionic constituents, these values were determined based on a basic sensitivity analysis of Equation 3.10).

In the plug experiments (Figure 3.2(a)), the core, initially saturated with the low salinity electrolyte, was placed in a rubber sleeve and attached to the low salinity reservoir, which was then filled. The chalk sample was wrapped in PTFE tape, a type of deformable filler, which was used to seal the contact between the core and the rubber sleeve. The high salinity reservoir was then filled; a valve at

the end of the core channel ensured that the reservoir did not leak. The water level in each reservoir was identical so no pressure gradients existed across the sample. Once the electrodes were attached the measurements started. Then the valve (V_1 Figure 3.2(a)) at the end of core channel was opened. At this point the electrical contact between the two reservoirs was established and the experiment began. All measurements were taken with reference to the electrode in the low salinity reservoir.

3.3.3.3.1 Measurements with natural electrolytes

In the GW/SW experiments the chalk samples were saturated with the groundwater prior to the experiments. The saturation procedure was the same as that described for the EK experiments in section 3.2.1. The average ionic concentration for groundwater is shown in Table 3.1 and for seawater in Table 3.2; these values were used in Equation 3.10 (Lanteri et al., 2009) to calculate the diffusion potential in the GW/SW experiments. A range of concentration values was available from repeat analysis of the water samples; this range was used to calculate the error in the calculated diffusion potential ($\in_{V_{ED}}$). The error, determined from the range of apparent voltages obtained from repeat measurements of the column ($\in_{V_{AC}}$) and plug ($\in_{V_{AP}}$) experiments, were added to the diffusion potential error in order to determine the final error ($\in_{V_{EED}}$) in the EED potential measurements (Equation 3.15), the error in the electrode potential (Equation 3.12) was calculated in a similar way (Equation 3.16):

$$\in_{V_{EED}} = \in_{V_{ED}} + \in_{V_{AP}} + \in_{V_{AC}} \qquad \textbf{Equation 3.15}$$

$$\in_{V_C} = \in_{V_{ED}} + \in_{V_{AC}} \qquad \textbf{Equation 3.16}$$

The seawater electrodes internal electrolyte was created from 55 mS/cm NaCl solution in deionised water (the conductivity of the deionized water was <1 µS/cm). The chloride content of these electrodes was c.24,160 mg/l. The groundwater electrodes internal electrolyte was created using the same starting electrolyte as the seawater electrode, but the solution was diluted by 100 times, giving an electrode with an internal conductivity of c.675 µS/cm. The chloride content of these electrodes was c.241 mg/l. In both cases the chloride content of the electrodes was slightly higher than the chloride content of the GW and SW used.

3.3.3.3.2 Measurements with high salinity contrast

In the pre-eq(DI/5M) experiments the low salinity electrolyte was prepared using deionised water pre-equilibrated with chalk samples. Similarly the high salinity electrolyte used 5 M solutions of NaCl. The average analysis of the low salinity electrolyte is shown in Table 3.4 and an average analysis of the 5 M electrolyte is shown in Table 3.5. The samples were only used in the calculation for the EED potential if they had a charge balance error < 10% (Appendix 2). The final error in the EED potential was then obtained using Equation 3.15. The high salinity electrode had an internal 5 M NaCl solution. The low salinity electrode was identical to the electrode used in the GW/SW experiments. The rest of the experimental procedure was the same as described for the GW/SW experiments.

Chemical species	Average concentration (mg/l)	Molarity (mM/l)	Milliequivalents (mEq/l)
Ca	20.96 ± 9.92	0.47 ± 0.25	1.05 ± 0.49
K	5.95 ± 3.03	0.15 ± 0.077	0.15 ± 0.077
Mg	2.08 ± 1.87	0.085 ± 0.077	0.17 ± 0.15
Na	4.29 ± 1.32	0.19 ± 0.057	0.19 ± 0.057
F	0.10 ± 0.021	0.0053 ± 0.0011	0.005 ± 0.001
Cl	10.06 ± 6.72	0.28 ± 0.19	0.30 ± 0.19
NO_3	10.78 ± 6.22	0.17 ± 0.10	0.17 ± 0.10
SO_4	11.93 ± 5.74	0.12 ± 0.060	0.25 ± 0.12
HCO_3	49.75 ± 4.37	0.81 ± 0.072	0.81 ± 0.072
Average TDS (mg/l)	**113.98 ± 33.47**		
Average Ionic Strength (M)	**0.0022 ± 0.0009**		
Average pH	**8.16 ± 1.03**		
Average Conductivity (µS/cm)	**160.95 ± 141.57**		

Table 3.4 - Average concentrations for each ionic species for the chalk equilibrated low salinity electrolyte used in the pre-eq(DI/5M) EED experiment.

Chemical species	Average concentration (mg/l)	Molarity (mM/l)	Milliequivalents (mEq/l)
Ca	2.33 ± 1.02	0.19 ± 0.025	0.12 ± 0.05
K	3.66 ± 1.14	0.35 ± 0.029	0.09 ± 0.029
Mg	1.85 ± 0.72	0.33 ± 0.029	0.15 ± 0.059
Na	114948.50 ± 6798.62	5000 ± 143.55	5000 ± 295.72
Cl	177265.00 ± 5089.37	5000 ± 295.72	5000 ± 143.55
SO_4	1755.98 ± 50.89	18.28 ± 0.53	36.56 ± 1.06
HCO_3	46.00 ± 7.00	0.74 ± 0.11	0.75 ± 0.11
Average TDS (mg/l)	**294040.06 ± 11954.98**		
Average Ionic Strength (M)	**5.04 ± 0.22**		
Average pH	**8.10 ± 0.55**		
Average Conductivity (mS/cm)	**232.54 ± 25.5**		

Table 3.5 - Average concentrations for each ionic species for the chalk equilibrated high salinity electrolyte used in the pre-eq(DI/5M) EED experiment.

3.3.3.3 Exclusion-diffusion potential measurements under confining pressure

In the confining pressure experiments, the chalk cores were confined at the start of the experiment using a confining cell similar to that used for the EK experiments (Figure 3.1) the only differences being that the core holder was acrylic and the chalk cores were not wrapped in PTFE. The rest of the experimental procedure was identical to that outlined above. Both GW/SW and pre-eq(DI/5M) experiments were conducted.

3.3 Results

Table 3.6 provides a summary of the results from both the EK and EED experiments from each of the chalk samples. Appendix 3 contains a summary of all of the repeated experiment results from the plug and column experiments for both the GW/SW and pre-eq(DI/5M) experiments.

	#	GW C_{EK} (mV/mH$_2$O)	SW C_{EK} (mV/mH$_2$O)	GW ζ (mV)	SW ζ (mV)
EK	T1	-0.575 ± 0.080	-0.0101 ± 0.0020	-20.1 ± 3.21	-8.7 ± 1.7
	S2	-0.522 ± 0.040	-0.0175 ± 0.0020	-20.3 ± 3.12	-15.4 ± 4.1
	S3				
	S4				
	X				
	#	GW/SW V_{EED} (mV)	GW/SW η	5M/DI V_{EED} (mV)	DI/5M η
ED	T1	22.22 ± 7.91	0.039 ± 0.024		
	S2	14.61 ± 8.90	0.092 ± 0.031	17.45 ± 7.68	0.11 ± 0.015
	S3	21.38 ± 9.81	0.045 ± 0.037	32.19 ± 5.77	0.05 ± 0.008
	S4	22.60 ± 8.62	0.037 ± 0.030	31.82 ± 7.37	0.05 ± 0.014
	X			-14.21 ± 5.74	0.24 ± 0.008

Table 3.6 – Summary of the electrokinetic and exclusion-diffusion experiments. The exclusion-efficiency (η) for each chalk sample is also shown. Note that Equation 2.13Equation 2.15 were used to calculate C_{EK} and ζ respectively. Equation 3.13 were used to calculate V_{EED}. The errors were calculated using Equation 3.15Equation 3.16. The exclusion-efficiency is discussed in section 3.5.2.2.

3.3.1 Electrokinetic potential experiments

The EK experiments used Seaford chalk samples and natural groundwater and seawater samples (Table 3.1 and Table 3.2 respectively). Two chalk samples were tested, sample T1 from an outcrop in Berkshire, and sample S2 from a borehole in the Worthing area in East Sussex (Table 3.3).

3.3.1.1 Electrokinetic experiments using natural groundwater

Figure 3.3(a) show the typical results of pumping in both directions through chalk sample S2 with groundwater (Table 3.1). The voltage responded in the opposite sense to the pressure, but was the same magnitude when pumping in the opposite direction; therefore, electrode polarisation effects were small. Figure 3.3(b) shows the electrical potential difference versus the pressure difference, the

gradient is linear yielding the EK coupling coefficient, -0.522 ± 0.040 mV/mH_2O with R^2 = 0.9996. The dashed line shows the maximum and minimum gradient possible from the variation in the stabilised voltage (error bars in Figure 3.3(a)). The coupling coefficient measured in groundwater yields a zeta potential of -20.3 ± 1.7 mV using Equation 2.15 and the formation factor in Table 3.3. The negative coupling coefficient and zeta potential indicate that an excess of positive charge is transported within the EDL. Therefore, the surface of the chalk is negatively charged. Chalk sample T1 showed a slightly more negative coupling coefficient, -0.575 ± 0.080 mV/mH_2O (R^2=0.9939) but a zeta potential identical, within experimental error, to sample S2 of -20.1 ± 3 mV.

3.4.1.2 Electrokinetic experiments using natural seawater

The second set of experiments used seawater (Table 3.2) from the English Channel. Figure 3.4(a) shows the typical pressure and voltage response for chalk sample S2 while pumping in opposite directions but at the same flow rate. Again, the pressure and voltage responded in opposite directions but with the same magnitude. However, the magnitude of the voltage response was much smaller than for the groundwater experiments (Figure 3.3). Figure 3.4(b) shows a plot of the electrical potential versus the pressure difference for four different flow rates. A linear regression through this data yields a value for the EK coupling coefficient of -0.0175 ± 0.0020 mV/mH_2O with R^2=0.9999. This gives a zeta potential of -15.4 ± 1.4 mV. Chalk sample T1 showed a more positive coupling coefficient of -0.0101 ± 0.0020 mV/mH_2O (R^2=0.9999) and a significantly more positive zeta potential of -8.7 ± 1.6 mV, which may be related to differences in the surface charge of the two chalk cores.

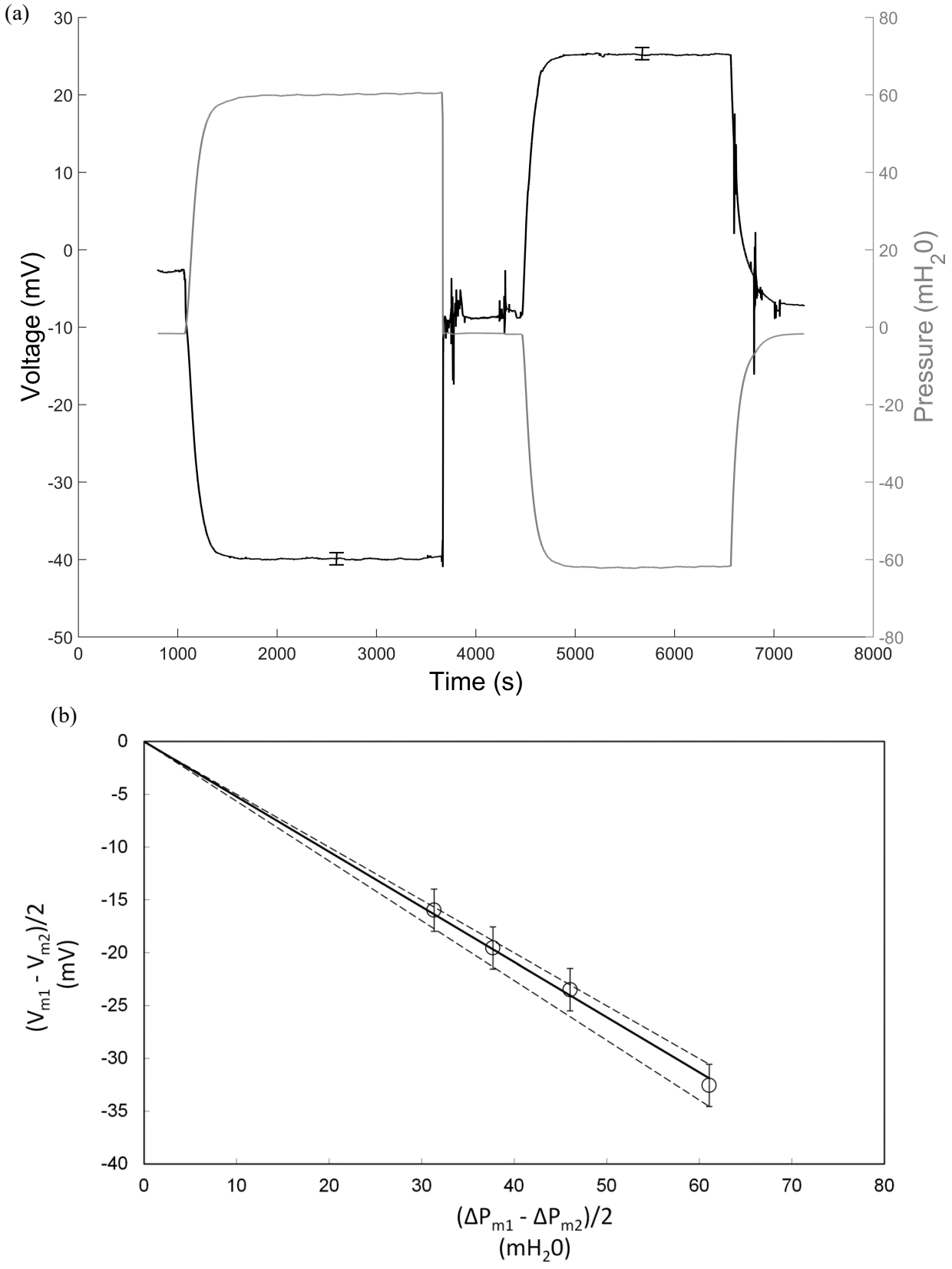

Figure 3.3 - Results for chalk sample S2 in groundwater (a) Pressure and voltage respond in opposite directions during pumping at 1 ml/min. (b) Change in pressure against change in voltage. The points represent the change in pressure for four flow rates (1 ml/min, 0.75 ml/min, 0.6 ml/min, 0.5 ml/min) and the gradient of the line is the coupling coefficient. The dashed lines show the maximum and minimum gradients based on the experimental error.

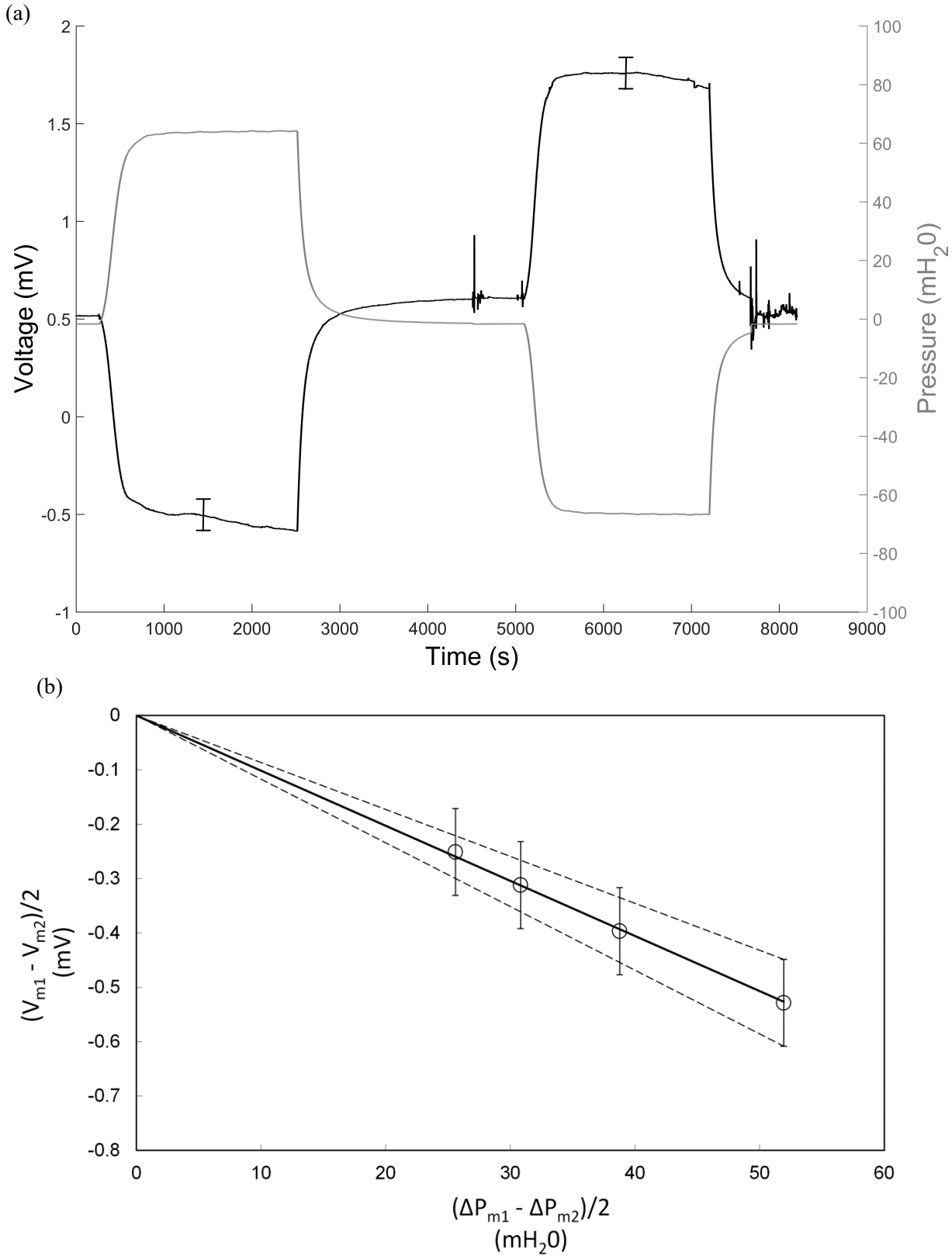

Figure 3.4 - Results for chalk sample S2 in seawater. (a) Pressure and voltage respond in opposite directions during pumping at 1 ml/min. (b) Change in pressure against change in voltage. The points represent the change in pressure for four flow rates (1 ml/min, 0.75 ml/min, 0.6 ml/min, 0.5 ml/min) and the gradient of the line is the coupling coefficient. The dashed lines show the maximum and minimum gradients based on the experimental error.

3.3.2 Exclusion-diffusion potential experiments

The EED experiments reported here used all of the samples shown in Table 3.3 including Seaford and Lewes Chalk core samples and a black shale sample. A typical result from the column experiment using GW/SW is shown in Figure 3.5.

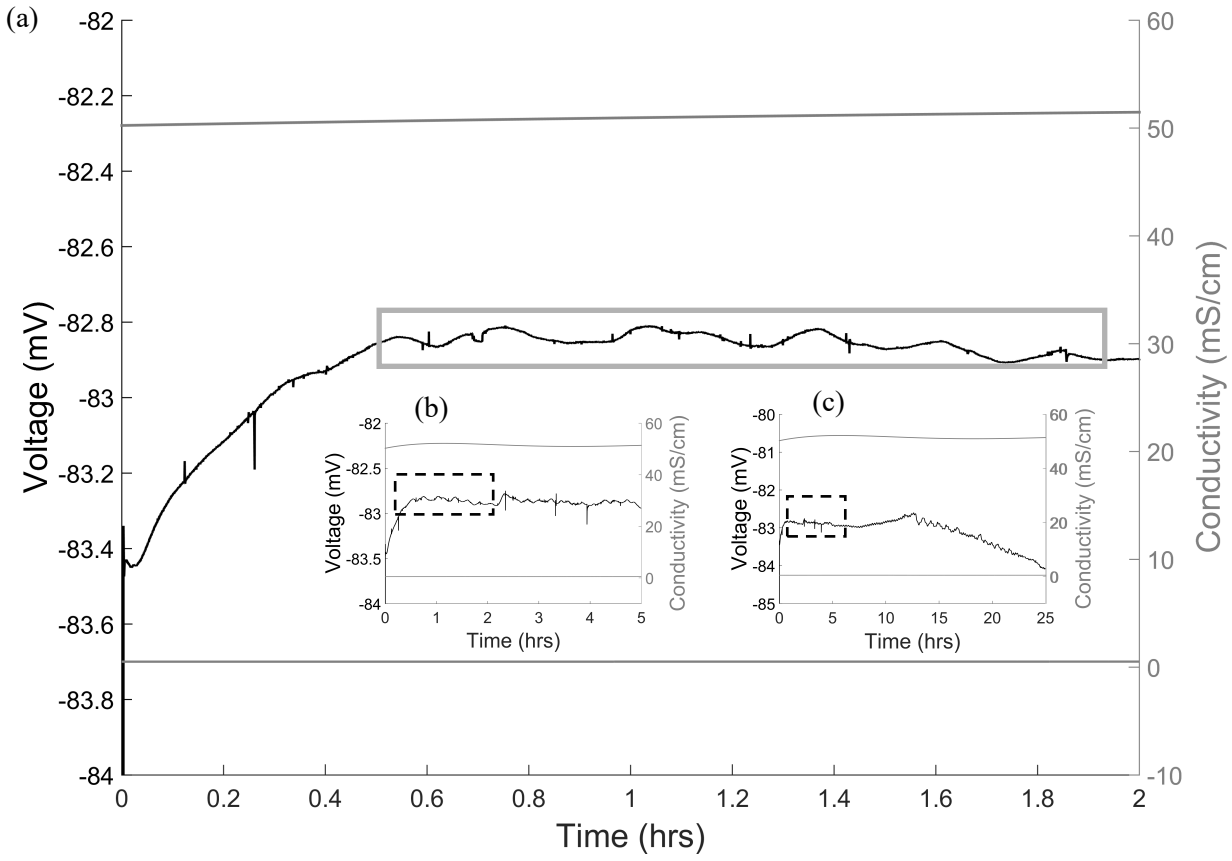

Figure 3.5 - Typical result for the column experiment using GW/SW. The main figure shows the results for the first two hours of the experiment, the grey box illustrates the area from which the apparent column voltage was taken; the stabilised voltage is highlighted by the thickness of the box. Inset (b) shows the results for 5 hours and highlights the area (dashed box) from which the results in (a) are taken, inset (c) shows the results from 25 hours and highlights the area (dashed box) from which the results in (b) are taken. (c) Illustrates that after the first few hours of the experiment significant drift of the voltage occurred.

The voltage drifted initially but then stabilised to within ± 50 μV. After a period of two hours the voltage drifted again. The drift, at later time, was due to diffusion across the electrode membrane and changes to the intrinsic potential of the electrodes. The conductivity in both reservoirs remained constant throughout this period. The stabilised voltage, averaged across a period of approximately 1.5 hours, after the initial drift, was taken as the apparent column voltage (V_{AC}, Equation 3.13), this value was used to calculate the electrode potential. The column experiment was repeated 15 times to assess the repeatability of the results for the GW/SW experiments and 5 times for the pre-eq(DI/5M)

experiments (Appendix 3). The final value used to calculate the electrode potential was the average value from the repeat experiments.

A typical experimental result from the plug experiment, using sample S3, is shown in Figure 3.6. Measurements of the voltage averaged across a period of about 1 hour were taken as the apparent plug voltage (V_{ac}, Equation 3.13). After one hour significant drift of the voltage occurred.

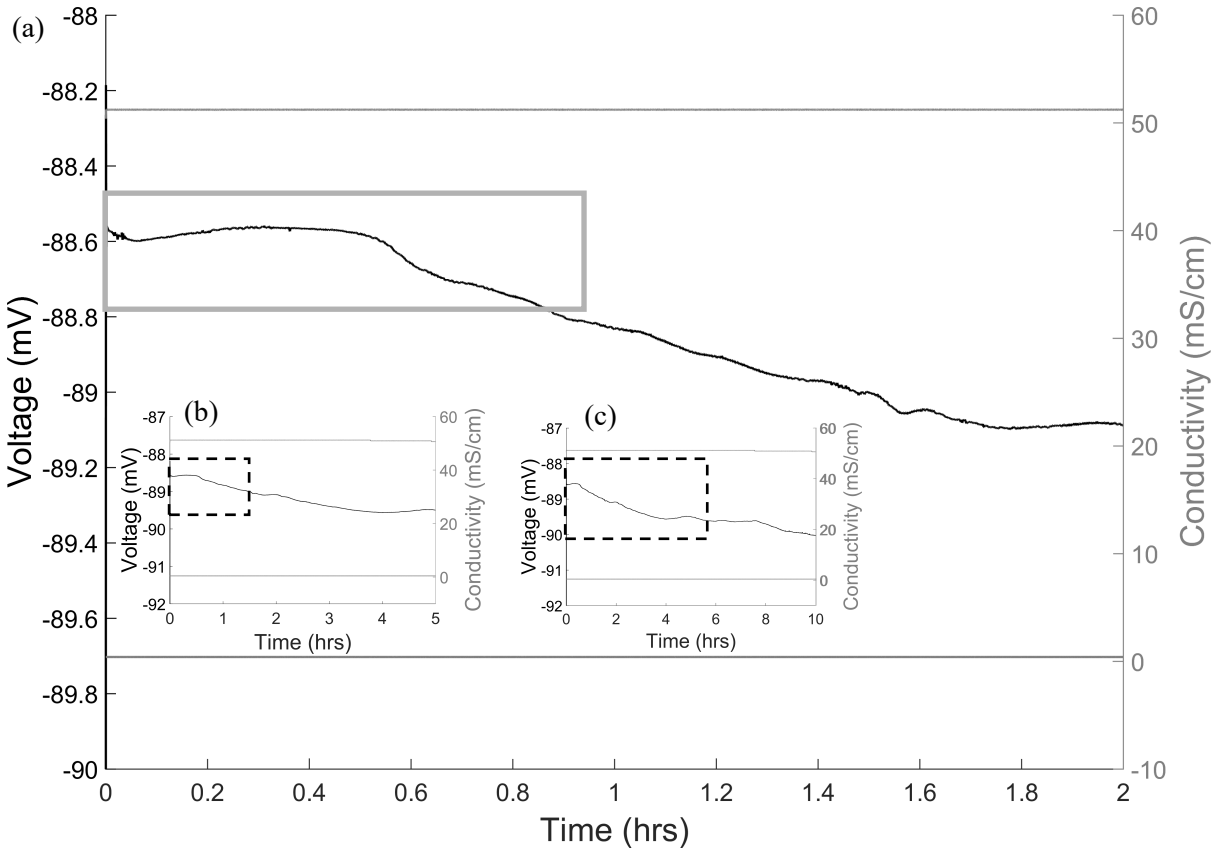

Figure 3.6 – Typical experimental result for the EED plug experiment using chalk sample S3 and GW/SW. The main figure shows the results for the first two hour of the experiment, the grey box illustrates the area from which the apparent plug voltage was taken; the stabilised voltage is highlighted by the thickness of the box. Inset (a) shows the results for the first 5 hours and the area (dashed box) from which the results in (a) are taken. (c) Shows the results for 10 hours illustrating that after the first hour of the experiment significant drift of the voltage occurred. Also shown is the area from which the results in (b) are taken (dashed box).

The faster on-set of voltage drift in the plug experiment occurred because the electrodes were placed much closer to the salinity front which was not stabilised by gravity. Therefore, once the core was connected to the high salinity reservoir, diffusion occurred between the core and the reservoir which in turn altered the salinity in the reservoir close to the electrode and altered the concentration gradient across the electrode membrane. It was not possible to achieve a longer period of stability due to the geometry of the plug experiment.

To obtain the errors for the apparent column ($\in_{V_{AC}}$) and plug ($\in_{V_{AP}}$) voltage measurements (Equation 3.15), a minimum of 3 repeat experiments were conducted for each chalk sample, for both the GW/SW experiments and the pre-eq(DI/5M). The original measurements can be found in Appendix 3. The average value from the repeat experiments for each core sample was used in the calculation for the EED potential (Equation 3.13). Note that, similar behaviour was observed in the pre-eq(DI/5M) experiments, so these results are not reproduced here (an example can be found in Appendix 3).

3.4.2.1 Electrode potential

The electrode potential was obtained by subtracting the diffusion potential calculated using Equation 3.10 from the apparent column voltage. This value was then subtracted from the voltage measured in the plug experiment to obtain the EED potential (i.e. Equation 3.13). The electrode potentials were found to dominate the apparent voltages measured in the plug and column experiments (Table 3.7). The error in the electrode potential was the sum of the repeatability of the column experiments and the error in the diffusion potential (Equation 3.16).

	Average column voltage (mV)	Diffusion potential (mV)	Electrode potential (mV)
GW/SW experiment	-80.93 ± 2.6	27.89 ± 4.8	-108.82 ± 7.4
Pre-eq(DI/5M) experiment	-128.22 ± 1.1	44.30 ± 4.6	-172.53 ± 5.7

Table 3.7 –The electrode potential results for the GW/SW experiments and the pre-eq(DI/5M) experiments. Equation 3.13 were used to calculate the electrode potential (V_C).

3.4.2.2 Exclusion-diffusion potential

Figure 3.7 shows the results of EED potential measurements after removing electrode effects. The results are expressed as a function of concentration ratio, calculated as the ratio of the total ionic strength of the high and low salinity electrolytes shown in Table 3.1 and Table 3.2 for the GW/SW experiments and Table 3.4 and Table 3.5 for the pre-eq(DI/5M) experiments. Also shown are the diffusion and exclusion limits obtained for NaCl for comparison with the results reported in Leinov and Jackson (2014).

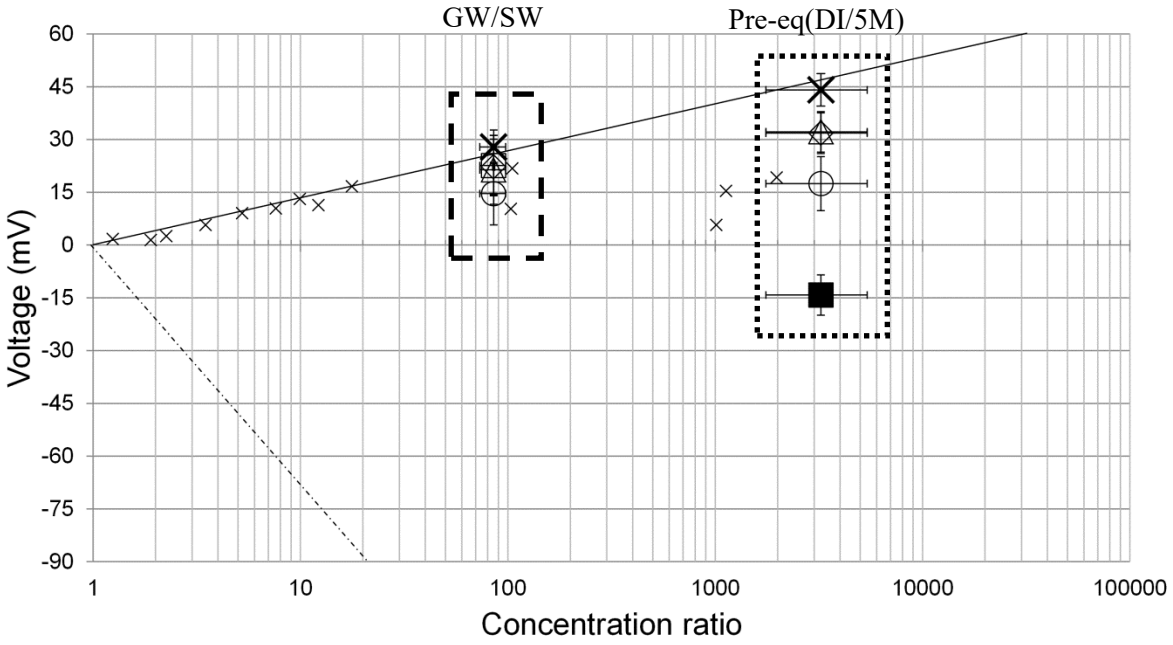

Figure 3.7 – EED potential measured in chalk. The black box with dashed lines shows the results from the GW/SW experiments and the black dotted box shows the results from the pre-eq(DI/5M) experiments. Also shown, using small crosses, are the results from Leinov and Jackson (2014) who used a 0.1 M NaCl electrolyte to saturate sandstone cores. All concentrations are reported as total ionic strength. The hollow squares show the result for chalk sample S4, triangle for sample S3, circle for S2 and diamond for sample T1. Also shown are the results of an EED experiment on a shale sample (black square) demonstrating that a very small pore radius is required to invert the polarity of the EED potential. The large black crosses show the limiting value of diffusion potential calculated using Equation 3.10. The black line represents the diffusion limit and the dashed line the exclusion limit calculated by Leinov and Jackson (2014). The diffusion potential limit calculated using Equation 3.10 is identical within experimental error to the expression used by Leinov and Jackson (2014) for NaCl electrolytes. The errors on the diffusion limits calculated using Equation 3.10 were based on the repeatability of water quality sample analysis carried out using IC.

At the GW/SW concentration ratio the maximum EED potential was +22.60 ± 8.62 mV measured in sample S4, and the smallest was +14.61 ± 8.90 mV in sample S2 (Table 3.6). For the pre-eq(DI/5M) experiments the maximum EED potential was +32.19 ± 5.77 mV in sample S3 and the minimum was +17.45 ± 7.68 mV in sample S2 (Table 3.6). In the pre-eq(DI/5M) experiments the measured values were further from the diffusion limit. However, for all chalk samples the EED potential is positive. Figure 3.7 also show the results from the black shale sample from the pre-eq(DI/5M) experiment. The shale sample measured -14.21 ± 5.74 mV (Table 3.6); thus, natural rock samples must have a micro-porous structure to record a negative EED potential. The much smaller pore throats in shale result in a more significant exclusion component of the EED potential.

3.4.2.2 Application of confining pressure

The EED experiments were repeated under a confining pressure equivalent to 100 m of overburden within the aquifer. The results for sample S3 are shown in Figure 3.8 for the GW/SW experiments. Application of a confining pressure resulted in a more negative voltage; consistent with increased

exclusion of ions from within the pore space (Figure 3.8). However, the magnitude of the change was not sufficient to reverse the polarity of the measured EED potential.

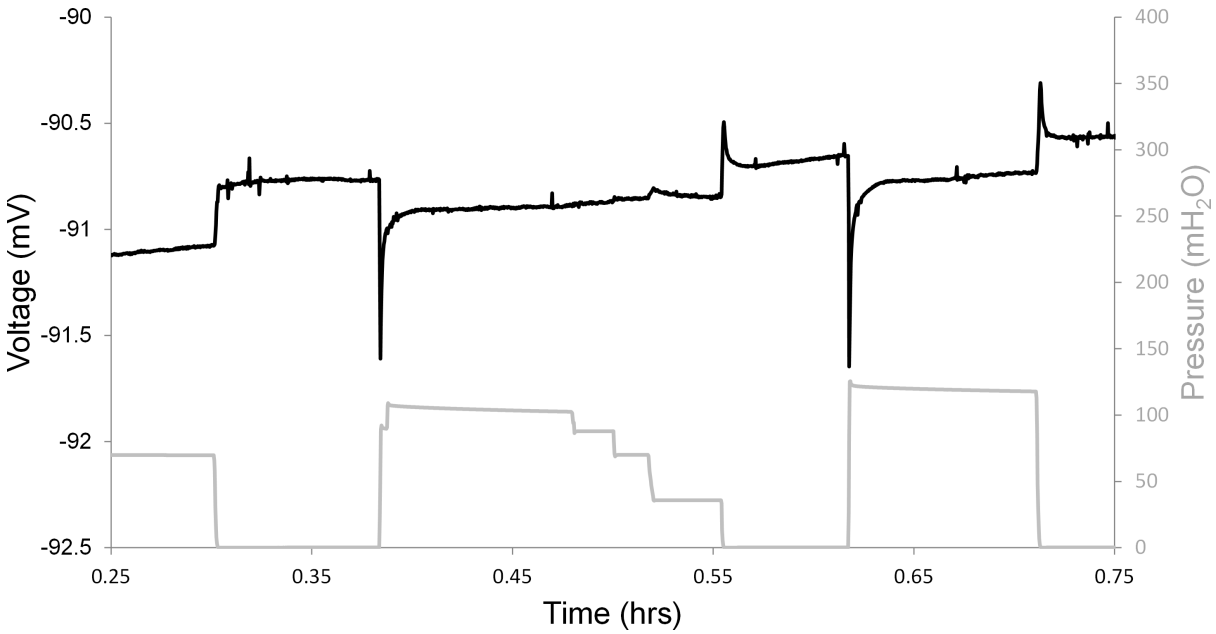

Figure 3.8 - Confining pressure results from sample S3 using GW and SW.

3.4 Discussion

3.4.1 Electrokinetic potential

The EK potential experiment results for chalk are consistent with the those reported by Jackson et al. (2012a). In fact the value they found for the EK coupling coefficient of chalk is identical, within experimental error, to the results for chalk sample T1 and S2 (Table 3.6). They found a coupling coefficient of -0.588 ± 0.04 mV/mH_2O, and a zeta potential of -13 ± 1 mV, using groundwater taken from the Seaford Chalk aquifer in Berkshire and chalk taken from the same source as sample T1.

The EK coupling coefficient measured with samples S2 and T1 saturated with seawater were both approximately an order of magnitude smaller than the groundwater coupling coefficient. The decrease of the coupling coefficients at high salinity is a well-known phenomenon and is due to the compression of the EDL (Vinogradov et al., 2010). The coupling coefficient at groundwater and seawater concentrations both showed negative values, confirming that the surface charge of Seaford chalk is negative at both salinities and that an excess of positive charge is transported in the EDL. However, the seawater coupling coefficient for chalk sample S2 was significantly more negative than the coupling coefficient measured in T1 using seawater.

Figure 3.9 shows the coupling coefficients measured for each chalk sample versus total ionic strength. Following Vinogradov et al. (2010) an empirical relation obtained from a regression through the data can be used to estimate the coupling coefficient at a given salinity for both chalk samples. In Figure 3.9 the coupling coefficients for the two chalk samples in SW are distinct but in GW they are the same within experimental error.

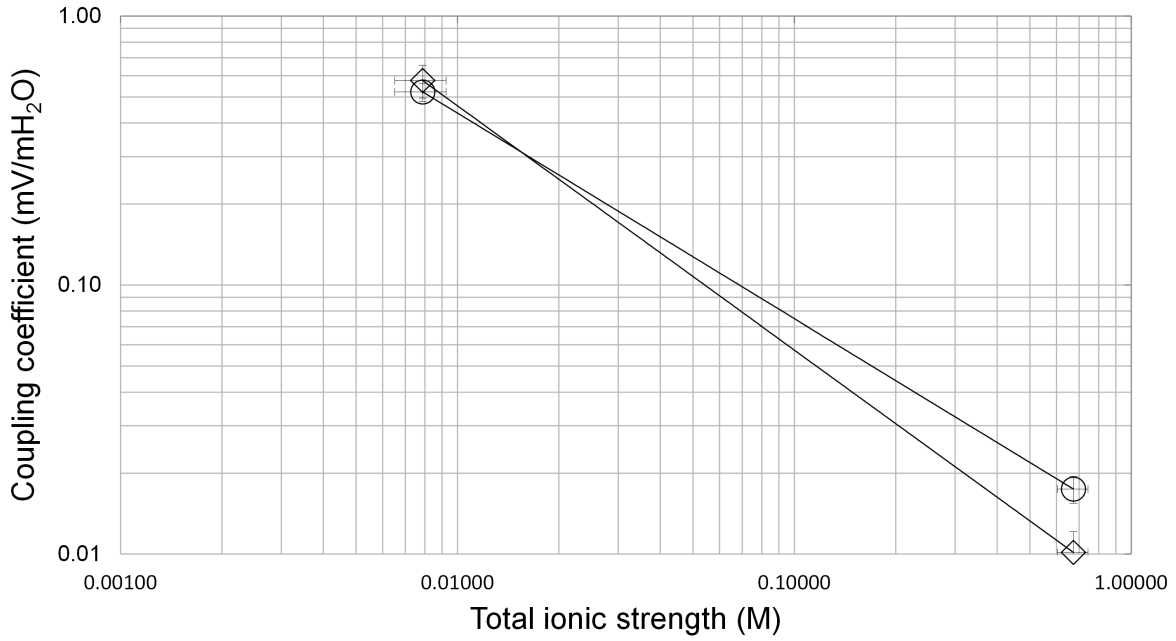

Figure 3.9 – EK coupling coefficient versus total ionic strength (M) for chalk samples S2 (circles) and T1 (diamonds). It is assumed that the coupling coefficient is related to salinity following the relationship determined by Vinogradov et al. (2010). Therefore, the coupling coefficient for sample T1 can be expressed as $C_{EK}=0.0071C^{-0.91}$ and for S2 it can be expressed as $C_{EK}=0.0129C^{-0.76}$.

The zeta potentials for chalk sample S2 and T1 (Table 3.6) for the seawater experiments are -15.4 ± 4.1 mV and -8.7 ± 1.7 mV respectively. Therefore, chalk sample S2 must have a higher surface charge than sample T1. The most likely explanation is the increased presence of organic matter on the surface of sample S2. The influence of organic matter on the chalk surface was discussed in section 2.3.2, where it was pointed out that organic matter is well known to have a strong negative charge. Therefore, even in small quantities organic matter can significantly influence the mineral surface charge (Cicerone et al., 1992, Vdovic and Biscan, 1998, Vdovic, 2001). If present within the chalk organic matter will result in a more strongly negative surface charge (i.e. sample S2).

The results from the EK experiments are shown compared to previous measured literature values of the zeta potential for carbonates against pCa (Figure 3.10). Following Alroudhan et al. (2016) pCa is

calculated from the negative logarithm of the Ca^{2+} concentration. Ca^{2+} is well known to be a potential determining ion (PDI) for the carbonate surface charge (Somasundaran and Agar, 1967, Thompson and Pownall, 1988, Cicerone et al., 1992, Strand et al., 2006, Zhang et al., 2007, Alroudhan et al., 2016) and is the dominant ion in the GW samples. The zeta potential of chalk was more negative than recent zeta potential measurements in Portland limestone reported by Alroudhan et al. (2016) even for similar values of pCa. Therefore, it appears that the chalk has a significantly higher surface charge than the Portland limestone. Note that, the average ionic strength of the groundwater samples used in the experiments reported here (Table 3.1) was one order of magnitude smaller than the ionic strength (0.05 M) used by Alroudhan et al. (2016), which may also explain the more negative zeta potential measured in the chalk samples. Measurements on Stevns Klint chalk by Zhang and Austad (2006) show significant differences in the relationship between zeta potential and pCa as compared to sample S2 and T1. One possible explanation for this is related to the environment in which the chalk was originally deposited and the resulting presence or absence of organic matter (Cicerone et al., 1992, Vdovic and Biscan, 1998, Vdovic, 2001). For example the Stevn's Klint has a different litohological and depositional setting, as highlighted by the presence of fish clay (Christensen et al., 1973) and Bryozoan Limestones (Surlyk et al., 2006) in Stevns Klint outcrops, which may have an impact on its eventual surface charge as measured by Zhang and Austad (2006).

The surface charge is primarily controlled by the PDIs (the role of PDIs was introduced in section 2.3.2). For example, Figure 3.10 shows that the lower Ca^{2+} concentration in groundwater resulted in a more negative zeta potential. However, it is well known that Mg^{2+} and SO_4^{2-} (Strand et al., 2006, Zhang et al., 2007, Alroudhan et al., 2016) are also PDIs for carbonates and are present in the seawater (Table 3.2). The presence of Mg^{2+} also results in a more negative zeta potential but it has a much lower concentration in the GW samples. The presence of SO_4^{2-} has the opposite effect. However, the dependence of the zeta potential on SO_4^{2-} is weaker than that of Ca^{2+} and Mg^{2+} (Alroudhan et al., 2016) and it also has a relatively low concentration in GW. From Table 3.1 it is clear that the concentration of Ca^{2+} is dominant in the GW samples; thus, Ca^{2+} is the primary control on the zeta potential and surface charge of the chalk in these experiments. Furthermore, because of the

decrease in the concentration of the PDIs (mainly Ca^{2+} and Mg^{2+}) and, as a result, the total ionic strength, from the SW to GW, the zeta potential of the chalk becomes more negative in the GW experiments (Thompson and Pownall, 1988, Cicerone et al., 1992). The difference in zeta potential between the Stevns Klint and Seaford Chalk does not have a clear explanation at present. However, under the conditions in which the measurements reported here are taken, and in those found in the UK coastal Chalk aquifer, the Seaford Chalk will almost certainly have a negative surface charge. The negative surface charge will arise even when seawater, which contains a much higher concentration of Ca^{2+} and Mg^{2+} than the GW, is in contact with the Seaford Chalk surface.

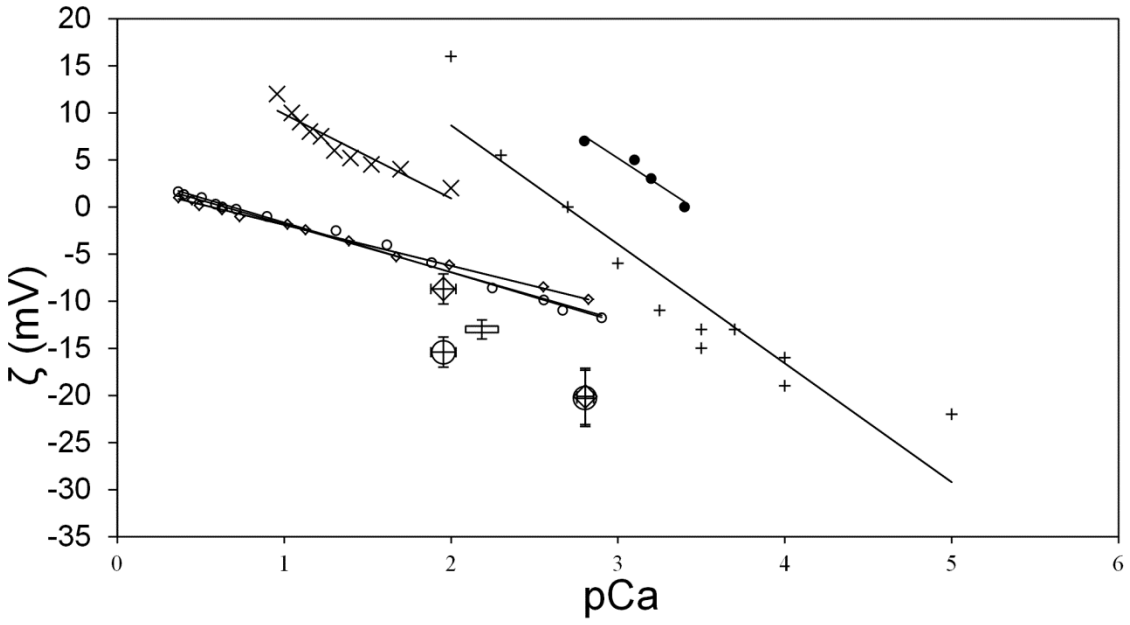

Figure 3.10 – Measurements of zeta potential on carbonate samples against pCa. The measurements for sample S2 are shown by the large hollow circles, and the measurements for sample T1 are shown by the large hollow diamonds. The measurement made on a chalk samples using groundwater by Jackson et al. (2012a) are also shown (hollow rectangle). Small open circles show measurements on Portland limestone using the electrophoretic method and the EK method by Alroudhan et al. (2016). Diagonal crosses show measurements made on Stevns Klint chalk using 0.573 M NaCl electrolyte at pH = 8.4 by Zhang and Austad (2006), black circles show measurements made on synthetic calcite and 0.02 M NaCl over the pH range 7-11 by Thompson and Pownall (1989) finally vertical crosses show measurements made on synthetic calcite and 0.03 M KCl over the pH range 8.5-10.5 by Cicerone et al., (1992).

From the perspective of seawater intrusion monitoring, these results show that the EK potential could be measured in the Chalk coastal aquifer, both in the groundwater and seawater regimes. In the seawater domain the EK potential is expected to be significantly smaller than in the freshwater zone, due to the compression of the EDL. However, there is likely to be a small, but potentially important, contribution to the measured SP during abstraction above a saline interface in coastal aquifers. Furthermore, any changes in pressure gradients caused by tidal process would be expected to generate

a measureable EK potential. In both cases, i.e. abstraction or tidally induced pressure changes, the EK potential measured in the field should respond in the opposite sense to change in the pressure gradient induced by pumping or tides.

3.4.2 Exclusion-diffusion potential

The new methodology developed for measuring the EED potential successfully produced stable and repeatable experimental results for natural electrolytes. In particular, it was very important to set the electrodes internal electrolyte concentration to have a chloride concentration similar to that of the natural electrolytes contained in each reservoir. In agreement with Leinov and Jackson (2014) the electrode potential was found to be dominant (Table 3.7) and must be accounted for.

The EED potential in all chalk samples was positive (with respect to a reference electrode in the low salinity reservoir) within experimental error for both the GW/SW and pre-eq(DI/5M) experiments. There was a small component of exclusion at both salinity contrasts, especially for chalk sample S2, although the deviation from the diffusion limit (indicated by the black line in Figure 3.7) appeared greater in the pre-eq(DI/5M) experiment. However, it is clear that in all chalk samples tested under conditions analogous to those encountered during seawater intrusion, the diffusion potential component was dominant and the polarity of the EED potential arising due to the concentration gradient between seawater and groundwater in the Chalk aquifer will be positive.

Leinov and Jackson (2014) emphasised the importance of rock texture in determining the value of the EED potential. In particular, they note that the pore throat radius (r) will influence the amount of exclusion occuring across a rock sample. Figure 3.11 shows the distribution of pore throat radii measured by mercury injection for each of the chalk samples used in the experiments.

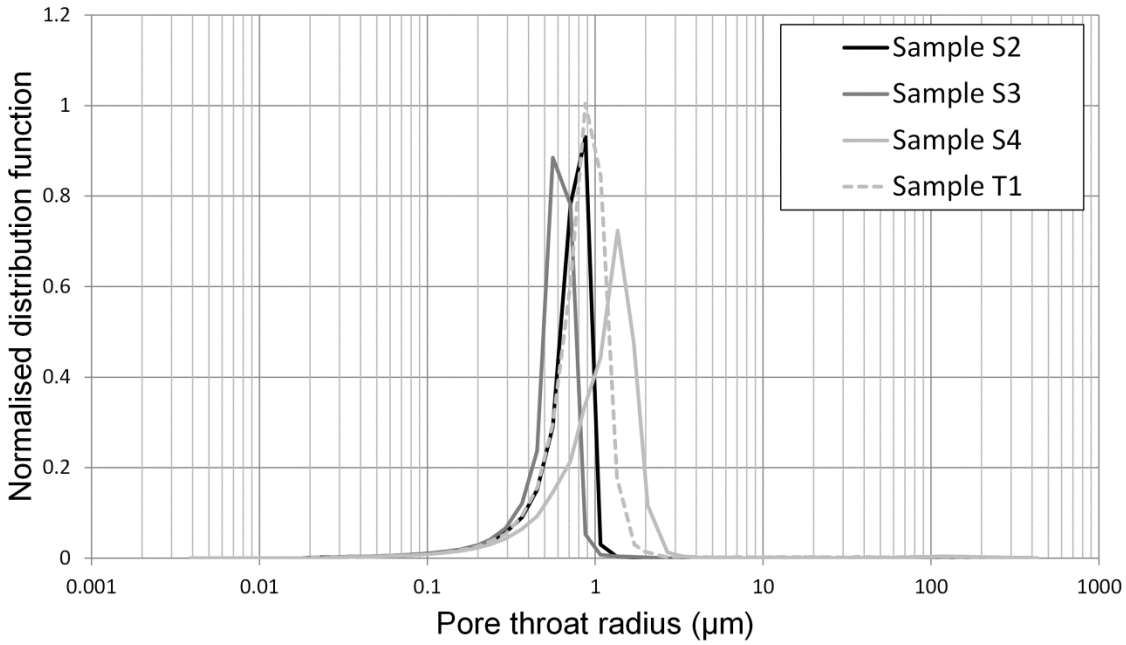

Figure 3.11 - Frequency distribution of pore throat radius measured in chalk samples S2, S3 and S4 using the mercury injection technique.

Although Leinov and Jackson (2014) used sandstone samples, and the pore throat radius of their samples was generally an order of magnitude larger than the chalk samples used in this study, the results reported by them (crosses in Figure 3.7) lie on a similar trend to the results reported here (other symbols in Figure 3.7). Leinov and Jackson (2014) used sandstone samples saturated with a 0.1 M NaCl. The saturating solution in the experiments reported here, i.e. either natural groundwater (~ 0.008 M) or pre-equilbrated chalk DI water (~ 0.002 M) (Table 3.1 and Table 3.4), have an ionic strenth approximately two orders of magnitude smaller than those used by Leinov and Jackson (2014); thus, more exclusion might be expected in the chalk. However, it is possible that since the chalk samples have more positive zeta potential than sandstone at similar low concentrations of saturating electrolyte (Vinogradov et al., 2010), that less exclusion of ions occurs within the chalk, since the exclusion of ions depends on the surface charge (Leinov and Jackson, 2014). The more positive zeta potential of chalk sample S2 (at seawater salinity), and the more negative EED potential of this sample also hints at the influence of the surface charge on the EED potential (Figure 3.7).

The relationship between the pore throat radius (r) and the ionic strength of the saturating electrolyte influences the magnitude and polarity of the EED potential because this relationship determines the relative influence of the EDL. The size of the diffuse layer within the EDL is dependant on the

salinity of the saturating fluid and is thicker at low salinity (Vinogradov et al., 2010). The thickness of the diffuse layer, also known as the Debye length (λ) (Table 3.8), was calculated using Equation 2.10, for the groundwater (Table 3.1) and the pre-equilbrated DI water (Table 3.4). Westermann-Clark and Christoforou (1986) and Leinov and Jackson (2014) investigated the EED potential using a capilliary tube model and found that when $\frac{r}{\lambda}$ is small (<0.1-1) the exclusion potential is dominant because the EDL dominates the pore space. The diffusion potential dominates when $\frac{r}{\lambda}$ is large (>10-100), because the EDL is thin relative to the pore throat radius, and the co-ions can pass more easily. When the value of $\frac{r}{\lambda}$ is greater than 4000, in other words when the pore radius is 4000 times greater than the Debye length, the exclusion component of the EED potential is negligible. The value of $\frac{r}{\lambda}$ for each of the chalk samples, saturated with the low salinity electroltye (i.e. GW or pre-equilbrated DI water), are shown in Table 3.8. The error in λ and $\frac{r}{\lambda}$ is based on the maximum and minimum concentrations measured for the GW and SW samples and the pre-equilibrated DI and 5 M samples. The diffusion potential was dominant in all of the experiments against the criteria defined by Westermann-Clark and Christoforou (1986) because the pore throat radii were about two orders of magnitude larger than the calculated Debye length at both saturating salinities (Table 3.8).

Description of electrolyte	Debye Length λ (nm)	Sample	Median pore throat diameter r (nm)	$\frac{r}{\lambda}$
Groundwater saturated core	3.44 ± 0.14	S2	817.6	237.91 ± 9.53
		S3	654.1	190.34 ± 7.63
		S4	1332.8	387.83 ± 15.54
		T1	950.6	276.61 ± 11.09
Chalk equilbrated pre-eq(DI) saturated core	6.40 ± 2.93	S2	817.6	127.68 ± 56.79
		S3	654.1	102.15 ± 45.43
		S4	1332.8	208.14 ± 92.58
		T1	950.6	148.45 ± 66.03

Table 3.8 - Debye length calculated from Equation 2.10 for the groundwater and chalk equilibrated DI water which were used to saturate the samples and which yield the largest value of r/λ used in the experiments. Also shown is the median pore throat radius for each chalk sample. The value for r/λ is also shown. Note that Aberdeen University reported that the errors on the measurements of the pore throat radius were negligible (Healy, 2016), hence why no errors are shown.

3.5.2.2 The exclusion-efficiency

Leinov and Jackson (2014) proposed the use of an exclusion efficiency to investigate, quantatitively, the relative contributions of the exclusion and diffusion potentials to the overall observed EED potential. They suggested that the exclusion efficiency can be modelled as a linear function of $\frac{r}{\lambda}$,

where r is the pore throat radius and λ is the Debye length. The exclusion-efficiency of the chalk samples was estimated by calculating the limiting value of the exclusion potential (V_{EE}) at the salinity contrasts used in this study, the activities in the expression used by Leinov and Jackson (2014) (i.e. Equation 2.22) were replaced by the total ionic strengths of the electrolytes (i.e. Revil et al. (2005)):

$$V_{EE} = -\frac{k_B T}{e} ln\left(\frac{C_{Mi}^{0}}{C_{Mi}^{\Delta X}}\right) \quad \textbf{Equation 3.17}$$

Note that the exclusion-efficiency was calculated using the ionic strengths for the two different experiments reported in Table 3.1 and Table 3.4, but because an equivalent expression to Equation 3.10 is not available for the exclusion potential in multi-ion electrolytes, V_{EE} was approximated by assuming a 1:1 electrolyte. The exclusion efficiency was calculated as follows:

$$\eta = \frac{V_{EED} - V_{ED}}{V_{EE} - V_{ED}} \quad \textbf{Equation 3.18}$$

Figure 3.12 shows the exclusion efficiency against $\frac{r}{\lambda}$. The errors in the exclusion efficiency were calculated based on the error for V_{EED} and V_{ED} reported in Table 3.6 and Table 3.7. The error in V_{EE} was based on the maximum and minimum ionic strengths reported in Table 3.1 and Table 3.2 for GW and SW respectively and Table 3.4 and Table 3.5 for the pre-equilibrated DI and 5 M electrolytes. The exclusion efficiency for chalk sample S2 was significantly higher than for samples, T1, S3 and S4, indicating more exclusion of positive ions from within the pore-space of sample S2, and explaining the more negative EED potential. The higher exclusion efficiency of chalk sample S2 can only be explained by the fact that it also had a higher surface charge as indicated by the more negative zeta potential compared to chalk sample T1 (Table 3.6) which had a similar distribution of pore throat radius (Figure 3.11). Thus, it appears that the higher zeta potential, possibly due to the presence of organic matter on the surface of chalk sample S2 (section 3.4.1), was responsible for the higher exclusion-efficiency. Figure 3.12 also illustrates that chalk has a lower exclusion efficiency at smaller values of $\frac{r}{\lambda}$ as compared to the sandstones used in the experiments conducted by Leinov and Jackson (2014). However, further work would be required to understand the reasons for this.

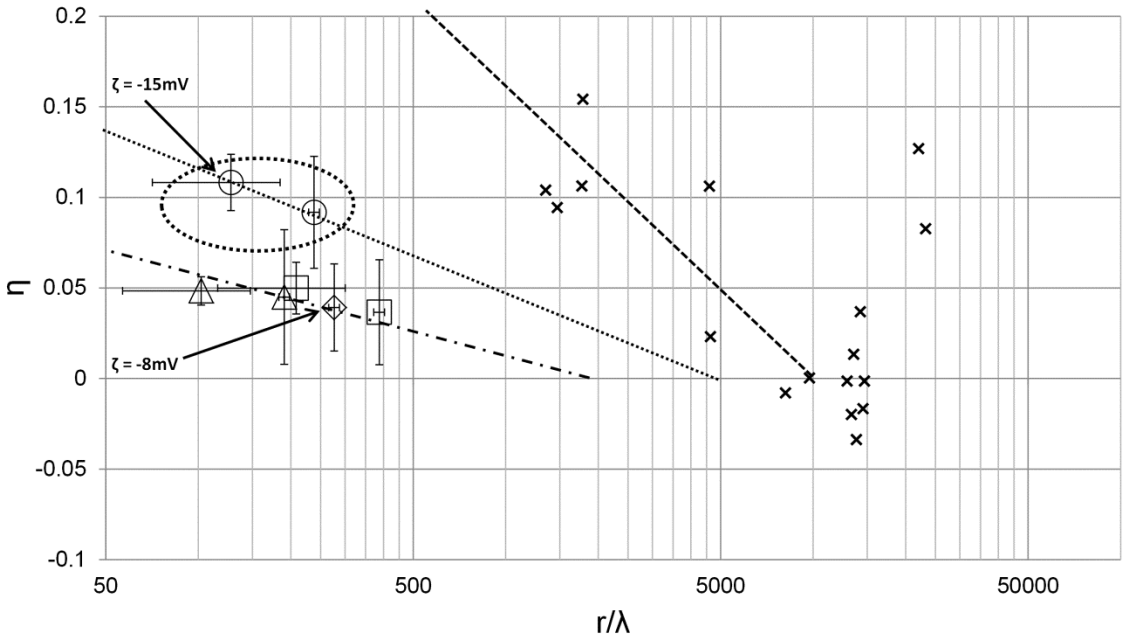

Figure 3.12 – (a) The exclusion efficiency as a function of pore throat radius. The squares show the result for chalk sample S4, triangle for sample S3, circle for S2 and diamond for sample T1. Also shown are the values of exclusion efficiency measured by Leinov and Jackson (2014) indicated by crosses. The dashed black line shows the linear model proposed by them, η=-01679ln(r/λ)+0.6633. The dotted black line shows a proposed linear fit for chalk sample S2 which has the equation η =-0.023ln(r/λ)+0.2203, and the dot-dashed black line shows a proposed linear fit through the remaining data points for chalk sample S3, S4 and T1, which has the equation η =-0.009ln(r/λ)+0.0865.

3.5.2.1 Application of confining pressure

Figure 3.8 shows that application of a confining pressure altered the absolute magnitude of voltages measured in the EED experiments. However, the application of a confining pressure was not sufficient to reverse the polarity of the EED potential; thus, within the active zone of the Chalk aquifer the EED potential will always be positive (with respect to a reference electrode in the groundwater). However, Figure 3.8 also revealed significant transient spikes (Figure 3.13) in the voltage data that responded immediately to the application of the confining pressure.

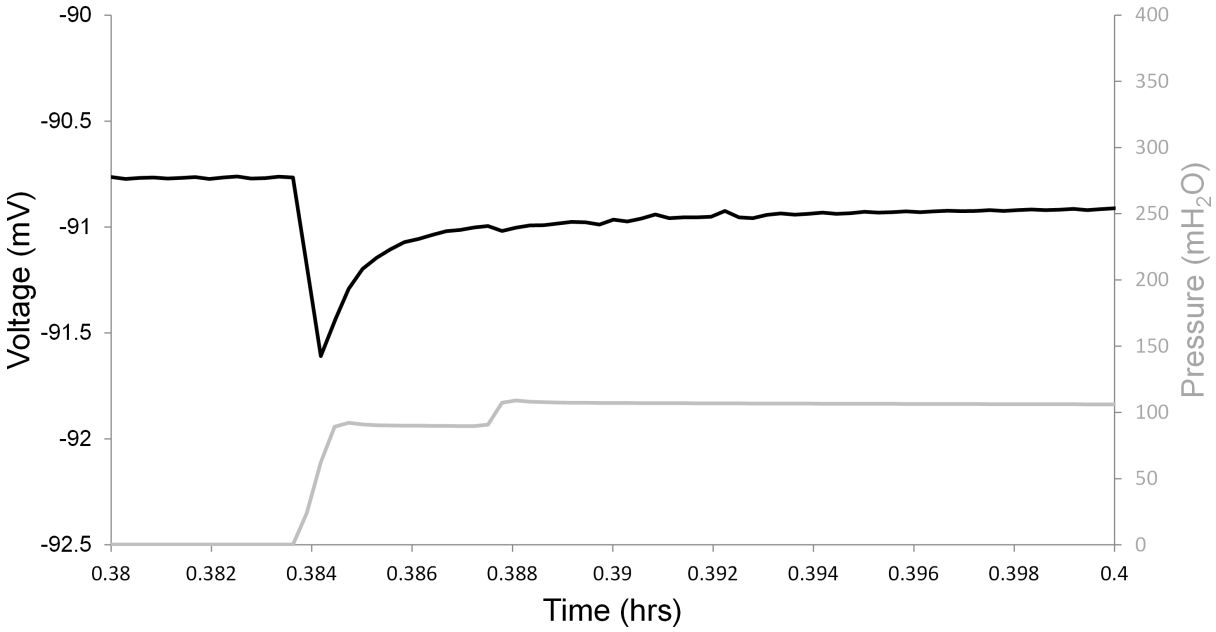

Figure 3.13 - The voltage responds immediately after pressure was applied to the chalk cores; an initial electrical burst was recorded that is related to the EK potential.

The spike in the voltage is related to the EK potential, because the application or release of the confining pressure triggers movement of fluid through and out of the rock. Figure 3.13(b) shows the first of these bursts of voltage which may be due to the superimposed effects of flow in both directions inside and out of the sample. The change in voltage was in the opposite sense to the change of pressure, which would be consistent with a negative EK coupling coefficient. However, because the pressure on either side of the sample was unknown it is not possible to calculate the coupling coefficient. The key finding is that the application of confining pressure did not significantly alter the EED potential measured in chalk for the GW/SW experiments.

3.4.3 Implications for seawater intrusion monitoring

It is clear that for seawater intrusion in the Chalk aquifer, the EED potential across the saline front and between the seawater and groundwater end members is positive (with repect to a reference electrode in the groundwater) and dominated by the diffusion component. Depending on the amount of organic material present in the chalk and the resulting surface charge, the exclusion component may play a more important role in some localities lowering the absolute magnitude, but never changing the sign of the potential difference across the saline front.

The results suggest that the EED potential may contribute significantly to the overall SP observed in a coastal aquifer. The value of the potential, due to the concenration gradient between groundwater and seawater, across the saline front in the experiments was tens of millivolts, ranging from c.14 mV in sample S2 with the highest exclusion efficiency to c.23 mV in the samples with the lowest exclusion efficiency (S4). In the diffusion dominated systems, such as a fracture or high permeability zone, the diffusion potential calculated using Equation 3.10 is c.27 mV.

The value of the EK coupling coefficient was relatively small in chalk, and would require significant pressure gradients to generate a similar magnitude of signal. For example, in the groundwater regime, where the largest coupling coefficient was obtained (-0.575 ± 0.080 mV/mH_20 in sample T1), a change in head of approximately 2 m would be required in order to generate a 1 mV EK signal. In the seawater dominated zone the drawdown required to generate a similar signal would have to be at least an order of magnitude larger. Thus, the EK component could reasonably be expected to be small in the coastal Chalk aquifer, unless there are very large tidally induced changes in the pressure gradients. Despite this, and without reporting the type of material in which their measurements were made or the coupling coefficients for that material, Kang et al. (2014) attributed the flow of seawater through a sea dyke to be the predominant mechanism for the generation of the SP they observed. Such an assumption appears unreasonable given the arguments outlined here. It is possible that such pressure gradients may arise in coastal aquifers, but this will most likely occur in areas dominated by large drawdowns due to pumping. Thus, in agreement with the results of previous authors (Ikard et al., 2012, Leinov and Jackson, 2014, Jougnot et al., 2015) the EED potential cannot be neglected when assessing the main source mechanisms for SP where salinity gradients occur, including in coastal areas. In fact, the EED potential may be the dominant source of SP in a coastal setting. Similarly, assuming that the EED potential simply falls on the diffusion limit may in fact lead to inaccurate estimates of the overall contribution to the EED potential in coastal aquifers, where there may be an important albeit small contribution from the exclusion potential.

The results emphasise the need to properly characterise chalk samples from different sources because the chalk samples used here have different EK and EED properties. Such variability may affect the

overall magnitude of the SP and the contribution of each of the components to that signal, from one location to another. Furthermore, this may create a risk for interpretation of the field monitoring data as spatial variability of the chalk properties may affect the signals observed. Finally, and crucially, the results reported here were used to simulate the electrodynamic properties of seawater intrusion in a coastal aquifer. The values of the EK coupling coefficient and the measured EED potential were used directly in the electrodynamic model of the coastal site. The simulation method is reported in chapter 4 and the results in chapters 5 and 6.

3.5 Conclusions

Electrokinetic potential measurements on chalk samples revealed a negative coupling coefficient, and zeta potentials of tens of mV for groundwater samples. The coupling coefficient and zeta potential were smaller in seawater, which is consistent with previous work, and is due, in part, to the compression of the electrical double layer. Sample S2 displayed a more negative surface charge as revealed by the more negative zeta potential at seawater salinity. A more negative surface charge may also be explained by the presence of organic material in the chalk matrix for sample S2. The importance of the PDI concentrations was also highlighted, particularly Ca^{2+}, on the absolute magnitude of the zeta potential, which becomes more positive with increased Ca^{2+} concentration and will also contribute to the smaller zeta potential measured in the seawater samples. The results appear consistent with previous measurements of the zeta potential in carbonates, with the exception of measurements made in Stevns Klint Chalk. However, there is currently no clear explanation as to why the results are so different for these two types of chalk. Despite this, the results reported here indicate that the EK potential will contribute a potentially small but significant component of the total SP likely to be observed in the Chalk coastal aquifer. The EK component is expected to be more significant in the freshwater zone, because of the larger coupling coefficient measured in groundwater.

The exclusion-diffusion potential across natural chalk samples in contact with natural groundwater and seawater has been measured. The method employed adapted a previous experimental method which was designed to remove electrode effects from the measurement of the potential difference

across a saline front. The method was adapted in order to account for the increased complexity of the natural electrolytes used. The new method successfully produced repeatable experimental results. The EED potential measured was in the range of tens of millivolts, and was dominated by the diffusion potential. This was true even at a much higher salinity contrast and under confining pressure. Sample S2 displayed the largest exclusion efficiency, and the EED potential measurements confirmed the EK measurements that suggested that the surface charge of this sample was more negative than the other samples. Thus, the EK measurements were also essential to the interpretation of the EED potential results. Since the EED potential was positive in all chalk samples the electrical double layer only plays a small role in excluding charge from within the pore space in a GW/SW environment. Local differences between chalks, as illustrated by the larger exclusion efficiency and higher surface charge of chalk sample S2, may slightly affect the overall contribution of the exclusion potential. However, in all cases measured the EED potential remains positive, with the exception of a shale sample that showed a negative potential and a much greater contribution to the overall EED potential from the exclusion component. The difference in polarity between the EK coupling coefficient and the EED potential across the saline front is important because the polarity of seasonal or tidal changes in SP in the coastal aquifer may facilitate investigation of the dominant SP component active in the aquifer.

The results suggest that the magnitude of the EED potential across the saline front is tens of mV, in order for the EK potential to be of similar magnitude head fluctuations induced either by pumping or tides would have to be very large and most likely beyond what was possible in the coastal aquifer where the field monitoring took place. Thus, for SP monitoring in coastal aquifers the EED potential is likely to contribute significantly to the overall observed SP. Finally, the relative contribution of the EK and EED potentials to the overall SP signal likely to be observed in a coastal aquifer are investigated further, using the laboratory measured values, in regional numerical models.

Chapter 4

Self-potential field monitoring and regional numerical modelling methodology

4.1 Introduction

The methods for the field monitoring and regional numerical models of the Chalk coastal aquifer are outlined in this chapter. The chapter begins by introducing both the inland and coastal sites in the Chalk and the methods used for SP monitoring at both sites. Many of the key frequency components likely to arise in the SP data at the coast have multiple source mechanisms other than ocean tidal processes (section 2.3.6.4). Therefore, the two sites were compared in order to identify processes that were unique to the coastal site and, so, more likely to be caused directly by ocean tidal processes occurring within the aquifer. The inland site is discussed first, followed by the coastal site.

The aim of the field monitoring campaign was to establish whether measurements of SP respond to tidal and seasonal changes in the pressure and concentration gradients at the coastal site. The objectives were: (i) measure SP signals generated in the coastal aquifer, (ii) determine whether tidal effects induce a measureable SP in the coastal borehole, (iii) assess the relative importance of other periodic effects that may lead to the generation of a periodic SP by comparing and contrasting inland and coastal SP measurements, (iv) establish whether measurements of SP provide spatial information on the location of the saline front relative to the coastal monitoring borehole and (v) establish whether measurements of SP provide early warning of the intruding saline front. The results of objectives (ii) and (iii) are presented in chapter 5, and the results of objective (iv) and (v) are presented in chapter 6.

The hydrodynamic and electrodynamic modelling methodology for the regional model of the coastal site is presented at the end of this chapter. The numerical modelling was used to support interpretation of the SP data observed at the coastal site and to further address the field monitoring aims and objectives outlined above. The specific aim of the numerical modelling was to gain a preliminary understanding of the contribution of the EK and EED potential source mechanisms and the possible

hydrodynamic processes that could lead to the generation of the observed SP at the coastal site. The primary aim was not to closely match the observed data, but to investigate the processes that may lead to the SP observed at the coastal site. The modelling objectives were: (i) develop a series of basic hydrodynamic models based on field data and a conceptual understanding of the site, (ii) compare and contrast different hydrodynamic cases and (iii) develop hypothesis as to the nature of the salinity distributions and the relative contribution of the EK and EED potentials that may lead to the observed SP in the coastal aquifer in East Sussex.

4.2 Field methodology

The discussion of long-term SP monitoring experiments in section 2.3.6.1 was used to guide the experimental design for the SP monitoring adopted in this study. Figure 4.1 shows the location of the coastal and inland SP monitoring sites. Figure 4.2 shows the layout of the surface and borehole arrays at the inland site near Trumpletts Farm in Berkshire. Figure 4.3 shows the layout of the coastal site and the design of the borehole array at the Saltdean monitoring borehole in East Sussex. Both sites are in the Upper Chalk aquifer; thus, are ideal for comparing observations of coastal and inland SP. Due to the possible influence of the geomagnetic field on the SP (section 2.3.6), geomagnetic data is also reported from three monitoring stations around the two sites (Figure 4.1)

Figure 4.1 – Location of the two SP monitoring sites, Trumpletts Farm (hollow grey square) and Saltdean (hollow grey circle), and the three geomagnetic monitoring stations (hollow triangles) used in this analysis, Hartwell (1) and Eskdalemuir (2) in the UK and Chambon-la-Foret (3) in Northern France. Also shown is the extent of the UK Chalk aquifer (shaded in black; modified from NERC UK Groundwater Forum by Wardle (2011)).

4.2.1 Inland site – Trumpletts Farm, Berkshire

4.2.1.1 Site description

The inland site has been extensively investigated for groundwater flow and transport as part of the UK Natural Environment Research Council research programme on lowland catchments (Williams et al., 2006, Wheater et al., 2007, Mathias et al., 2007, Butler et al., 2009). The site consists of six 100 m deep boreholes drilled close to an environment agency (EA) abstraction borehole. The boreholes penetrate several chalk intervals, including the New Pit Chalk at the base, then the Lewes Nodular Chalk, assumed to be c.20 m thick (Schürch and Buckley, 2002, Woods, 2006). At the base of the Lewes Nodular Chalk is a 3 m thick layer of Chalk Rock. The Seaford Chalk then overlays the Lewes Nodular Chalk and extends to the surface. Three of the boreholes are left open and the remaining three are completed as piezometers. The site is on the side of a dry valley, there is difference in height between the abstraction borehole and the northern borehole (PL10B) of about 5 m. The water-table was approximately 20 m below ground, with a difference in elevation of c.0.5 m between the abstraction borehole and PL10B. The hydraulic gradient is approximately 0.001 from north to south (Williams et al., 2006). The site was previously used to monitor the SP response to pumping with a small submersible pump placed in PL10B (Jackson et al., 2012a). The borehole SP array for that experiment was in the Seaford Chalk horizon in PL10A, which has significant inflows, assumed to be related to discreet fracture horizons (Mathias et al., 2007, Butler et al., 2009). A negative SP was observed during pressure drawdown and a positive response during recovery (Jackson et al., 2012a).

Here, PL10B was instrumented with four SP electrodes and a FEC/T/P probe at the top of the water column. A surface array was installed to assess the impact of temperature, geomagnetic, atmospheric, and/or Earth tide effects, and their relative magnitude in the SP data. All of these mechanisms have diurnal or semi-diurnal periods that may drive process that manifest in the SP data (Kulessa, 2003, Trique et al., 2002) (section 2.3.6.4). Therefore, to ensure observations of diurnal or semi-diurnal SP in the coastal aquifer were driven purely by ocean tides, these other process must first be ruled out as a significant source of the periodic SP, which was the purpose of the inland monitoring experiment.

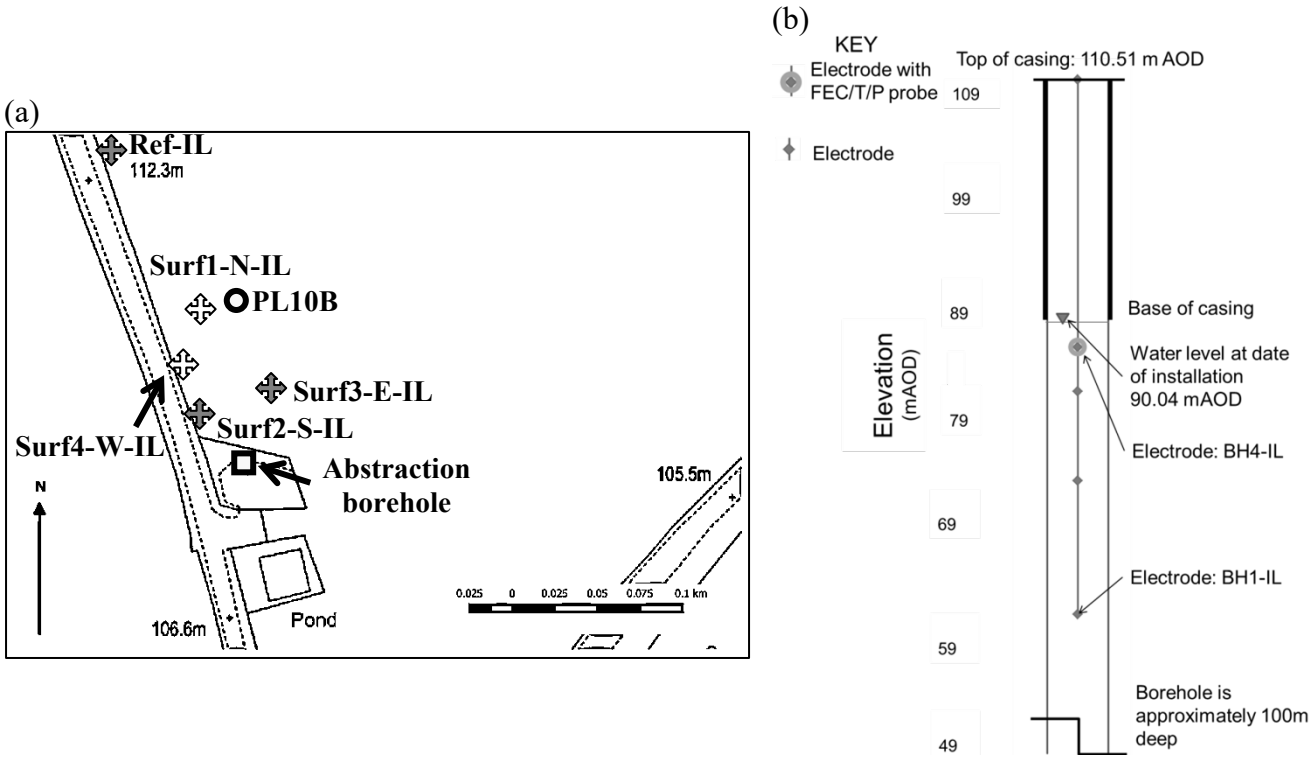

Figure 4.2 – (a) Site layout at Trumpletts Farm. The surface array is shown (crosses) and the borehole containing the vertical array is highlighted (hollow circle). Temperature measurements are taken at the reference electrode (Ref-IL), the southern (Surf2-S-IL) and the eastern electrodes (Surf3-E-IL) all shaded in grey. The notation IL indicates the inland site and Surf indicates electrodes in the surface array; Ref indicates the surface reference electrode. The abstraction borehole used for the pumping test is highlighted (hollow square). (b) The borehole array in PL10B. Four electrodes were installed in the borehole with a maximum separation of 24 m, intermediate separations with respect to the shallowest electrode of 12 and 8 m and a minimum separation of 4 m, matching electrode spacing in the Saltdean borehole (Figure 4.3). The notation BH indicates electrodes in the borehole array. The BH4-IL was attached to an FEC/T/P probe. The borehole has a diameter of c.143 mm. The details of the borehole construction are taken from Williams et al. (2006). Map: © Crown copyright and database rights 2015 Ordnance Survey (Digimap License).

4.2.2 Coastal site – Saltdean, East Sussex

4.2.2.1 Site description and history of saline intrusion

Seawater intrusion has been an issue in the Chalk aquifer of the South Downs for many years, with the first recorded abandonment of a water supply borehole in 1879 (Robins et al., 1999). After the severe drought of 1956 the water authority adopted a policy that involved use of coastal boreholes in the winter and inland boreholes in the summer (Robins et al., 1999). The policy was developed to exploit the 'leakage' of freshwater to the sea during high water levels in the winter. Therefore, inland water levels were allowed to recover and freshwater was 'stored' inland during the winter. During the summer, when water levels were low, the inland boreholes were exploited. As a result, the coastal sources were known as leakage sources and the inland sources as storage sources. The net result of this policy was to increase freshwater heads in the storage boreholes by as much as 5 m; furthermore, the policy resulted in a decline in chloride concentrations across the Brighton Chalk block.

Balsdean (c.2.5 km inland) is a key water supply for eastern Brighton and has a history of elevated salinity, up to 400 mg/l chloride in 1949 and 200 mg/l in 1989 (Jones and Robins, 1999). It is believed that the high salinities are due to a direct, high permeability, connection between the Balsdean borehole and the sea. Jones and Robins (1999) stated that most of the water abstracted from Balsdean derives from a discrete fracture 21 m below the water table. Historically Balsdean pumping regimes have been strictly managed to minimise the risk of seawater intrusion (section 2.2.3.2). The maximum historical water table depth recorded at Balsdean was c.3.7 mAOD, but water levels can fall as low as c.0.3 mAOD (Jones and Robins, 1999).

The Saltdean borehole (Figure 4.3), the only accessible coastal borehole in the area, is used to monitor salinity seaward of the Balsdean abstraction borehole (section 2.2.3.2). Saltdean was previously used as an abstraction borehole, but was abandoned in 1936 (Robins et al., 1999, Jones and Robins, 1999) in favour of Balsdean which was further inland and thought to be at reduced risk of contamination by intruding seawater. Jones and Robins (1999) reported that conductivity within the Saltdean borehole can reach as high as 15,000 μS/cm (~ 7500 mg/l). They suggested that water levels in the Saltdean borehole are affected by pumping at Balsdean but that the salinity is not. However, long term increases in salinity at Balsdean appear to be reflected by seasonal increases in salinity at Saltdean.

On the basis of the above, and after discussions with Southern Water, the Saltdean borehole was identified as the best site for SP monitoring of seawater intrusion in the Chalk aquifer of the South Downs. Saltdean is located c.1.7 km from the coast (Figure 4.3) and is c.1.3 km from the Balsdean abstraction borehole. The Saltdean borehole penetrates the fine-grained Upper Cretaceous Seaford Chalk in the upper part of the borehole and coarse grained Lewes Nodular Chalk in the lower 12 m of the borehole, both are a sub-unit of the Upper Chalk which is the main regional aquifer (Bristow et al., 1997). The borehole has a water column of c.30 m, is c.60 m deep and has a diameter of c.1 m. Figure 4.3 also shows the location of the tidal gauge at Newhaven where ocean tidal data is recorded (BODC, 2015). Finally, a second observation borehole (OBH), the Balsdean OBH (Figure 4.3), was drilled in July 2014 and SP and conductivity profiles were conducted in this borehole in November 2015. The Balsdean OBH is c.2.5 km from the coast, and less than 1 km from the Saltdean borehole.

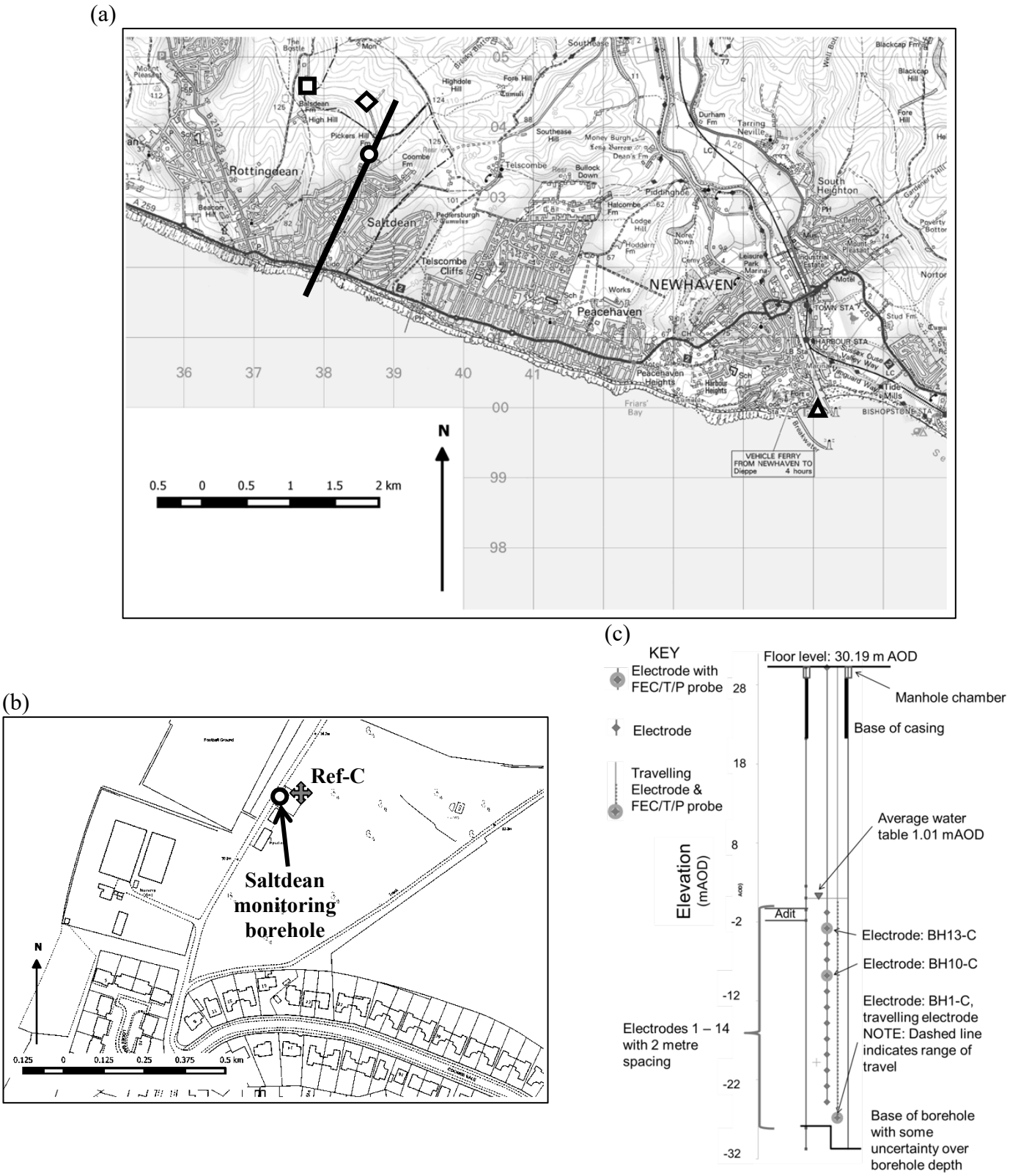

Figure 4.3 - (a) The area around the Saltdean monitoring borehole (hollow circle), also shown is the location of the Balsdean abstraction borehole (hollow square), the Newhaven tidal gauge (hollow triangle) and the Balsdean OBH (hollow diamond). The black line illustrates the extent of the 2D aquifer model. (b) The Saltdean borehole (hollow circle) and the surface reference electrode (Ref-C grey cross). Temperature measurements were taken at Ref-C. The notation C indicates the coastal site. (c) The Saltdean borehole has a water column of c.30 m, is c.60 m deep and has a diameter of c.1 m. The borehole was equipped with an array of 14 non-polarising electrodes and 3 FEC/P/T probes. Maps: © Crown copyright and database rights 2015 Ordnance Survey (Digimap License).

4.3 Self-Potential data acquisition

At both sites the borehole monitoring tool comprised non-polarising Silvion Ag/AgCl WE300 potable water electrodes (Silvion, 2015) (Figure 4.2(b) and Figure 4.3(c)). The WE300 electrodes have a 0.05 M internal KCl concentration, and a chloride concentration of c.3,727 mg/l. These electrodes were selected following laboratory monitoring of electrode dipoles immersed in groundwater over a 3 week period, which showed they were stable to within 25 μV and displayed a drift of less than 5% of the initial voltage (Appendix 4). All of the surface electrodes (Ref-IL, Surf1-N-IL, Surf2-S-IL, Surf3-E-IL, Surf4-W-IL) at the inland site (Figure 4.2(a)) and the surface reference electrode (Ref-C) at the coastal site (Figure 4.3(b)) were Silvion Ag/AgCl WE200 soil electrodes (Silvion, 2013). The WE200 electrodes have a 0.5 M KCl internal concentration; thus, a chloride content of c.37,275 mg/l. The design of both electrode types is similar to the electrode configuration shown in Figure 2.14.

At both sites the electrodes and monitoring equipment were logged using a 5 minute sampling rate with a Campbell Scientific CR3000 high impedance datalogger. This device has a 20 GΩ internal impedance, which is suitable for measuring SP signals, a minimum resolution of 0.67 μV and an accuracy of 0.04%. The electrodes were connected to the logger using 5 mm diameter coaxial cable; the signal is carried by the inner cable while the outer cable acts as a Faraday cage to reduce noise.

For the analysis of periodic fluctuations in chapter 5 a section of the data at the coastal site was used, from June 2013 to September 2013. Data was collected between May 2015 and August 2015 at the inland site. In chapter 6 the full coastal time-series is reported from May 2013 to August 2015.

4.3.1 Inland site

At the inland site, an array of five surface electrodes was installed to assess the impact of telluric currents, and other processes, on the SP (Figure 4.2). The electrodes were installed at the north (Surf1-N-IL), south (Surf2-S-IL), east (Surf3-E-IL) and west (Surf4-W-IL) of the field. All of the electrodes were referenced against a fifth electrode (Ref-IL) 90 m north of Surf2-S-IL. The configuration facilitated assessment of the effect of the horizontal component of the geomagnetic field on the SP.

The impact of the vertical component of the geomagnetic field was assessed using four electrodes (BH1-IL – BH4-IL) installed in borehole PL10B (Figure 4.2). At the inland site the borehole electrodes were spaced; with respect to the shallowest electrode, at c.24 m, c.12 m, c.8 m and c.4 m. The maximum spacing between these electrodes was chosen to match the maximum spacing of the electrodes at the coastal site. An AquaTroll 200 FEC/T/P probe was installed at the top of the borehole and measured fluid electrical conductivity (FEC), temperature (T) and pressure (P).

At the inland site the surface electrodes were installed at a depth of c.0.5 m, in a bucket filled with saturated bentonite (similar to that shown in Figure 2.15). This approach ensured a good electrical connection with the ground (Corwin, 1990, Perrier et al., 1997, Trique et al., 2002). The temperatures at Ref-IL, Surf2-S-IL and Surf3-E-IL were measured using a Campbell Scientific 107-L thermistor.

4.3.2.1 Electrokinetic pumping test experiment

In addition to ambient SP monitoring, a pumping test was conducted at the inland site from February to the end of March 2011. The pumping test provided a useful guide as to the likely magnitude of the EK response expected for a certain change in head within the borehole, and guided assessment of the likely contribution of the EK potential to the tidal SP in a coastal aquifer. The experiment was similar to that reported by Jackson et al. (2012a) (see section 1.1); however, instead of installing a small submersible pump in PL10A, the pump in the abstraction borehole was used (Figure 4.2). SP was monitored using two Silvion WE300 potable water electrodes installed in PL10B approximately 30 m from the abstraction borehole. The two electrodes were placed about 3 m apart with the shallowest electrode placed at about 80 mAOD. The electrodes were referenced against a Silvion WE200 soil electrode placed approximately at the same position as the reference electrode in the ambient monitoring experiment. The abstraction borehole was pumped at 6.44 Ml/d for 8 consecutive days.

4.3.2 Coastal site

At the coastal site, fourteen electrodes spaced at two metres were installed in a vertical array. In addition three AquaTroll 200 FEC/T/P probes were installed at the top, middle and bottom of the water column within the borehole (Figure 4.3). The lowermost FEC/T/P probe and SP electrode (BH1-C) were attached to one another and were free to traverse the entire water column, allowing

regular profiles of the borehole to be conducted. A similar configuration was used for the conductivity and SP profiles conducted in the Balsdean OBH in November 2015. The spacing between the shallowest and deepest electrodes was c.24 m.

The borehole array (BH1-C to BH13-C) was initially referenced against the surface reference electrode (Ref-C, Figure 4.3). In order to minimize exposure to diurnal and seasonal temperature variations, the reference electrode (Ref-C) was buried at a depth of c.1.5 m in a plastic bucket filled with bentonite and saturated with groundwater (similar to that shown in Figure 2.15). The temperature was monitored at Ref-C using a Campbell Scientific 107-L thermistor, allowing the temperature response of Ref-C to be identified and eliminated (Corwin, 1990). It was not possible to install a surface array at the coastal site due to land access and spatial constraints.

In addition to in-situ measurements of conductivity, water samples from both the Balsdean abstraction borehole and the Saltdean borehole were taken, using a bailer with a ball check valve to sample from specific depths. The samples were then filtered on site using a 20 μm filter and were transported and stored at 4°C. Sample analysis consisted of anion and cation IC and titration and was conducted as soon as possible after sample collection (see section 3.2.1 and Appendix 2 for more details on water quality analysis methods).

4.3 Seawater intrusion and SP modelling method

4.3.1 Hydrodynamic model

The hydrodynamic model was solved using Eclipse 100 (Schlumberger, 2010), which is capable of solving multiphase and density dependent flow. Eclipse is a fully implicit, three-phase simulator used extensively in the oil and gas industry. The simulator uses a finite-difference, finite-volume scheme to solve implicitly for pressure, concentrations and saturations of each fluid phase. The advantage of using Eclipse was that the SP simulator was specifically designed to be compatible with Eclipse outputs. Furthermore, its ability to model variable density flow was essential to effectively solve for the properties of the hydrodynamic problem expected to be encountered in the coastal aquifer. Eclipse has previously been used for groundwater modelling due to its ability to model multiphase, solute and variable density flow (Maliva and Missimer, 2012). For example, it has been used for modelling the

movement of volatile organic compounds in aquifers (Zhou and Arthur, 1994), to model flow in the unsaturated zone (Thatcher et al., 2006), to model aquifer storage and recovery (Levannier, 2009) and most recently for integrated modelling of groundwater and coal-seam gas reserves (Howell et al., 2013). Due to its ability to model variable density flow, it has also been used to model seawater intrusion (Labregère et al., 2006). Labregère et al. (2006) used Eclipse to investigate management strategies for controlling the lateral intrusion of seawater into aquifers and the model reported below is based on an adapted and expanded version of their original model. The main drawback of Eclipse is that it does not allow either diffusion or hydrodynamic dispersion of salt; rather, it simplifies salt transport using an advective miscible transport approach, the salt is transported by advection through the model grid and is then mixed within each cell. Note that Eclipse uses units of Darcy (D) for permeability, which is used in the following text, but hydraulic conductivity (m/d) is also shown. Equation 4.1 and Equation 4.2 show the relationships used to convert between transmissivity (τ), hydraulic conductivity (K) and permeability (k):

$$\tau = Kd \qquad \textbf{Equation 4.1}$$

$$k = K\frac{\mu_w}{\rho g} \qquad \textbf{Equation 4.2}$$

Here d is the saturated thickness of the aquifer (assumed to be 50 m see section 4.3), μ_w is the dynamic viscosity of water (0.0013 kg/m.s at 10°C), ρ is the density of water and g is the acceleration due to gravity. One Darcy is equivalent to 9.87 x 10^{-13} m^2.

The two-dimensional models described here were not designed to simulate accurately the hydrodynamics of the study site, but rather were used to investigate various possible salinity distributions based on observed and anecdotal evidence from the site and the literature. Thus, these models served, at best, as a starting point to understand the dynamics of the SP source mechanisms, their likely polarity and relative contribution to the overall observed SP. Inevitably, there were a number of assumptions and simplifications that were made in the modelling process; for example, diffusion was not explicitly modelled. Furthermore, the dual porosity system was not explicitly modelled; rather, an equivalent porous medium (EPM) approach was used (Long et al., 1982,

Berkowitz et al., 1988, Singhal and Gupta, 2010) with a uniform permeability and porosity based on the bulk rock properties. Moreover, recharge to the aquifer was not modelled and the pumping that occurs at the Balsdean abstraction borehole was neglected (Figure 4.3). Finally, unsaturated zone processes were also neglected due to the complexity of this region in the Chalk (Mathias et al., 2005). Instead, a simplified unsaturated zone was included in the model to allow the flow of electric current through this zone.

The use of Eclipse meant that transport processes were approximated by assuming that advection was the dominant process. The assumption is justified because the Chalk is often considered to demonstrate karstic behaviour (Banks et al., 1995, Maurice et al., 2006) and the relatively high bulk permeability known to exist in the Saltdean area (Jones and Robins, 1999, Robins and Dance, 2003) results in rapid flows through the aquifer. Cook et al. (2012) found that simulating contaminant transport in the Chalk only by advection produced similar results to including explicitly the diffusion component in their EPM model. Diffusion will obviously occur in reality, and as a result important micro-scale effects might occur between the rock matrix and the primary and secondary fracture components. However, for this preliminary numerical study these micro-scale effects were neglected, which was an inevitable simplification to the real system (Cook et al., 2012). The use of the EPM approach assumes a dense and highly interconnected fracture system in order to be valid for modelling such systems (Berkowitz, 2002), an approximation that is acceptable for the purposes of this study and is valid in the Chalk aquifer (Price, 1987).

The models reported here were based on a simple conceptual understanding of the groundwater flow in coastal East Sussex (Figure 2.7) (Jones and Robins, 1999, Robins and Dance, 2003), and explicitly model the high transmissivity zone below the dry valley in which the Saltdean borehole is located. Modelling was conducted in two steps, first a steady state saline wedge was developed; this was then perturbed by introducing a tidal boundary condition. Two different model groups (Table 4.3) were examined based on two alternative variations of the permeability structure at depth and a high and low inland head boundary for development of the saline wedge. The approach facilitated investigation of the effect of different salinity distributions on the SP and allowed first order assessment of the EK and

EED SP source mechanisms active within the coastal aquifer. On this basis more rigorous hypothesis as to the primary SP source mechanisms at the site were developed.

4.3.1.1 Model domain

The domain and grid size for the two model groups were the same. The inland boundary was placed at the foot of the interfluve and was 2.5 km from the coast, approximately equal to the distance of the Balsdean abstraction borehole from the sea. Thus, water levels from Balsdean were used to inform the choice of inland boundary conditions. The sea was explicitly included within the model domain and extended 500 m beyond the coastline. Figure 4.4 shows the approximate extent of the model.

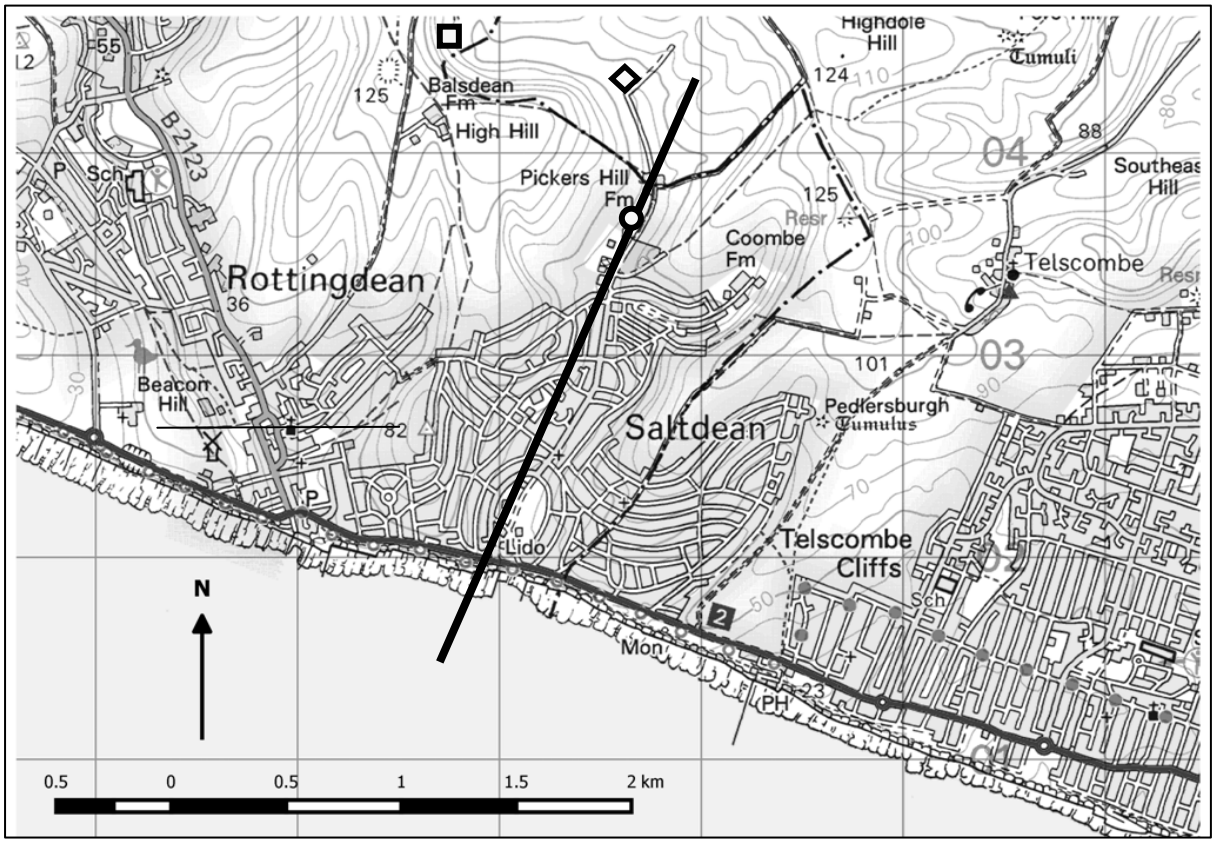

Figure 4.4 - The cross-section highlighted by the thick black line used for the 2D aquifer model. Also shown are the locations of the Saltdean observation borehole (circle) the Balsdean abstraction borehole (square) and the Balsdean OBH (diamond). © Crown copyright and database rights 2015 Ordnance Survey (Digimap License).

The active part of the Chalk aquifer is generally considered to be the upper 50 m (Allen et al., 1997, Jones and Robins, 1999), with very little flow occurring below this depth (Williams et al., 2006). However, in order to ensure realistic boundaries for the electrodynamic problem, the hydrodynamic model was extended 100 m below the active zone of the aquifer, resulting in an overall aquifer thickness of 200 m. The unsaturated zone was approximately 30 m deep at the Saltdean monitoring

borehole and extended to 50 m at the inland boundary. Thus, the domain was 200 m thick at the landward boundary. At the seaward boundary the model was 150 m thick. The upper and lower boundaries were no-flow boundaries.

The cross-section of the model domain is shown in Figure 4.5. The model grid was refined laterally in the area between the sea and 250 m beyond the location of the monitoring borehole. The grid was refined around the fracture that is known to exist at the base of the borehole. For computational purposes, it was assumed that the fracture occurred within a zone of enhanced permeability which was c.30 cm wide and three cells thick. The borehole was c.1 m in diameter and was 10 cells thick. However, due to convergence problems the borehole was not explicitly included in the hydrodynamic models. In the electrodynamic model the borehole cells were assigned a higher conductivity, by setting a porosity of 1 in the borehole (more details in section 4.3.2). The grid was also refined around an adit that may exist at the top of the borehole and 2.5 m either side of the initial water-table. There were approximately 90,000 active cells. Models with and without the adit were compared.

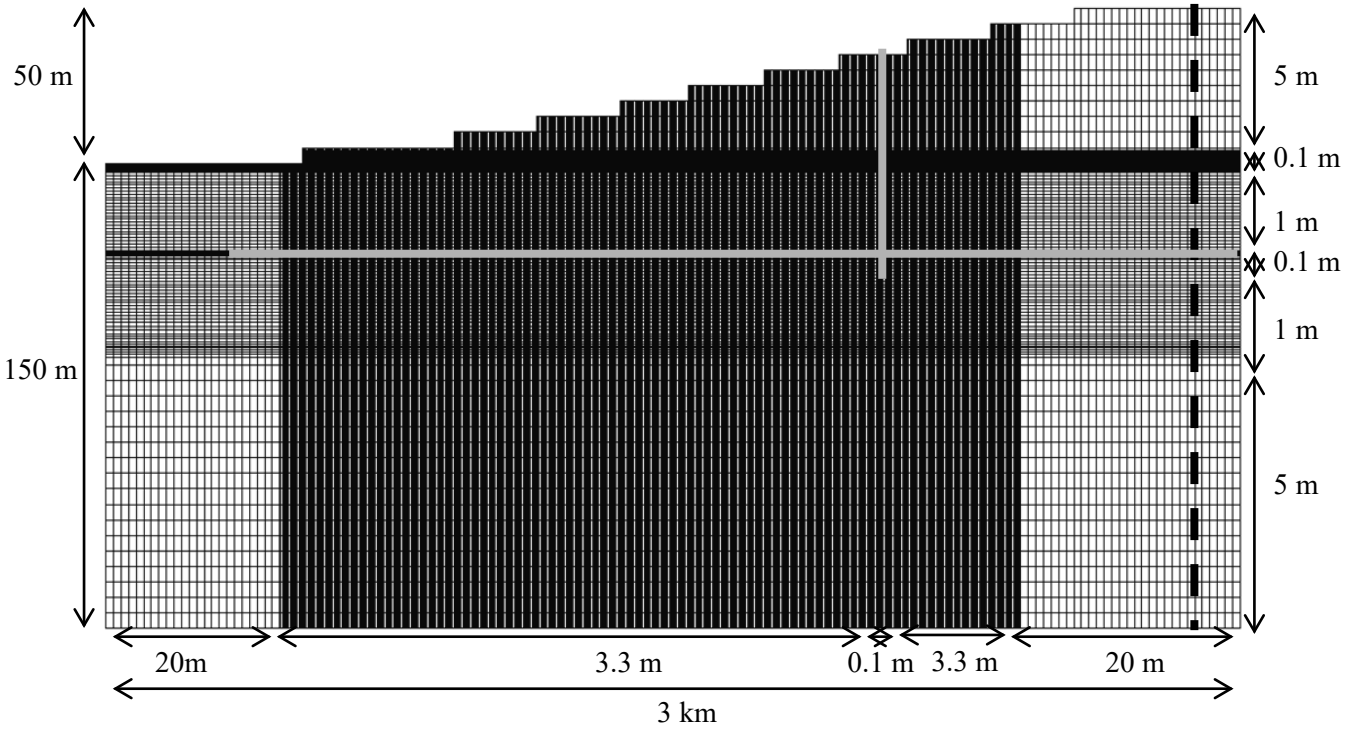

Figure 4.5 - Grid dimensions for the hydrodynamic model. In the vertical direction the grid was coarsest in the unsaturated zone, and highly refined in the area of water table fluctuations, the model was moderately refined below the water table and highly refined in the fracture zone. In the horizontal direction the area where the saline wedge was developed was highly refined, and the grid was coarse in both the sea and inland areas. The thick black dashed line indicates the model extent used for the electrodynamic model. The vertical grey line shows the position of the observation borehole, and the horizontal grey line shows the position of the fracture zone.

4.3.1.2 Model parametrisation

The hydrodynamic model parametrisation reported here was informed by the discussion of Chalk hydrogeology in section 2.2.3. The median porosity of the Chalk matrix is 38.8% for the Chalk in the East Sussex area (Bloomfield et al., 1995), which is approximately equal to the average porosity of the chalk samples measured in the laboratory (40%, Table 3.3). However, it is well known that most of the flow occurs within the fractures and it is this secondary porosity that results in the Chalk being a productive aquifer. Flow in the matrix is relatively insignificant in comparison. Thus, the fracture porosity and bulk permeability of the aquifer was modelled. The Chalk fracture porosity is widely considered to be about 1% (Butler et al., 2012) and this value was used throughout the model.

The bulk permeability of the top 100 m of the model was tested for a range of permeability's from 15 D to 60 D (i.e. c.10 m/d to c.40 m/d) based on the work of MacDonald and Allen (2001) who examined 2100 pumping tests throughout the UK Chalk aquifer. They found median values of transmissivity ranging from 150 – 2,600 m^2/d depending on the region; the median value for Chalk in the South Downs area is 440 m^2/d and for unconfined Chalk is 923 m^2/d. Furthermore, this range is consistent with estimates of the primary fracture component found in various field studies reported by Price (1987). A simple sensitivity analysis found that the change in extent and shape of the wedge was minimal over this permeability range. Chalk permeability is known to spatially heterogeneous. However, the bulk permeability of the Chalk was considered to be isotropic (Price, 1987) which is a reasonable first order assumption particularly for the Seaford Chalk, due to the presence of orthogonal fracture sets and the lack of marl seams (Bristow et al., 1997, Jones and Robins, 1999). Furthermore, there is evidence of solution enhanced vertical fractures within the Chalk (Maurice et al., 2012). The saturated thickness of the aquifer, used to convert from transmissivity to permeability (Equation 4.1 and Equation 4.2), was only considered to consist of the top 50 m, i.e. the active zone of the aquifer (Williams et al., 2006). The active zone is determined by the presence of a secondary fracture permeability which acts to increase the bulk permeability of the rock (Price, 1987).

The permeability of the Chalk aquifer is considered to decreases with depth; however, there is no clear evidence as to how this may affect salinity distributions at the site. Thus, to investigate the effect

of different salinity distributions the permeability structure at depth was modelled in two ways. The first simply assumed a linear decrease in permeability to 1 D (i.e. c.0.5 m/d) at the base of the model. The second assumed that the decrease was exponential, with the permeability at the very bottom of the model falling to the matrix permeability of the chalk, i.e. a minimum value of 2 mD (i.e. c.0.0013 m/d) (Table 3.3). The former model assumed that the primary fracture component contributed to flow in the deeper zone and the latter that flow was negligible below 50 m, i.e. all fractures were closed by the rock overburden or by the formation of secondary calcite (Price, 1987).

Jones and Robins (1999) suggest that in the Saltdean area the transmissivity could be as high as 9,000 m^2/d (> 100 D or c.65 m/d depending on the saturated thickness), and it is well known that transmissivities are generally higher in the valleys than on the interfluves (Jones and Robins, 1999, Robins and Dance, 2003). The only other published attempt at modelling groundwater flow and transport in the area found that transmissibility had to be set greater than 2,500 m^2/d to reproduce the salinity patterns observed inland at Balsdean (Nutbrown et al., 1975). Thus, a high permeability solution enhanced (secondary) fracture zone was introduced to account for the higher bulk permeability. The layer was modelled as a horizontal discrete fracture zone, which are common in the Chalk (Price, 1987), and acted to increases the overall bulk horizontal transmissivity of the model.

Jones and Robins (1999) claimed, on the basis on geophysical logging, that there is a fracture zone at the base of the Saltdean borehole that acts a conduit allowing saline water to enter the borehole. There is little evidence available as to the properties of this fracture zone, so it was assumed to have a porosity of 2% based on the assumption that the fractures in this zone contribute an additional 1% to the overall porosity of the zone (Price, 1987). The zone was set to be 30 cm wide, which is within the range for fracture zones known to exist within the Chalk (Bloomfield, 1996, Maurice et al., 2006, Worthington and Ford, 2009, Worthington, 2015). The fracture zone intercepted the base of the borehole and it was assumed that the zone extended to the sea. The permeability of the fracture zone chosen resulted in head fluctuations of c.0.5 m similar to those observed at the Saltdean borehole, and ranged from 2,500 D to 100,000 D (i.e. c.1,600 m/d to 65,000 m/d) which is in line with the range of estimates reported by Price (1987). Typically, the fracture permeability is two to three orders of

magnitude greater than the matrix permeability (Williams et al., 2006), consistent with estimates by Price (1987).

Adits are common in the South Downs area and were dug during the construction of water supply boreholes to increase yield, often by deliberately intersecting fracture zones in the aquifer (Robins et al., 1999). There is anecdotal evidence of adits in the modelled area including an adit that may intersect the Saltdean borehole (Cook, 2012). Thus, an adit was added to test its effect on the hydrodynamic and electrodynamic behaviour at the site. Note that there is no clear evidence of the extent and storage provided by these adits, so it was very difficult to accurately simulate the effect it has on the dynamics of the modelled area. Therefore, the impact of the adit was assessed in separate models (Table 4.3) and the possible implications of the adit are discussed. The adit was placed just below the initial position of the water-table, i.e at 50 m deep within the model or 0 mAOD which is a typical elevation of adits in the area (Jones and Robins, 1999). Note that well developed fracture systems are also often found at this depth (Price, 1987) which may cause similar flow and storage behaviour to the presence of an adit. However, due to the available anecdotal evidence this feature was modelled as an adit. Typical adit dimensions of 2 m x 1.7 m were used in the model (Jones and Robins, 1999). In reality the adit is most likely to run perpendicular to the valley; clearly it was not possible to achieve this in the two dimensional models. Instead, the storage provided by the adit was simulated by setting a porosity of 5000 which was calculated to represent the storage of a typical 1 km long adit (Jones and Robins, 1999). The adit permeability was one order of magnitude larger than the fracture zone and was set to ensure the correct head fluctuations in the borehole. In order to achieve the c.0.5 m head fluctuations at the Saltdean borehole with the adit, the bulk matrix and fracture permeability had to be increased to the upper ends of the permeability ranges summarised in Table 4.1 and Table 4.3. The adit was only added in the tidal runs after the steady-state saline wedge was developed (section 4.3.1.3).

The seawater salinity was set to 35,000 mg/l based on typical seawater (Table 2.1 and Table 3.2). The groundwater concentration was set to 375 mg/l and was based on analysis of the Balsdean groundwater used in the EK and EED potential experiments (Table 3.1). The relationship between

density and concentration used in the model was assumed linear (Figure 4.6(a)) with groundwater density assumed to be 1000 kg/m^3 and seawater 1025 kg/m^3. Empirical relationships between ionic strength and TDS exist (Langmuir et al., 1997); however, they overestimate the ionic strength measured in both the groundwater and seawater experiments, and are known to be valid only for TDS values less than 1000 mg/l (Bitton, 1998). Thus, a linear relationship between ionic strength and TDS was assumed (Figure 4.6(b)).

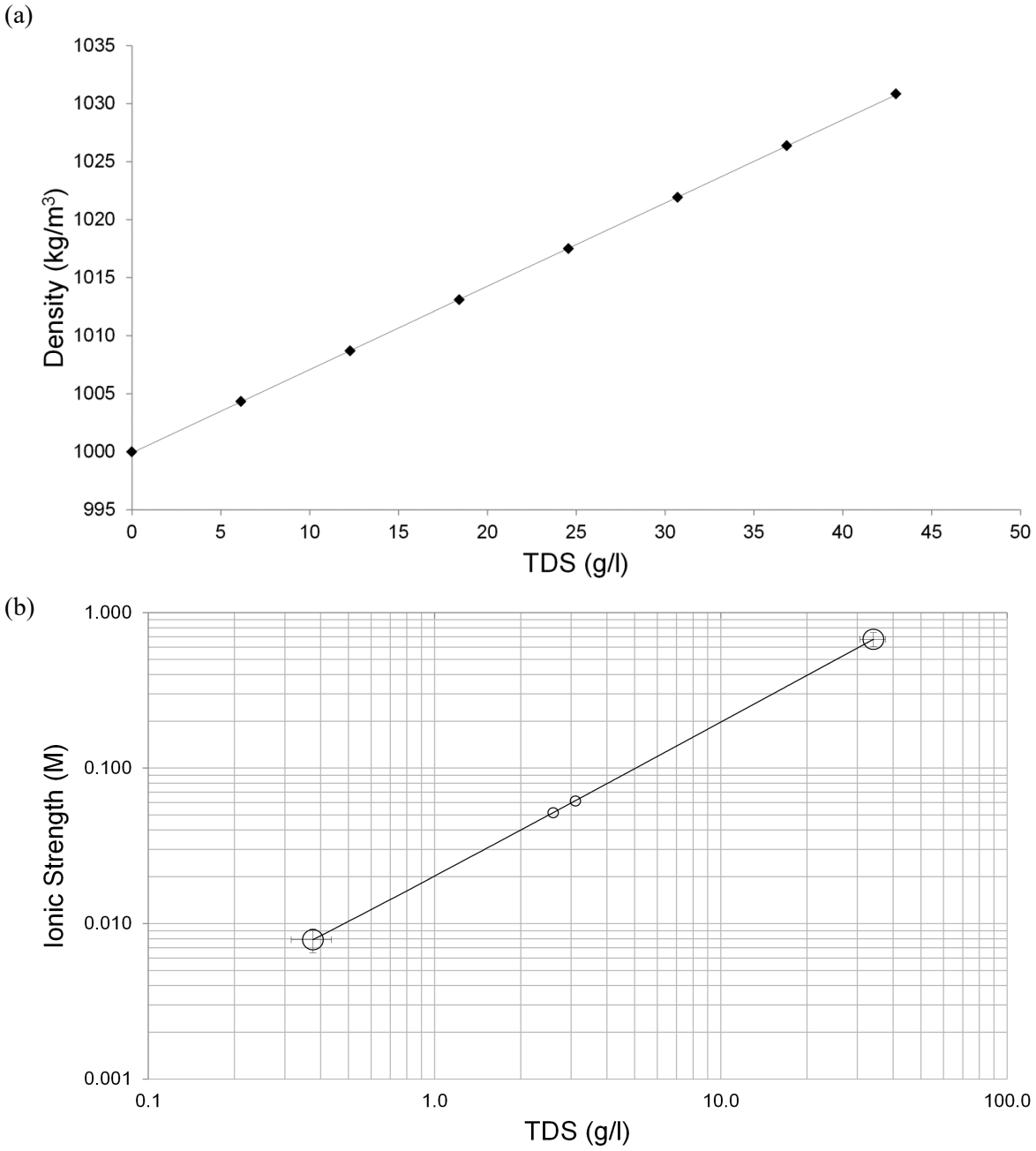

Figure 4.6 – (a) The relationship between TDS and density used in the models. Here ρ=0.72TDS+1000. (b) The relationship between TDS and ionic strength based on laboratory data. The two end members are groundwater from Balsdean and seawater. The intermediate points are samples taken from the Saltdean borehole during periods when substantial mixing occurred. Here I = 0.0197TDS+0.0005.

Finally, the air-entry pressure was set to 30 m (Price, 1987). Thus, the unsaturated zone was almost fully saturated. In reality, there are several flow processes taking place within the unsaturated zone (Mathias et al., 2005), such as matrix and fracture flow, determined by the intensity of the rainfall event, and saturation and desaturation of fractures; however these processes are neglected in the preliminary models. The hydrodynamic model parameterisation is summarised in Table 4.1.

<table>
<tr><th>Property</th><th colspan="2">Bulk Aquifer</th><th colspan="2">Fracture/Adit</th><th>Groundwater</th><th>Seawater</th><th>Air</th></tr>
<tr><td>Viscosity (kg/m.s)</td><td colspan="2">N/A</td><td colspan="2">N/A</td><td>0.00113597 (Labregère et al., 2006)</td><td>0.00113603 (Labregère et al., 2006)</td><td>0.02</td></tr>
<tr><td>Density (kg/m^3)</td><td colspan="2">N/A</td><td colspan="2">N/A</td><td>1000</td><td>1025</td><td>1.225</td></tr>
<tr><td>Compressibility (bars^{-1})</td><td colspan="2">1x10^{-5} (Mathias, 2005)</td><td colspan="2">N/A</td><td>4.8852x10^{-5} (Labregère et al., 2006)</td><td>4.8749x10^{-5} (Labregère et al., 2006)</td><td rowspan="5"></td></tr>
<tr><td>Concentration (mg/l)</td><td colspan="2">N/A</td><td colspan="2">N/A</td><td>375</td><td>35,000</td></tr>
<tr><td rowspan="2">Porosity</td><td colspan="2" rowspan="2">0.01 (Butler et al., 2012)</td><td>Fracture</td><td>0.02</td><td colspan="3" rowspan="5"></td></tr>
<tr><td>Adit</td><td>5000</td></tr>
<tr><td rowspan="3">Permeability (D and m/d)</td><td colspan="2">15 – 60 D (c.10 – 40 m/d) (MacDonald and Allen, 2001, Price, 1987)</td><td rowspan="2">Fracture</td><td rowspan="2">2500 – 100,000 D (c.1,600 – 65,000 m/d) (Price, 1987)</td></tr>
<tr><td rowspan="2">Deep Perm-eability</td><td>Config. 1: 1 D (0.6 m/d)</td></tr>
<tr><td>Config. 2: 2 mD (0.0016 m/d)</td><td>Adit</td><td>1,000,000 D (640,000 m/d)</td></tr>
<tr><td>Air entry pressure (m)</td><td colspan="2">30 (Price, 1987)</td><td colspan="2">N/A</td></tr>
</table>

Table 4.1 - Hydrodynamic model properties, ranges indicate a simple sensitivity analysis of the parameter.

4.3.1.3 Initial and boundary conditions

As already highlighted the simulations were conducted in two main parts; first the saline wedge was developed by conducting a model run designed to achieve dynamic equilibrium, i.e. creating a steady saline wedge between the freshwater and the seawater. The model was initially filled with seawater below the water-table. Freshwater was then injected from the inland boundary using a constant head. The water-table was set at 50 m within the model (i.e. 0 mAOD). The high air-entry pressure meant that the unsaturated zone filled with water immediately. It took about 250 model years to achieve steady state, a relatively short time because of the low porosity used in the models. Then the tide was

added, perturbing the dynamic steady-state and a new dynamic equilibrium, indicated by a steady saline wedge and consistent average position of the saline front within the fracture zone, was reached after 1 model year. Finally, the tidal model was run again for a single spring/neap cycle.

To develop the steady saline wedge, the mid-tidal level (i.e. 0 mAOD) was used as the seaward pressure boundary. The inland head was based on water levels recorded at the Balsdean abstraction borehole (Figure 4.7). Two values of inland head (Table 4.2) were tested for the two different permeability cases described above and in Table 4.1. The highest inland head set in the models was 3 mAOD which has been observed during periods of high rainfall (for example winter 2013-2014), and was slightly less than the maximum water level reported by Jones and Robins (1999). A second model was tested with a head of 1 mAOD, which was close to the higher end of the range of minimum annual water levels reported by Jones and Robins (1999).

Once dynamic equilibrium between the freshwater and seawater had been achieved for the steady state and dynamic tidal runs, the model boundaries were changed to model the movement of the salinity front with the tides. For computational efficiency and to ensure the saline front moved quickly towards the monitoring borehole, in the final spring/neap cycle, the inland head was instantaneously dropped to 0.5 mAOD (Figure 4.7) which was just above the lower end of the range of minimum annual water levels reported by Jones and Robins (1999). The drop in inland head, although a simplification of the real system, allowed investigation of drought conditions when saline breakthrough at the borehole is most likely and the movement of the saline front is most rapid.

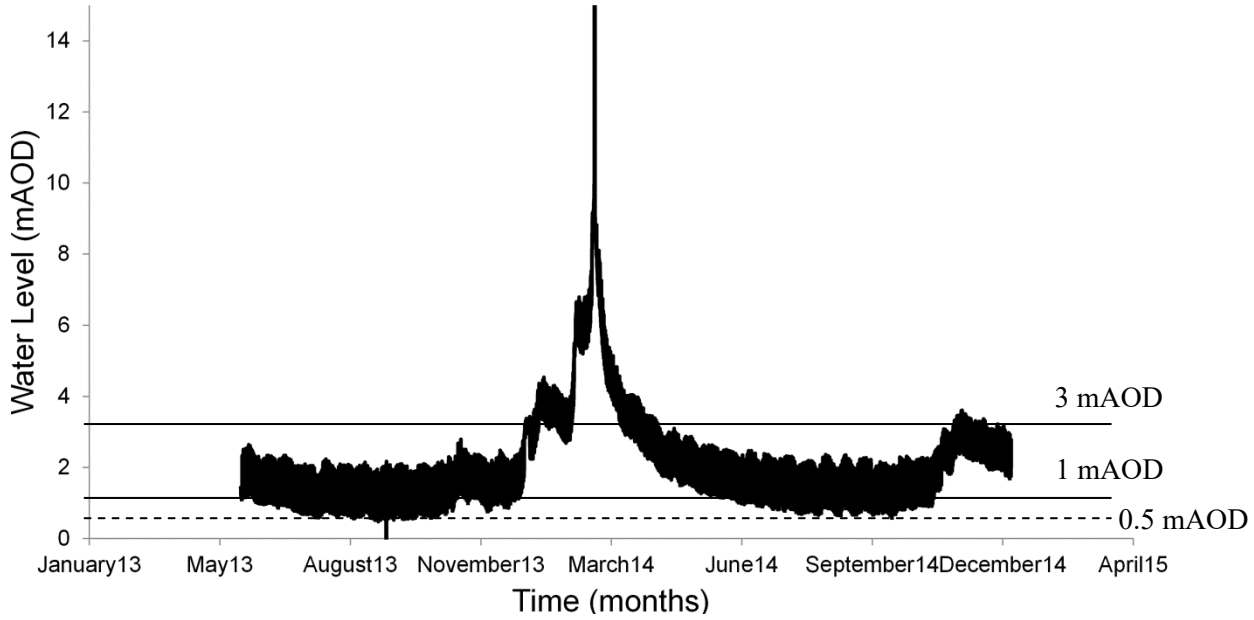

Figure 4.7 - Water levels from the Balsdean abstraction borehole guided the choice of inland boundary; the inland boundary in the steady-state models is indicated by the solid line and the spring/neap tidal models by the dashed line.

Tidal fluctuations were modelled using a fluctuating pressure boundary based on the data from the tide gauge at Newhaven, approximately 8 km east of the Saltdean site. Two overlapping sine functions were applied at the seaward boundary. The seaward boundary fluctuated between high and low tide and the spring and neap tides with a maximum tidal range of c.7 m (the maximum tidal range at Newhaven was 7.69 m in 1983 (NTSLF, 2015)). The tide had a principal solar lunar (M_2) period (Table 2.4). The spring tide ranged from 3.5 mAOD to -3.5 mAOD and the neap tides ranged from 1.5 mAOD to -1.5 mAOD (BODC, 2015). The boundary conditions are summarised in Table 4.2.

Boundary	Base model simulation	Tidal simulation
Seaward	Constant head: 0 mAOD Constant concentration: 35,000 mg/l	Spring tide: -3.5 mAOD to +3.5 mAOD Neap tide: -1.5 mAOD to + 1.5 mAOD Constant concentration: 35,000 mg/l
Landward	Inland head configuration 1: 1 mAOD Inland head configuration 2: 3 mAOD Constant concentration: 375 mg/l	Constant head: 0.5 mAOD Constant concentration: 375 mg/l
Bottom	No flow	No flow
Top	No flow	No flow

Table 4.2 - Hydrodynamic model boundary conditions.

4.3.1.4 Model sensitivity analysis

A simple sensitivity analysis examined the impact of the permeability structure at depth, the inland head boundary, and the effect of the inclusion of the adit on the SP. The sensitivity analysis is

summarised in Table 4.3 and the models are labelled for later reference. Model 3 produced the closest match to the field data; thus, most of the results in chapter 5 and 6 focus on this model.

	Inland Head Configuration 1: 1 mAOD		**Inland Head Configuration 2: 3 mAOD**	
Permeability Configuration 1: Linearly decreasing permeability at base of model	NF	Model 1(a)	NF	Model 2(a)
	FNA	Model 1(b)	FNA	Model 2(b)
	FA	N/A	FA	N/A
Permeability Configuration 2: Exponentially decreasing permeability at base of model	NF	Model 3(a)		
	FNA	**Model 3(b) – Bulk rock: 15 D (c.10 m/d) Fracture: 2,500 D (c.1,600 m/d)**		
	FA	**Model 3(c) Bulk rock: 60 D (c.40 m/d) Fracture: 100,000 D (c.65,000 m/d)**		

Table 4.3 - Summary of the different base models used to investigate the SP signal in the coastal aquifer. The effect of the inclusion of the fracture and adit on each of these models were investigated, NFNA – no fracture and no adit, FNA – fracture but no adit, FA – fracture and adit. Each model is given a number to which it is subsequently referred. The models highlighted in bold are those that most closely matched the field observations of SP.

4.3.2 Electrodynamic Model

The general approach to SP modelling was summarised in section 2.3.5, where the relationship between the hydrodynamic and electrodynamic problem was introduced. The electrodynamic and hydrodynamic problem were related in the coastal aquifer at Saltdean using Equation 4.3 (Revil, 1999a, Gulamali et al., 2011, Jackson et al., 2012b, Leinov and Jackson, 2014, Jackson, 2015):

$$j = -\sigma_{rec}\nabla V + L_{EK}\nabla(P_w - \rho_w g z) + L_{EED}\nabla ln\,(\sigma_{fec}) \qquad \textbf{Equation 4.3}$$

Note that Equation 4.3 is similar to Equation 2.23, but the concentration term has been replaced with the fluid conductivity (σ_{fec}) (Revil, 1999a). At all boundaries $\nabla V = 0$ and $\nabla(P_w - \rho_w g z) = \nabla\, ln(\sigma_{fec}) = 0$. It was also assumed that there were no external current sources or sinks and that the current flow through the model boundaries was zero (Equation 2.24). The electrodynamic problem was solved using a control volume finite difference method (Recktenwald, 2012) based on the scheme developed by Saunders et al. (2008) and extended by Gulamali et al. (2011), Jackson et al. (2012b) and Ijioma and Jackson (2014). The discretised problem was then solved in MATLAB using the minimum residual (MINRES) Krylov subspace iterative method (Barrett et al., 1994, Van der Vorst, 2003). The cross-coupling terms were expressed in terms of the rock electrical conductivity and the coupling coefficients for both the EED and EK components of the SP (Equation 2.8).

Total dissolved solids (TDS) were converted to fluid electrical conductivity using a conversion factor of 0.7, which approximates the conductivity of seawater and carbonate rich groundwater (Walton, 1989), and was considered adequate for the purpose herein. The actual fluid electrical conductivity (σ_{fec}) was then corrected for temperature using the following expression (Hayashi, 2004):

$$\sigma_f = \sigma_{f_{spec}}(1 + 0.02(T - 25)) \quad \textbf{Equation 4.4}$$

Here $\sigma_{f_{spec}}$ is the specific fluid electrical conductivity of the brine at 25^0C, T is the measured temperature which from field measurements in the borehole was essentially constant at about 11.3^0C (standard deviation of 0.05^0C). It was assumed that the temperature was constant throughout the model including in the top layers, a reasonable assumption given the mean annual soil temperature at 30 cm in South Eastern England is 10 – 11^0C (MET, 2015). The electrical conductivity of the porous media was calculated using Archie's law (Telford et al., 1990):

$$\sigma_{rf} = \phi^m \sigma_{fec} S_w^n \quad \textbf{Equation 4.5}$$

Here ϕ is the porosity, m is the cementation exponent of the rock, n is the saturation exponent and S_w is the water saturation. The cementation factor, $m = 2.4$, was based on laboratory measurements (Table 3.3) and was consistent with measurements conducted by Witthüser et al. (2003). The saturation exponent was set to $n = 2$ based on the work of Anderson (1986) who found that this is a typical value in water wet carbonate systems. Note that since the air entry pressure was set to 30 m, most of the unsaturated zone is actually fully saturated; thus, all of the terms that refer to partial saturation only apply in a very small part of the model domain. In the hydrodynamic models the fracture porosity of the system was modelled because it was assumed that flow in the aquifer is controlled by fractures. However, in the electrodynamic model the matrix was considered to be a key flow pathway for current flow; therefore, the porosity value used throughout the electrodynamic model was 0.4 based on the average porosity measured in the laboratory (Table 3.3) and close to the mean value of chalk porosity in East Sussex (Bloomfield et al., 1995). In the discrete fracture zone the porosity was set to 0.41 to be consistent with the porosity set in the fracture zone in the hydrodynamic model. The borehole was also explicitly accounted for in the electrodynamic model by setting the

porosity of the refined borehole cells to be 1. Thus, the borehole provided a more conductive pathway for current flow than the surrounding chalk, which was believed to occur at the field site. It was also assumed that the adits capacity for storage did not affect current flow in the same way as it did fluid flow; therefore, in the electrodynamic model the porosity of the adit was set to 1.

The EK coupling coefficient was taken from the results of the EK measurements conducted in the laboratory (section 3.3.1). The coupling coefficient was modelled using the expression derived from Figure 3.9 and is based on Seaford Chalk sample T1 which had the largest coupling coefficient:

$$C_{EK} = -0.0071 C_M^{-0.908} \quad \textbf{Equation 4.6}$$

Following Jackson et al. (2012b), the relative EK coupling coefficient (C_{rEK}) was modelled at intermediate water saturations (S_w) using the following expression:

$$C_{rEK} = S_w^{0.6} \quad \textbf{Equation 4.7}$$

The EED potential of chalk (Table 3.6) is dominated by the diffusion component (V_{ED}), which was accounted for by applying a scaling factor (V_{scale}) to the exclusion potential (V_{EE}) limit (Figure 3.7). Unlike V_{ED} (Equation 2.20), V_{EE} depends only on concentration (Equation 2.22). For consistency with Equation 4.3 the electrical conductivity of SW and GW was used to calculate V_{EE} (Revil, 1999):

$$V_{EE} = -\frac{k_b T}{e} ln\left(\frac{\sigma_{sw}}{\sigma_{gw}}\right) \quad \textbf{Equation 4.8}$$

Again $T = 11.3^0$C, σ_{sw} is the seawater conductivity and σ_{gw} is the groundwater conductivity. The scaling factor (V_{scale}) was used to scale V_{EE} to match the EED potential observed in the laboratory experiments (Table 3.6). Thus, V_{EED} was given by:

$$V_{EED} = V_{EE} x\, V_{scale} \quad \textbf{Equation 4.9}$$

Newhaven Chalk (sample S4), which is present at the base of the borehole, had the largest EED potential (22.60 mV from Table 3.6; thus, V_{scale} = -0.2) and was used in the simulations. The expression for the relative EED coupling coefficient at intermediate values of water saturation was

developed by Jackson et al. (2012b) who found that the following expression provided a reasonable match to the experimental data reported by Ortiz Jr. et al. (1973):

$$V_{rEED} = (1 - S_w)^3 \qquad \textbf{Equation 4.10}$$

The electrodynamic models were initially tested on a 1D representation of the chalk plug experiment (section 3.3.2). The results, in appendix 5, showed the correct potential difference across the saline front, between groundwater and seawater end members, using the scaling factor approach, i.e. c.22 mV. The EK component was also the correct polarity and magnitude. The regional modelling results are reported in the following chapters and supported interpretation of the field data. The periodic components of the observed SP are discussed first in chapter 5 and the spatial and transient effects observed in the long-term SP time-series are discussed in chapter 6.

Chapter 5

Origins of the coastal diurnal and semi-diurnal self-potential (SP)

5.1 Introduction

The importance of periodic SP signals likely to be observed in the coastal aquifer has already been discussed in section 2.3.6.4. This chapter focusses on the periodicity of the SP monitoring results from the inland and coastal monitoring sites. The broad aims of the field work and numerical modelling were set out in section 4.1. However, the specific aim of the analysis reported here was to identify the periodic components of the SP data at the coastal site that were purely related to ocean tidal processes. The objectives were to: (i) compare the SP results from the coastal and inland sites in the frequency domain in order to identify components of the SP signal that were unique to the coastal site, (ii) conduct an analysis of the coastal SP data in the time domain to begin to separate the EK and EED components of the total observed SP data and (iii) use numerical models to determine the relative contribution of the EED and EK components to the overall observed tidal SP. Thus, the analysis presented below focuses on the coastal and inland SP data in the frequency domain and then discusses the likely source mechanisms for the coastal periodic SP signals. The spatial and transient effects observed in the SP data, including observations of a constant vertical SP gradient (see Figure 6.16 – Figure 6.19 and section 6.5.1), are discussed in chapter 6.

5.2 Frequency analysis method

The Lomb-Scargle power spectral density (PSD) method (Lomb, 1976, Scargle, 1982) was used to analyse the SP in the frequency domain. The Lomb-Scargle PSD, a least squares spectral analysis technique, was chosen as the analysis method because it can be used with time-series data that have gaps or that are not evenly spaced in time (Lomb, 1976, Trauth, 2010). In the case of the coastal site there were regular gaps in the data set, because additional measurements with higher sampling rates were regularly taken using the same instrumentation. Thus, these measurements, including

conductivity and SP profiles in the borehole, interrupted the continuous time-series. Similarly, at the inland site gaps in the data were created whenever the data logger battery was changed. Other spectral analysis techniques, including the Fast Fourier Transform (FFT), cannot deal with data gaps or unevenly sampled data (Trauth, 2010). It is also worth noting that data that are not evenly sampled in the frequency domain have a reduced alias effect; thus, have fewer problems with leakage of power from high to low frequencies; this is true even for slight unevenness in the data and enables better resolution of the frequency components of the SP signal (Scargle, 1982, Yi et al., 2006). Finally, the Lomb-Scargle PSD allowed determination of the probability of a certain frequency peak being related to a real periodic signal and not the result of random fluctuations; this is known as the probability of detection (Trauth, 2010). Here the probabilities of detection were set at 50, 90, 99 and 99.99% significance levels, and are shown (as horizontal dashed lines) on all of the PSD plots in the result section (section 5.3). Note that no smoothing or filtering was conducted prior to the spectral analysis of the data. The data from the coastal aquifer were also analysed for the phase difference between tidal, head and voltage data using a Discreet Fourier Transform (DFT) (Sedláček, 2003, Sedlacek and Krumpholc, 2005) applied to a section of the data that was regularly sampled and without any gaps in the time-series. The surface array and borehole arrays used to gather the SP data at the inland site are shown in Figure 4.2, and the borehole array used at the coastal site is shown in Figure 4.3.

Table 2.4 shows the main periodic tidal components that were expected at the coastal site, along with their amplitudes relative to the principal lunar component (M_2). Note that the diurnal period S_1 and the semi-diurnal period S_2, and their harmonics S_3 and S_4, also have non-tidal source mechanisms. For example, atmospheric pressure fluctuates with a twice daily period (S_2) and diurnal temperature fluctuations have a period of 1 day (S_1). Where mechanisms other than tidal processes were believed to be the main source of these periodicities, this is clearly stated.

5.3 Field monitoring results

5.3.1 Inland site results

Note that the temperature data from the surface array did not coincide exactly with the voltage data from the surface array. The temperature probes were installed only after it became apparent that

differences in diurnal voltage fluctuations in the surface array could be explained by differences in temperatures across the site. Furthermore, the temperature probes failed on two occasions, on the second occasion ending the experiment. Therefore, the surface voltage data had a time-series length of approximately 3.5 months, and the temperature data had a length of c.2 months. The layout of the surface and borehole arrays for the inland site can be found in Figure 4.2.

5.3.1.1 Temperature

Figure 5.1 shows the temperature data recorded at the surface reference electrode (Ref-IL) and the temperature measured within the borehole, at the shallowest electrode (BH4-IL).

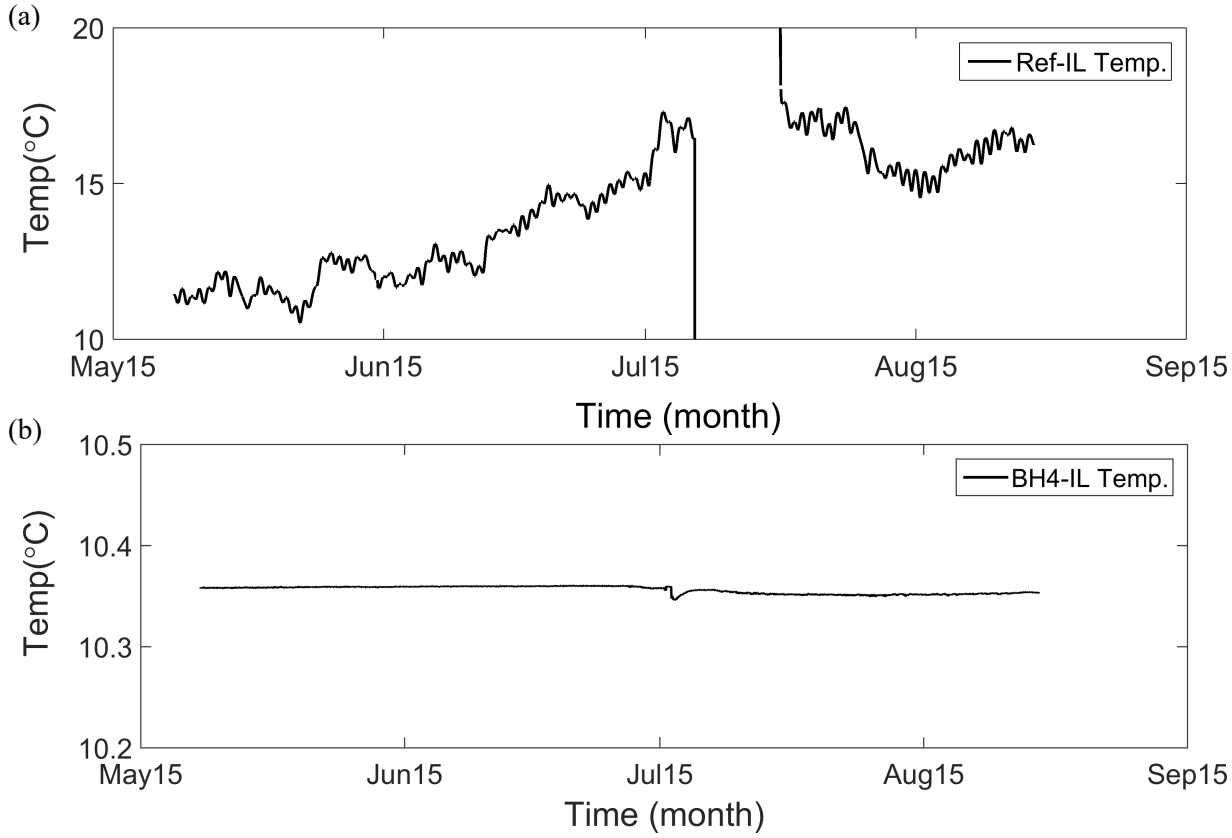

Figure 5.1 - (a) Inland temperature data from the reference electrode (Ref-C). The gap in the data was due to a failed temperature probe that was later replaced. (b) Temperature data from within the inland borehole (PL10B).

There were clear low frequency fluctuations within the surface temperature measurements (Figure 5.1(a)), but the borehole temperature measurements were stable throughout the duration of the experiment (Figure 5.1(b)). The small perturbation in the borehole temperature in July was caused by the nearby abstraction borehole being turned on for testing by the EA. Figure 5.2 shows the temperature PSD from electrodes Ref-IL, Surf2-S-IL and Surf3-E-IL. The temperature dominated S_1

component that arose between Surf2-S-IL and Ref-IL (Figure 5.2(d)) was smaller than the S_1 temperature component that arose between Surf3-E-IL and Ref-IL (Figure 5.2(e)). The temperature measurements all displayed a clear diurnal temperature fluctuation driven by the principal solar mechanism (S_1, Table 2.4). There was no evidence of the S_2 harmonic. Note that spikes in the PSD with periods less than 1 day are artefacts of the analysis method caused by noise, trends in the data and the finite length of the time-series (Trauth, 2010), but are left in the plots for veracity.

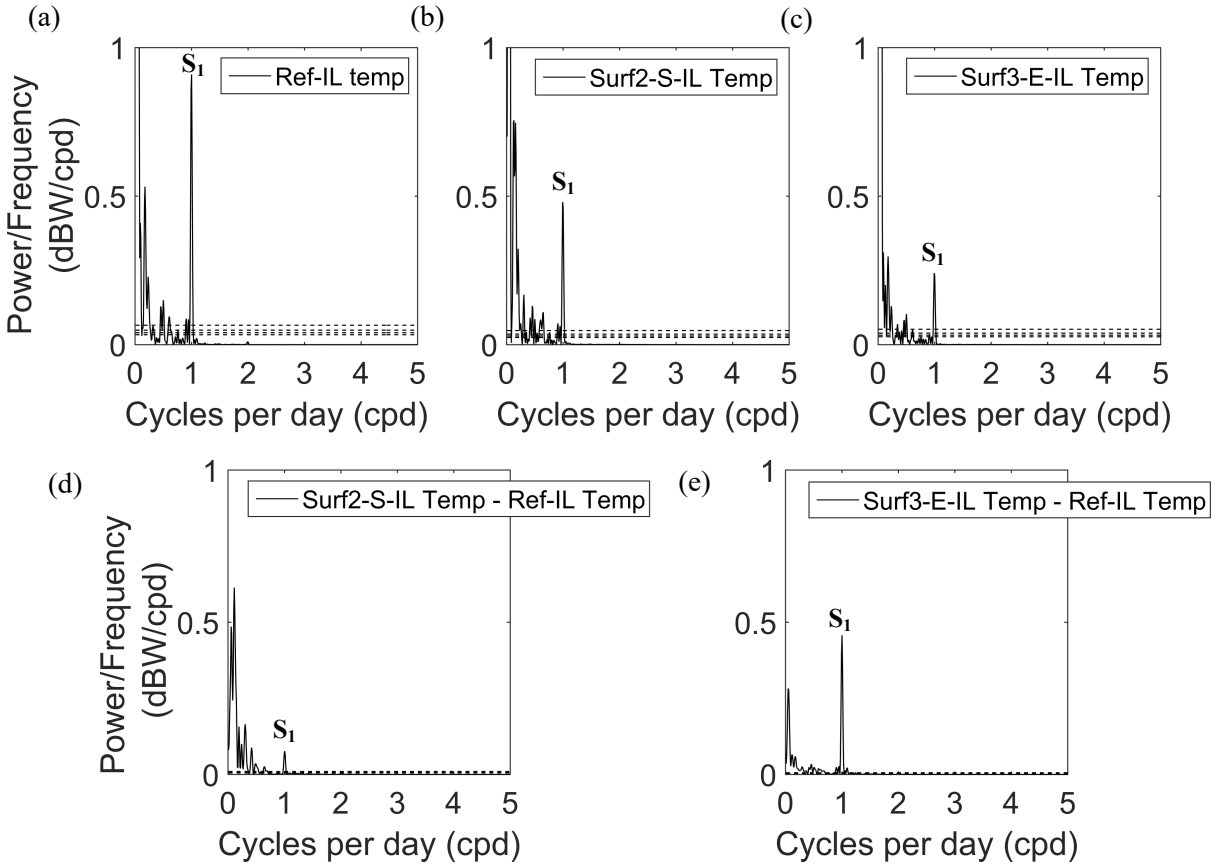

Figure 5.2 - Temperature data from the inland surface reference array. (a) - (c) Temperatures at each of the electrodes. (d) and (e) show the difference between the temperature at Ref-C and Surf2-S-IL and Surf3-E-IL the two surface electrodes that had temperature measurements. The dashed lines show the 50, 90, 99 and 99.9% significance levels.

5.3.1.2 Surface array SP

Typical results for the voltage measured in the inland SP surface electrode array are shown in Figure 5.3. Unless otherwise stated, all voltages were referenced against Ref-IL.

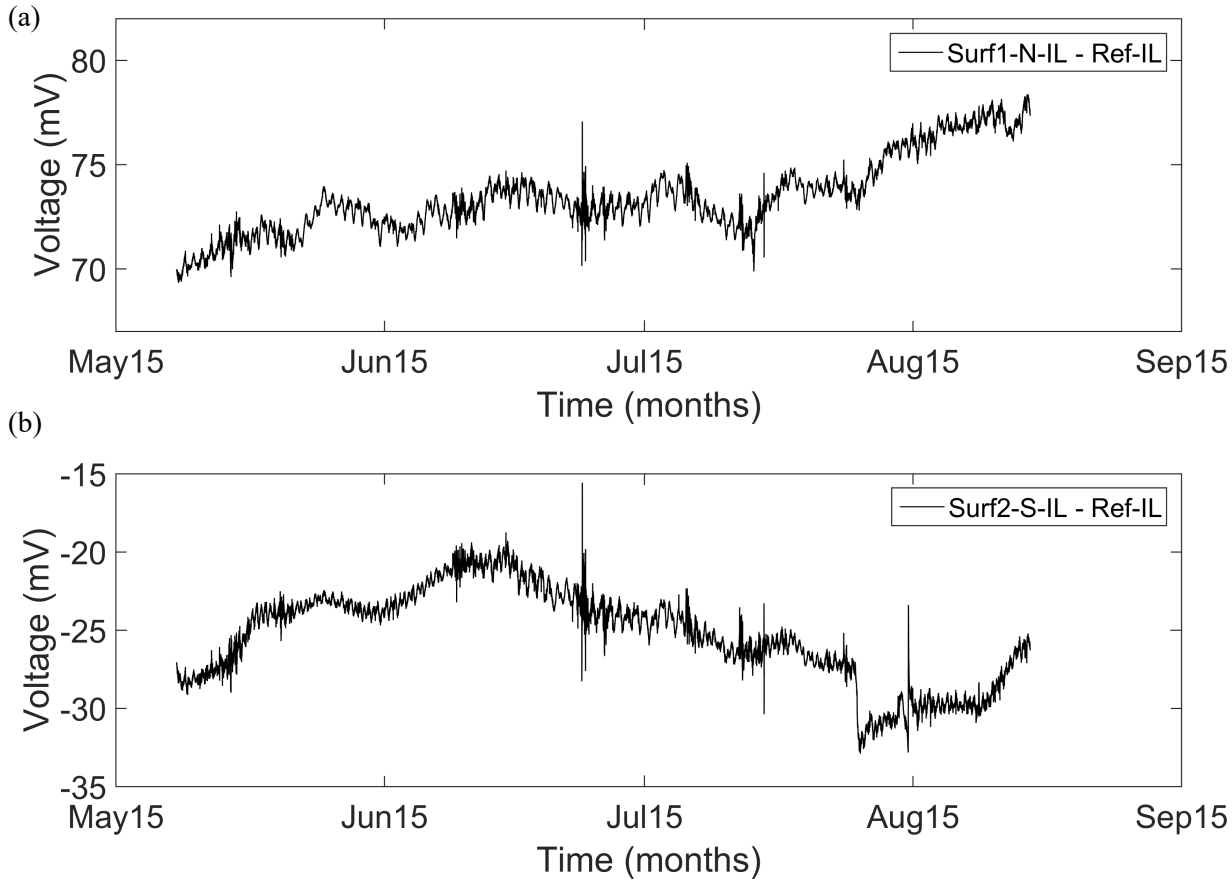

Figure 5.3 - Typical results from the inland surface electrode array against the reference (Ref-IL, Figure 4.2).

The PSD estimate for Surf1-N-IL, Surf2-S-IL, Surf3-E-IL and Surf4-W-IL referenced to Ref-IL are shown in Figure 5.4. All four electrodes display S_1 and, surprisingly at this inland location, the principal lunar component (M_2, Table 2.4). In contrast to Surf2-S-IL (Figure 5.4(b)), at Surf1-N-IL (Figure 5.4(a)), Surf2-S-IL (Figure 5.4(c)) and Surf4-W-IL (Figure 5.4(d)) S_1 was the most significant component. At Surf2-S-IL a stronger M_2 component was recorded. The difference between the temperatures at Surf2-S-IL and Ref-IL has a smaller S_1 component than the other surface dipoles (Figure 5.2(d)).

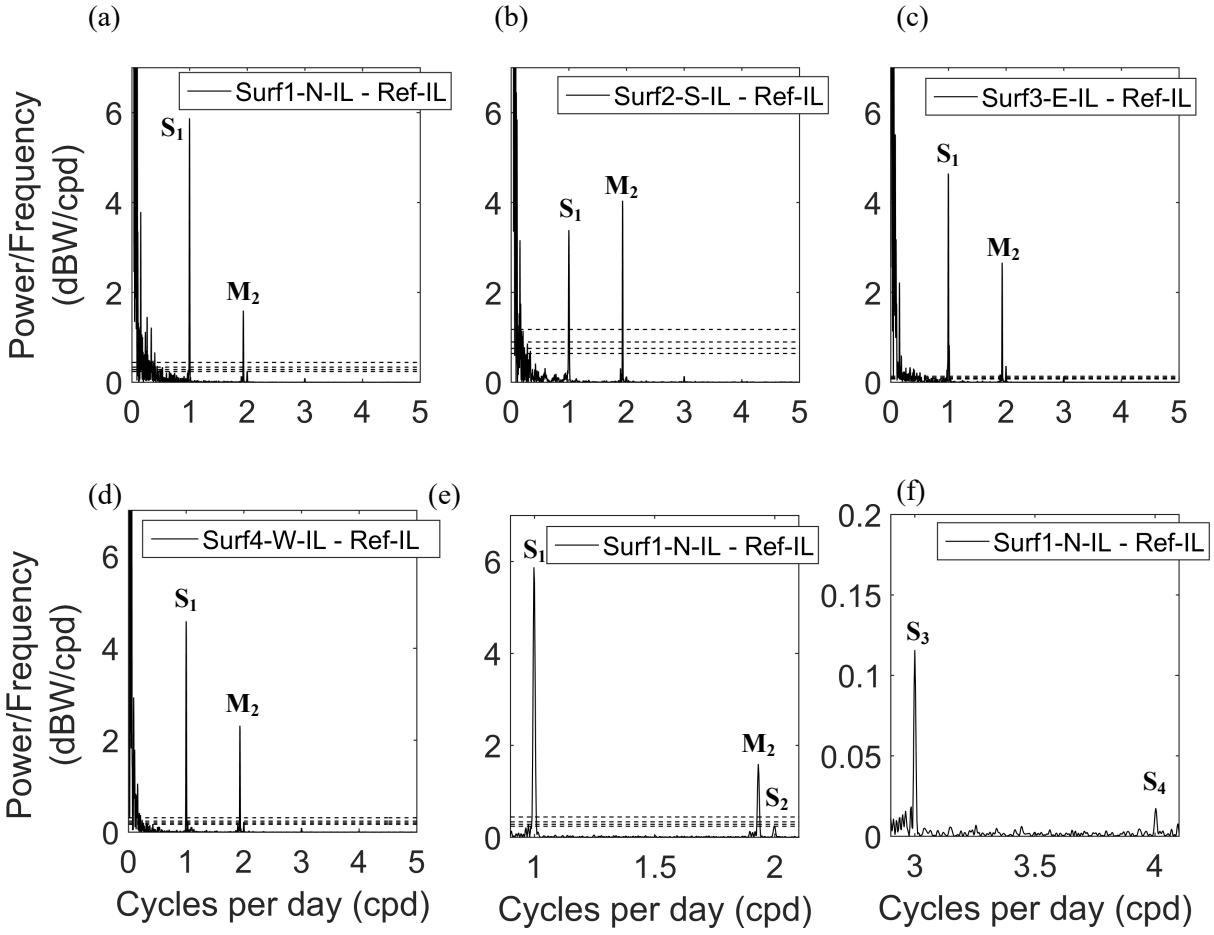

Figure 5.4 – (a) – (d) PSD from inland SP surface array for the time-series in Figure 5.3. (e) Surf1-N-IL in (a) zoomed on the diurnal and semi-diurnal frequencies. (f) Surf1-N-IL in (a) zoomed to ~3 and 4 cycles per day.

Figure 5.5(a) – (c) show the results for three north/south dipoles, obtained by subtracting the data from different electrodes in the surface array. The two longest dipoles were referenced against Ref-IL. Figure 5.5(d) shows one of the two predominantly east/west dipoles. It is clear that the dominant component of these dipoles was S_1, again with the exception of Surf2-S-IL (Figure 5.5(a)). There was a clear distinction between the north/south (Figure 5.5 (a) – (c)) and east/west dipoles (Figure 5.5 (d)), with the M_2 component absent in the east/west dipole. Furthermore, comparing the three north/south dipoles it is apparent that the relative magnitude of the M_2 frequency decreased with the length of the dipole, but was still present in the shortest (c.30 m) dipole. Even inland the M_2 component was present in the voltage data referenced at the surface, although the magnitude depended on the length and orientation of the dipole.

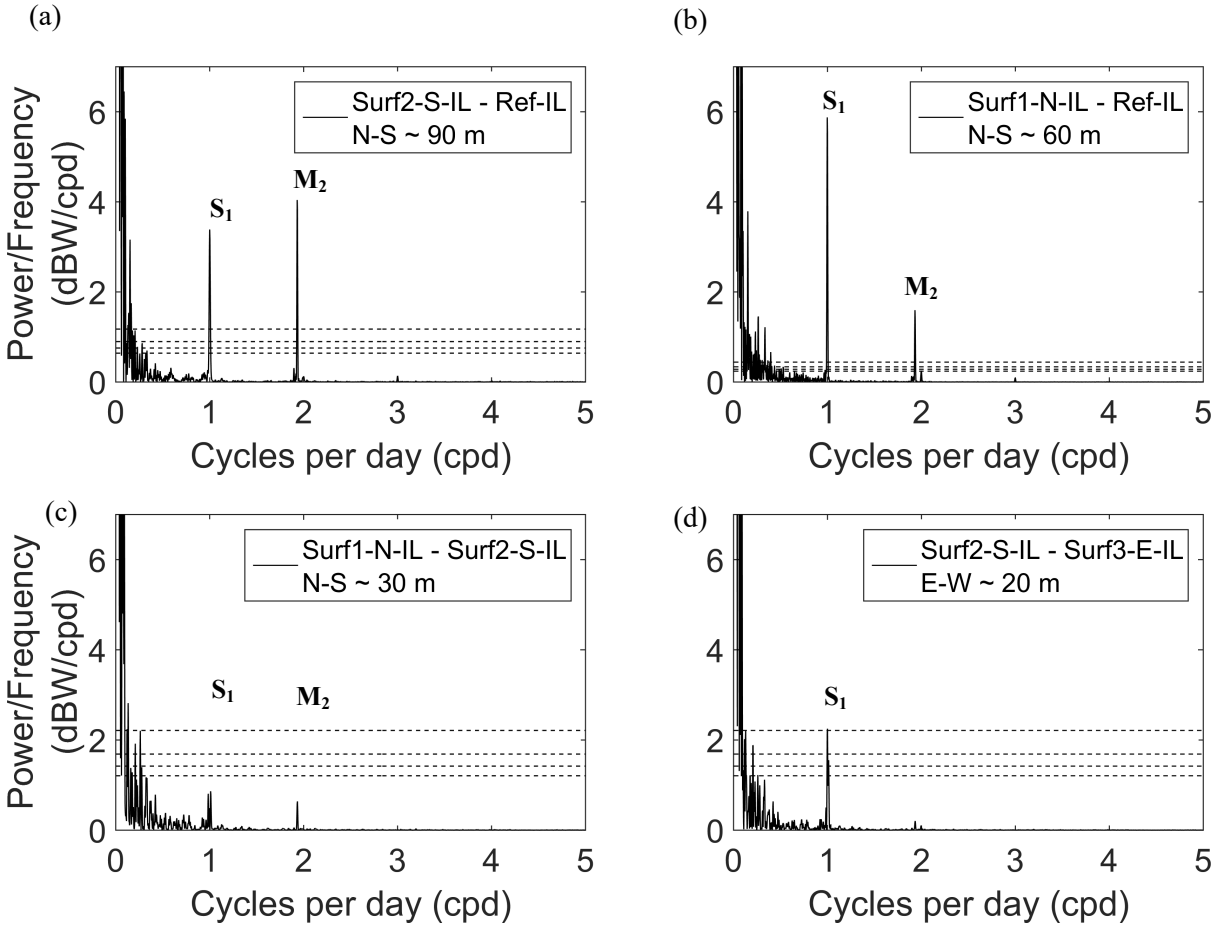

Figure 5.5 – (a) – (c) SP PSD from inland dipoles orientated in an approximately N-S direction. From (a) to (c) the separation between electrodes decreased. (d) One of the E-W dipoles.

5.3.1.3 Surface referenced borehole SP

The borehole SP data did not coincide exactly with the voltage data from the surface array because when the EA switched on the pump the water level in the borehole (PL10B) dropped below the position of electrode BH4-IL. As a result, the electrode's performance deteriorated causing problems with the PSD analysis. To compare the surface and borehole referenced data directly the 3 month period before the pump was switched on was used. Figure 5.6 shows the PSD of the borehole electrode data referenced sequentially against the electrodes in the surface array. As the distance of the reference electrode from the borehole increased the M_2 component increased in magnitude. When the borehole array was referenced against Surf1-N-IL, the M_2 component was not visible (Figure 5.6(c)). The small M_2 in the surface referenced borehole data (Figure 5.6) compared to the surface array (Figure 5.4) was because the borehole electrodes experienced a much smaller M_2 fluctuation.

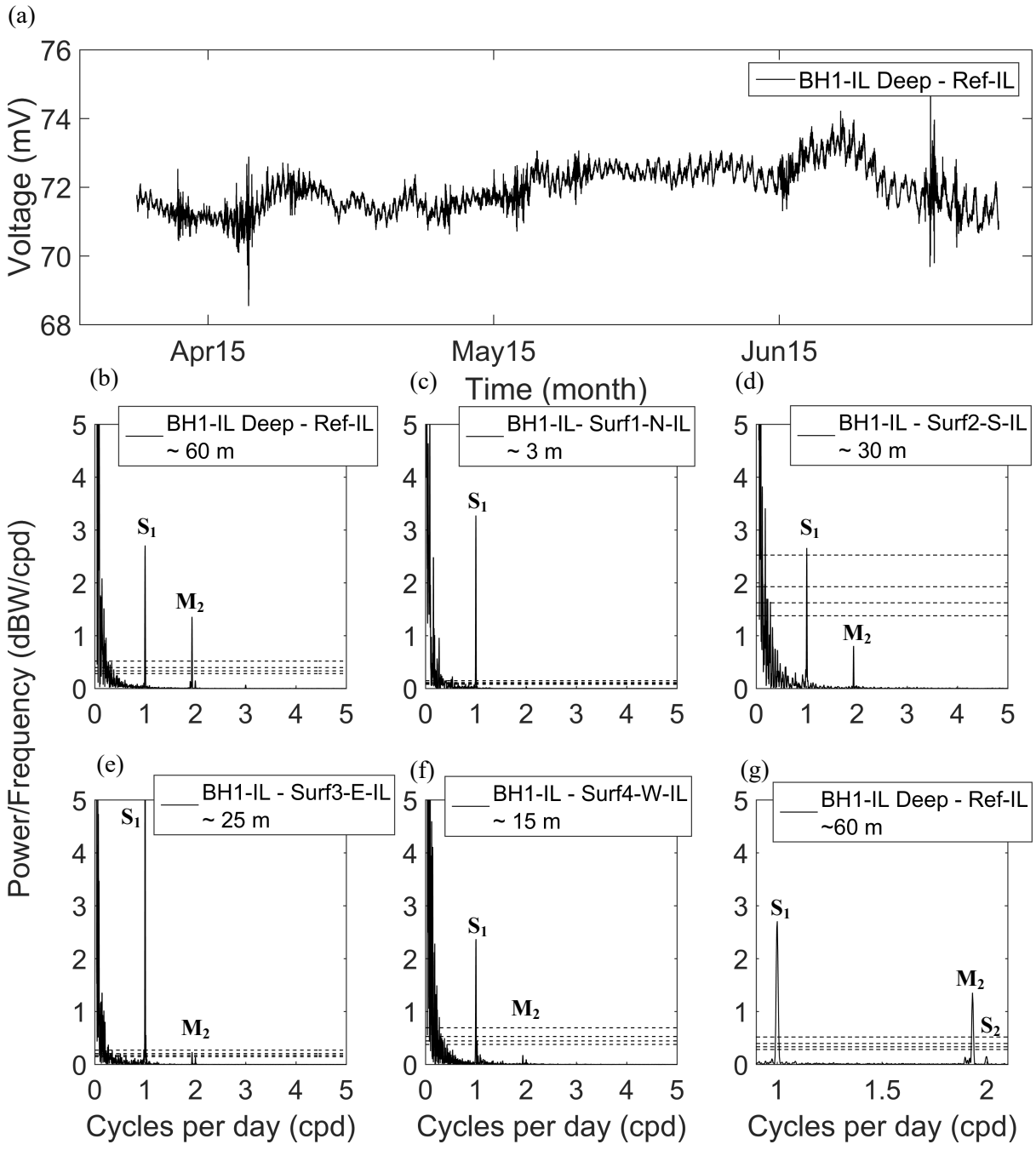

Figure 5.6 – (a) Voltage data from BH1-IL - Ref-IL (Figure 4.2) (b) – (f) PSD of the data, (c) shows no M_2 signal. (g) PSD of BH1-IL in (b) zoomed on the diurnal and semi-diurnal frequencies. The distances shown are the lateral distances between the surface electrodes used as the reference and the top of the borehole.

5.3.1.4 Borehole referenced SP

Figure 5.7 shows the PSD of the borehole electrode data referenced against the shallowest electrode, BH4-IL. Critically, there were no periodic components recorded in the BH data above the 50% significance limit. Figure 5.8 shows the PSD of the normalised head data recorded in the borehole. The head data contained S_1 and S_2 components.

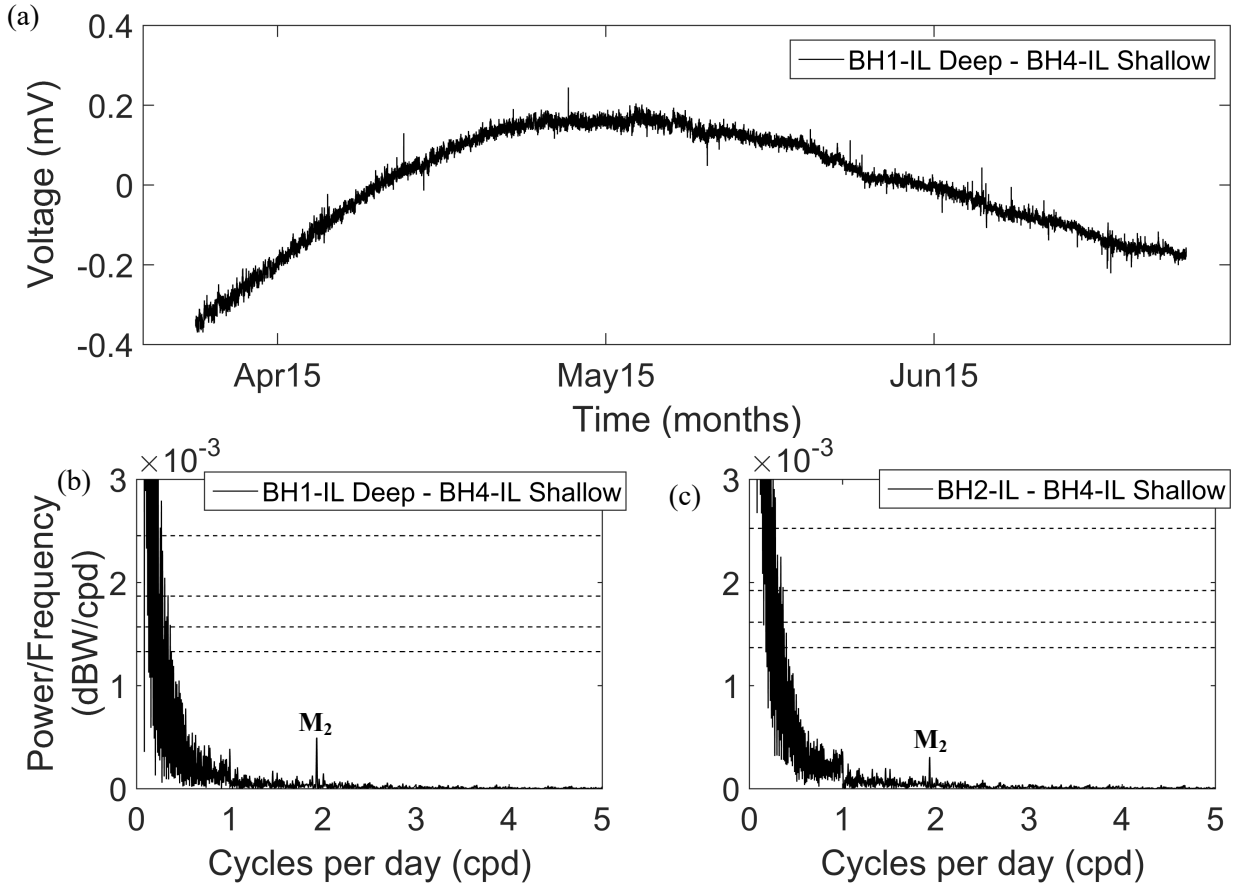

Figure 5.7 – (a) Voltage data from the inland borehole electrodes referenced against the shallowest borehole electrode (BH4-IL, Figure 4.2). (b) – (c) Borehole referenced SP data from BH1-IL and BH2-IL.

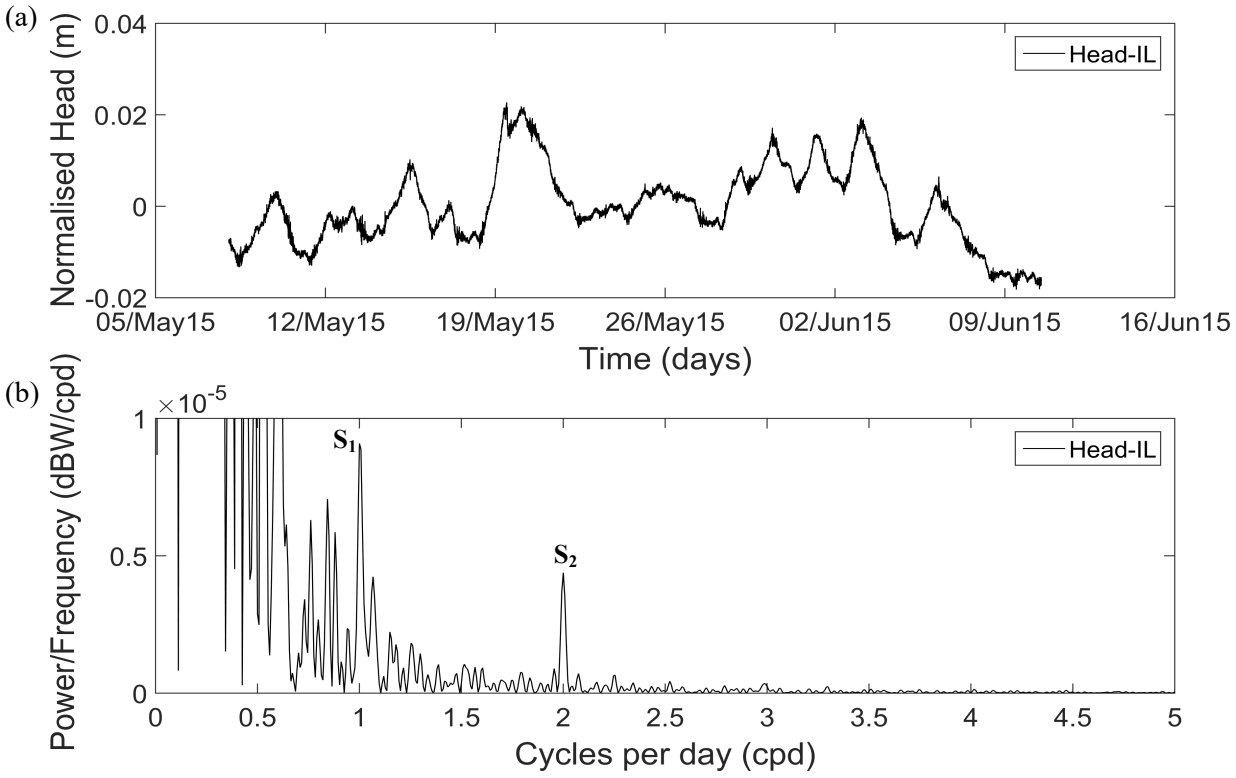

Figure 5.8 – (a) Inland head data (b) the same data analysed in the frequency domain. Note that significance levels are well below 50% and are not plotted here.

5.3.1.5 Pumping test results from the inland site

The results from the pumping test at the inland site are shown in Figure 5.9. In Figure 5.9(a) there is a voltage response of c.2 mV which is anti-correlated with a c.3.5 m change in head. The voltage response is superimposed upon the short term diurnal and semi-diurnal fluctuations discussed above. When the voltage was referenced in the borehole (Figure 5.9(b)) there was again a c.2 mV change in voltage; therefore, it appears that the choice of reference electrode did not affect the voltage response if the SP source mechanism is EK and; therefore, driven by changes in the pressure gradient.

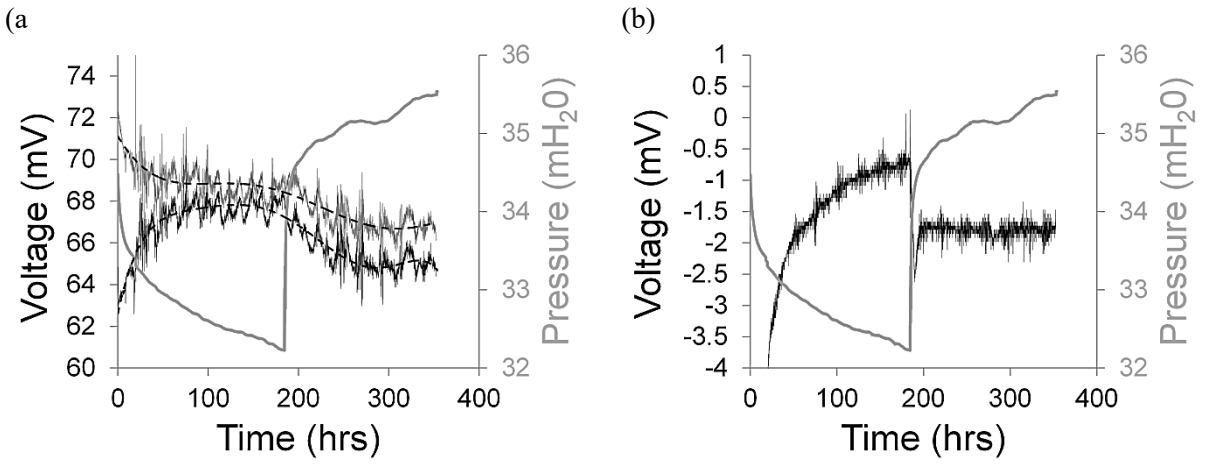

Figure 5.9 – Pumping test results. (a) Results from two borehole electrodes referenced against the surface electrode between February and March 2011, cross-plotting this data yields a coupling coefficient: 0.311 ± 0.3 mV/mH_2O with R^2=0.25. The poor R^2 is because of superimposed periodic effects (section 5.4.1). (b) Results from the 3 m borehole dipole, note that the coupling coefficient cannot be obtained from these data (see section 5.6.1.1 for explanation).

5.3.2 Coastal site results

The layout of the borehole array at the coastal site can be found in Figure 4.3. In order to relate the PSD analysis from the inland and coastal sites directly it was necessary to use a similar time-series length (~3 months). Comparing 1.5 years of data (the PSD of full the time-series is in Appendix 6) from the coast with three months of data from the inland site would have produced an analysis biased in favour of the coastal site because longer time-series improve the frequency resolution of spectral analysis (Karl, 1989, Trauth, 2010). Therefore, it would have undermined the purpose of the second site and the comparison it facilitated. Unfortunately, it was not possible to gather a longer time-series from the inland site. The full coastal time-series data are discussed in chapter 6. The three months of data chosen at the coastal site was from May to August 2013, prior to saline water breakthrough in the borehole (Figure 6.4). Thus, problems associated with the deterioration of electrode performance as a

result of diffusion of salts into the electrodes (section 6.5.1.1) were avoided, which was important because non-stationary data can adversely affect the PSD analysis and can mask some, if not all, of the periodic components of SP (Warner, 1998, Trauth, 2010, Båth, 2012). Conducting analysis on segments of a data set is a common way to deal with these types of problems (Warner, 1998). Table 5.1 summarises the results from the long-term voltage time-series. Figure 5.11 shows the results for the PSD analysis for the full time-series of BH1-C – BH13-C. Crucially, the short time-series contains all of the same components as the long time-series. The Newhaven tide (Figure 5.10) was dominated by the lunar solar (M_2) component, with K_1, S_2, N_2, MN_4, M_4 and MS_4 also present (Table 2.4).

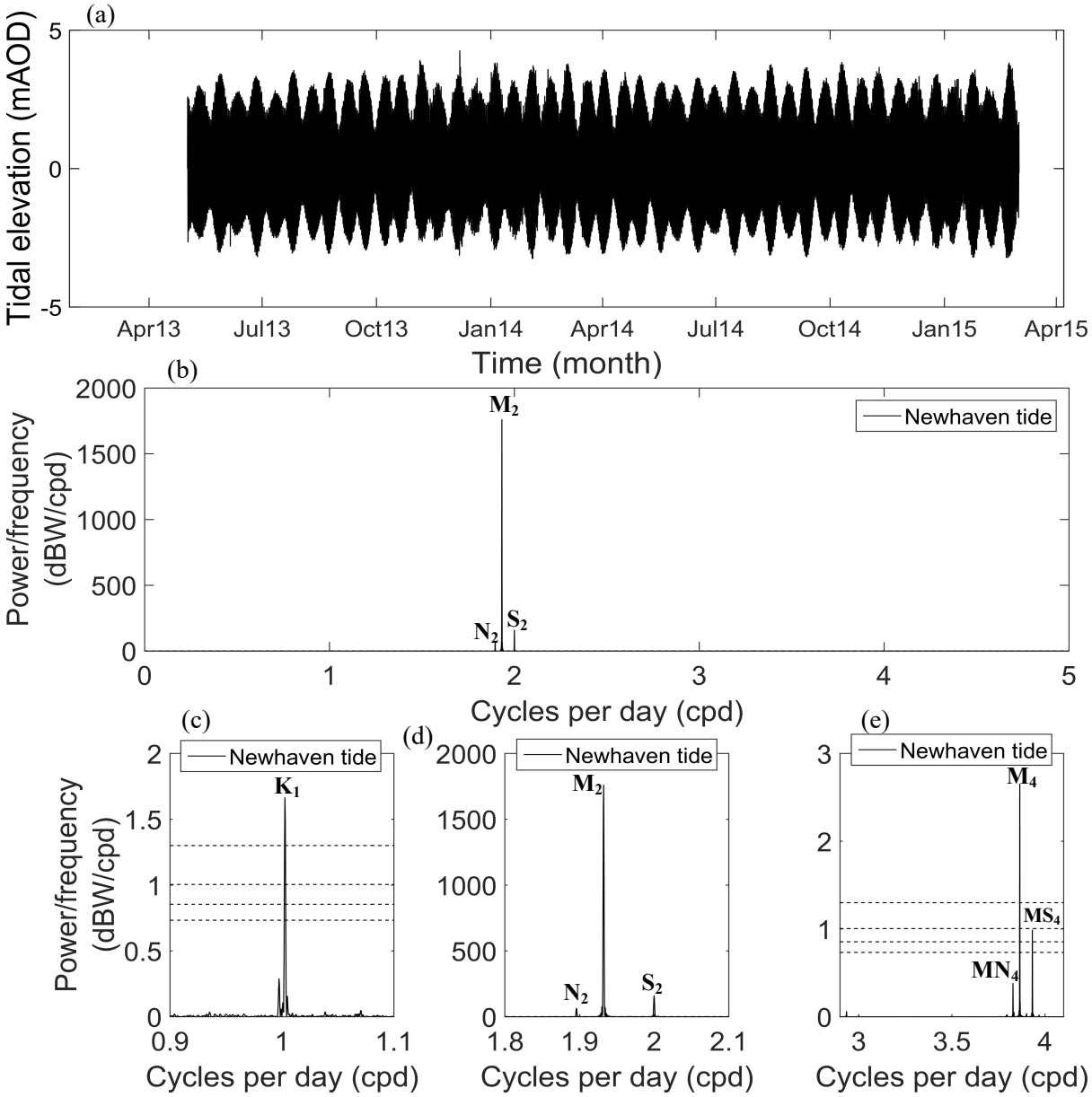

Figure 5.10 - a) Newhaven tidal data (Figure 4.3) from the full duration of the coastal monitoring experiment. b) PSD of the tidal data. c) Diurnal periodicity. d) Semi-diurnal periodicity. e) Higher frequency tides.

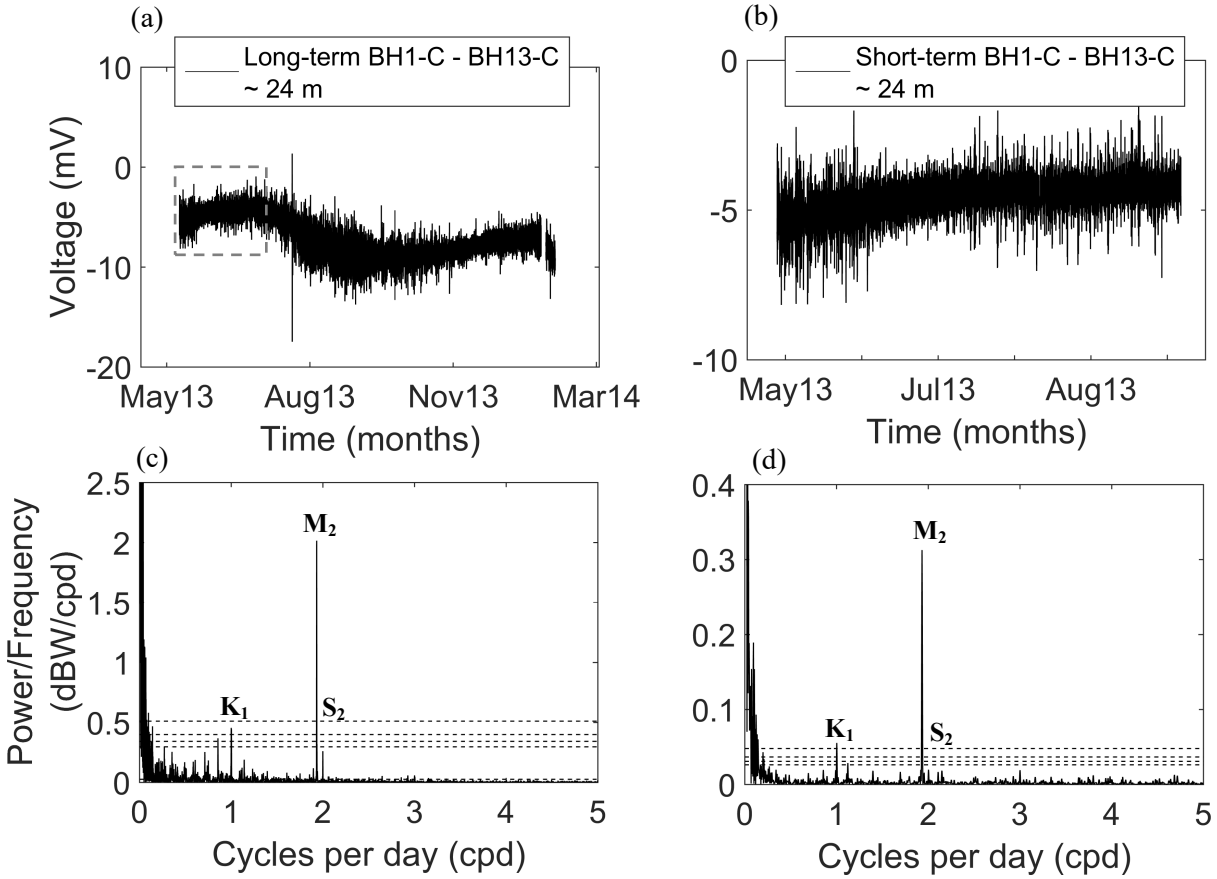

Figure 5.11 - (a) Long-term borehole referenced voltage data from the vertical dipole BH1-C – BH13-C at the coastal site (Figure 4.3), the period shown was the optimum period for the PSD analysis producing the most clearly distinguishable periodic peaks. The dashed box shows the region from which the short-term data series was obtained. (b) Short-term borehole referenced data from the coastal site. (c) The long-term data in the frequency domain. (d) The short-term data in the frequency domain. The dashed lines show the 50%, 90%, 99% and 99.9% significance limits. Notice that the two series are very similar in the frequency domain with all of the main components present in the short-term data. The only real difference is that the longer term frequency data displays a higher magnitude for each of the main components.

Data set	Tidal constituent	Amplitude relative to M_2	Hypothesised primary source
Borehole referenced SP	S_2	0.13	Oceanic tide
	M_2	1	Oceanic tide
	N_2	0.06	Oceanic tide
	K_1	0.22	Oceanic tide
	P_1	0.23	Oceanic tide
Surface referenced SP	S_2	0.14	Oceanic tide
	M_2	1	Oceanic tide
	N_2	0.43	Oceanic tide
	K_1	0.17	Oceanic tide
	P_1	0.18	Oceanic tide
	S_3	**0.025**	**Geomagnetic**
	MN_4	0.008	Oceanic tide
	M_4	0.016	Oceanic tide
	MS_4	0.012	Oceanic tide
	S_4	**0.011**	**Geomagnetic**

Table 5.1 – SP components recorded at the coastal site, and their hypothesised origin (those thought to be due to processes other than hydraulic effects of the ocean tide are highlighted in bold), observed in the PSD of the longest available SP time-series (c.1.5 years) from the surface and borehole referenced SP data. The amplitudes are inferred from the PSD estimate and are shown relative to the M_2 period.

5.3.2.1 Borehole head, temperature, and conductivity

Figure 5.12(a) shows the groundwater head fluctuations in the coastal borehole for the three months used in the PSD analysis. The head fluctuations were tidal in origin and contained the main tidal components, M_2, N_2, S_2 and K_1. The variation in head over the tidal cycle was typically c.0.5 m.

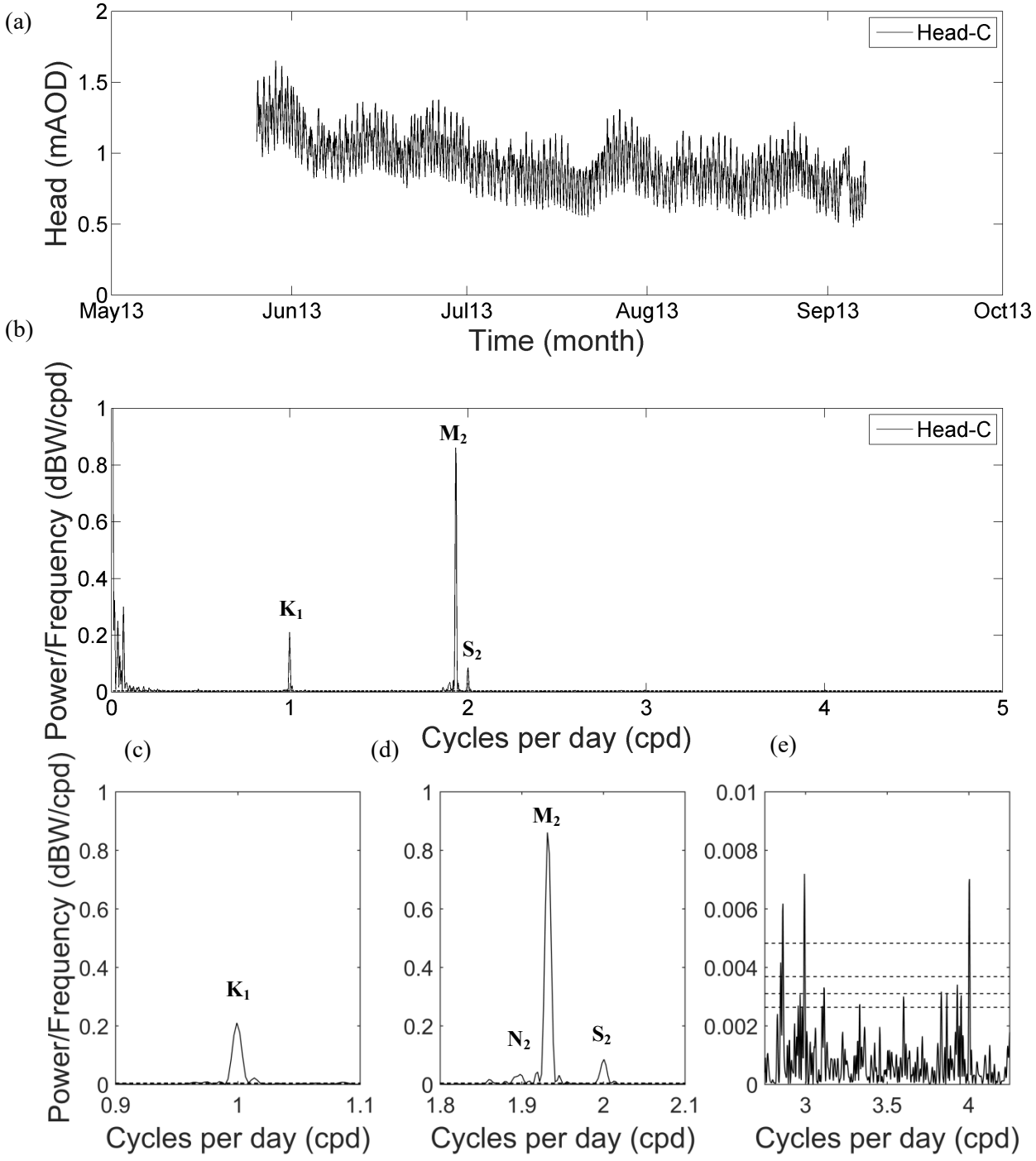

Figure 5.12 – a) Head data from the coastal site. b) – d) PSD analysis of the head data showing the main diurnal and semi-diurnal tidal components. e) Higher frequency components. Note that in b) – d) the significance limits are not clearly visible.

The conductivity and temperature data from the inland site are shown in Figure 5.13. The FEC in the borehole fluctuated with an M_2 period around a mean of c.831 μS/cm (Figure 5.13(b)). The conductivity variations were related to the tide forcing slightly more saline water in and out of the borehole. In mid-August 2013 saline water entered the borehole (section 6.2 and section 6.5.2 for more detailed discussion of this observation). Very small M_2 temperature fluctuations occurred in the borehole (<0.1°C, Figure 5.13(a)). There were no significant temperature fluctuations at the surface reference electrode (Ref-C) (Figure 5.13(c)).

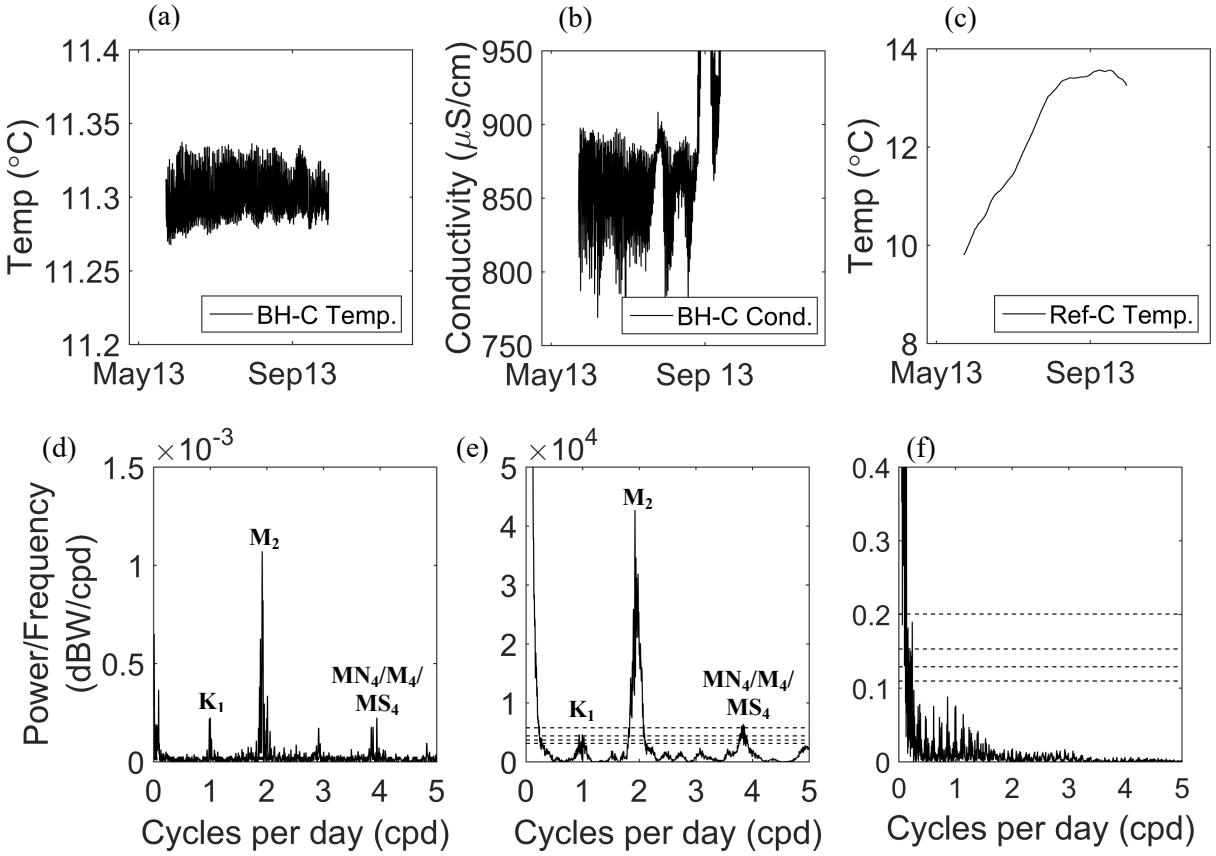

Figure 5.13 – Conductivity and temperature data from the coastal site. (a) The temperature in the borehole measured at BH10-C. (b) Conductivity in the borehole, saline breakthrough occurred in August 2013 (Figure 6.4). (c) The temperature at the surface reference electrode (Ref-C). (d) BH temperature PSD. (e) BH conductivity PSD. (f) Surface temperature PSD.

5.3.2.2 Surface referenced borehole SP

Figure 5.14(a) shows the surface referenced voltage data recorded by BH1-C and the results of the PSD analysis for a number of surface referenced electrodes in the borehole array.

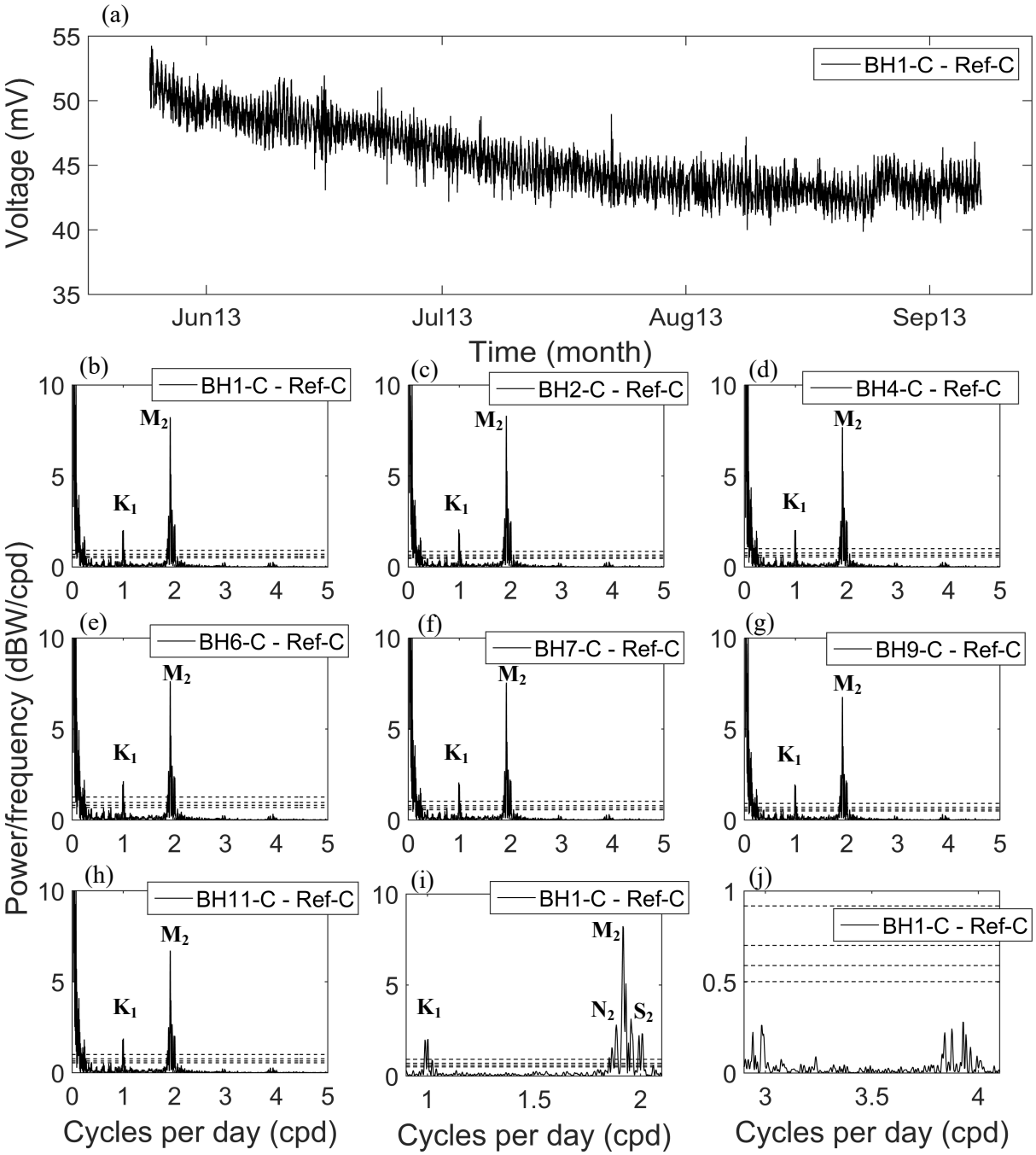

Figure 5.14 - (a) Typical voltage data at the coastal site over the period from which the PSD estimate was made. (b) - (h) PSD results from the borehole array with decreasing electrode depth. (i) PSD of BH1-C in (b) zoomed on the diurnal and semi-diurnal frequencies. (j) PSD of BH1-C in (b) zoomed on the higher frequency components.

The phase lag between the voltage and the head data was about 6.21 hours, so the voltage was anti-correlated with the head. The principal lunar (M_2) tidal component was the most significant component of the voltage; however, there was also evidence of the principal lunar-solar (K_1), the semi-diurnal solar (S_2) and the lunar elliptic (N_2) components (Table 2.4). The M_2 component at the coastal site was an order of magnitude larger than that observed using a similar referencing configuration at the inland site (Figure 5.6(f)).

5.3.2.3 Borehole referenced SP

Figure 5.15 shows the voltage data from dipole BH1-C - BH13-C and the results of the PSD analysis for the borehole referenced data.

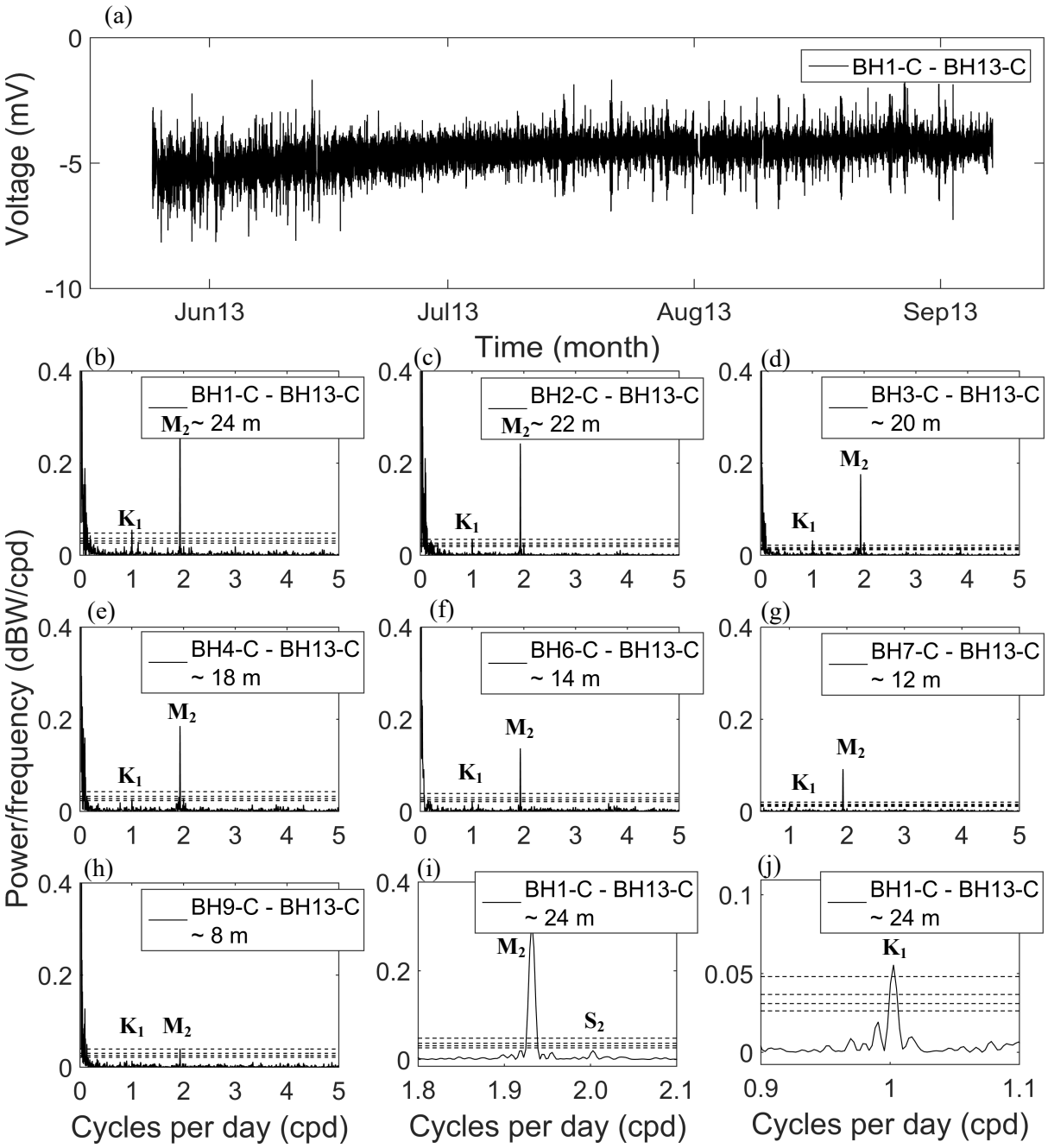

Figure 5.15 - (a) Typical voltage data from the coast from BH1-C - BH13-C over the period from which the PSD estimate was made. (b) - (h) decreasing separation from the reference electrode, BH13-C, at the top of the borehole. (i) PSD of BH1-C in (b) zoomed on the semi-diurnal frequencies. (j) BH1-C in (b) zoomed on the diurnal frequencies.

It is clear that the M_2 component was again dominant in the voltage. However, there is also evidence of the K_1 component (Figure 5.15(i)). The higher frequency components were not distinguishable. The magnitude of the K_1 and M_2 components increased as the separation of the electrodes increased.

At the smallest separation (c. 8 m, Figure 5.15(h)) the M_2 component was still visible in the PSD analysis. Crucially, the borehole SP at the coastal site clearly displayed a strong ocean tidal signature.

5.4 Field monitoring discussion

5.4.1 Inland and coastal site comparison

Table 5.2 shows a summary of the periodic SP data and the possible source mechanisms for the diurnal and semi-diurnal signals observed at both the inland and coastal sites. Crucially, the semi-diurnal components of the SP referenced in the borehole at the coastal site almost exactly match the ocean tidal data; the coastal SP also contained the main diurnal components although it did not share the exact amplitude patterns of the diurnal ocean tide components. Furthermore, the complete absence of any tidal constituents in the borehole referenced SP at the inland site assists in ruling out Earth, atmospheric or geomagnetic tides as primarily responsible for the tidal SP signal at the coast.

	Data set	Semi – diurnal			Diurnal			Largest period	Hypothesised primary SP mechanisms
		M_2	S_2	N_2	K_1	O_1	S_1		
SP data	Coastal surface ref. (section 5.3.2.2)	**3**	1	2	2	2	0	M_2	Oceanic tide (EED/EK)
	Coastal BH ref. (section 5.3.2.3)	**3**	2	1	2	2	0	M_2	Oceanic tide (EED/EK)
	Inland surface array (section 5.3.1.2)	2	1	0	0	0	3	S_1	Temperature (Electrode)
	Inland surface ref. (section 5.3.1.3)	2	1	0	0	0	3	S_1	Temperature (Electrode)
	Inland BH ref. (section 5.3.1.4)	0	0	0	0	0	0	N/A	N/A
Possible source mechanisms for SP data	Oceanic tide (section 5.4.2-section 5.6)	**3**	2	1	2	1	0	M_2	
	Geomagnetic field (section 5.4.1.2)	1	2	0	0	0	3	S_1	
	Temperature (section 5.4.1.1)	0	1	0	0	0	3	S_1	
	Earth tide* (section 5.4.1.3)	**3**	2	1	2	1	0	M_2	
	Atmospheric tide* (section 5.4.1.3)	0	3	0	0	0	1	S_2	

Table 5.2 - Summary of the main diurnal and semi-diurnal periods found in the SP data and the possible source mechanisms. The dark grey fields highlight the borehole referenced data and the ocean tidal data. The lighter grey highlights the surface referenced data. The periodic components are ranked in terms of their magnitude in the frequency domain, 3 represents the largest magnitude, 2, intermediate magnitudes, and 1 the smallest magnitudes, 0 indicates that this component was not present in the data or that it was below the significance levels determined by the PSD analysis. Finally, the hypothesised primary source mechanisms are also shown.* Note that the Earth and atmospheric tidal component rankings were estimated from literature, Earth tides from Agnew (2007) and atmospheric tides from Lindzen and Chapman (1969) and Dai and Wang (1999).

Figure 5.16 shows the M_2 component for the surface and borehole referenced data at both sites. Crucially, the M_2 component was orders of magnitude larger in the coastal SP data, hinting at the dominance of ocean tidal effects driving changes within the aquifer at the coastal site.

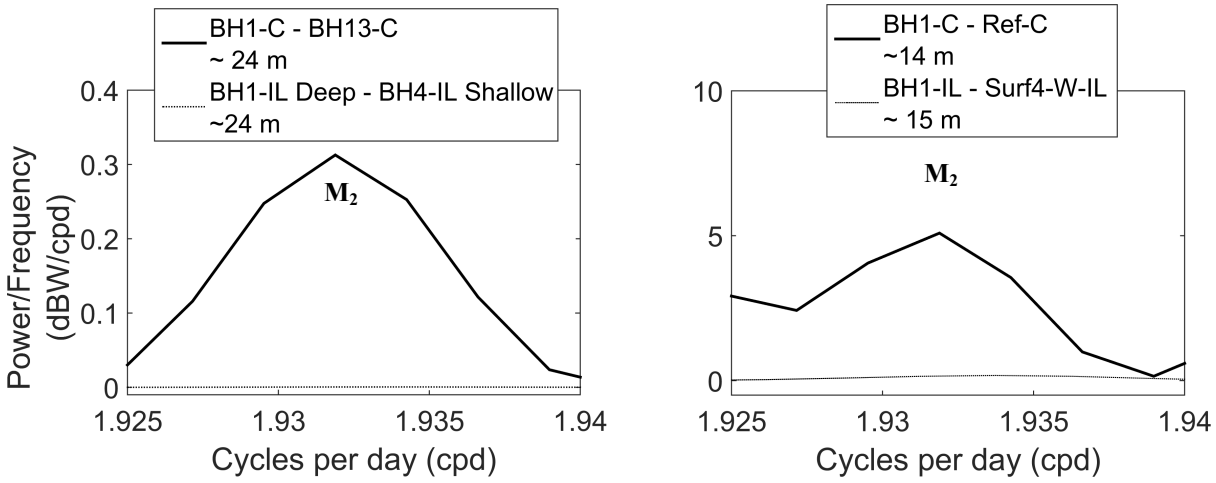

Figure 5.16 - (a) PSD of the M_2 component for the borehole referenced coastal (thick black line, from Figure 5.15(b)) and inland SP (thin dashed line, from Figure 5.7(a)), the length of the vertical dipole at each site is indicated. (b) The PSD of the M_2 component for the surface referenced borehole SP at the coastal (thick black line, from Figure 5.14(b)) and inland boreholes (thin dashed line, from Figure 5.6(f)), the distance from the surface electrode to the borehole is indicated.

The fact that the principal lunar component (M_2, Table 2.4) is present at the inland site (Table 5.2) suggests that caution is required before attributing the M_2 signal observed at the coast to purely ocean tidal processes. Due to the presence of the M_2 component and other periodic components inland other processes must contribute to the periodic SP observed inland and at the coast. The following discussion takes a systematic approach to rule out each of these components as the primary source mechanism for the periodic SP observed at the coast. To begin the effect of temperature is dealt with, and then the other mechanisms that share the key periodicities of the ocean tide are discussed.

5.4.1.1 Temperature

It is well known that temperature has an effect on measurements of SP (Corwin, 1990, Perrier et al., 1997, Woodruff et al., 2010). For example, at the inland site Surf2-S-IL (Figure 5.2(b)) recorded a larger principal solar SP period (S_1, Table 2.4) than Surf3-E-IL (Figure 5.2(c)). The difference in the S_1 period at Surf2-S-IL and Surf3-E-IL was primarily driven by changes in temperature, which was apparent when the differences between the temperature measurements at these locations were analysed. The smaller S_1 temperature fluctuation in the N/S dipole (i.e. Surf1-N-IL – Ref-IL, Figure

5.2(d)) was responsible for the smaller S_1 voltage in that dipole (Figure 5.5(a)). Therefore, it is important to have a number of temperature measurements within a surface electrode array for long-term SP monitoring (Corwin, 1990). Perrier (2000) noted that changes in temperature may not simply indicate the penetration of the S_1 temperature fluctuation down to the electrode, but that temperature also fluctuates in response to capillary flow through the unsaturated soil. It is possible that a similar mechanism may be partially responsible for the diurnal (S_1) period of the surface voltage data recorded at the inland site. Temperature correction of the SP data was not attempted at the inland site because the relationship between temperature and SP is non-linear due to small differences in electrode properties, caused by salt diffusion into the electrode chamber, changing the temperature coefficients (Perrier et al., 1997). Furthermore, phase shift between temperature and voltage can arise due to small differences in the position of the measurements. There were no detectable temperature variations within the inland borehole (Figure 5.1(b)). Furthermore, temperature was clearly not a source of the diurnal SP at the coastal site (Figure 5.13(b)), because Ref-C was buried at a depth of 1.5 m, far below the penetration depth of diurnal temperature fluctuations (Perrier et al., 1997). At the coastal site, temperature fluctuations in the borehole were only 0.08°C (Figure 5.13(c)) and did not cause any significant change in SP; thus, temperature fluctuations could not explain the predominant M_2 period at the coastal site.

5.4.1.2 Geomagnetism

Other studies have also observed the M_2 signal in inland SP data. For example, Trique et al. (2000) observed an M_2 component in the French Alps and attributed this to ocean tidal modulation of the geomagnetic field. The decay of the M_2 signal as the dipole length decreased, in the SP surface array at the inland site (Figure 5.5), suggests that some of the SP signal may be related to telluric currents of geomagnetic origin (Orihara et al., 2012). Trique et al. (2002) did not observe correlations between SP fluctuations and dipole length; however, this may be due to differences in temperature or electrical conductivity of the subsurface across their c.5 km surface monitoring array.

The tidal component of telluric currents is caused by the motion of a conductive body (the ocean) through the geomagnetic field and is known as the ocean dynamo (Rosser and Schlapp, 1990, Palshin

et al., 1996, Palshin et al., 1997). The ocean dynamo is known to generate telluric currents in the UK, but most studies report this in areas nearer the coast than at the inland site studied here (Chapman and Kendall, 1970, Osgood et al., 1970, Brown and Woods, 1971, Hart et al., 1983a, Hart et al., 1983b). The presence of the M_2 component at the inland site suggests that the geomagnetic field could be one of a possible number of sources of the tidal SP observed at the coastal site.

Figure 5.17 shows the PSD of the geomagnetic data from the three stations around the inland and coastal SP monitoring sites (Figure 4.1). The geomagnetic field vector consists of three components, the northerly (X), easterly (Y) and vertical (Z) intensity. From these three components the horizontal intensity and declination can be calculated, where $H = \sqrt{X^2 + Y^2}$ and $D = arctan\frac{Z}{H}$ respectively.

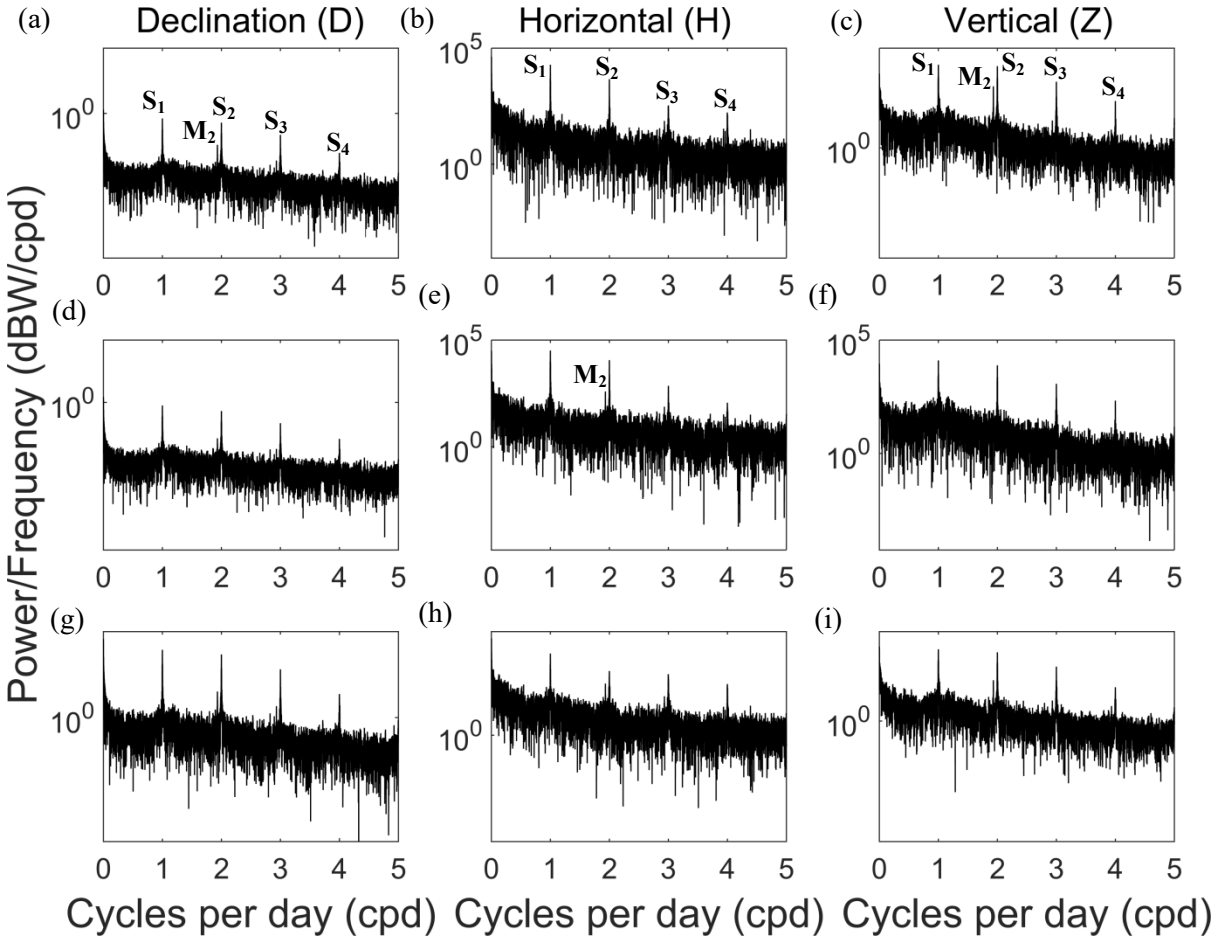

Figure 5.17 – PSD of the geomagnetic data for the duration of the inland monitoring experiment from the three monitoring stations shown in Figure 4.1: 1. Hartland (a, b, c), UK; 2. Eskdalemuir (d, e, f), UK and; 3. Chambon-la-Foret (g, h, i), France. The data is presented on a semi-log scale.

The geomagnetic data is dominated by the lunar solar component (S_1) but also contains the S_2, S_3 and S_4 harmonics. The presence of the S_3 and S_4 components at the inland (Figure 5.4) and coastal sites

(Table 5.1) provides further evidence for geomagnetic influence on the SP at both sites, because S_3 and S_4 cannot be explained by ocean tidal processes (Table 2.4). Therefore, the geomagnetic field must have an impact on the surface referenced SP data at both sites. The principal lunar (M_2) signal was present at all of the geomagnetic monitoring stations. M_2 was most prominent at Hartland, which is about 3 km from the coast, comparable to the distance of the coastal borehole from the sea (Figure 4.3). Figure 5.6(b) indicates that strategic placement of a surface reference electrode can minimise geomagnetic effects; when the inland borehole data was referenced against Surf1-N-IL about 3 m from the borehole (Figure 4.2), there was no evidence of the M_2 signal in the SP data. There was also no evidence of the M_2 component in inland dipole BH1-IL - Surf4-W-IL which had a horizontal length of 15 m and a similar orientation to the coastal dipole BH1-C - Ref-C, which had the largest M_2 component at the coastal site.

The relative magnitude of each component at the three geomagnetic monitoring stations was approximately the same across all geomagnetic stations (Figure 5.17). Most significantly, the M_2 component was consistently smaller than S_1 and S_2 (Figure 5.17). In most other locations globally the geomagnetic field has a larger S_2 component than M_2 (Maus and Kuvshinov, 2004, Love and Rigler, 2014, Bindoff et al., 1988). Some authors report that it is, at most, comparable in magnitude (Cochrane and Srivastava, 1974). However, M_2 is almost certainly smaller than the dominant S_1 component (Cochrane and Srivastava, 1974, Maus and Kuvshinov, 2004). Thus, the SP data at both the inland and coastal sites would be expected to reveal a similar pattern to the geomagnetic data if telluric currents were solely responsible for the periodic SP. In fact, the SP PSD had a different pattern to the geomagnetic PSD at the inland (Figure 5.5, Figure 5.6 and Figure 5.7 - $M_2 > S_2$) and coastal sites (Figure 5.14, Figure 5.15 and Table 5.1 - $M_2 > S_2$ and S_1). Thus, geomagnetism was not solely responsible for the observed frequency patterns in SP at either site. The SP, at the coastal site in particular, was substantially different from the geomagnetic data (Table 5.2). Trique et al. (2002) claimed that SP signals with a period of one minute to one day can simply be attributed to the geomagnetic field. However, given the discussion above this is an unreasonable assumption, which is actually also apparent in their SP (their Figure 8(b)) and geomagnetic data (their Figure 8(a)).

The discussion above applies primarily to the horizontal component of the geomagnetic field. However, there is also evidence in the comparison between the two sites that rule out telluric currents as the source of the coastal borehole SP. The M_2 component at the coastal site was larger than the M_2 component at the inland site (Figure 5.16). In the borehole it was 2-3 orders of magnitude larger (Figure 5.7 and Figure 5.15) and it was an order of magnitude larger when referenced at the surface (Figure 5.6 and Figure 5.14). The discrepancy in magnitude between the surface and borehole referenced measurements between the two sites strongly suggests that the M_2 signal in the coastal borehole was caused by ocean tidal effects within the aquifer. If the M_2 component was driven purely by telluric currents then the difference in the magnitude between the surface and borehole referenced SP at the two sites would be expected to be approximately the same, which was not the case. Furthermore, the depth to the water-table at the inland site was about half of the depth to the water table at the coastal site; thus, attenuation of the telluric current with depth would be expected to be greater at the coastal site, further reducing the influence of the telluric current in the coastal borehole and pointing to sources of the M_2 component other than geomagnetism. In summary, the geomagnetic field cannot be ruled out as one of a possible number of sources for the M_2 component. However, in isolation telluric currents cannot explain the observation of M_2 at either site. Therefore, the following section discusses the possible impact of Earth and atmospheric tides which also display the M_2 period.

5.4.1.3 Earth and atmospheric tides

Small head fluctuations, with the principal solar lunar component (S_1, Table 2.4) and its harmonic (S_2), were observed in the inland borehole (Figure 5.8). The head fluctuations were most likely to be caused by atmospheric pressure. Atmospheric pressure fluctuates with an S_1 and S_2 period (Dai and Wang, 1999), the latter of which is one of the most regular metrological phenomenon (Lindzen and Chapman, 1969). Rojstaczer and Riley (1990) and Kumpel (1997) showed that diurnal (O_1, S_1) and semi-diurnal (M_2, S_2) water level fluctuations in boreholes can be caused by fluctuating atmospheric pressure and Earth tides and can occur in both confined and unconfined aquifers. Head fluctuations driven by Earth tides have previously been reported in inland boreholes (Rojstaczer and Riley, 1990,

Zeumann et al., 2009, Cutillo and Bredehoeft, 2011) and have actually been used in fractured aquifers to characterise aquifer properties (Bower, 1983, Burbey, 2010).

Earth tides share the same relative amplitude for each of the periodic components found in the ocean tidal data (Agnew, 2007); thus, they may contribute to the M_2 component observed at the inland site. Furthermore, Earth tides have previously been used to explain SP signals in glacial boreholes (Kulessa, 2003). Kulessa et al. (2003) invoked Earth tides as the primary driving mechanism for sub-glacial flow leading to a significant principal-lunar solar (K_1) component in their SP data. It is possible that Earth tides could also drive changes in head in the inland borehole (Figure 5.8) and may help explain the diurnal spike in the SP recorded in the borehole at the inland site. Gokhberg et al. (2009) modelled the impact of Earth tides on kilometre long cables in Japan and attributed the presence of all of the main tidal components (O_1, P_1, K_1, N_2, M_2, S_2, Table 2.4) to the EK potential in the near surface; they suggested that Earth tide forcing was primarily responsible. However, assuming that Earth tide effects are relatively constant between the inland and coastal sites (Agnew, 2007), it would appear that Earth tide effects are too small to fully explain the periodic SP components at the coastal site, primarily because of the absence of any significant M_2 Earth tide component within the inland borehole (Figure 5.16).

5.4.1.3.1 Earth and atmospheric tidal influence on processes in the unsaturated zone

Adler et al. (1997) attributed fluctuations, from a few hours to 1 day, in SP measured in an underground limestone quarry in France to periodic variations in saturation driven by atmospheric fluctuations. The principal lunar (M_2) component is a constituent of atmospheric tides (Geller, 1970, Vial and Forbes, 1994, Forbes et al., 1994), albeit not as prominent as the S_1 or S_2 frequency components (Lindzen and Chapman, 1969); thus, atmospherically driven changes in saturation may partially explain the presence of both the M_2 and S_2 components in the data recorded inland. Kulessa et al. (2003) invoked this mechanism to explain the dominance of the S_2 component in their SP data, suggesting that the semi-diurnal atmospheric fluctuations were responsible for flow below the glacier at their study site. Earth tides or fluctuations in atmospheric pressure may not generate any significant change in water levels or pressure fluctuations within the borehole, but rather may drive flow in the

unsaturated zone which may be large enough to be recorded by the inland surface monitoring array; thus, explaining the M_2 signal recorded in the inland surface array. Evidence suggests that the effective excess charge density, which arises due to an unequal distribution of positive and negative ions within the EDL, in the unsaturated zone can be amplified as the saturation reduces (Jougnot and Linde, 2013). Given that Jackson (2010) showed that the relative EK coupling coefficient is dependent on the excess charge density, and the coupling coefficient, Earth tide or atmospherically driven fluctuations in the unsaturated zone may generate the M_2 signals observed in the SP surface array at the inland site and enhance the M_2 signal of the surface referenced borehole data at the coast.

The above analysis demonstrates that long-term temporal surface SP monitoring in coastal aquifers is fraught with interpretation difficulties, including multiple overlapping source mechanisms; these difficulties undermine the value of such data for the purpose of seawater intrusion monitoring. However, the analysis also indicates that the M_2 component measured in the coastal borehole (Figure 5.16(a)) must be primarily caused by changes in the aquifer, most likely changes in the pressure and salinity gradients driven by the tides in the English Channel, hinting at an EK or EED source.

5.4.2 Coastal SP source mechanisms

5.4.2.1 Electrode effects

Before attributing the M_2 and other tidal components observed in the coastal SP data to EK or EED potentials generated within the aquifer, it was important to investigate whether the observed voltage fluctuations were due to cyclical changes in the conditions at the electrodes. The borehole conductivity and temperature at the coastal site also displayed the M_2 signature (Figure 5.13), and variations in both could have affected the electrode response. Temperature fluctuations were c.0.08°C over a tidal cycle (Figure 5.13(c)). The electrodes have a temperature coefficient of -0.65 mV/°C (Silvion, 2015) which would result in a maximum temperature electrode effect of c.5 μV across the tide, much smaller than the observed voltage of c.2 mV observed when referenced against the surface electrode (Ref-C) and smaller than the value of c.400 μV measured when referenced against the borehole electrode (BH13-C) (Figure 5.18(a) & (c)). Similarly, conductivity fluctuations were a maximum of c.50 μS/cm over a tidal cycle, and laboratory measurements suggest the conductivity

sensitivity of the electrodes is c.1 S/cm/decade, so voltage changes in response to conductivity fluctuations were at most c.50 μV. Moreover, the conductivity fluctuations measured over the tide were not reflected in the voltage fluctuations (Figure 5.18(b) & (d)) and did not respond to the decrease in amplitude of the conductivity measurements recorded in July 2013. Therefore, conductivity and temperature variations in the borehole did not significantly affect the electrodes over the tidal cycle. Thus, having ruled out multiple possible mechanisms for the tidal SP components M_2, S_2, N_2, K_1 and P_1, using PSD analysis and accounting for the electrode effects the primary source of the periodic SP recorded in the coastal borehole must be due to tidal fluctuations driving processes within the aquifer (Table 5.2).

5.4.2.2 EK and EED source mechanisms

Two likely source mechanisms for the periodic SP response in the coastal aquifer remain to be investigated. The first is the EK potential, which arises as a result of head gradients (Rizzo et al., 2004, Maineult et al., 2008b, Jackson et al., 2012a). The second is the EED potential arising as a result of the concentration gradient associated with seawater intrusion (Revil, 1999a). EK arises as the pressure gradient fluctuates with the tide. The EED potential may also fluctuate across the tide with the movement of the salinity front. To begin the EK contribution is assessed, based on the common assumption that a distant reference electrode is unaffected by changes in pressure within the aquifer; thus, the pressure potential difference between the surface reference electrode (Ref-C) and the borehole electrodes is known (Rizzo et al., 2004, Maineult et al., 2008, Jackson et al., 2012a).

Figure 5.18 shows the SP, head and conductivity data from a 48 hour period in July 2013. The SP is anti-correlated with head, which would be consistent with a negative EK coupling coefficient. The SP data was smoothed using a second order Savitzky-Golay (SG) moving average filter with a window of 125 minutes. The SG filter is a low-pass filter that performs data smoothing using a local least-squares polynomial approximation. It is capable of smoothing noisy data while maintaining the shape and height of waveform peaks (Savitzky and Golay, 1964, Press and Teukolsky, 1990, Schafer, 2011) and has previously been used for SP data analysis (Byrdina et al., 2003, Maineult et al., 2008a, Damgaard et al., 2014). A common problem with other filters is that filtering introduces phase delay, the SG

filter does not have this problem (Eilers, 2003). Furthermore, the SG filter can deal with short sections of missing data (Eilers, 2003).

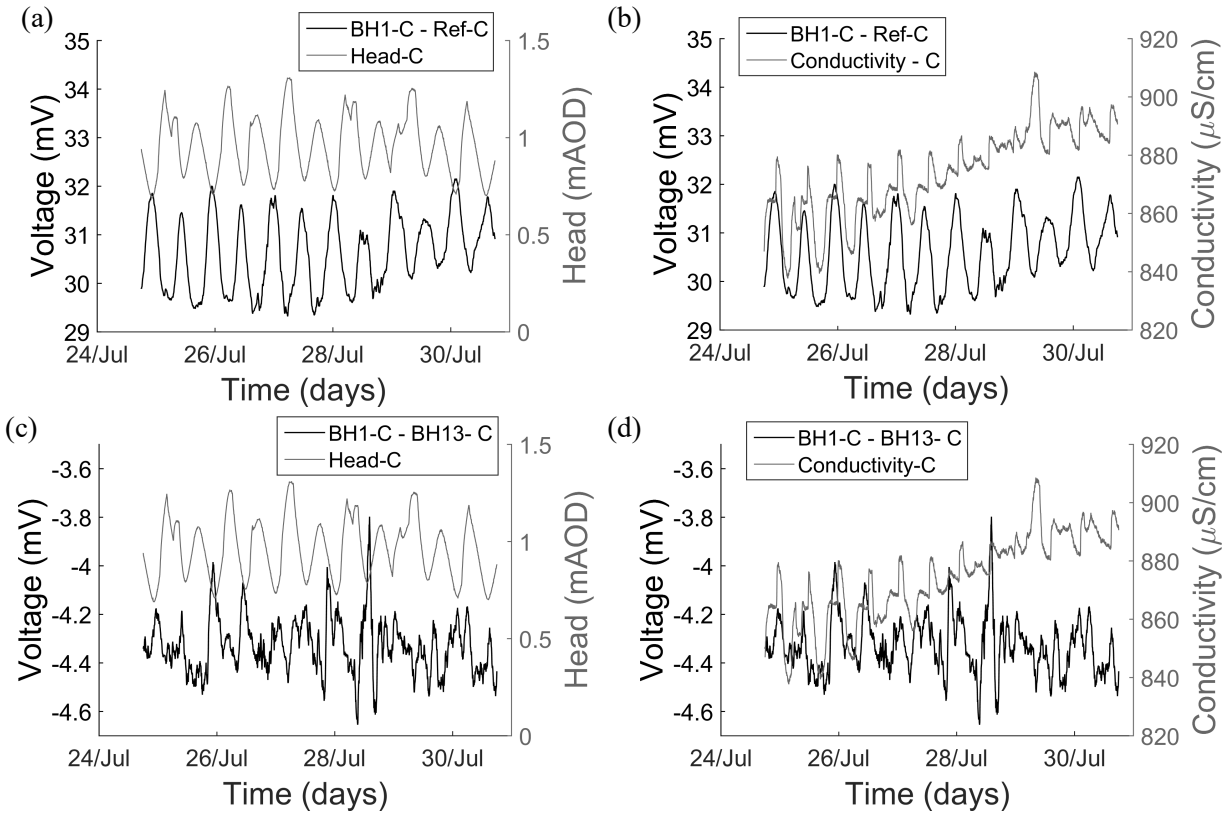

Figure 5.18 – (a) Coastal head and surface referenced voltage, (b) Conductivity and surface referenced voltage, (c) Head and borehole referenced voltage. (d) Conductivity and borehole referenced voltage. SP and head are anti-correlated. SP and conductivity variations are correlated but have a different shape.

Previous evidence suggests that oceanic tidal processes can generate SP signals in coastal areas. For example, Gokhberg et al. (2009) modelled the effect of Earth tides on the electric potential recorded at the surface and note that their results actually underestimated the observed tidal fluctuations recorded on kilometre long cables. They suggested this was because of the addition of ocean tidal effects in the coastal zone where the measurements were made. Furthermore, they suggested that the enhanced tidal fluctuations observed were caused by the EK component of the SP driven by pressure fluctuations induced by ocean tides in the coastal zone.

Kang et al. (2014) reported SP measurements along a sea dyke, and claimed these were generated by the EK potential as water was forced through the dyke with the tide. However, their measurement procedure was questionable. They used steel rods which are notoriously unstable and of inadequate quality for monitoring SP signals. If changes in salinity occurred at their steel electrodes, as seawater

moved through the dyke, then redox potentials would have arisen (Castermant et al., 2008). They also claimed that temperature effects would have had no effect on their measured SP because they buried the electrodes at depths of at least 50 – 80 cm. However, a similar burial depth was used at the inland site (section 4.3.1) and significant temperature effects were observed (Figure 5.2 and Figure 5.3). Furthermore, their reference electrode was located 2 km from their main survey lines which made their measurements particularly vulnerable to the impact of the geomagnetic field. However, they assumed that telluric and other sources of noise were negligible over the time frame of the tide. Analysis of the inland site (Figure 5.5) demonstrated that this is not a valid assumption, most clearly indicated by the increased magnitude of the M_2 component as the dipole length increased (section 5.4.1.2).

Figure 5.18(a) & (c) show that the voltage was anti-correlated with head, which is consistent with a negative EK coupling coefficient and an excess of positive charge moving down the head gradient. If the voltage response was dominated by the EK potential, then the gradient of a linear regression through the data yields the EK coupling coefficient (see section 3.3.1). However, the gradients obtained in this way from the surface referenced data vary from tidal cycle to tidal cycle, over the range -1 mV/mH_2O to -6 mV/mH_2O (Figure 5.19(c)). Therefore, the gradients obtained from the surface referenced data are 2 to 10 times larger than the EK coupling coefficient for chalk saturated with groundwater (-0.575 ± 0.080 mV/mH_2O, Table 3.6). Furthermore, many tidal cycles did not exhibit a linear relationship between voltage and head (Figure 5.19(b)); indeed, when referenced against the surface electrode (Ref-C) only 60% of falling and rising tidal cycles displayed this (defined such that a linear regression has a quality of fit $R^2 > 0.8$). These non-linear effects could be due to noise or pumping at the abstraction borehole. If the latter, this would support the argument that EK effects cannot be the sole explanation for the periodic SP, because if the SP fluctuations were purely EK in origin there would also be a clear linear response to pumping which does not appear evident in Figure 5.19(b). It is also possible that non-linear processes occur in the unsaturated zone (Maineult et al., 2008b), and that changes in saturation maybe correlated with the tide (Iglauer and Muggeridge, 2013). Given the inverse relationship between effective charge density and saturation

(Jougnot and Linde, 2013, Jackson, 2010, Jougnot et al., 2012) the voltage fluctuations recorded when referenced against Ref-C may be higher than expected due to such unsaturated zone processes. Furthermore, the larger fluctuations in the surface referenced data may have been amplified by the ocean dynamo effect or the other effects discussed in section 5.4.1.

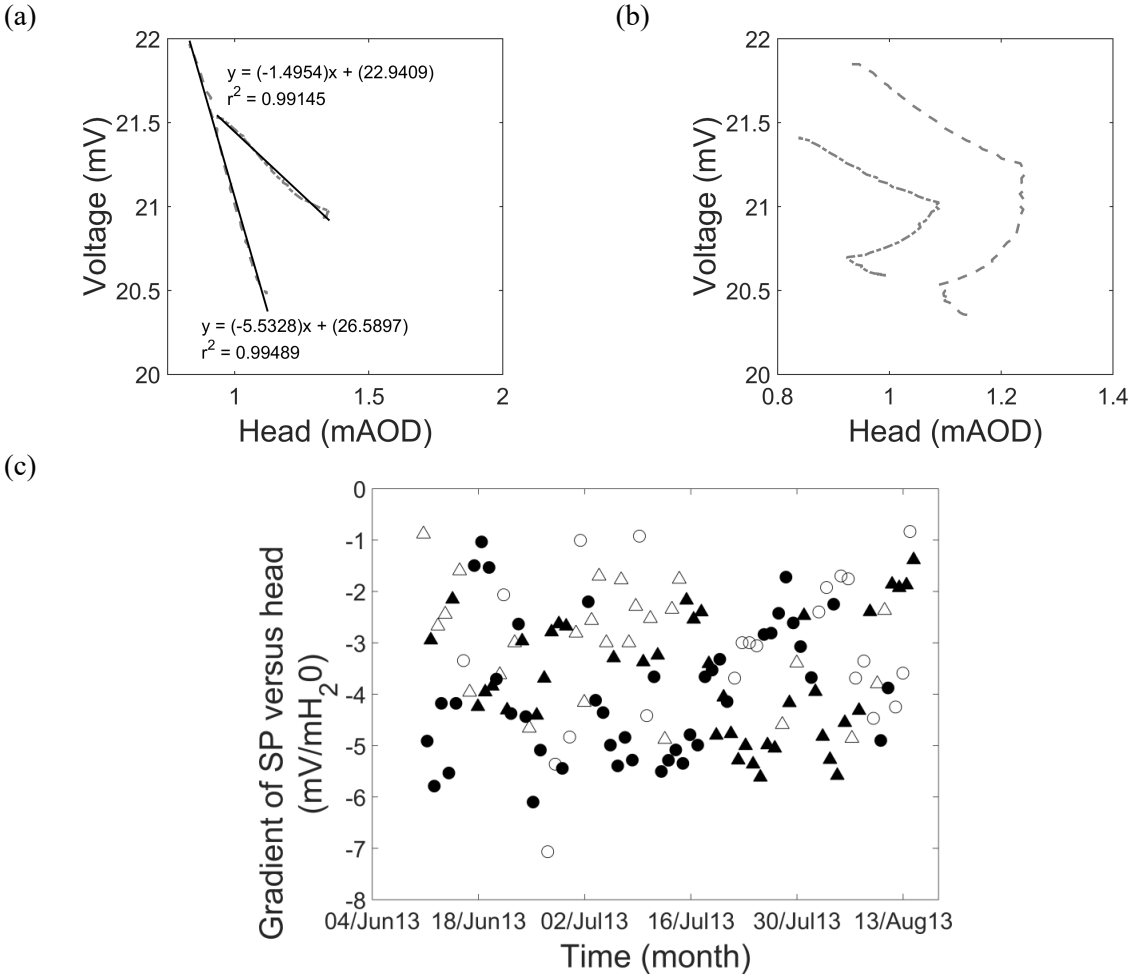

Figure 5.19 - Analysis of surface referenced data from the coastal borehole monitoring array. (a) SP at BH1-C versus head for the maximum and minimum gradients from regression analysis. (b) SP at BH1-C versus head, for $R^2 < 0.8$, showing the minimum (thick line) and maximum R^2 relationships. (c) Gradient of SP versus head. Solid symbols show cycles where the response was linear (such as the data shown in (a)); open symbols show cycles where the response was non-linear (such as the data shown in (b)). Triangles indicate data from the rising tides and circles data from falling tides. Note that this is only for the period between the 4th June and 13th August 2013. However, similar plots from other parts of the data show similar patterns but are not reproduced here.

The maximum EK contribution from a c.0.5 m change in head can be estimated from the laboratory measured coupling coefficient (-0.575 ± 0.080 mV/mH_2O, Table 3.6) resulting in a c.290 µV EK tidal fluctuation, much less than the c.2 mV observed using the surface reference (Ref-C, Figure 5.18). Furthermore, Jackson et al. (2012a) conducted a pumping test at the inland site, in which a drawdown of c.0.1 m produced an SP response of c.60 µV; consistent with estimates of the SP response using the

laboratory measured coupling coefficient. Consequently, it appears that the EK potential cannot be solely responsible for the coastal M_2 tidal SP, and that the EED potential must contribute.

Further evidence for this claim is provided by the pumping test data shown in Figure 5.9. The pumping experiment demonstrated that in order to obtain a c.2 mV SP signal from a purely EK source mechanisms the change in head required was c.3-4 m, significantly larger than the c.0.5 m head fluctuations observed at the coastal site. In addition, the EK coupling coefficient, obtained from the pumping test, referenced to the surface reference electrode (Figure 5.9(a)) was close to that measured in the laboratory, which was not the case for tidal head fluctuations at the coastal site (Figure 5.19). The inland pumping test also showed approximately the same change in voltage whether referenced at the surface or in the borehole (Figure 5.9). Such an observation is inconsistent with the observations made at the coastal site where the borehole referenced voltage fluctuations were much smaller than the surface referenced voltage fluctuations (Figure 5.18(a) & (c)). The borehole referencing scheme adopted at the coastal site was not ideal as it is possible that the borehole reference electrode (BH13-C) may also have been affected by processes occurring in the aquifer including the presence and movement of a salinity gradient. Thus, the potential difference recorded by two electrodes in the borehole would be significantly less than the potential difference recorded by a reference electrode much further from the source, i.e. at the surface. The results from the inland pumping test suggest that this is not the case for the EK component; thus, backing the claim that the EED potential contributed to the voltage fluctuations recorded at the coast.

The findings of Maineult et al. (2005) and Jougnot et al. (2015) are consistent with the conclusion that the EED potential must contribute significantly to the observed SP at the coastal site. They were unable to simulate the magnitude of the SP response observed in a laboratory and field tracer experiment respectively, solely by invoking the EK contribution. In both cases, the EED potential component was believed to be underestimated. In the former study they found they had to apply a multiplication factor to their dispersion coefficient of 100 times to obtain the correct magnitude of the SP, in the latter, they arbitrarily applied a multiplication factor of 7 in order to obtain the correct magnitude of SP response to the movement of the saline tracer.

5.5 Tidal SP numerical modelling results

The analysis above suggests that the SP recorded at the coastal site must have an origin related to salinity or pressure gradients within the aquifer. Furthermore, the weight of evidence from examination of the periodicity of the signal (section 5.4.2.2) appears to rule out a purely EK source mechanism. Numerical modelling was used to further investigate this claim, and to assess the relative contribution of the EK and EED potentials to the tidal SP signal at the coast. To reiterate, the primary aim was not to accurately match the SP field data but to investigate the processes and mechanisms that lead to the generation of the SP at the coastal site. Note that in this section the field and simulated data were normalised by subtracting the initial value of each time-series from the remainder of the time-series in order to allow a direct comparison between the simulated and observed data.

5.5.1 Simulated hydrodynamic and electrodynamic results

The model used to generate the following results was model 3 (Table 4.3). The model properties were varied iteratively in order to obtain these results; model 3(b) without the adit provided the closest match to the field data and is discussed first. The impact of the adit is discussed in section 5.6.2. Note that because the permeability structure at depth exponentially decreased in this model, the salinity was only c.4 m from the base of the borehole (Figure 6.27). Note also that the fracture had to be present within the model to provide an SP response of the same order of magnitude as the field data.

Figure 5.20 shows the modelled head and conductivity fluctuations against the normalised observed head fluctuations for the period from the 28th July 2013 for 2 days. Note that both data-sets are taken at the approximate time of high water levels caused by a spring tide. The modelled head fluctuations provide a reasonable fit to the observed fluctuations (Figure 5.20(a)). Note that the head and conductivity fluctuations in the field include a contribution from pumping at the Balsdean abstraction borehole. Pumping was not included in the models, explaining the slight discrepancy in the shape of the tidal response between the observed and simulated head and conductivity. The simulated conductivity fluctuations are similar to the fluctuations observed in the field (Figure 5.20(c)); however, the magnitude of conductivity in the model was slightly lower (Figure 5.20(b)). A possible explanation for this was the lack of diffusion in the model. Some of the saline water may diffuse into the matrix around the vicinity of the borehole during periods of low inland head when the saline front

is nearer the borehole. This would then raise the background conductivity in the vicinity of the borehole and result in higher baseline conductivity in the borehole itself.

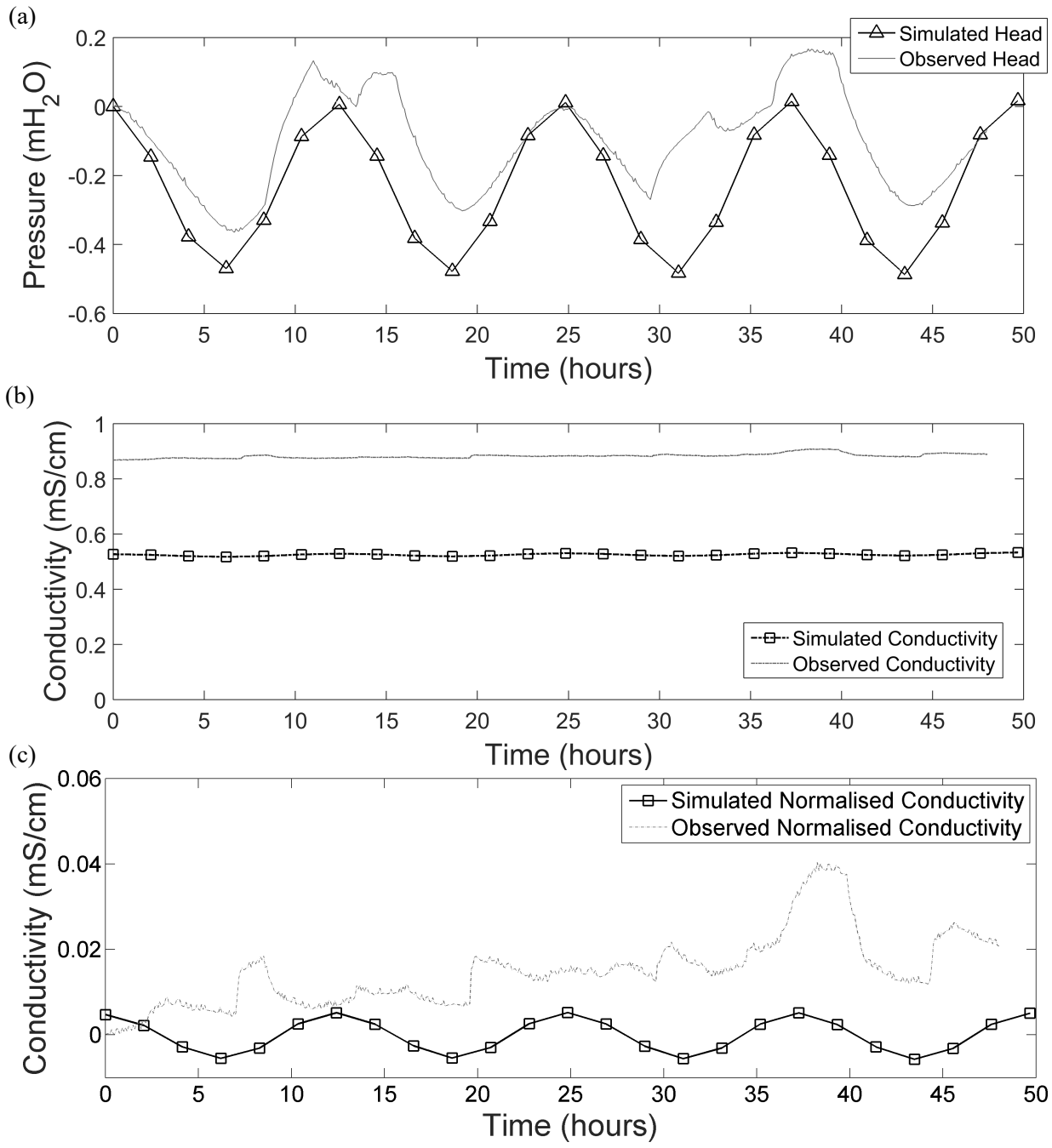

Figure 5.20 – (a) Simulated head versus observed head. The heads are normalised by subtracting the initial value from each data-set from the remainder of the time-series. (b) Simulated conductivity versus observed conductivity. (c) The normalised conductivity fluctuations are approximately the same magnitude.

Figure 5.21(a) shows the modelled and observed total SP. For all the simulation results the voltages are presented with reference to a position in the top of the borehole which is equivalent to the referencing scheme adopted at the coastal site where the shallowest borehole electrode was used. The model replicates the magnitude of the periodic SP signals observed in the field reasonably well

(Figure 5.20 – Figure 5.21). Most importantly the total SP from the model is anti-correlated with head (Figure 5.22) which is consistent with the field observations (Figure 5.18).

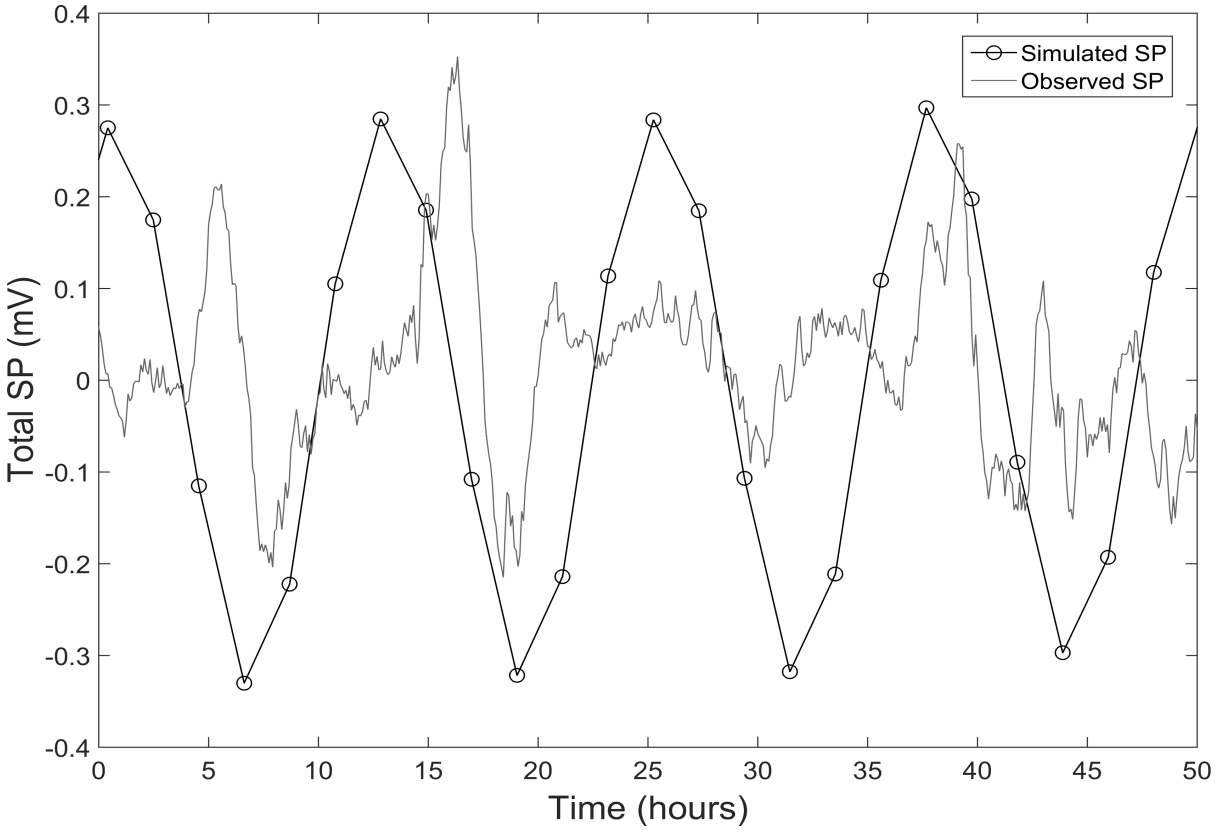

Figure 5.21 – Simulated SP against the observed SP (smoothed using a second order SG filter) for two days. The data in the borehole at the coastal site was very noisy explaining the slight mismatch between observed and simulated SP. The mean difference between the simulated and observed SP was 0.0322 mV over a spring neap tidal cycle, which suggests a good model fit to the observed data.

5.5.2 EK component of the electrodynamic model

The numerical model allowed the EK and EED component to be independently assessed. Figure 5.22 shows the simulated EK contribution to the tidal SP from model 3(b). The EK contributes only c.20 μV to the total observed SP. Note that the EK component was also slightly out of phase with the head fluctuations, which was not observed in the measured data from the coastal aquifer (Figure 5.15).

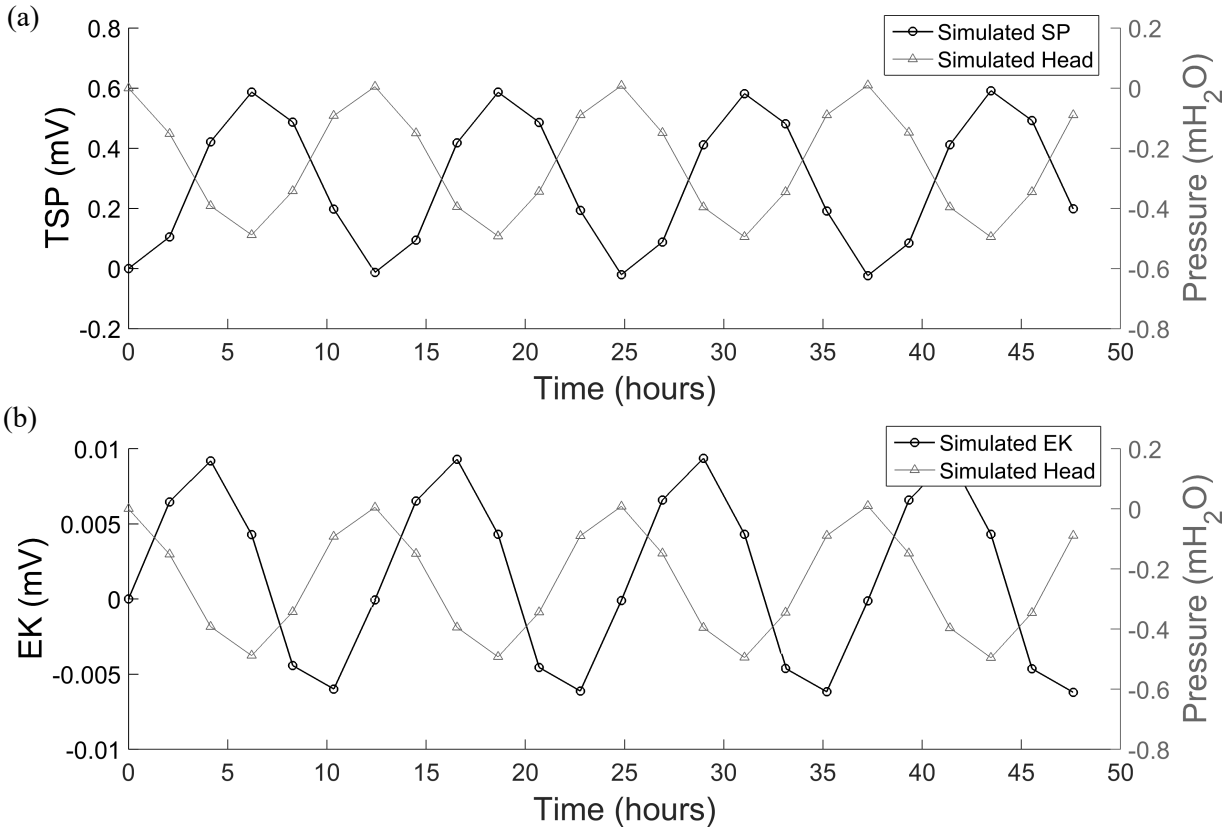

Figure 5.22 – (a) Total SP (TSP) and head fluctuations. (b) EK contribution to the total SP and head fluctuations.

5.5.3 EED component of the electrodynamic model

Figure 5.23 shows the simulated EED contribution to tidal SP for model 3(b). The EED potential was the dominant component of the SP signal with a magnitude of c.600 μV. Since the EED was anti-correlated with head, the total SP was also anti-correlated with head which was consistent with observations (Figure 5.18).

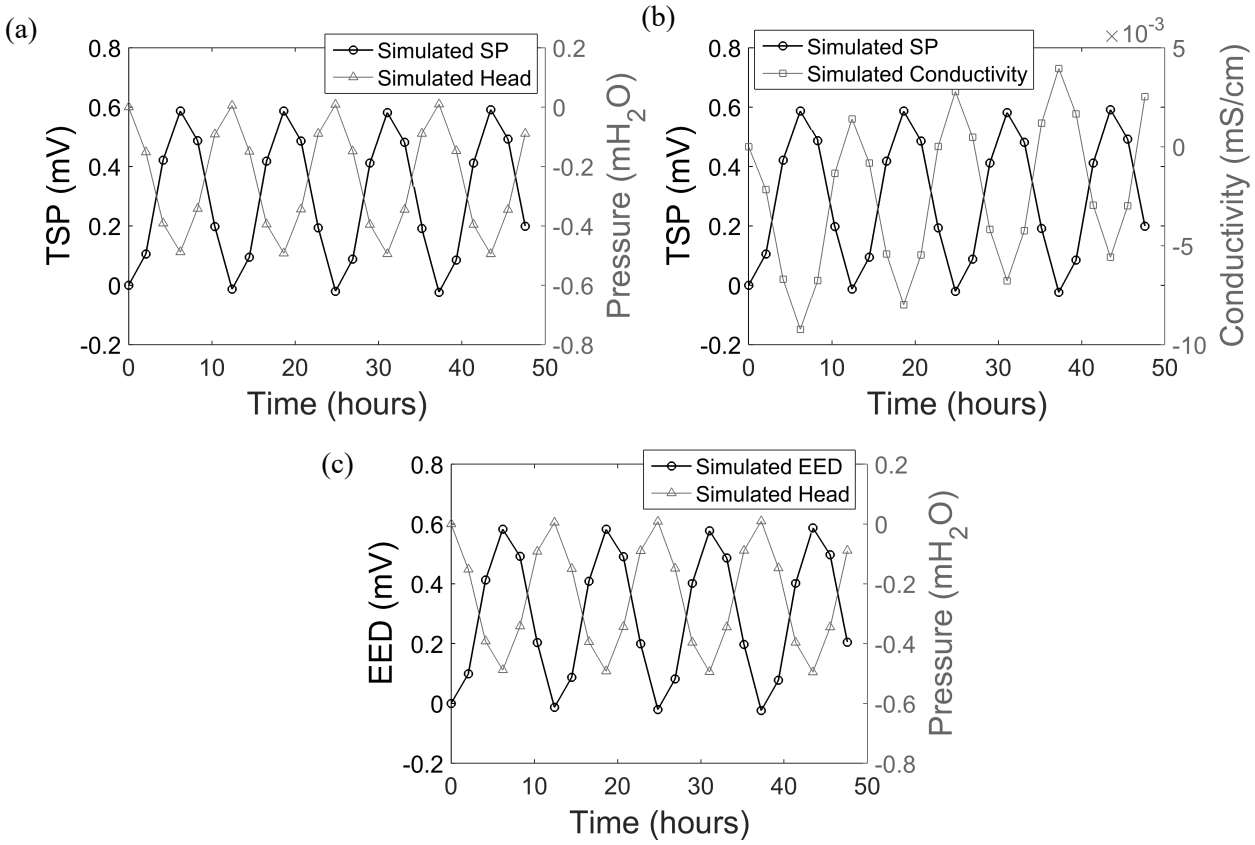

Figure 5.23 – (a) Total SP (TSP) and head fluctuations. (b) Total SP and conductivity. (c) EED contribution to the total SP.

5.5.4 Impact of permeability structure at depth

A simple sensitivity analysis of the SP results was conducted by examining the effect of the permeability structure at depth. The analysis is discussed in more detail in chapter 6 with regards to the vertical gradient that was observed in the SP data. However, a brief analysis of the effect of the permeability structure at depth is included here in order to assess its impact on the periodic SP. Model 2(b), without an adit (Table 4.3), had a higher base permeability and higher inland head boundary during the development of the steady state saline wedge. These properties resulted in a much steeper saline front which was also much further from the base of the borehole (Figure 6.30(b)). Figure 5.24 shows the total SP and the EK and EED contributions for model 2(b). The EED component was marginally smaller in model 2(b), c.500 µV compared to c.600 µV in model 3(b) (Figure 5.23). The slight decrease in the EED can be explained by the fact that the salinity front, in the matrix, was further from the base of the monitoring borehole (c.40 m, Figure 6.30(b)) and the more mobile part of the saline front, in the fracture, was more distant from the borehole (> 200 m) than in model 3(b). The

latter was indicated by smaller conductivity fluctuations at the borehole in model 2(b) (Figure 5.24(b)). The magnitude of the EK contribution was comparable between model 2(b) and 3(b).

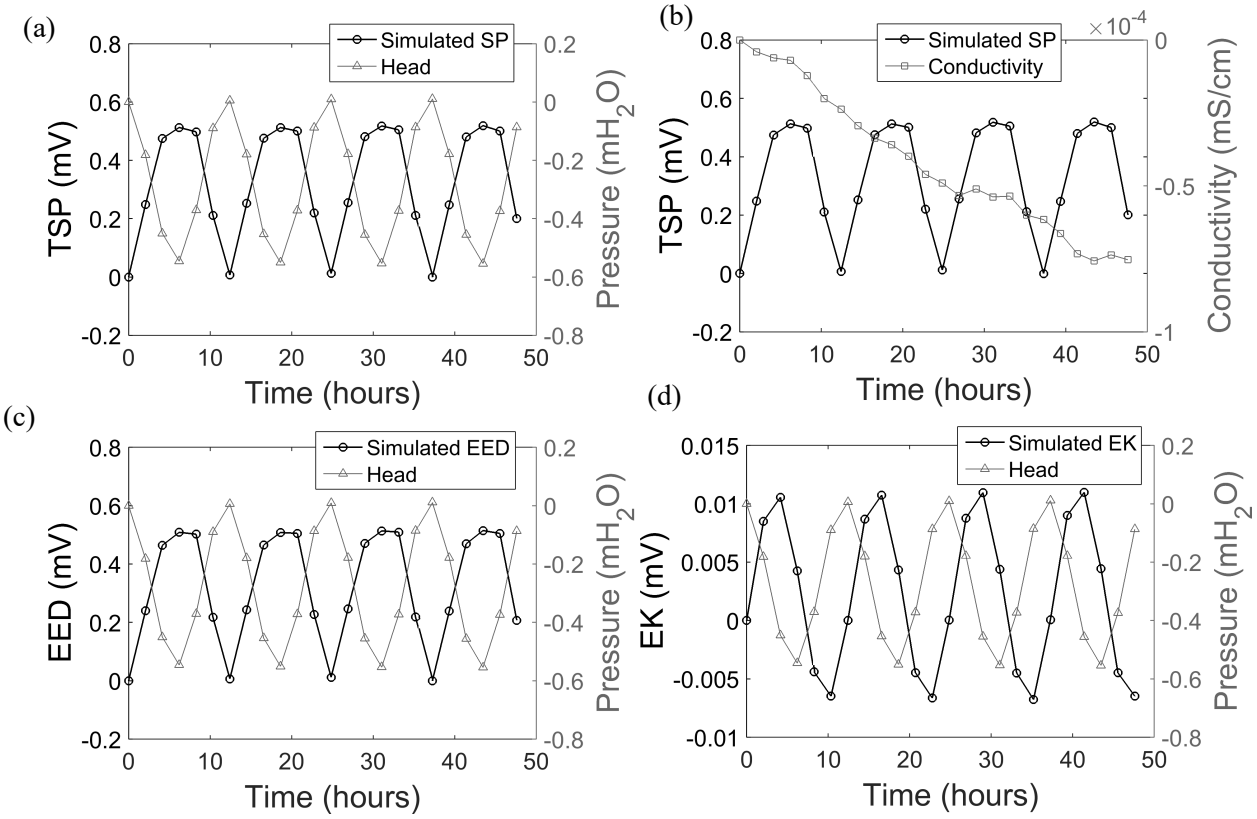

Figure 5.24 – Sensitivity of the simulated SP results to the permeability structure at depth. (a) TSP and head fluctuations. (b) TSP and conductivity. (c) EED and head fluctuations. (d) EK and head fluctuations.

In general the tidal signature, at least, did not appear to be significantly influenced by the permeability structure at depth and the impact this had on the proximity of the front to the observation borehole. Rather, it seems that the lateral movement of the seawater through the fracture controls the magnitude of the dominant EED component. However, the permeability structure at depth did have a significant impact on the observed vertical SP gradient, which is discussed in section 6.4 and section 6.5.1.

5.6 Discussion of the tidal SP simulations

The SP modelling results provide insight into the possible mechanisms that lead to the generation of the periodic SP at the coastal site. The modelling results support the assertion (in section 5.4.2) that EK is not the sole mechanism generating the observed tidal SP; rather, there is an important, and potentially dominant, contribution from the EED component.

5.6.1 The relative contribution of EK and EED components

5.6.1.1 Contribution of the EK potential

Examination of a cross-plot of the EK against the head fluctuations for model 3(b) (Figure 5.25) revealed that the relationship was non-linear and that the interpreted coupling coefficient was two orders of magnitude smaller than the GW coupling coefficient measured in the laboratory (Table 3.6). There are two possible reasons; the first is that saline water was actually very close to the monitoring position; thus, the EK coupling coefficient may have been smaller due to the compression of the EDL (Figure 3.9), resulting in a very small EK response. Secondly, the voltage component was obtained, as in the field, by referencing the measurements to an electrode in the top of the borehole; therefore, it was the difference between the SP measured in the top and the bottom of the borehole. In order to obtain the coupling coefficient the difference between the pressures at these two electrodes must be used; this was not possible in the field, despite having measurements of pressure at these two locations, because the depths were deduced from the pressure measurements and so included the hydrostatic pressure. As a result, there was no independent measurement of the depth at the electrodes accurate enough to deduce the difference in pressure above hydrostatic (only 1 cm in Figure 5.25(b) whereas the electrode position was within ± 10 cm at best). However, when the difference between the pressures at the two electrode locations in the model were accounted for the coupling coefficient was within the range for chalk reported in the chapter 3.

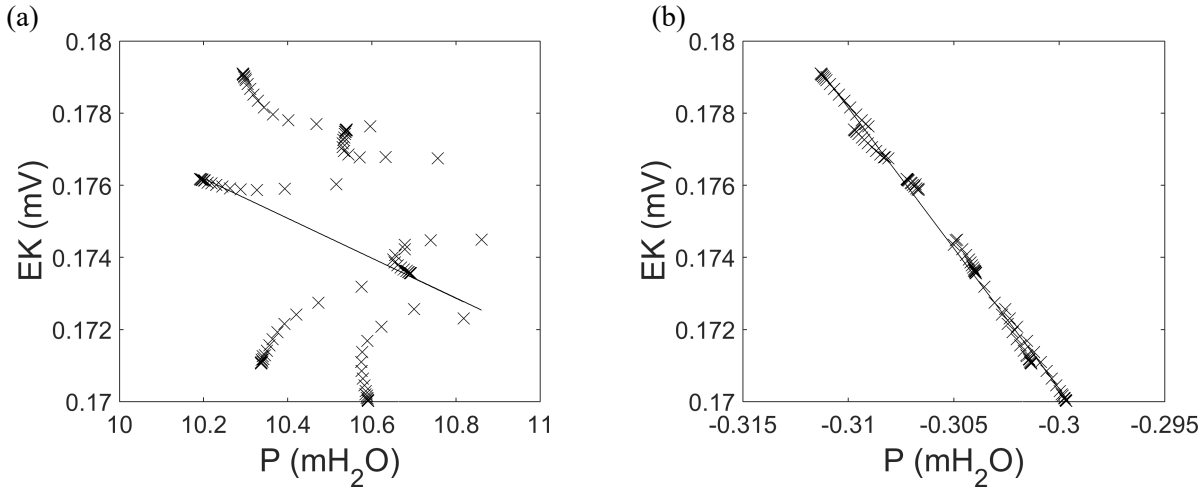

Figure 5.25 – (a) Cross-plot of the EK versus total change in pressure; the regression yields a coupling coefficient of -0.0055 mV/mH_2O. (b) Cross-plot of the EK versus the difference in pressure between the reference position at the top of the borehole and the bottom of the borehole, equivalent to how the voltages were obtained. The relationship is linear with a coupling coefficient of, -0.779 mV/mH_2O, consistent with the laboratory measured coupling coefficient.

There is not a linear relationship between the total change in pressure shown in Figure 5.25(a) and the EK, because the EK was slightly out of phase with the head fluctuations (Figure 5.22). On the other hand, when the coupling coefficient was obtained using the difference in pressure between the two electrode locations (Figure 5.25(b)), the regression shown yields a value for the coupling coefficient that is greater than the laboratory measured coupling coefficient (-0.575 ± 0.08 mV/mH_2O). The larger coupling coefficient may be related to the dimensionality of the problem and the spreading of the current through the two dimensional medium (Revil and Linde, 2011). Therefore, as previously suggested by Revil and Linde (2011) the use of the equation $C_{EK} = \frac{\Delta V}{\Delta P}$ is restricted to the one dimensional problem and may not be appropriate when using the borehole referencing scheme. Thus, the coupling coefficient in Figure 5.25(b) is an apparent coupling coefficient.

The results shown in Figure 5.25 imply that unless the estimate of EK, based on the laboratory measured coupling coefficient (-0.575 ± 0.08 mV/mH_2O), uses the pressure difference between the locations of the two electrodes in the dipole of interest (i.e. c.24 m in the borehole array), then the EK component is likely to be overestimated. As a result, the change in pressure measured in the field (c.0.5 m) may actually yield a much smaller EK component than previously estimated (section 5.4.2.2) further indicating that EK is unlikely to be the sole contribution to the tidal SP.

The modelling results suggest that the EK potential responds primarily to local pressure changes near the borehole (Figure 5.25), including changes in the vertical pressure gradient (see section 6.5.1); thus, it is only of limited value for the spatial warning of an intruding saline front that is of primary interest to water resource managers. In contrast, Saunders et al. (2008), Jackson et al. (2011), Gulamali et al. (2011), Saunders et al. (2012) and Jackson et al. (2012b) all found that the EK contributed significantly to the total change in SP measured at an abstraction borehole tens to hundreds of metres away from an advancing saturation front in oil reservoir monitoring.

5.6.1.2 Contribution of the EED potential

Before discussing the EED potential results it must be pointed out that some uncertainty remains with regards to the results from this component of the model. The results shown above were all obtained using the MATLAB implementation of the minimum residual (MINRES) solver (Barrett et al., 1994,

Van der Vorst, 2003) and used a tolerance of 10^{-5}. However, when the tolerance was lowered to 10^{-7} the EED component became negligible (Figure 5.26). The solver reported convergence at each of these tolerances, however when the tolerance was lowered further (10^{-8}) the solver stagnated. The problem was not encountered when solving for the EK component.

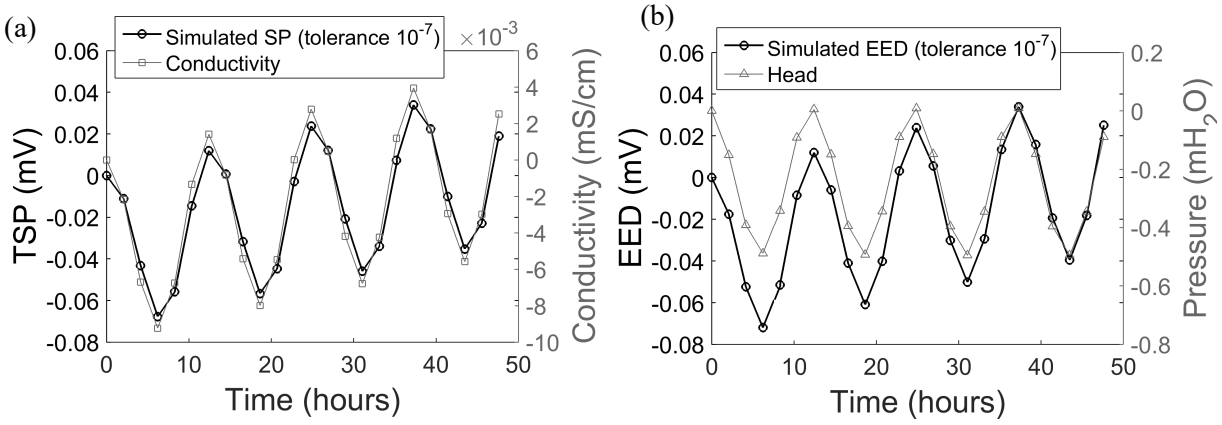

Figure 5.26 – EED simulation runs with 10^{-7} tolerance. (a) and (b) show the simulated TSP and EED for model 3(b) against conductivity and head respectively.

When the solver tolerance of 10^{-7} was used the EED component had the wrong magnitude and polarity, resulting in tidal SP that was correlated and not anti-correlated with head. It appears that when the lower tolerance was used the EED component simply followed the change in conductivity in the borehole (Figure 5.26(a) & (c)). The issues related to the choice of tolerance are discussed further in section 6.5.4.

However, when using a solver tolerance of 10^{-5} the EED contribution was c.600 μV (Figure 5.23) compared to the c.20 μV contribution of EK (Figure 5.22). The movement of the saline front through the fracture, some distance (c.200 m) from the monitoring borehole, driven by the tide and superimposed on smaller tidal fluctuations of the front within the matrix (c.4 m from the base of the borehole), provided the source for the EED potential. Thus, it appears that the periodic SP measured in the borehole responded to the movement of the front across a tidal cycle towards the borehole.

Regardless of the uncertainties related to the EED results, the evidence provided by the EK simulations alone (Figure 5.22) point to the EED component as being the primary source mechanism for the generation of the total tidal SP observed in the field. The dominance of the EED component (Figure 5.23) is backed by evidence in the literature. For example, both Gulamali et al. (2011) and

Jackson et al. (2012b) demonstrated that the EED component may actually be dominant in oil fields when an intruding saturation front has a significantly lower concentration (0.5 M) than the formation water already present in the reservoir (5 M). Furthermore, the importance of the EED potential is consistent with the findings of other studies in more similar sub-surface environments and has been demonstrated in both laboratory sand tank experiments (Maineult et al., 2004, Martinez-Pagan et al., 2010, Ikard et al., 2012) and field tracer experiments (Sandberg et al., 2002, Jougnot et al., 2015). Ikard et al. (2012) modelled a laboratory sand tank experiment where a saline plume was introduced into sand saturated with freshwater. They separated the EED contribution from the EK contribution numerically, demonstrating that the EED contributed approximately the same order of magnitude as the EK (Ikard et al., 2012). Jougnot et al. (2015) conducted a field tracer experiment in the unsaturated zone and calculated the EED and EK contribution using numerical models and demonstrated that the EED component was dominant, although they introduced a far larger concentration gradient than exists between seawater and fresh groundwater by injecting brine with a conductivity of c.230 mS/cm; which is approximately 5 M NaCl (Table 3.5) and was similar to the largest concentration gradient investigated in the laboratory experiments which showed a diffusion end member twice that of the SW/GW gradient (Table 3.7). These latter studies prove along with this work that in areas with a significant concentration gradient induced or naturally present the EED component cannot be neglected as it was by Revil (2005), Bolève et al. (2011) and Kang et al. (2014), and may in fact be dominant.

Measurements of SP in fractured media were discussed in section 2.3.6.3, and the results reported above suggest that the tidal SP signal was primarily controlled by the presence of the fracture, because the fracture zone had to be present in model 3(b) in order for the total SP to have a magnitude similar to that observed (section 5.6.1). In fact, the enhancement of the SP signal in fractures is consistent with previous studies. For example, Gulamali et al. (2011) and Jackson et al. (2012b) showed that the presence of high permeability layers in an oil reservoir enhanced the SP anomaly detected at the abstraction borehole, primarily through an increased EED contribution. Similarly, Jardani et al. (2013) demonstrated that in areas of low permeability the SP was very small. They attributed this to much

smaller concentration gradients in these areas. Multiple studies have demonstrated the utility of the SP method for characterising fracture flow (Hunt, 2000, Suski et al., 2008, Wishart et al., 2008, Robert et al., 2011b), but none have done so in areas where significant concentration gradients exist such as in the Chalk coastal aquifer; thus, the key findings reported in this chapter (i.e. Figure 5.16, Figure 5.18, Figure 5.22 and Figure 5.23) provide the first field evidence, supported by numerical modelling, of the remote detection of a fluctuating salinity front in fractured porous media.

5.6.2 Impact of the adit

As highlighted in section 4.3.1.2 there is anecdotal evidence of the presence of an adit at the top of the Saltdean borehole, results from model 3(c) with the adit included are shown in Figure 5.27. In model 3(c) the total SP was overestimated (Figure 5.27(a)), primarily because of the larger EED contribution (Figure 5.27(e), obtained with a tolerance of 10^{-5}). There was also a larger contribution from EK when the adit was included (c.100 μV in Figure 5.27(c))); however, the EK alone still failed to explain the overall observed SP (c.600 μV). The larger EK contribution was related to vertical flow created by vertical pressure gradients introduced by the adit (more details in section 6.5.1). As a result, when the adit was removed from the model 3(c) the EK voltage fluctuations reduced to c.10 μV (Figure 5.27(d)) despite the much larger head fluctuations (Figure 5.27(d)) of c.1 m (twice the size of the head fluctuations observed at the coastal site (Figure 5.20(a)). Chapter 6 examines the evidence for vertical flow in the borehole, provided by conductivity profiles, in relation to the vertical SP gradient that was observed. It is also worth noting, that because the borehole was not explicitly included within the hydrodynamic model (section 4.3.1), the pressure gradients required to force water through the bulk rock, were likely to be significantly larger than the actual pressure gradients that are required to generate vertical flow in the borehole in reality. Therefore, the EK component was likely to be substantially overestimated in model 3(c).

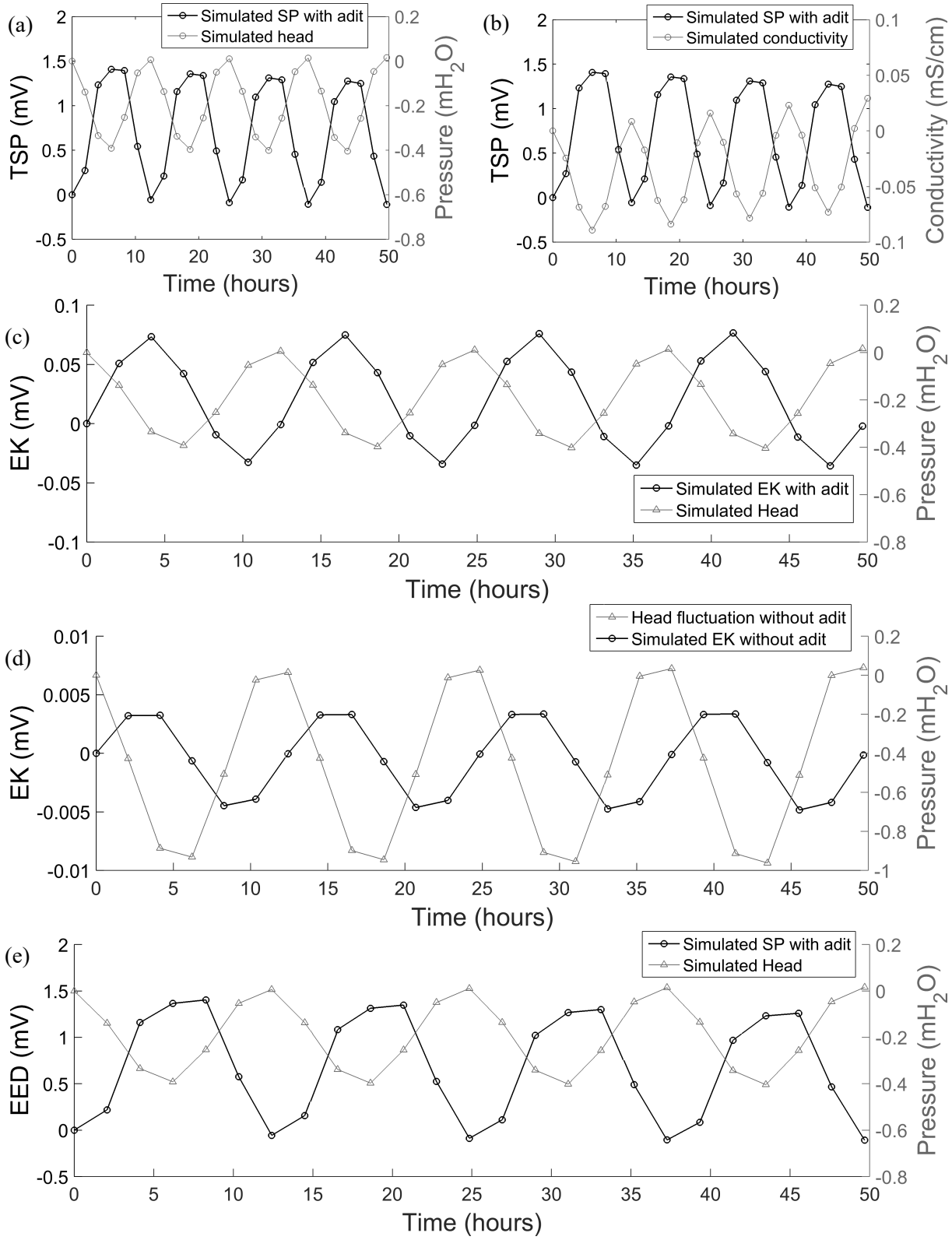

Figure 5.27 - (a) Total SP (TSP) and head fluctuations with the adit included and higher bulk permeability. (b) Total SP (TSP) and conductivity with adit. (c) EK contribution to the total SP and head fluctuations with the adit. (d) EK and head fluctuations without the adit but with the same bulk permeability as model 3(c) in (c). (e) EED contribution to the total SP with the adit (obtained with a tolerance of 10^{-5}).

In order for the EK alone to be able to explain the observed SP the head fluctuations would have to be significantly larger than the c.1 m in Figure 5.27(d). The modelling results suggest that the EK component would have to be four to five times larger than the maximum contribution modelled with the adit (Figure 5.27(c)). Such large head fluctuations so far inland are difficult to justify and would require bulk rock permeabilities far beyond the range found in the literature. Therefore, it is very difficult to invoke the EK as the sole source of the tidal SP even when the adit is included. Note, that a straight forward, but erroneous (section 5.6.1.1), estimate of the EK component using a 1 m head fluctuation and the GW coupling coefficient measured in the laboratory (Table 3.6) would suggest that EK could, in fact, explain the semi-diurnal SP component entirely, (-575 $\mu V/mH_2O$ x 1 m = 0.575 mV) illustrating the danger of over estimating the EK contribution with a simplistic application of the laboratory measured coupling coefficient.

The conductivity fluctuations were much larger in model 3(c) (Figure 5.27) than in model 3(b) (Figure 5.23) because of the higher permeability in both the fracture (x4) and the matrix (x10), which were required to match the observed head fluctuations, and allowed the saline front to propagate inland much more quickly. As a result, the presence of the adit resulted in an SP that was overestimated relative to the field observations primarily due to an enhanced EED component (1.5 mV). In order to better match the field data using model 3(c) in which the adit was included further model calibration would be required. However, in both cases, i.e. with (Figure 5.27) and without the adit (Figure 5.23), the EED component (obtained using a tolerance of 10^{-5}) was one order of magnitude larger than the EK component, strongly suggesting that the EED component must be dominant in the coastal aquifer.

5.7 Conclusions

At the coastal site all of the main diurnal and semi-diurnal tidal constituents were present in the borehole referenced SP data, providing evidence that the signal responds to ocean tidal effects in the aquifer. However, the main M_2 component was also observed at the inland site, but was less significant than the S_1 component which was driven by the diurnal temperature cycle. The analysis suggested that M_2 at the inland site, and in surface referenced SP, is likely to be influenced by a

combination of Earth, atmospheric and geomagnetic tides. However, when the inland borehole referenced data was examined the M_2 signal was below the 50% PSD significance level. Critically, in the coastal borehole the M_2 signal was at least two orders of magnitude larger and was significantly above the 99.9% significance level (Figure 5.16). Furthermore, the M_2 signal was always dominant at the coastal site, but in some cases was completely absent in the inland SP data. Therefore, the coastal SP signals must be driven by ocean tidal process in the aquifer.

Having established that the periodic SP observed at the coastal site was primarily driven by the EK and/or EED potential the relative importance of each of these contributions was assessed, using both field data and numerical modelling. The field data clearly suggested that EK could not be the primary source mechanism. More importantly, the numerical modelling results showed that the maximum plausible contribution from the EK component under the scenarios tested was c.20 μV, which was one order of magnitude lower than the observed SP (c.600 μV). Despite the problems with the EED solver, the modelling results suggest that the EED potential must be the dominant component of the tidal SP in the coastal aquifer. The results imply that the coastal periodic SP primarily arose as a result of the movement of a saline front through a fracture some distance from the borehole. They also indicate that borehole SP measurements can be used to characterise flow regimes in coastal aquifers and confirm that SP can be used to remotely monitor seawater intrusion.

Chapter 6

Spatial and transient SP from long-term seawater intrusion monitoring in the coastal Chalk aquifer

6.1 Introduction

This chapter reports results from the long-term monitoring program at the Saltdean coastal site (Figure 4.3) and focusses on spatial and transient effects within the SP data. The broad aims of the field and numerical modelling were set out in section 4.1. However, the specific aim of the analysis reported below was to determine whether long-term measurements of SP in the Saltdean borehole could be used to provide spatial and temporal warning of the movement of a saline front towards a monitoring borehole. The main objectives were: (i) to make long-term measurements of the SP and hydrodynamic process in the coastal aquifer, (ii) determine whether there were any systematic spatial patterns within the SP data (iii) determine whether there were any temporal or transient SP effects that indicated the movement of the saline front towards the coastal monitoring borehole and (iv) use numerical models to determine the main SP source mechanism for the spatial and transient SP signals observed. Section 6.2 reports the hydrodynamic results from the coastal monitoring borehole and discusses implications for flow and SP in the coastal aquifer in the Saltdean area. Sections 6.3 – 6.5 report and discuss the results of the long-term SP monitoring program and the results of the numerical models used to investigate the SP source mechanisms.

6.2 Borehole and aquifer dynamics in the coastal UK Chalk aquifer

6.2.1 Head and salinity patterns in the Saltdean coastal monitoring borehole

Borehole SP monitoring was conducted over a year and a half from May 2013. Thus, in addition to the tidal effects discussed in chapter 5, longer term seasonal, spatial, temporal and transient effects were captured. The general conceptualisation of groundwater flow in the South Downs was discussed in section 2.2.3.2 (Figure 2.7), including the influence of seasonal changes in inland head on seawater intrusion in the area. In this section the seasonal hydrodynamic processes observed in the Saltdean borehole are reported and discussed, and a conceptual model for groundwater flow in and around the

coastal borehole is presented. To begin, the head and the tidal level above ordinance datum (mAOD) for the full duration of the experiment are shown in Figure 6.1. Figure 4.3 shows the location of the Newhaven tidal gauge in relation to the Saltdean borehole.

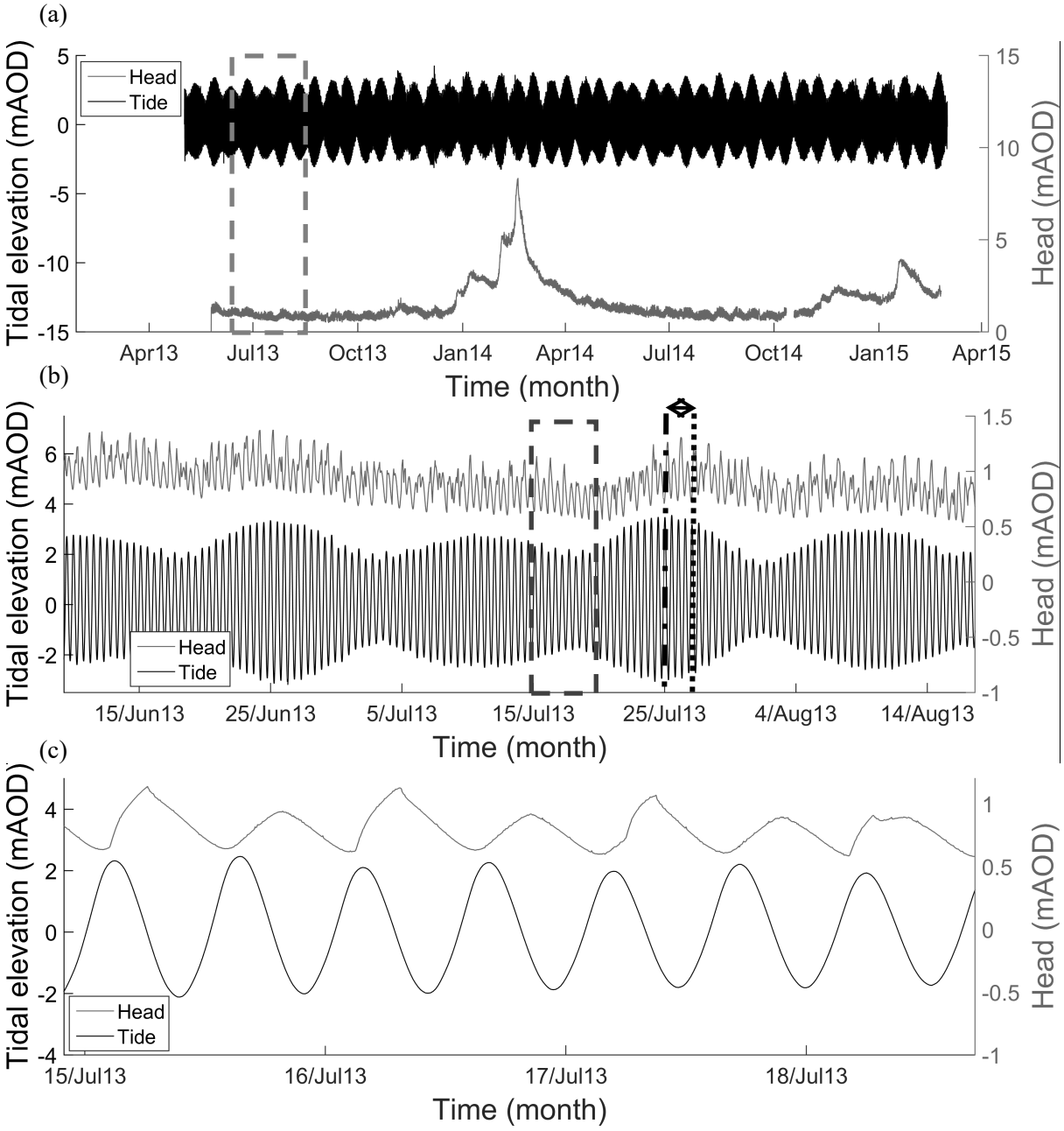

Figure 6.1 – (a) Tidal levels at Newhaven and groundwater levels in the Saltdean borehole for the duration of the monitoring experiment. The grey dashed box highlights the origin of the data shown in (b) which illustrates the spring and neap tides in the water level data. Also shown is the delay between the spring tide at Newhaven and the peak water level at Saltdean, illustrated by the difference between the dot-dashed line and the dashed line. (c) Data from the 15th to the 18th July 2013 showing the tides and head data.

During 2013 and 2014 there was a clear decline in head within the borehole throughout the summer, and into late autumn, before the groundwater heads started to recover with the onset of winter. In winter 2013/2014, the head rose dramatically due to very high rainfall in January. In fact,

groundwater levels in the borehole increased by about 9 m, but quickly returned to levels less than 2 mAOD. A similar, but less dramatic, increase in head was observed in winter 2014/2015, and the fall in head after the winter recharge events occurred again. As discussed in section 5.3.2 there was a 6.21 hour phase lag between the voltage and head. Similarly, the phase lag between the head in the Saltdean borehole and the tide at Newhaven was approximately 3.7 hours, explaining why the tide and head appear almost anti-correlated (Figure 6.1(c)). The lag, determined via DFT (section 5.2), was a result of the delay of the tidal pressure wave propagating inland. There was a clear correlation between the spring and neap tides and the water levels, but the peak water level over the spring/neap cycle in the borehole was delayed by a few days compared to the spring tide at Newhaven (i.e. the difference between the dotted and dot-dashed line in Figure 6.1(b)).

The rainfall data for the monitoring period is shown in Figure 6.2. The increase in head was clearly correlated with very high rainfall in winter 2013/2014, although there appeared to be a slight delay between maximum rainfall and the peak in the head data. The delay may be due to temporary storage of the infiltrating rainfall in weathered chalk near the surface which attenuates rainfall infiltration rates and allows the bulk of the recharge flow to be accommodated in the matrix (Butler et al., 2012). The slow decline in head over the summer months was due to high levels of evaporation and low levels of net rainfall resulting in inadequate recharge (Jackson and Rushton, 1987, Rushton, 2005).

The pumping signature from the Balsdean abstraction borehole was also apparent in the Saltdean borehole records. Figure 6.3 shows clear correlations between water level and pumping in mid-September 2013 when the pump was switched on and off at the Balsdean abstraction borehole over a period of about 12 hours. The drawdown and recovery, of c.0.1 m (dashed box in Figure 6.3), at the Saltdean borehole lagged the onset of pumping at Balsdean by 2-3 hours. However, it is clear that the dominant control on the head fluctuations was the tidal signature, of c.0.5 m (dotted box in Figure 6.3, also see Figure 5.18).

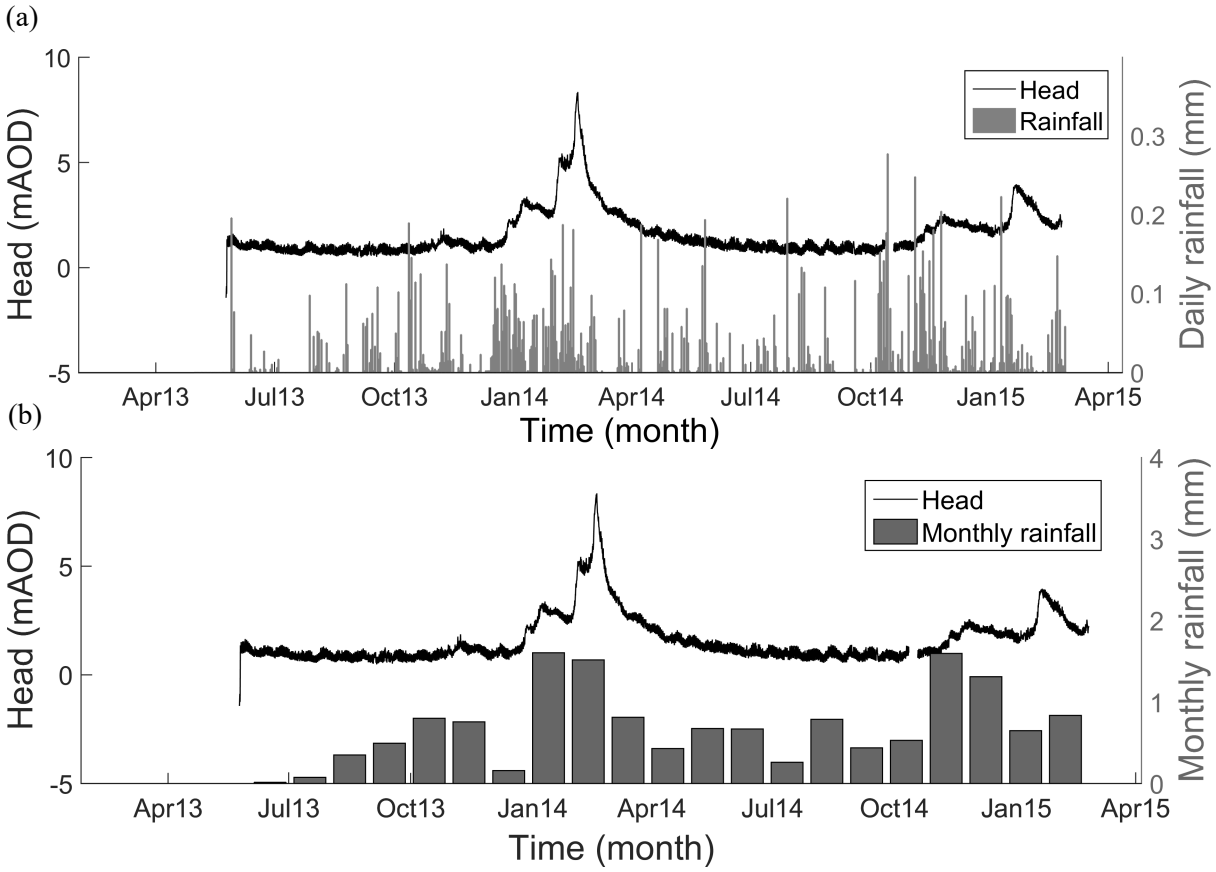

Figure 6.2 – a) Daily rainfall and head; b) Monthly cumulative rainfall and head. The rainfall was measured 12 km away at the Ditching Road rainfall gauge in North Brighton, the nearest to the site (Figure 4.3).

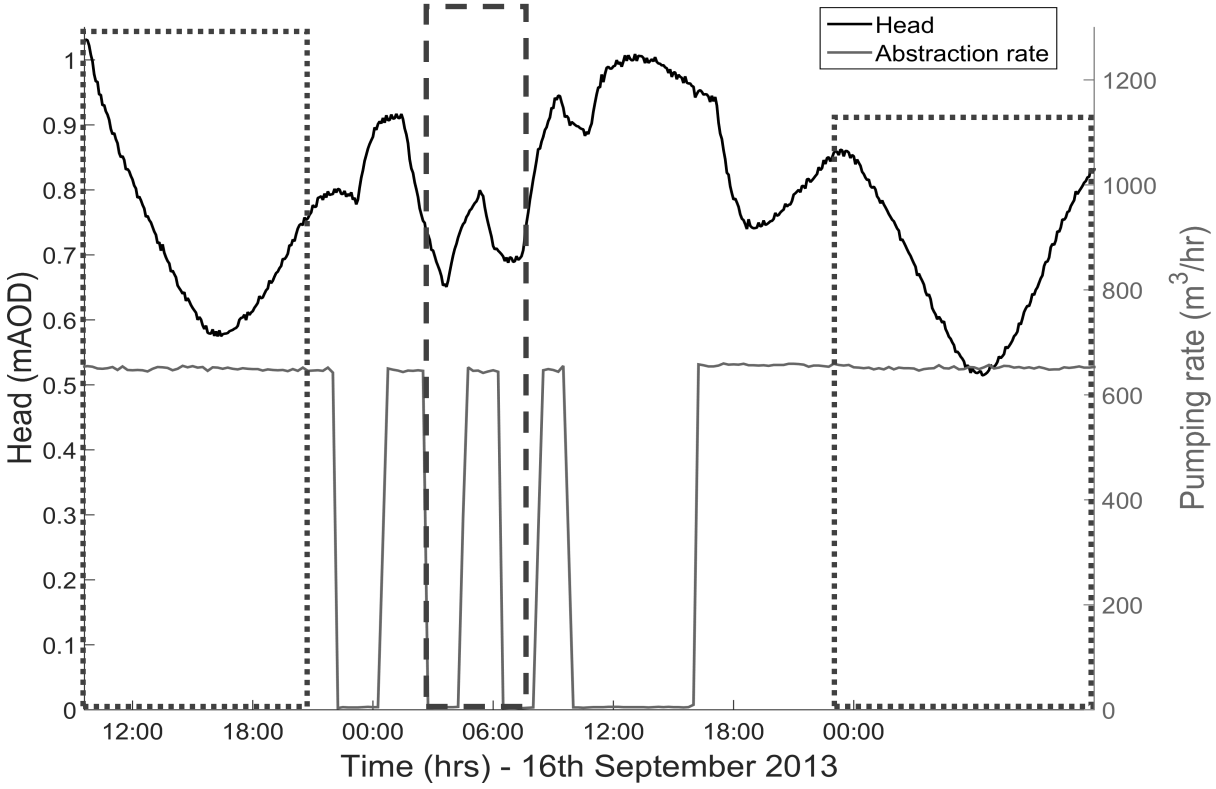

Figure 6.3 – Pumping rate at the Balsdean abstraction borehole and the corresponding water level at the Saltdean observation borehole. Notice in the area highlighted by the dashed box that between 00:00 and 06.00 there was a sudden increase in the water level at Saltdean that appears to be related to the pump switching off. Just after 00.00 the pump then switched on again and the water levels fell. The dotted boxes show tidally driven head changes.

Figure 6.4 shows head and conductivity for the duration of the monitoring experiment. There were two periods of saline breakthrough in the monitoring borehole (breakthrough is defined here as an increase in the background salinity in the borehole to greater than 1000 mg/l or 1,430 µS/cm), both occurred around the autumn equinox. In both cases, it was apparent that a gradual decline in head preceded the breakthrough of saline water in the borehole. In Figure 6.4 the dashed lines show the period of each of the spring/neap cycles. Changes in conductivity were correlated with the highest water level in the borehole during the spring tide, such as in late August 2013. Smaller changes in conductivity were also observed in July and early August 2013 when small deviations from the baseline conductivity occurred.

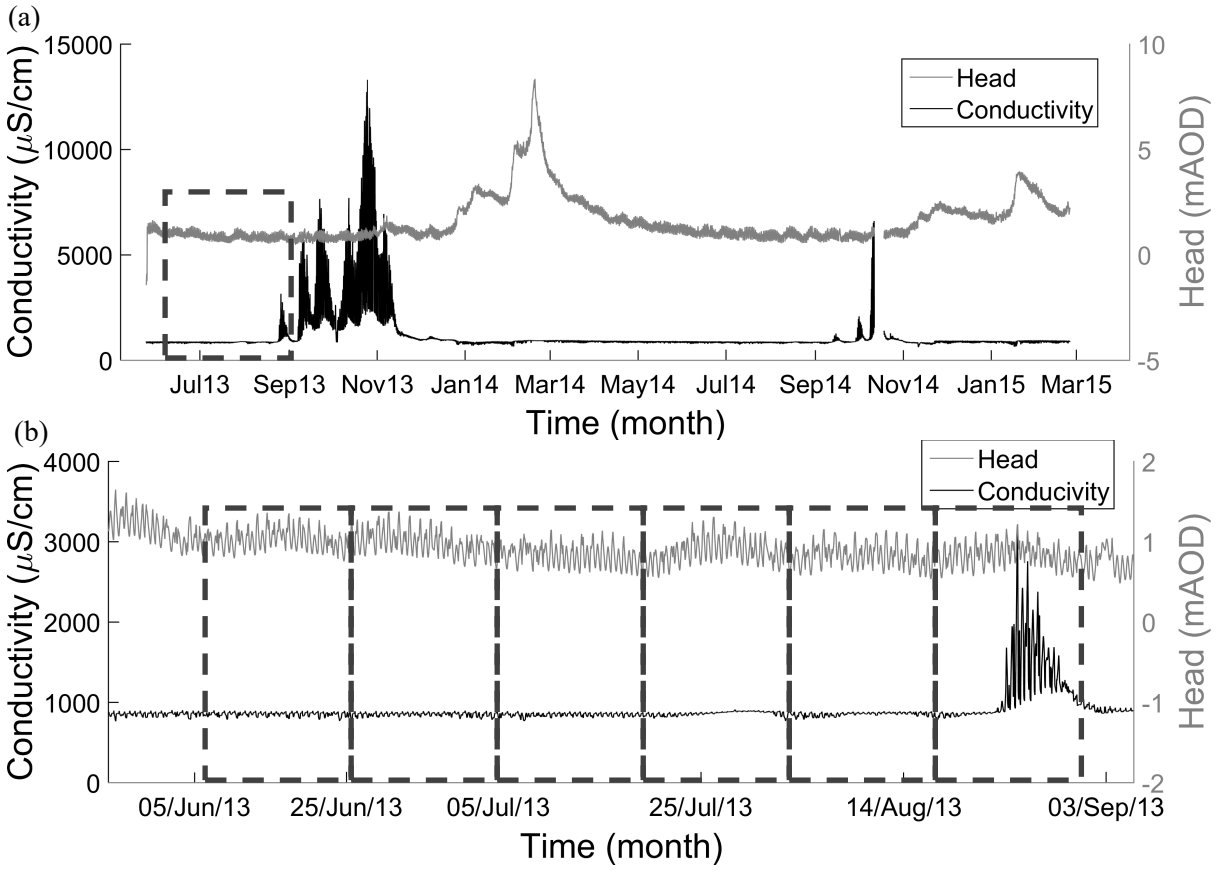

Figure 6.4 – (a) Head and conductivity data from the Saltdean borehole for the duration of the monitoring experiment. (b) Head and conductivity data from July to August 2013, showing breakthrough of saline water in the Saltdean borehole and illustrating the influence on the spring and neap tides on the conductivity within the borehole. Note all conductivities are reported in specific conductivity (at 20°C) unless otherwise stated.

Table 6.1 shows a chemical analysis of the water quality in the Saltdean borehole prior to and after saline breakthrough in 2013. Also shown are the ratios Na/Cl and Cl/SO_4, both of which indicate the marine origin of the elevated salinity recorded in the borehole (Bear et al., 1999). Figure 6.5 shows a

piper diagram (Zaporozec, 1972, Hounslow, 1995) which reveals that over a tidal cycle the water in the borehole moved from the baseline level, i.e. groundwater of calcium bicarbonate type (left hand quadrant of the diamond), through mixed type (centre) and then to an increasingly sodium-chloride dominated system (right hand quadrant) (Hounslow, 1995).

Type	Deepest (50 mBGL) Sampled at 12.00 Concentration		Intermediate (40 mBGL) Sampled at 12.07 Concentration		Shallow (31 mBGL) Sampled at 12.13 Concentration		Saltdean Baseline Concentration	
	(mg/l)	(mM/l)	(mg/l)	(mM/l)	(mg/l)	(mM/l)	(mg/l)	(mM/l)
Cl	1512.51	43.00	1187.96	33.00	98.60	3.00	60.726	1.71
NO_3	41.43	0.70	44.98	0.70	50.54	0.80	59.848	0.97
Br	4.74	0.06	3.85	0.05	0.65	0.01	0.222	0.00
SO_4	215.38	2.20	177.25	2.00	42.90	0.40	38.792	0.40
F	<0.03	0.00	0.16	0.01	<0.03	0.00	0.058	0.00
Na	765.00	33.00	622.20	27.00	50.18	2.00	34.10	1.48
Ca	169.32	4.20	165.24	4.12	148.92	3.72	136.00	3.39
K	23.77	0.60	18.97	0.50	2.93	0.07	1.99	0.05
Mg	81.50	3.30	65.99	2.72	7.59	0.31	6.22	0.26
Sr	0.73	0.01	0.64	0.01	0.27	0.00	0.238	0.00
HCO_3	287.09	4.70	304.05	5.07	349.63	5.83	335.61	5.50
TDS (mg/l)		3101.47		2591.29		752.21		673.80
Ionic Strength (mM)		129.01		107.768		46.89		25.94
Conductivity (µS/cm)		4430.67		2591.29		1074.59		962.57
Charge balance error (CBE)		3.4%		2.0%		0.5%		0.9%
Cl/SO_4 ratio		7.02		6.70		2.29		1.56
Na/Cl ratio		0.51		0.52		0.51		0.56
Balsdean (Table 3.1)	**Cl/SO_4**	3.03						
	Na/Cl	0.56						

Table 6.1 – Chemical analysis showing the baseline concentrations measured on 16-7-2014. Also shown are concentrations at different depths below ground level (mBGL) from the period of peak salinity in the borehole measured after saline breakthrough on the 31-10-2013. Conductivities are estimated from TDS. Note that these measurements were made by the Natural History Museum using ICP-AES for anions and IC for cations and no errors were provided.

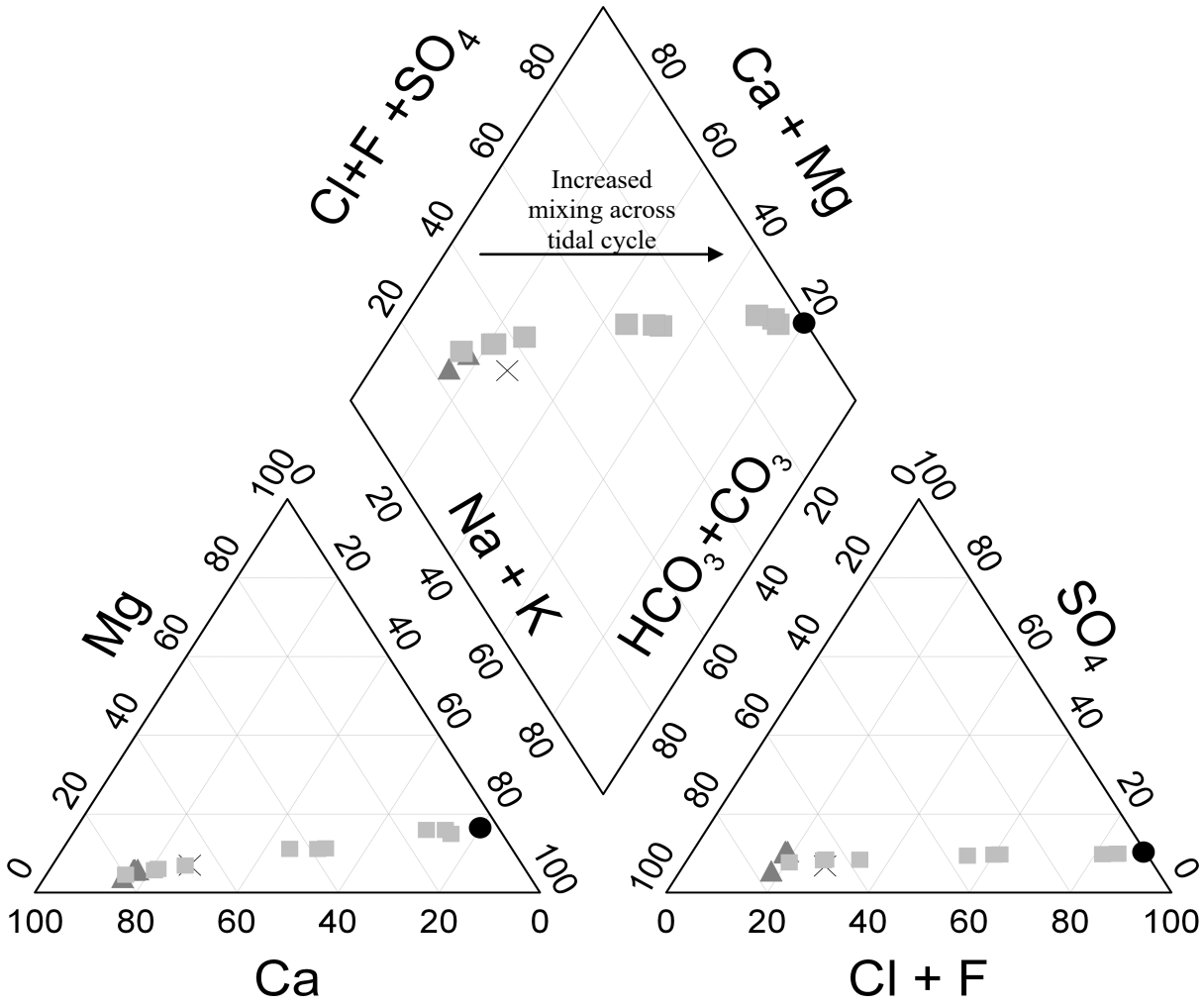

Figure 6.5 - Piper diagram illustrating water quality in the Saltdean borehole. The cross represents the average Balsdean analysis (Table 3.1), the circle represents the average seawater analysis (Table 3.2), the triangle represents the baseline water quality in Saltdean on 16-7-2014 and the squares represent the water quality measured across the tide during peak salinity on 31-10-2014. Adapted from Halford (2005).

Prior to and after saline breakthrough occurred several conductivity profiles were conducted in the Saltdean borehole. Figure 6.6 shows the baseline conductivity in the Saltdean borehole in August 2013 and the baseline conductivity measured in the Balsdean OBH (Figure 4.3) in November 2015. Data from the conductivity profiles over a neap tide in 2013 are shown in Figure 6.7. Figure 6.8 and Figure 6.9 show conductivity profiles over the spring tide during intermediate and peak conductivities in 2013 and Figure 6.10 shows conductivity profiled over a spring tide in October 2014.

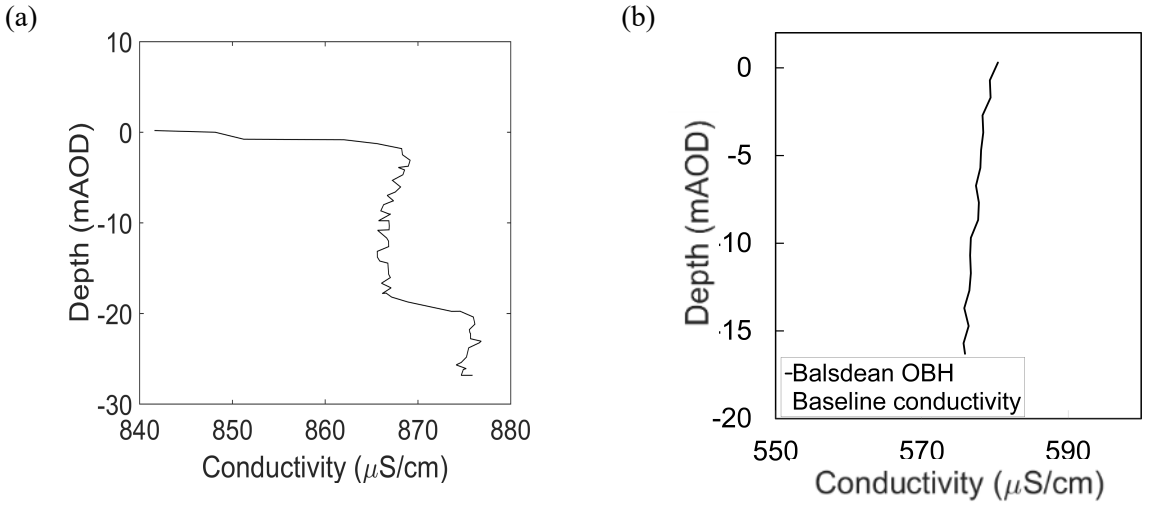

Figure 6.6 – (a) Baseline conductivity in the Saltdean borehole on the 8th August 2013. (b) Baseline conductivity in the Balsdean OBH (Figure 4.3) on the 15th November 2015.

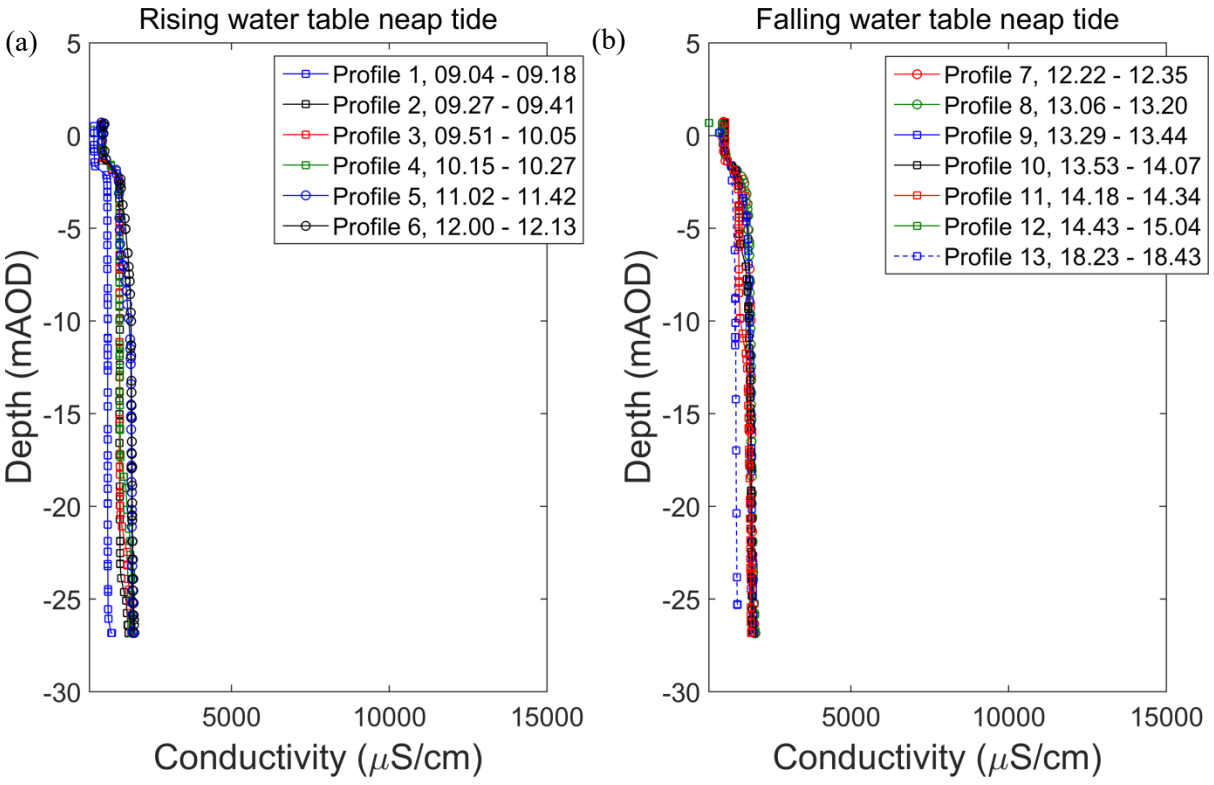

Figure 6.7 – (a) Conductivity profiles from a neap tide over a rising water table on the 2nd October 2013 after saline breakthrough. (b) Conductivity profiles during falling water tables on the 2nd October 2013.

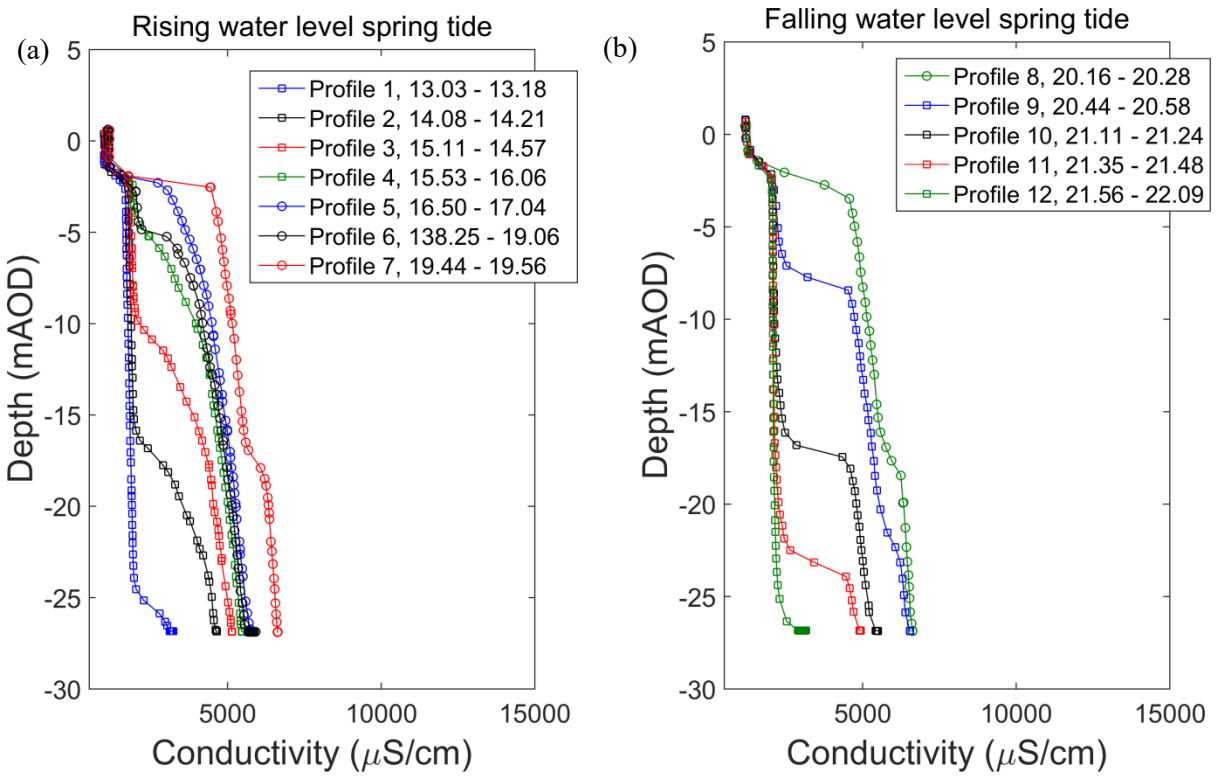

Figure 6.8 – (a) Conductivity profiles from a spring tide over a rising water table on the 10th October 2013 after saline breakthrough. (b) Conductivity profiles during falling water tables on the 10th October 2013.

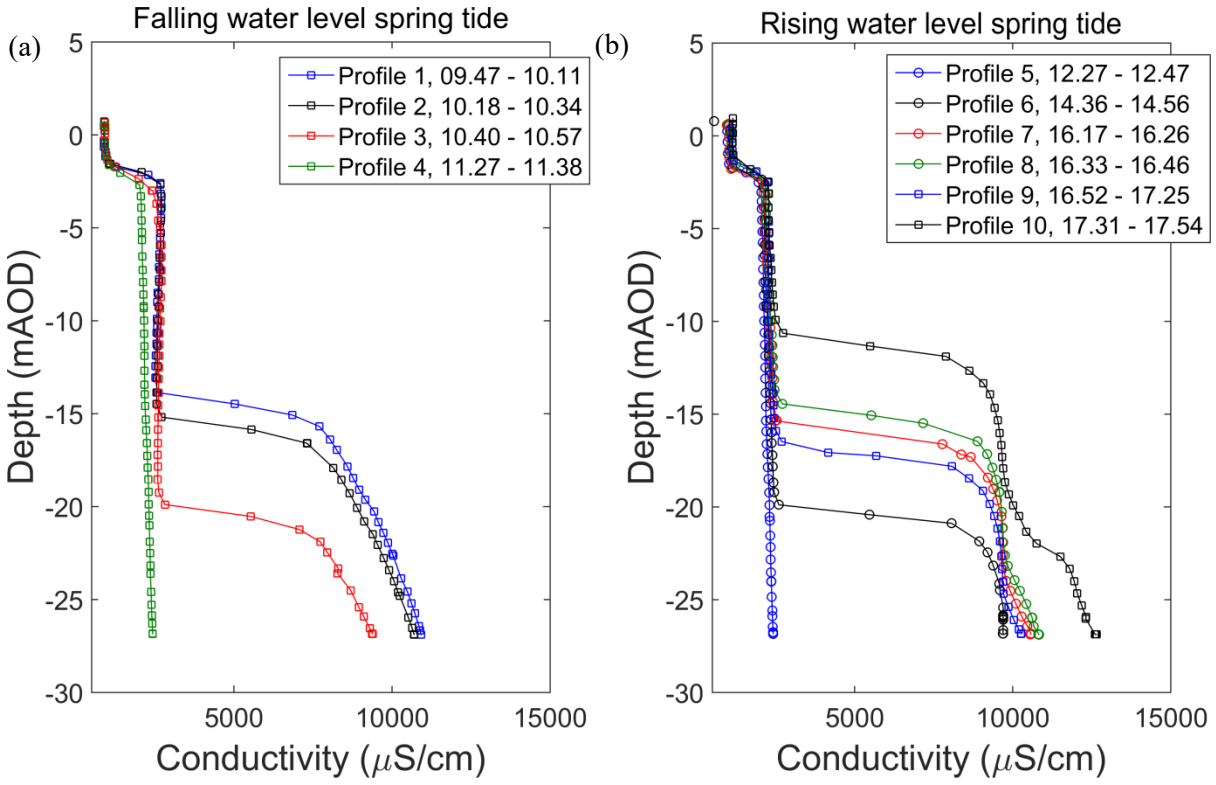

Figure 6.9 - a) Conductivity profiles from a spring tide over a rising water table on the 24th October 2013 after saline breakthrough. (b) Conductivity profiles during falling water tables on the 24th October 2013. In comparison to Figure 6.8 the saline water did not move as far up the borehole.

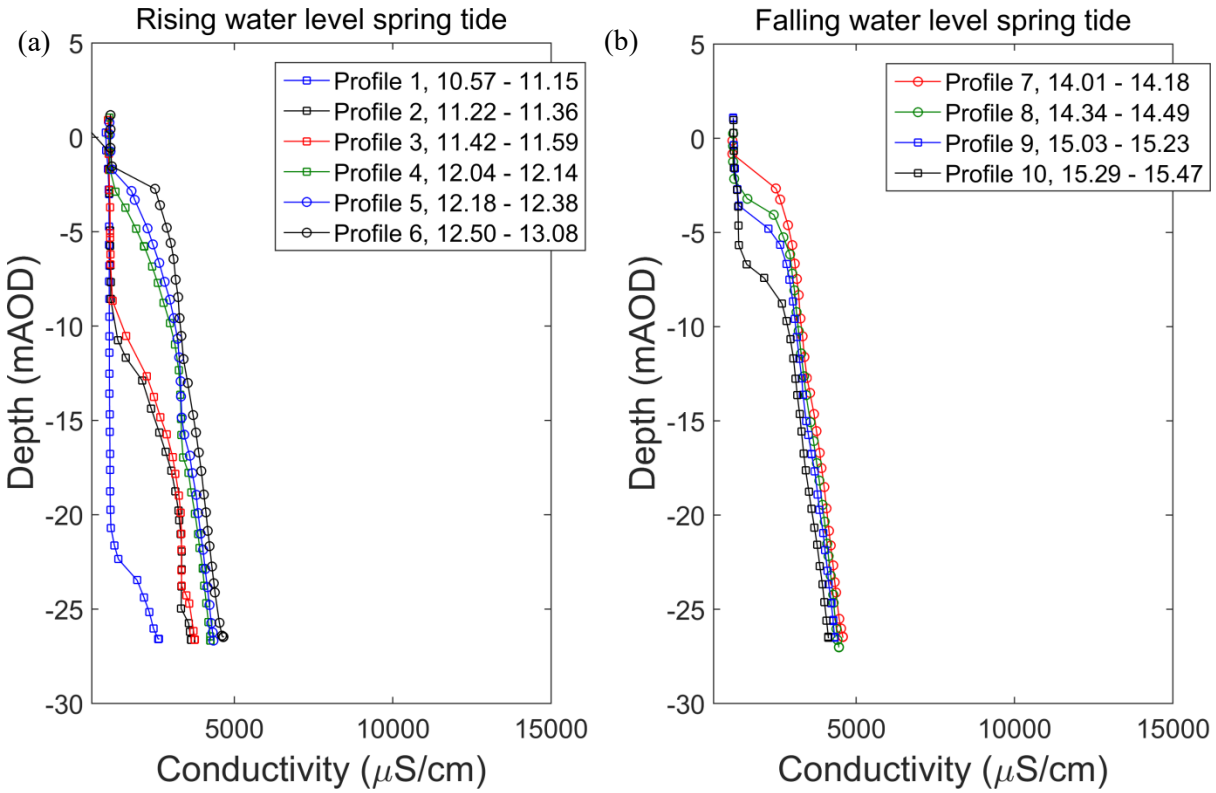

Figure 6.10 – (a) Conductivity profiles from a spring tide over a rising water table on the 9th October 2014 after saline breakthrough. (b) Conductivity profiles during falling water tables on the 9th October 2014.

There are several important observations from these profiles. First, it is clear from all profiles that the conductivity remained constant in the top 2 - 3m of the borehole, suggesting that there was an inflow at the top of the borehole. Second, as the water level in the borehole rose due to the rising tide, the salinity appeared to enter the borehole at the base. The conductivity then moved up the borehole as the water level continued to rise, on most occasions reaching the top of the borehole, but occasionally only moving partially up the length of the borehole (Figure 6.9). Conversely, as the water level in the borehole declined the conductivity also fell and saline water appeared to exit the borehole at the base once again. Finally, the baseline conductivity at the Balsdean OBH, which is only 1 km further inland, was much lower than the baseline conductivity in the Saltdean monitoring borehole (Figure 6.6(b)). The lower baseline conductivity in the Balsdean OBH suggests that the saline front was much closer to the Saltdean borehole than the Balsdean borehole.

6.2.1 Implications for the coastal aquifer at Saltdean

From the analysis in chapter 5, it is clear that semi-diurnal fluctuations in head in the borehole are controlled by the tide at the coast (Figure 6.1). However, the inland head also plays an important part

in seasonal borehole flow and salinity patterns (see section 2.2.3.2), and the inland extent of seawater intrusion (Jones and Robins, 1999). Figure 6.4 reveals that the decline in inland head in the autumn of 2013 and 2014 was responsible for the rapid movement of saline water through the aquifer and the resulting introduction of saline water into the monitoring borehole. Furthermore, the conductivity patterns displayed a correlation with the spring and neap levels recorded in the borehole. Thus, when the tidal level was highest the saline water appeared to be pushed further inland increasing the conductivity recorded in the borehole. These results suggest that significant movement of the saline front is possible over relatively short periods of time. Furthermore, the higher baseline conductivity within the Saltdean borehole compared to the Balsdean OBH (Figure 6.6) suggests the Saltdean borehole may have been, and is likely to still be, much closer to the saline interface than the Balsdean OBH. Since the Balsdean OBH is about another 1 km further inland this makes sense (Figure 4.3).

Once the saline water was washed out of the borehole a very rapid increase in the water level in the borehole was observed, which was related to significant rainfall through winter 2013/2014 (Figure 6.2). However, the water level very rapidly dropped; the reason for this rapid decline was to maintain the dynamic equilibrium in the coastal aquifer. Since the average hydraulic head at the sea is constant, within the tidal range, the large increase in the water levels created a sudden and very large hydraulic gradient between the borehole and the sea. As the recharge to the aquifer declined, there was nothing to maintain the inland head and the water quickly flowed to the sea and out of the aquifer.

The elevated levels of Br and Sr in Table 6.1 are clear indications that saline breakthrough was of marine origin (Pulido-Leboeuf et al., 2003), as was the significant increase in the Cl/SO_4 ratio after breakthrough (FAO, 1997, Bear et al., 1999). The piper diagram (Figure 6.5) reveals a very typical pattern for seawater intrusion in coastal carbonate aquifers (Pulido-Leboeuf et al., 2003, Chae et al., 2012, Tomaszkiewicz et al., 2014) and clearly demonstrates that as the water level increased in the borehole the water became increasingly dominated by seawater sodium chloride. The water samples and conductivity measurements in the borehole suggested that the bottom of the borehole was most vulnerable to elevated salinity, and that the top few metres were relatively unaffected by the significant increases in salinity experienced in the lower parts of the borehole. In fact, the conductivity

profiles further strengthen the existing evidence for a fracture zone at the base of the borehole (see section 4.3.1.2 and Jones and Robins (1999) pg. 74); suggesting that the water entered through this fracture zone and moved up the borehole as the water level increased.

The lower conductivity in the top few metres of the water column indicates inflow in this area, which may be due to increased permeability due to dissolution enhancement of fractures at the water-table (Price, 1987). However, anecdotal evidence (Power, 2012, Cook, 2012) suggests that an adit is likely to be present at the top of the water column, and adits constructed at this elevation are common in the area (Jones and Robins, 1999) (see section 4.3.1.2 and section 5.6.2). The presence of the adit, or a fracture zone, may lead to the vertical flow observed during conductivity logging. Vertical flow is common in boreholes drilled in fractured aquifers (Fleet et al., 1977, Butler et al., 2009). In the Saltdean borehole vertical flow may be caused by small differences in hydraulic head between the fracture at the base of the borehole (Jones and Robins, 1999) and the adit at the top. Slight changes in the head gradient (possibly caused by pumping) results in changes to the vertical flow patterns in the borehole. For example, across some tidal cycles saline water only moved about half-way up the borehole (Figure 6.9). Vertical flow between adits and/or discreet fracture zones at different elevations within the aquifer may make the Chalk aquifer even more vulnerable to seawater intrusion. For example, the drilling of boreholes may connect these discreet fracture horizons (or in this case a fracture and an adit) introducing new pathways for saline water to move through the aquifer. Furthermore, the conductivity profiles suggest, along with the geophysical evidence (Jones and Robins, 1999), that the movement of saline water towards the Saltdean borehole was dominated by fracture flow. Figure 6.11 shows a conceptualised summary of flow processes in and around the borehole.

Jackson et al. (2012b) found that measurements of borehole SP indicated the movement of a saturation front through an oil reservoir (section 2.3.6.5). The results reported above indicate a similar scenario in the Saltdean area. Therefore, the subsequent sections detail the interpretation of the SP data, to assess whether the movement of the saline front through the aquifer was detected using SP monitoring prior to saline breakthrough at the observation borehole.

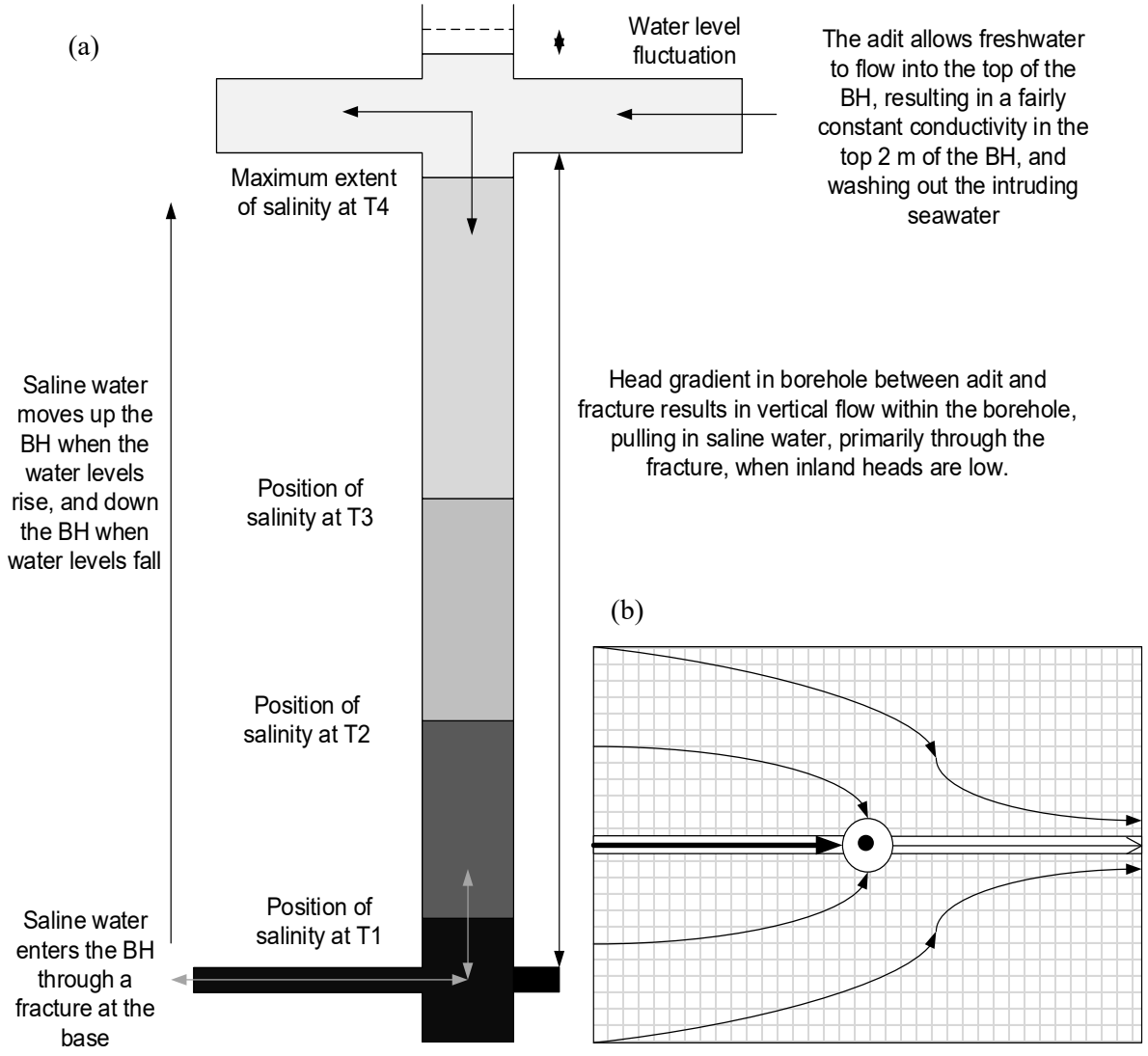

Figure 6.11 – A conceptual model of the flow and salinity patterns in the Saltdean borehole across a tidal cycle as outlined in the text above. (a) Vertical flow in the borehole, the position of the salinity front is marked at four different times (T1 – T4) across the rising tide. Across the falling tide the flow will move back down and out of the borehole as indicated by the double headed arrows. (b) Plan view of flow in the fracture and matrix (cross hatched area) around the borehole. The vertical head gradient introduced by the presence of the fracture and adit induces flow towards the borehole, primarily through the fracture (indicated by the thick arrow), as the water levels rise and vice versa when the water levels fall. Note that the lateral extents of the fracture and adit are unknown. The diagrams are not to scale.

6.3 Spatial, temporal and transient SP results from long-term field monitoring

In chapter 5 the periodic SP results from both borehole and surface referenced SP were presented. It appeared that borehole referenced SP measurements were preferable as they were not influenced by processes occurring in the near surface (section 5.4.1). Thus, the borehole referenced measurements allowed the tidal SP fluctuations with an origin in the aquifer to be more easily distinguished (Figure 5.16). However, surface referenced SP may still be useful for non-periodic spatial or transient SP, because the reference electrode is further from the anticipated source (see previous discussion of this in section 5.4.2.2) and so is unlikely to be influenced by the processes of interest within the aquifer. Therefore, measurements of the differential voltage between the reference electrode (Ref-C) and the borehole array (BH1-C – BH13-C) may still hold value for SP monitoring at the coast. Thus, the results from the surface referenced borehole array are presented first, followed by the borehole referenced data (reference electrode BH13-C). The layout of the borehole array and position of the surface reference electrode are shown in Figure 4.3.

6.3.1. Surface referenced SP

Figure 6.12 shows the full SP time-series for the surface referenced voltage from the deepest electrode (BH1-C) the temperature at the surface reference electrode (Ref-C) and the temperature corrected SP from BH1-C. The data was smoothed using a moving average filter with a window of 25 data points (125 minutes). The temperature correction was applied based on a linear regression between temperature and voltage (Woodruff et al., 2010) from June to October 2013, marked by the dashed black box in Figure 6.12. Based on this linear regression ($R^2 = 0.89$), a temperature coefficient of 1.92 mV/°C was applied to the full time-series to remove the effect of the temperature at the surface reference electrode from the voltage data. Note that the temperature correction was only possible because the temperature in the borehole was approximately constant throughout the monitoring period. Between October and January 2014 there were changes in the voltage that may be related to recharge and saturation changes at Ref-C. The voltage then stabilised again until July 2014 when a constant trend appeared until the end of the experiment in January 2015.

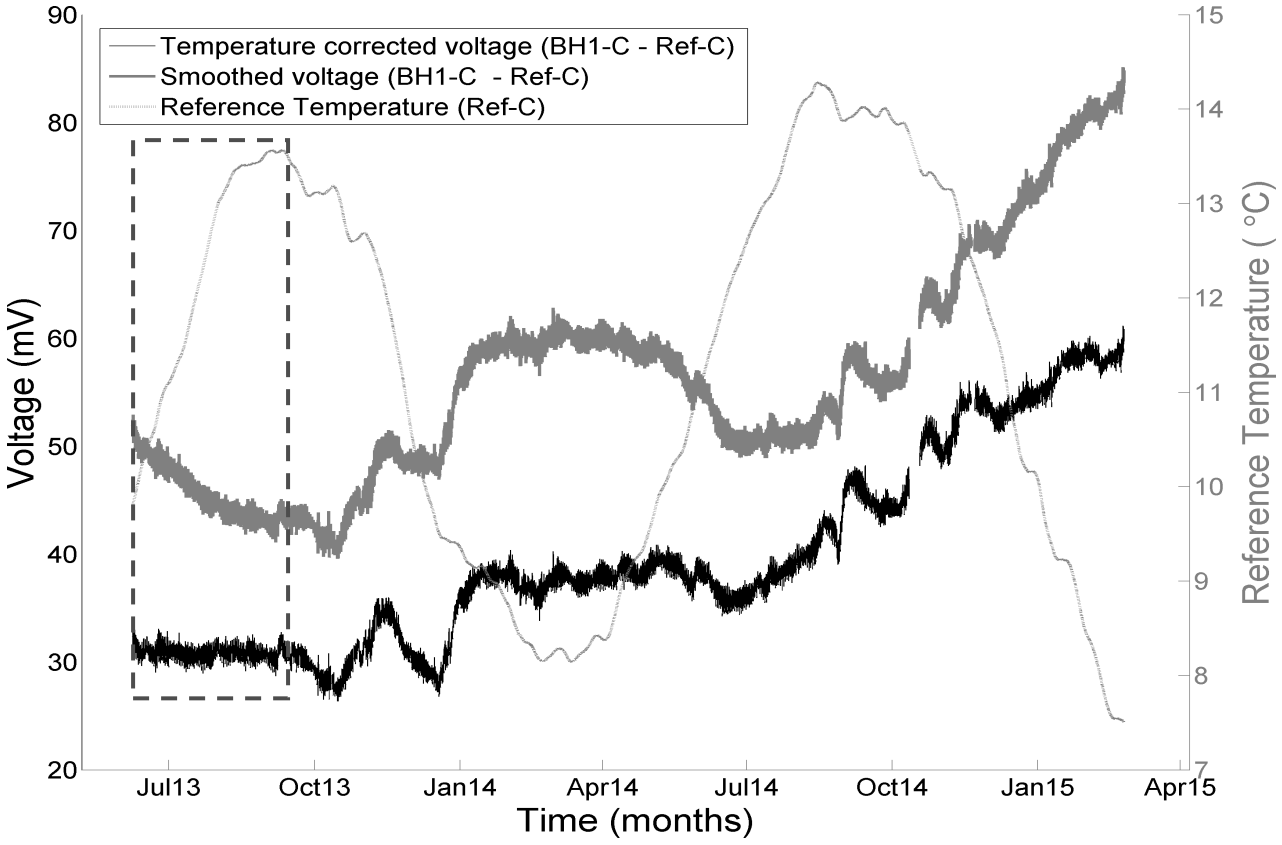

Figure 6.12 – Smoothed voltage (V_R - grey) and the smoothed voltage corrected for temperature (V_C - black) for BH1-C, the correction factor was determined using a linear regression through the data between June and late September 2013 (dashed box). The linear regression (R^2=0.89) yields an equation for the temperature correction, V_C=1.91(T-20°C)+V_R, where the voltages are corrected to a reference temperature of 20°C (Silvion, 2013, Silvion, 2015), similar to the method for correcting conductivity to a standard reference temperature (i.e. specific conductivity at 20°C). Note all subsequent surface referenced voltages are reported corrected for temperature.

Figure 6.13 shows the temperature corrected voltage from BH-1C – Ref-C against the rainfall data for the duration of the monitoring experiment. Rainfall and changes in the voltage appear to be correlated in Figure 6.13. For example, as the rainfall increased throughout September 2013, the SP appeared to decrease until mid-October 2013, when a significant increase in rainfall led to a change in the voltage trend. As the rainfall decreased through late October and early November 2013 the trend remained constant, until the rainfall increased again in mid-November 2013. The trend then changed again and the voltage started to decrease. The rainfall then remained low through the rest of November and into December 2013 and the voltage continued to decrease. However towards mid-December rainfall dramatically increased and remained high through December 2013 and January and February 2014 (leading to dramatic increases in head, Figure 6.2), leading to another change in the voltage trend which steadily increased through January and flattened out through February, possibly as the ground in the area became saturated.

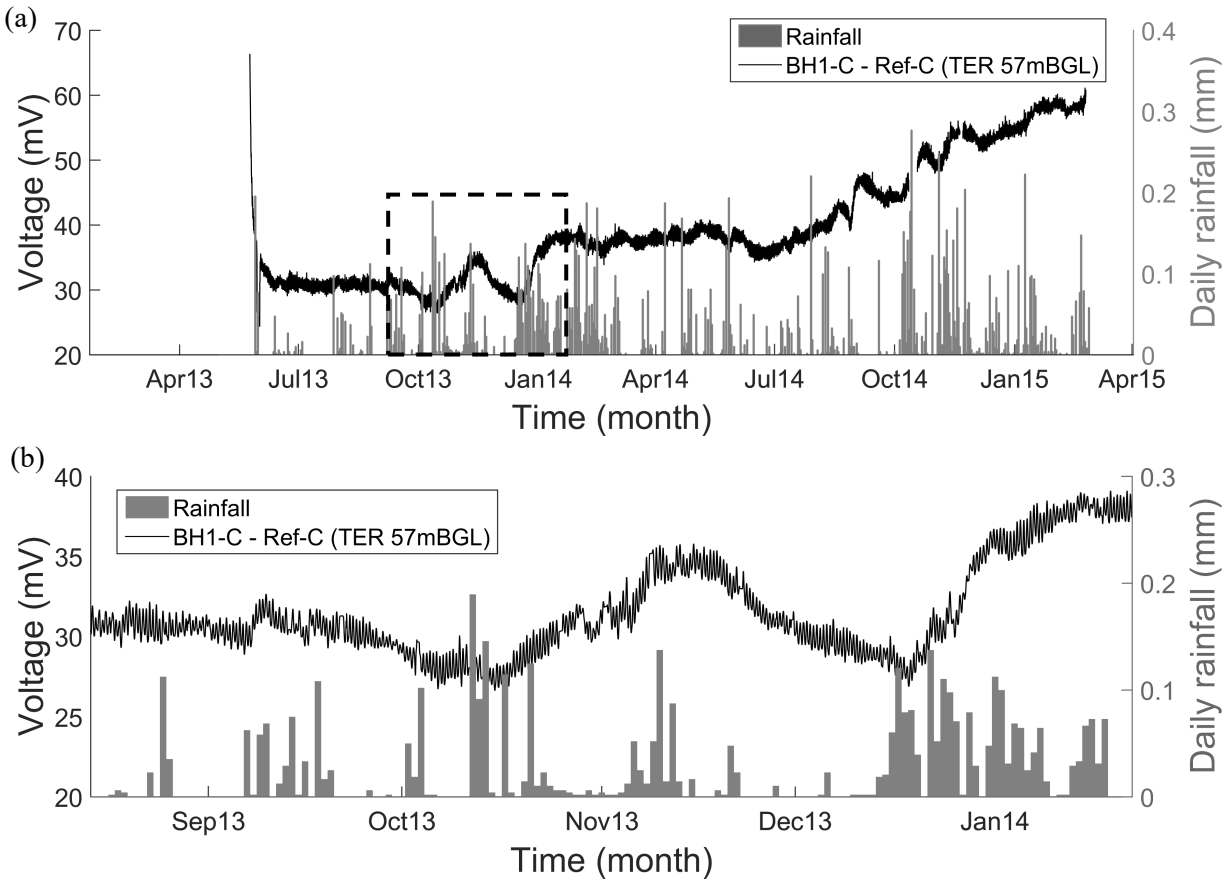

Figure 6.13 – a) Voltage from BH1-C – Ref-C and rainfall data recorded at Ditchling Road. It appears that significant changes in surface referenced voltage are related to rainfall events (highlighted by the dashed box). b) Area highlighted by the dashed box in a) showing voltage and rainfall for autumn 2013 through winter 2013/2014.

Figure 6.14 shows the pumping data from the Balsdean abstraction well in September 2013. The pumping signature did not appear in the SP data, which may be due to the very small drawdown (c.0.1 m) observed in the Saltdean borehole. It is also apparent that the tidal signature was dominant in the SP. Thus, the analysis presented here does not address the effect of pumping on SP.

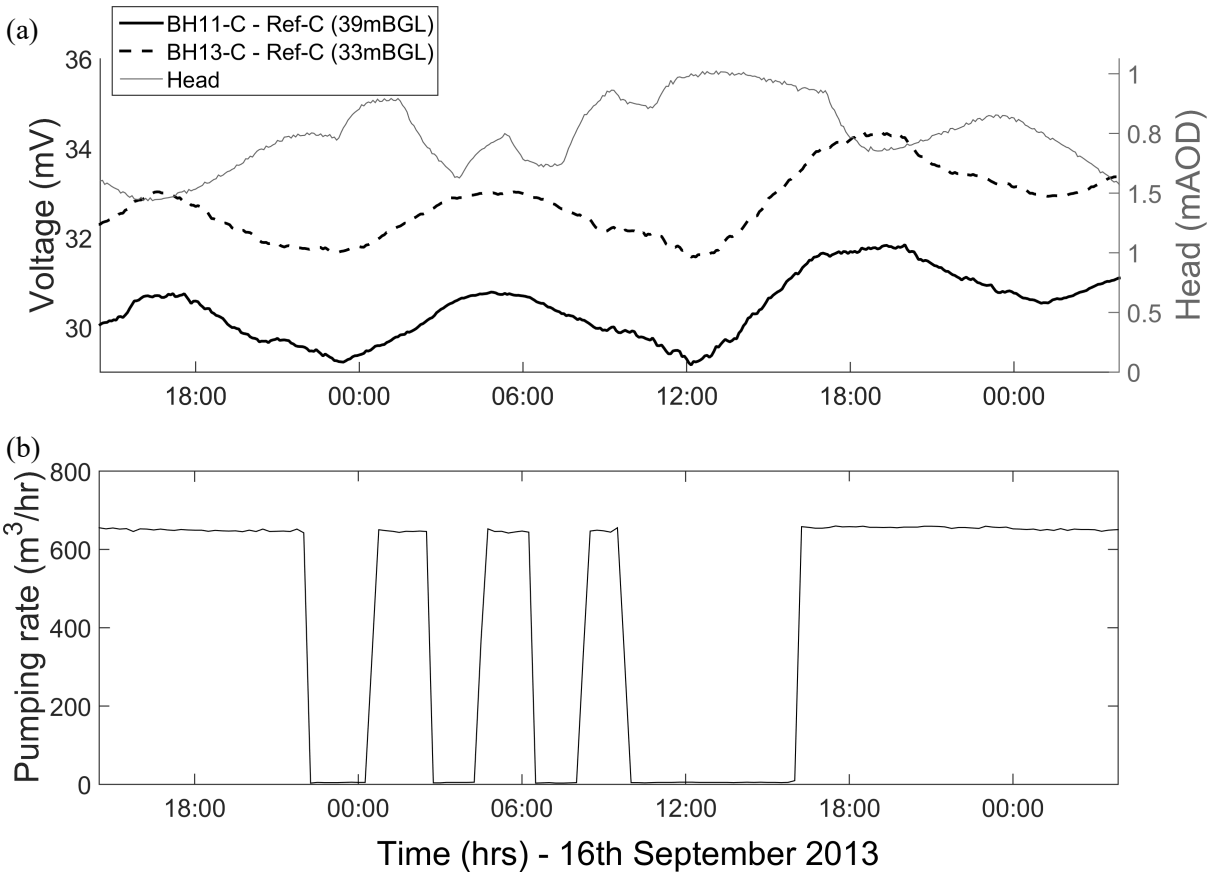

Figure 6.14 – a) Head and voltage data. b) Pumping data from the Balsdean observation well. The pumping signal is not apparent in the smoothed voltage data.

Figure 6.15 shows SP, from various depths in the borehole, along with the measured conductivity. The spring/neap effects on the voltage are apparent in the areas highlighted by the dotted box. There is no clear evidence of the surface referenced SP responding to the breakthrough of saline water at the borehole. However, there is evidence of a vertical gradient in SP with depth, with the deepest electrode showing the lowest voltage. After saline breakthrough the gradient increased.

Figure 6.16 - Figure 6.19 show vertical SP profiles within the Saltdean borehole. The gradient, which was c.0.22 mV/m, remained relatively constant across a tidal cycle with a vertical difference in SP from the top of the borehole to the bottom (i.e. c.30 m) of c.-6 ± 1 mV. Figure 6.17 compares the gradients recorded in the Saltdean borehole, with the gradient in the Balsdean OBH only about 1 km further inland (Figure 4.3), and at the inland site at Trumpletts Farm in Berkshire (Figure 4.2). There was no evidence of any gradient of SP with depth at either of these locations. Also shown are the voltages measured at each individual electrode in the array during each SP profile. Figure 6.18 clearly illustrates the advantage of having a travelling electrode (TER) as the gradient recorded by this

electrode (BH1-C) remained approximately the same before and after saline breakthrough, but the permanent electrode array recorded a significant change in voltage after breakthrough. The change in voltage recorded by the permanent array appeared to be a result of the changing salinity within the borehole and its impact on electrode performance, rather than due to any effect occurring in the aquifer. Figure 6.19 shows the gradient recorded by the permanent array from May – August 2013 prior to saline breakthrough. Also shown is the change in gradient recorded by the permanent array for this period. The gradient in the borehole appeared to become systematically shallower from early July until saline breakthrough in late August, an effect that is particularly apparent for the mid-section of the borehole (Figure 6.19(a)). Note that regardless of whether the voltage was referenced to the surface electrode (Ref-C) or the borehole (BH13-C) the gradient remained approximately the same, in terms of its magnitude and polarity, throughout the experiment. Thus, Ref-C was used to investigate the vertical gradient in order to compare results directly between the different sites. At the inland site no borehole reference was available.

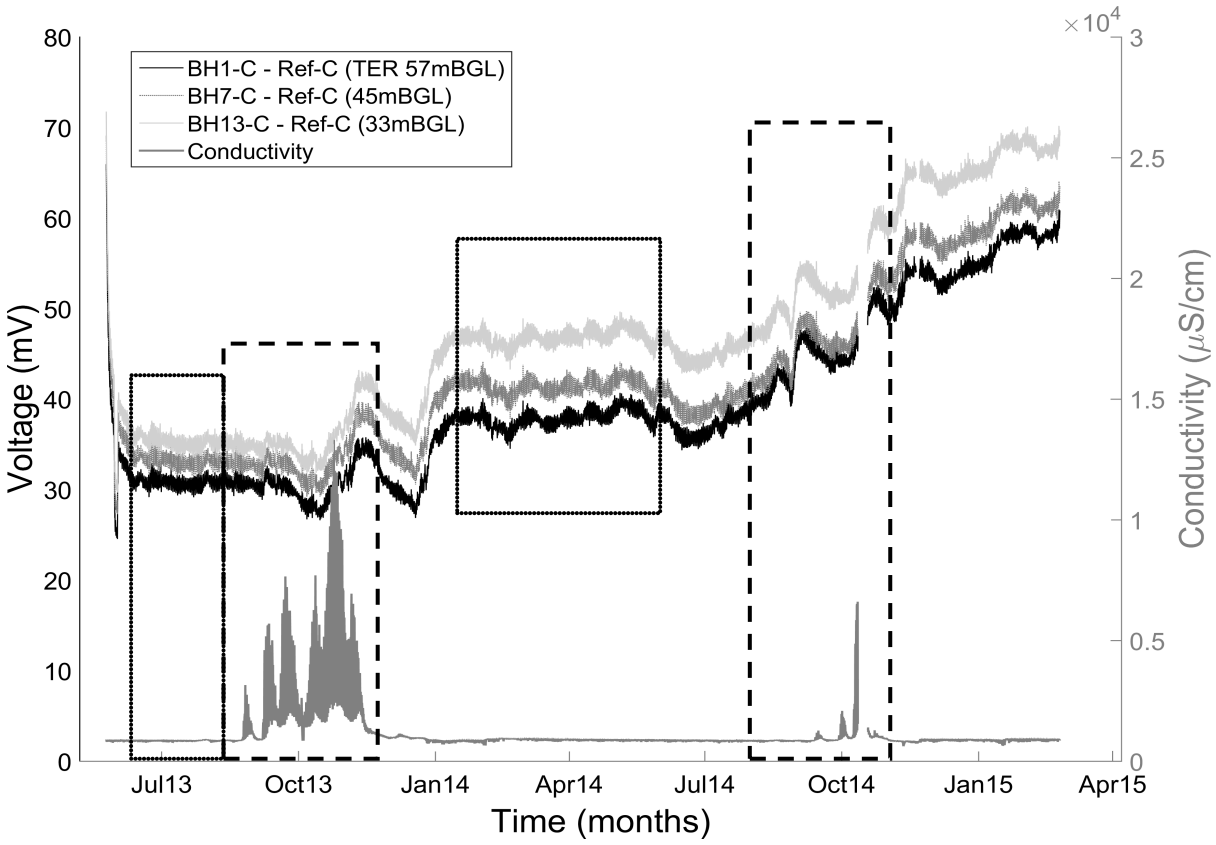

Figure 6.15 - Surface referenced voltage and conductivity for the duration of the experiment. Voltages from the top, middle and bottom of the borehole are shown. The dashed boxes highlight periods of saline breakthrough. The dotted boxes highlight areas that display clear evidence of the influence of the spring and neap tides in the voltage records.

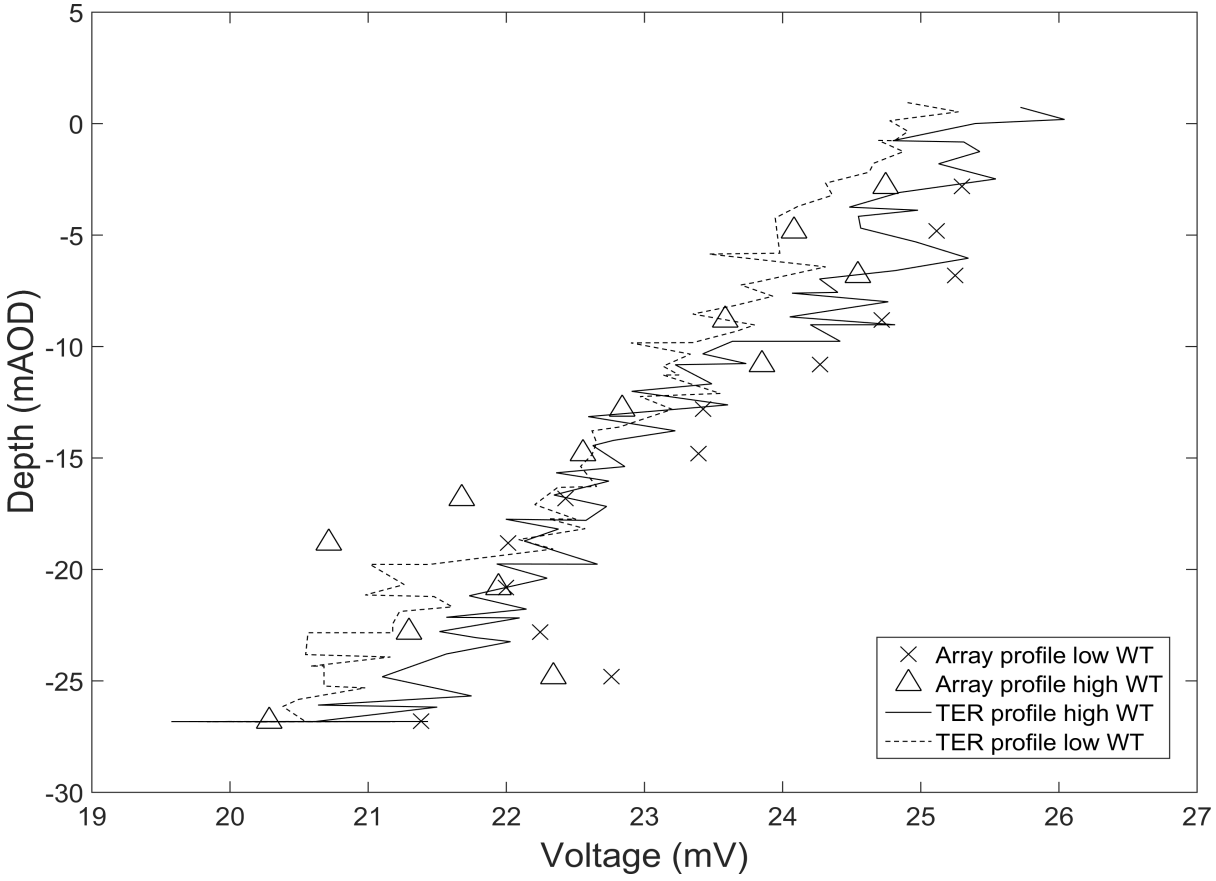

Figure 6.16 – Voltage with depth recorded by the travelling electrode (TER), for high and low water tables on the 8th August 2013, prior to saline breakthrough. The SP recorded by the permanent electrode and the travelling electrode are approximately the same, the main exceptions are BH2-C at -25 mAOD and BH4-C at -20 mAOD, where there appears to be a discrepancy between the permanent electrodes and the TER.

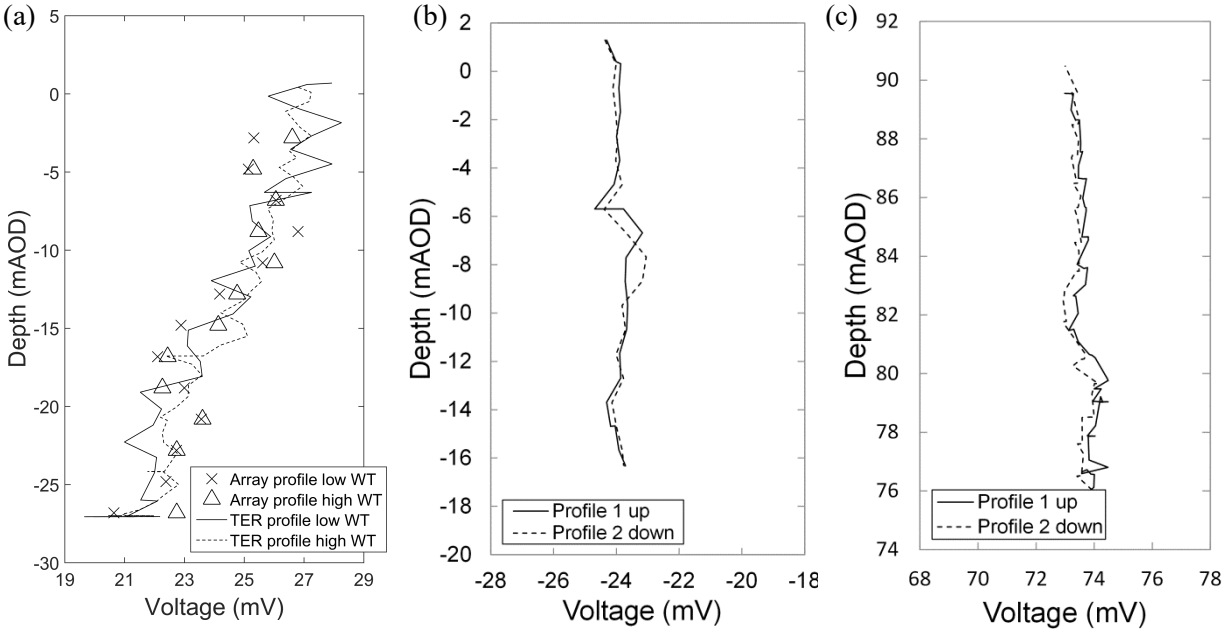

Figure 6.17 – (a) The voltage with depth recorded by the TER, for high and low water tables on the 24th October 2013 (Figure 6.9 for conductivity profiles from the same day). (b) The voltage with depth recorded in the Balsdean OBH (Figure 4.3) on 17th November 2011. Data from the Balsdean OBH was kindly shared by Malcolm Graham at ICL. (c) The voltage with depth recorded inland at Trumpletts Farm in borehole PL10B (Figure 4.2) on 16th July 2013.

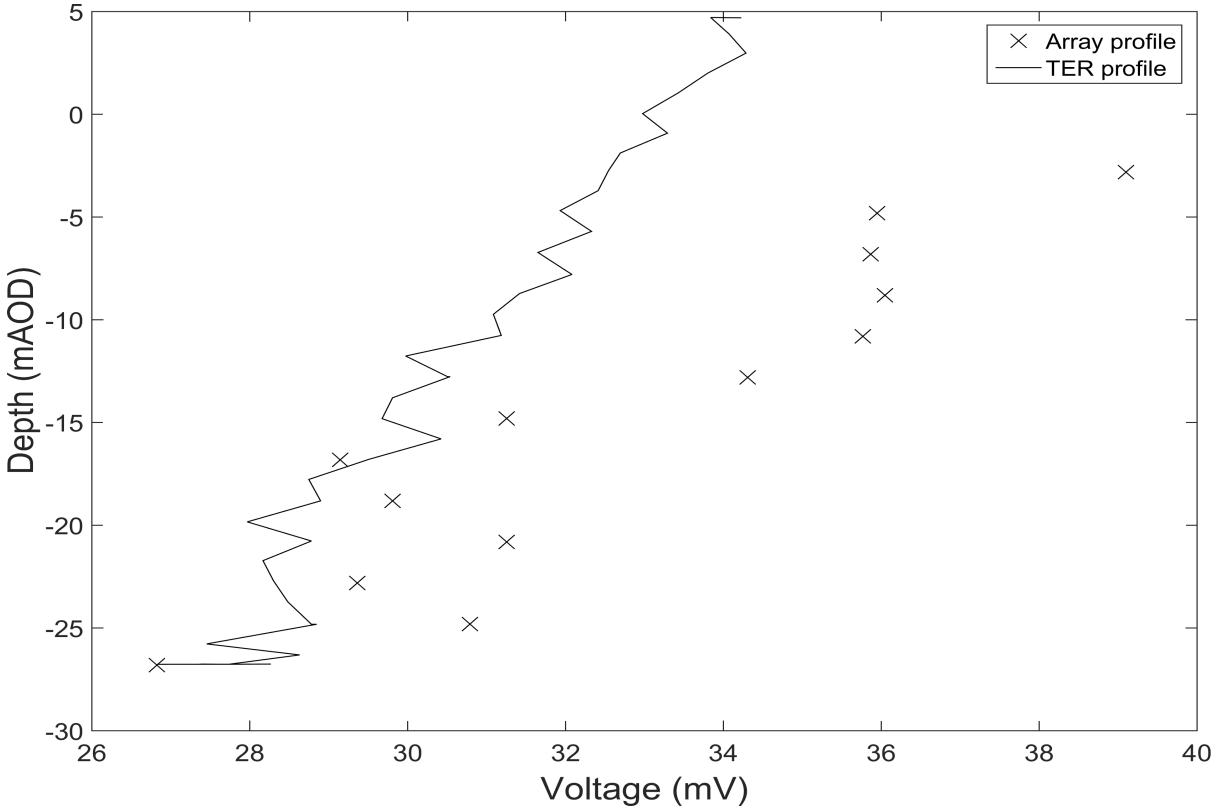

Figure 6.18 - Voltage with depth from permanent array and TER on the 6th February 2014. The difference between the TER and permanent array voltages are significant due to changes in salinity at the electrodes (see section 6.5.1.1).

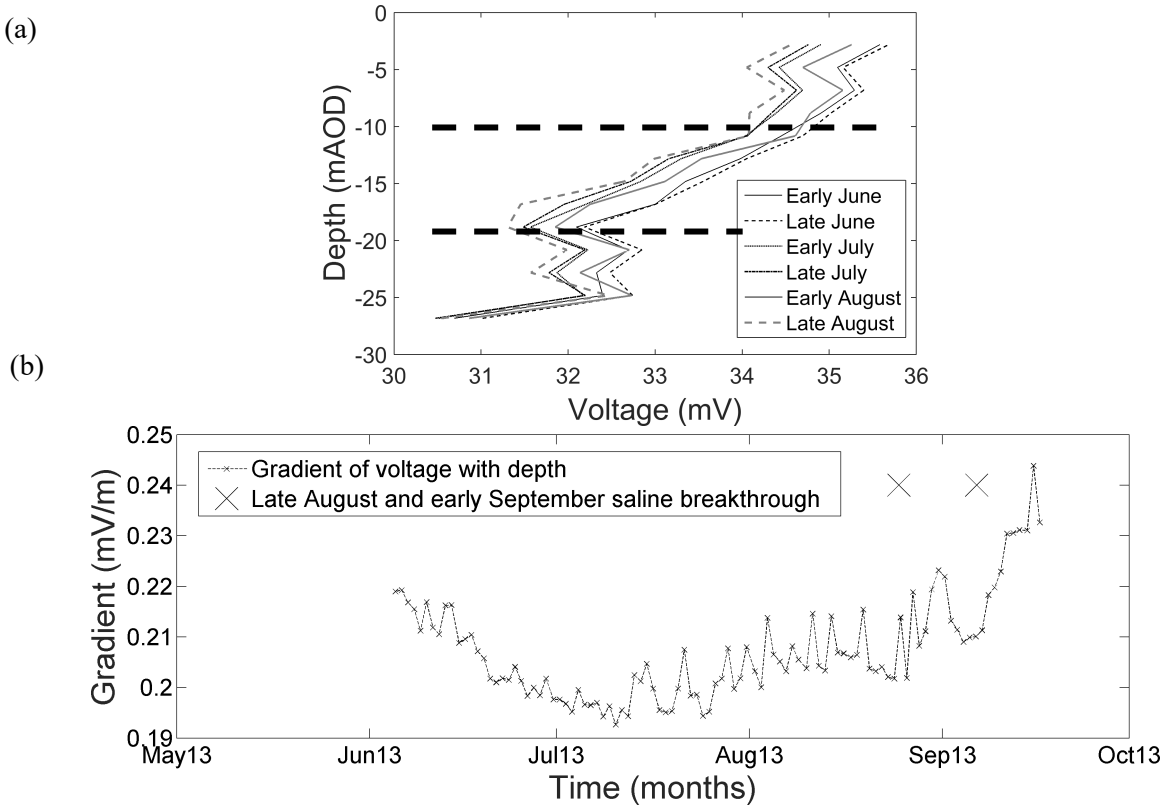

Figure 6.19 – (a) Average voltage, over a period of 12 hours, with depth recorded by the permanent array from early June to late August 2013, prior to saline breakthrough. Notice that there appears to be a change in the gradient (indicated by the dashed lines) at about -10mAOD, the gradient between c.-10mAOD and c.-20mAOD, appears to become shallower as summer progresses. (b) Change in gradient with time, crosses mark saline breakthrough.

6.3.1.2 Borehole referenced SP

There appeared to be little evidence, with the possible exception of the vertical SP gradient, of any significant pre-saline breakthrough voltage precursor in the surface referenced data. However, this may be due to complex processes taking place at the surface reference electrode (Ref-C), which mask the transient effects in the surface referenced data (discussed in section 6.5.1). Therefore, the remaining analysis focuses on the borehole referenced data. Unless otherwise stated all the electrodes were referenced against BH13-C (Figure 4.3) for this analysis. Figure 6.20 show the borehole temperature and voltage for the full monitoring experiment. The voltage data is smoothed using a second order SG filter (see section 5.4.2.2) with a window of 25 data points (125 minutes).

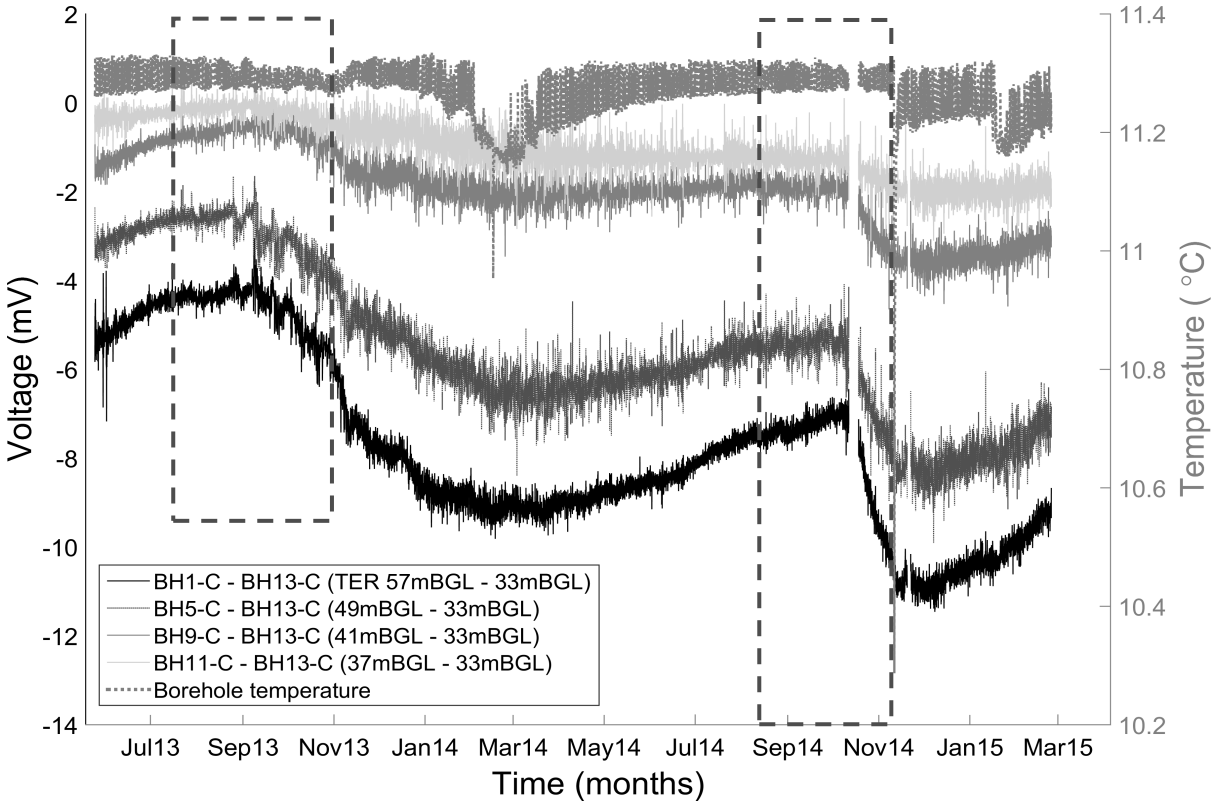

Figure 6.20 – Borehole referenced SP data and temperature in the borehole. The dashed boxes highlight the two periods of saline breakthrough at the borehole.

The temperature in the borehole remained relatively stable at c.11.25 ± 0.1^{0}C. Therefore, temperature could not have caused any transient change in voltage. The voltage steadily increased prior to breakthrough in 2013 and there were significant voltage fluctuations around breakthrough in August 2013 (indicated by the dashed box in Figure 6.20). The vertical gradient is also apparent in Figure 6.20, as is the increase in the gradient after the breakthrough in autumn 2013.

Figure 6.21 shows the borehole referenced SP data further smoothed using a seven day window; the window was chosen in order to minimise the tidal component and the noise in the SP. This filter window also dampened the longer period fluctuations including the fortnightly cycle leaving only the most significant long period fluctuations and transient SP effects to be investigated. Note that other filtering methods were avoided because they typically introduce a phase delay into the signal (Eilers, 2003). Such a phase delay was unacceptable, as accurate times for the onset of transient events were necessary to assess whether there were any SP effects that could be tied to saline breakthrough. It was also important that a consistent analysis approach was used throughout, so that direct comparisons between the different events observed could be made. Therefore, forward/backward filtering, which eliminates filter phase delay was not applied; because of a loss of data as a result of a temporary failure of the monitoring equipment it was not possible to apply forward/backward filtering to the voltage data around breakthrough in September 2014 (Figure 6.20). Figure 6.22 shows the smoothed SP and the conductivity from the period in 2013 highlighted by the black box in Figure 6.21.

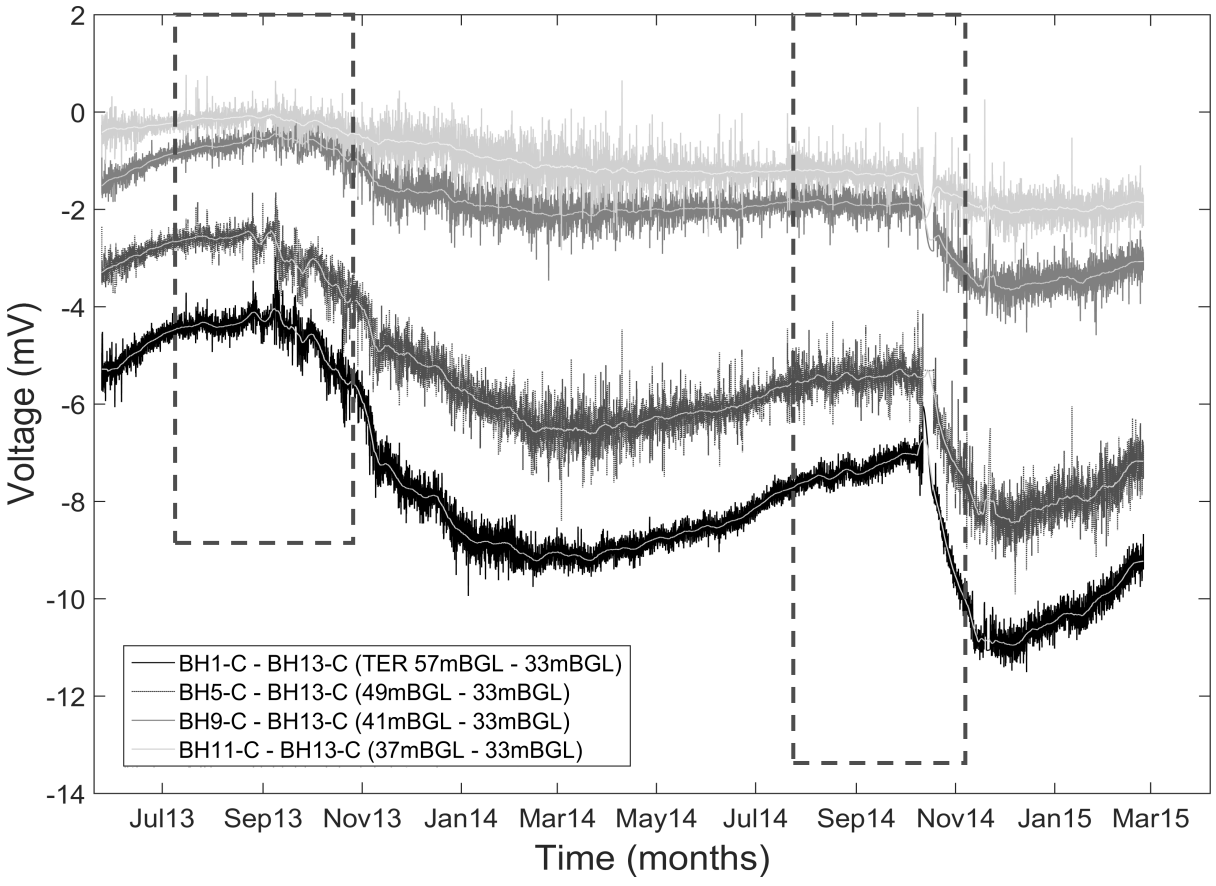

Figure 6.21 - Smoothed and filtered BH voltage data. The filtered voltages are shown in light grey. The dashed boxes highlight the two periods of saline breakthrough at the borehole.

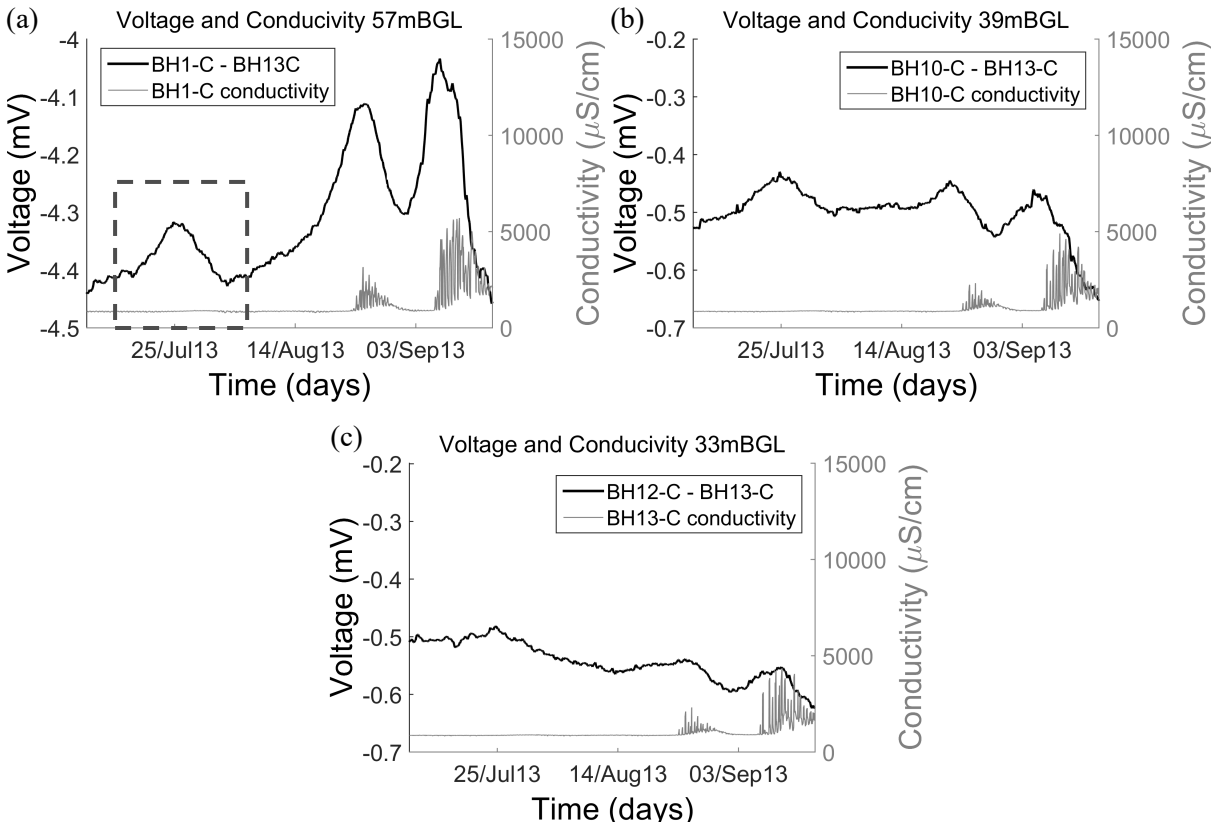

Figure 6.22 – Smoothed SP data and conductivity for the period just prior to and after breakthrough of saline water in the borehole in 2013. (a) Voltage and conductivity from BH1-C, the dashed box shows a SP peak that does not appear to correlate with any changes in salinity, Figure 6.23 shows this area in more detail. (b) Voltage and conductivity from BH10-C. (c) Voltage from BH12-C and conductivity from BH13-C.

In Figure 6.22 it appears that there was a systematic increase in SP prior to the increased conductivity in the borehole. After the initial increase in conductivity, the saline water was washed out of the borehole, and the SP decreased. However, prior to a second increase in the conductivity the SP again appeared to increase before the saline water re-entered the borehole. This effect was apparent throughout the electrode array, although the magnitude of the increase in SP decreased with the dipole length up the borehole. The precursor had a magnitude of c.300 μV at the deepest electrode (BH1-C) and c.100 μV at the shallowest (BH12-C). Prior to the two SP peaks shown in Figure 6.22 there appeared to be another peak in the SP in late July (Figure 6.23). There were also very subtle changes in the conductivity in the Saltdean borehole that occurred towards the end of July. These small changes may be indicative of the movement of the saline front in close proximity to the borehole, but without any significant saline breakthrough actually occurring in the borehole. Even without breakthrough, there did appear to be a systematic increase in SP, of approximately c.100 μV, prior to the subtle change in conductivity observed.

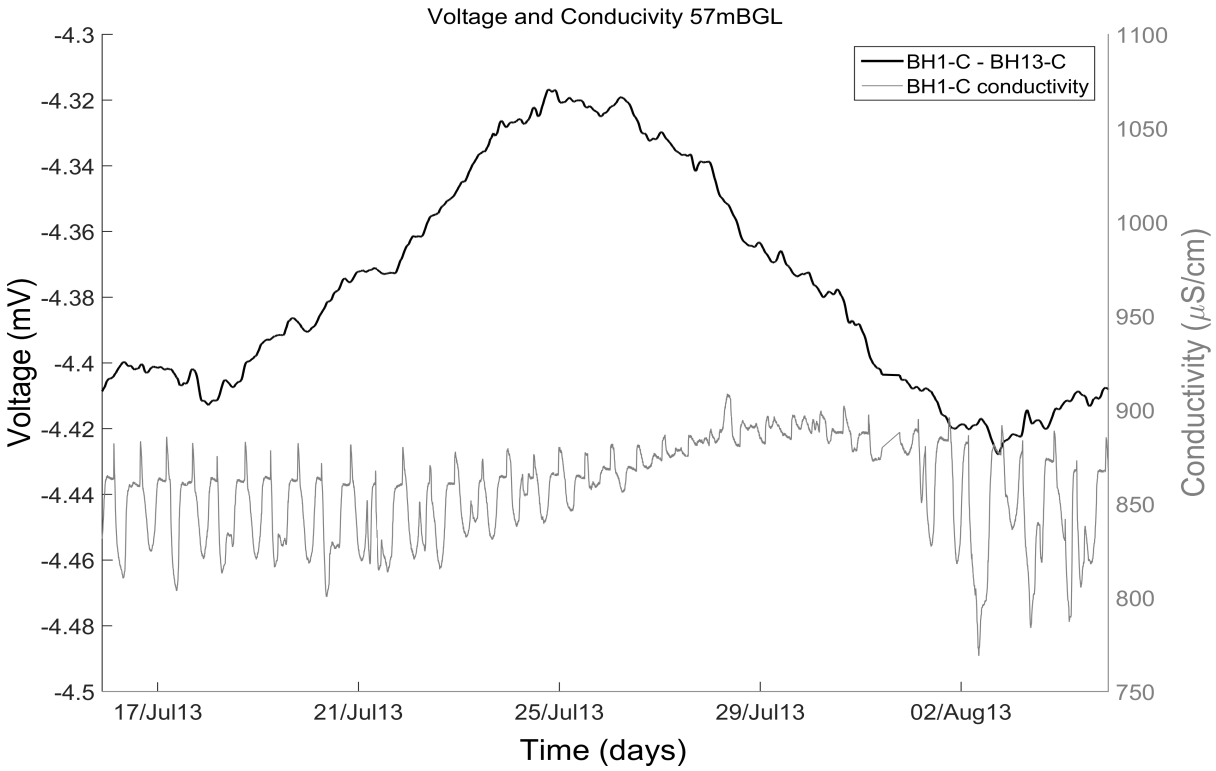

Figure 6.23 – The SP displayed a systematic change in voltage prior to a subtle change in conductivity, indicating that SP responded to larger salinity changes away from the borehole while only subtle changes occurred in the borehole.

Figure 6.24 shows the change of the vertical SP gradient, referenced in the borehole, for the three months prior to saline breakthrough in 2013. To reiterate, whether the voltages were referenced to the surface electrode (Ref-C) or to the borehole electrode (BH13-C) the gradient was approximately the same (see Figure 6.19(b)). The gradient referenced against BH13-C decreased throughout June 2013. At the start of July the gradient began to increase; however the gradient decreased again slightly before the period of marginally increased conductivity shown in Figure 6.23. The gradient then increased again until just before saline breakthrough when there was again a decrease in the gradient, corresponding to the precursor signals (Figure 6.22).

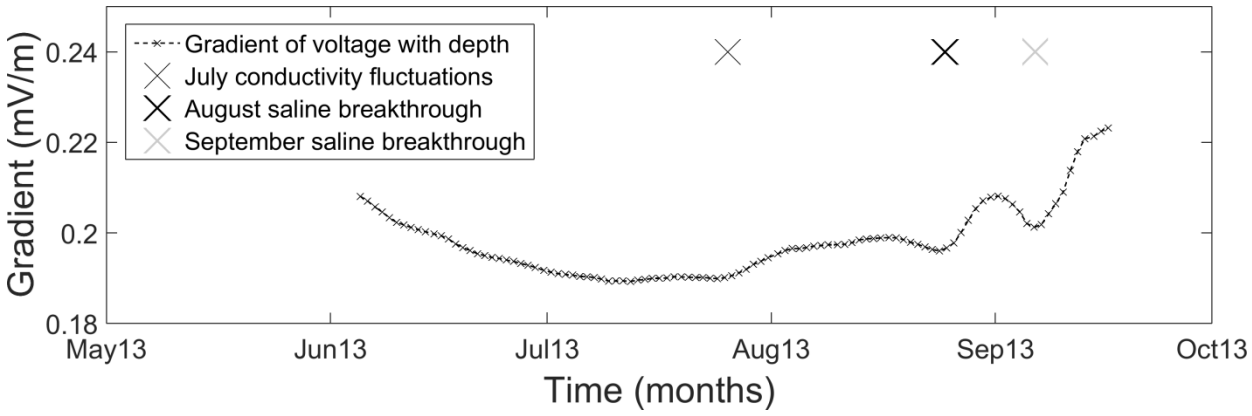

Figure 6.24 – The change in the vertical SP gradient using the smoothed data averaged over 12 hours shown in Figure 6.21. The precursor signal is evident in the gradient time-series. There is also a steady decrease in voltage just prior to small changes in conductivity in July and between then and the breakthrough at the end of August 2013.

Saline breakthrough occurred again in mid-September 2014. In Figure 6.25(a) there does not appear to be a significant SP precursor prior to saline breakthrough, although two peaks around early and late August do again appear to precede very subtle changes in conductivity, the latter effect only occurred higher up the borehole. The reason that a precursor is not apparent in Figure 6.25(a) may be that the performance of the electrodes deteriorated after saline breakthrough occurred in 2013. In addition, there were problems with the monitoring equipment just after breakthrough in 2014. The equipment temporally failed, which may have distorted the smoothing procedure applied to the data. However, a precursor did appear at the two shallower electrodes although, at c.50 μV, it was relatively small compared to 2013. However, the array contained a fourteenth electrode (BH14-C) at the top of the borehole that was disconnected for most of the experiment (Figure 4.3). Once it became apparent that only the shallowest part of the borehole was unaffected by increased conductivity (Figure 6.7 - Figure 6.10) this electrode was reconnected providing an alternative reference electrode. Figure 6.26 shows voltage from early August to mid-September 2014 referenced against BH14-C. When the data was referenced against BH14-C the precursor appeared more clearly with a magnitude similar to that in 2013 (Figure 6.22). Again the magnitude of the precursor decreased up the borehole.

Other peaks did appear in the smoothed time-series, most significantly from December 2013 to March 2014 (Figure 6.21). These peaks appeared to be correlated with saline water being washed out of the borehole. However, they were significantly smaller than the c.300 μV peaks that occurred prior to saline breakthrough in late summer 2013 and 2014 and, so, are not discussed here.

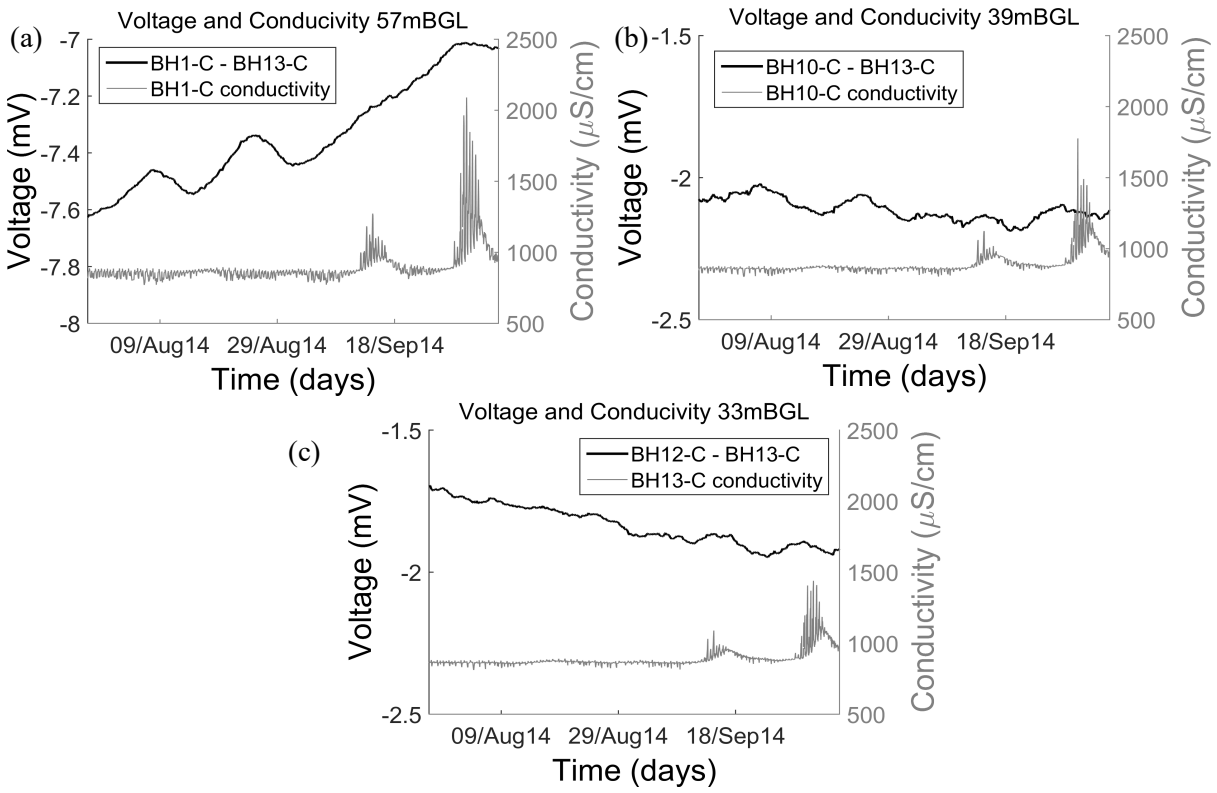

Figure 6.25 – Voltage precursors in 2014. (a) Voltage and conductivity from BH1-C. (b) Voltage and conductivity from BH10-C. (c) Voltage from BH12-C and conductivity from BH13-C. There are clear precursors around the 9th and 29th August, but the voltage does not seem to so clearly indicate breakthrough in September 2014.

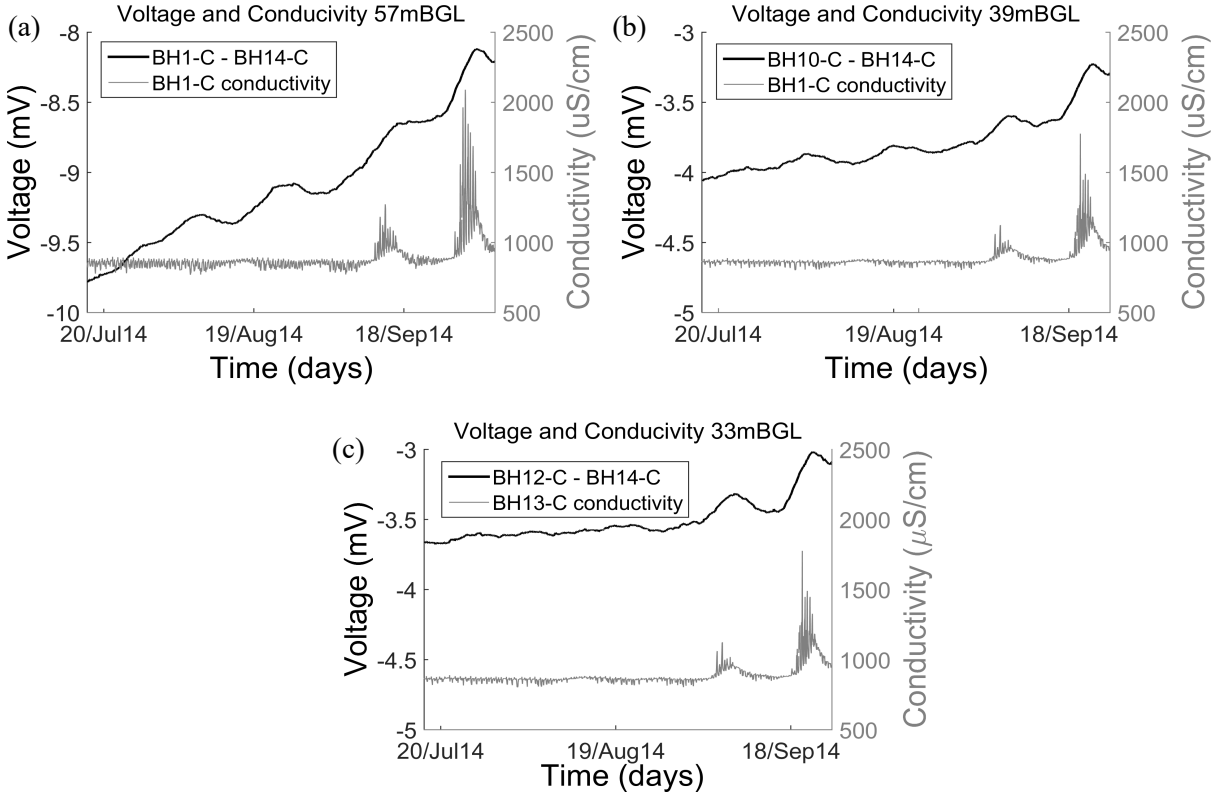

Figure 6.26 - Voltage precursors in 2014. (a) Voltage and conductivity from BH1-C. (b) Voltage and conductivity from BH10-C. (c) Voltage from BH12-C and conductivity from BH13-C. BH14-C was the reference electrode. Note that the salinity at BH14-C remained low. Peaks around the 9th and 29th August indicate movement of the saline front towards the borehole but without breakthrough. Two peaks in September preceded breakthrough at the borehole.

6.4 Modelling spatial, temporal and transient SP in the coastal aquifer

The results reported here are from model 3 (Table 4.3). Figure 6.27 shows contour plots of the salinity and SP distribution for model 3(b) for the spring tide using a tolerance of 10^{-5} for the EED component (see section 5.6.1.2). As highlighted in section 5.5.1 the presence of the fracture zone was necessary to explain the field observations. The zone introduced a high permeability pathway for movement of the saline front and a high conductivity pathway, along with the borehole, for current flow.

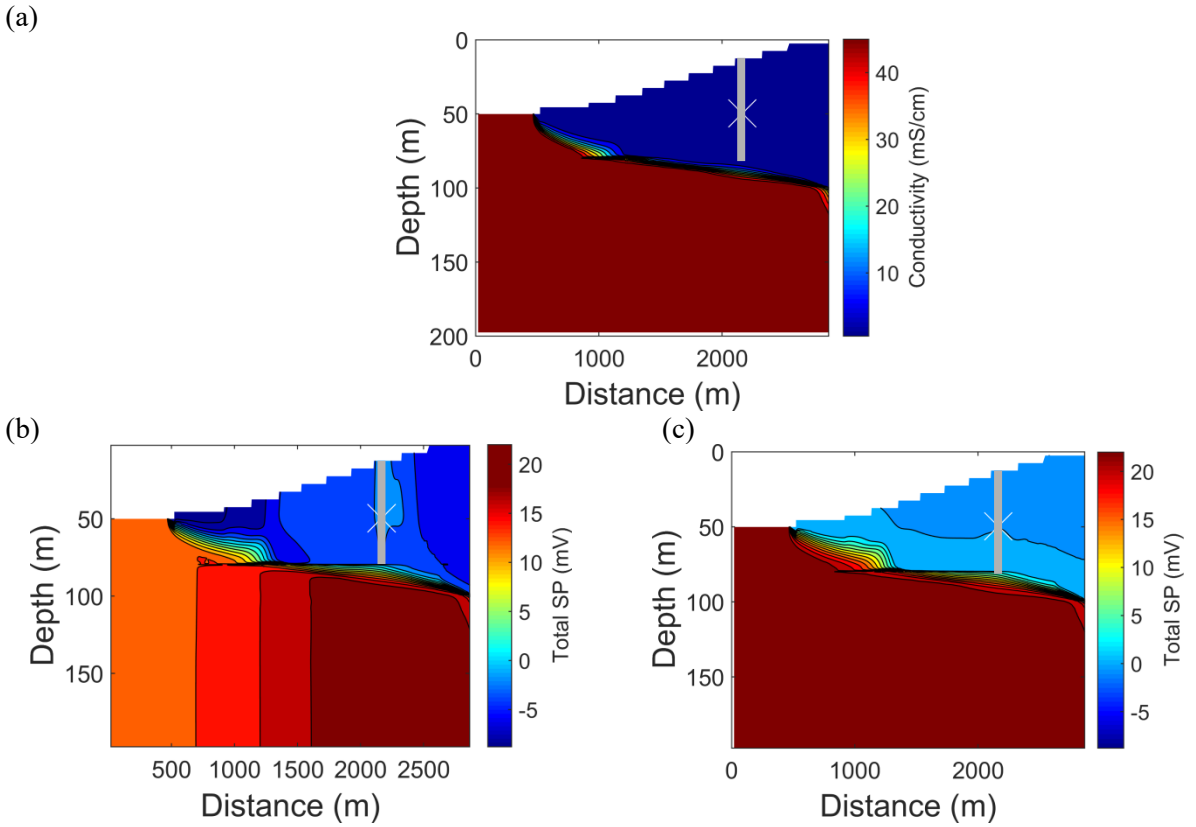

Figure 6.27 – (a) Simulated conductivity contour map. (b) Total SP (TSP) contour map (10^{-5} tolerance). (c) TSP contour map (10^{-7} tolerance). The white cross represents the voltage reference, equivalent to the borehole referencing scheme used in the field. The grey line marks the borehole location.

Figure 6.28 shows the simulated and observed gradient using both tolerance values for the EED component. The simulated gradients showed a reasonable match to the observed gradient when the lower model tolerance was used (10^{-5}), when the saline front was near the base of the borehole, and when the fracture was present providing a high conductivity pathway for current flow. The vertical SP gradient was dominated by the EED component. However, when using the higher tolerance (10^{-7}) for the EED component the results did not match the field observations, displaying a steep gradient, caused by EK, in the opposite sense to that observed, due to the vertical head gradient. The EED

component was lower than the observed gradient by a factor of about 100. However, its presence may provide some additional confidence in the role of the EED potential in the observed gradient.

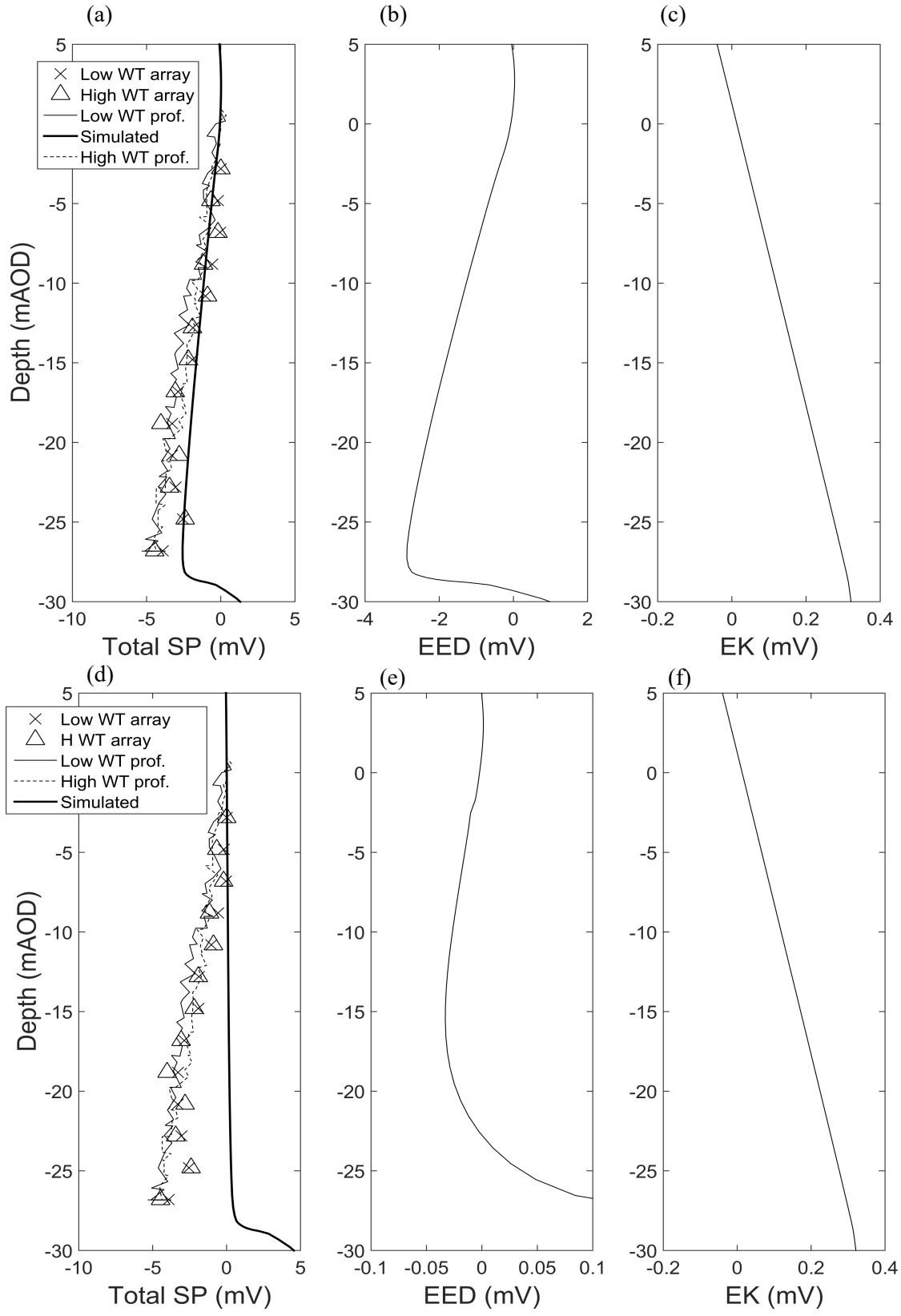

Figure 6.28 – (a) Simulated (thick black line) and observed gradient against depth (10^{-5} tolerance). (b) EED component of the gradient. (c) EK component of the gradient. (d) Simulated (thick black line) and observed gradient against depth (10^{-7} tolerance). (e) EED component of the gradient. (f) EK component of the gradient.

Note that none of the model results show the increase in gradient just before saline breakthrough that was observed in the field, because the precursor (Figure 6.23 – Figure 6.26) was not replicated in any of the models. However, they did show the gradient becoming increasingly shallow with time, as observed (Figure 6.24), which is shown in Figure 6.29 for a model run of one month. The gradient became shallower as the saline water moved through the fracture at the base of the borehole due to the decreased inland head between the steady-state (1 mAOD) and tidal runs (0.5 mAOD).

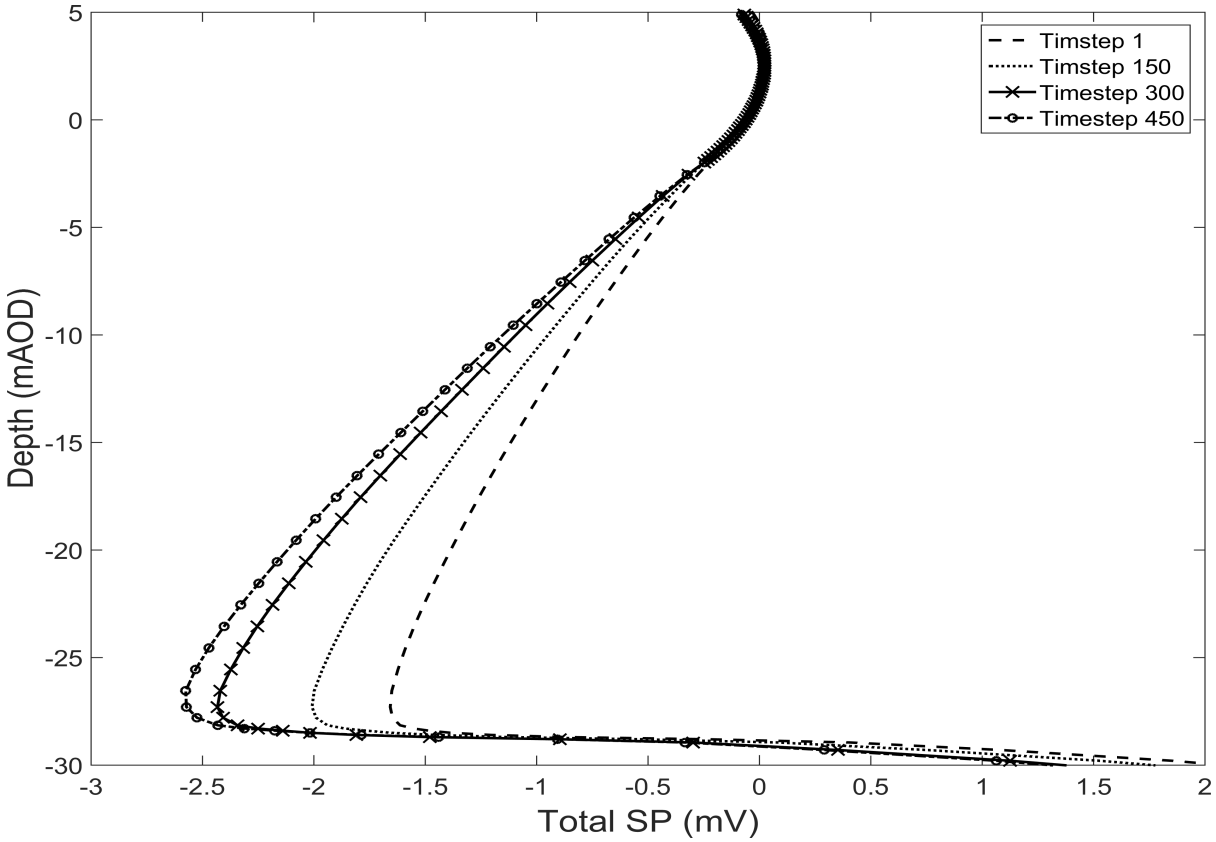

Figure 6.29 – (a) Change in gradient with time in the model runs with a tolerance of 10^{-5}, note each of these profiles was taken from the tidal cycle at high tide, so tidal movement of the saline front is not the reason for the change in gradient. Each time-step was two hours so the change in gradient over 21 days is shown, in increments of 7 days.

6.4.1 Impact of permeability structure at depth

The effect of the permeability structure at depth on the gradient was compared for Model 1(b) and Model 2(b) (Table 4.3). The SP contour plots for each of these models are shown in Figure 6.30 for the solver tolerance of 10^{-5}. As the saline front became steeper and moved further from the base of the borehole, the vertical SP gradient disappeared (Figure 6.31).

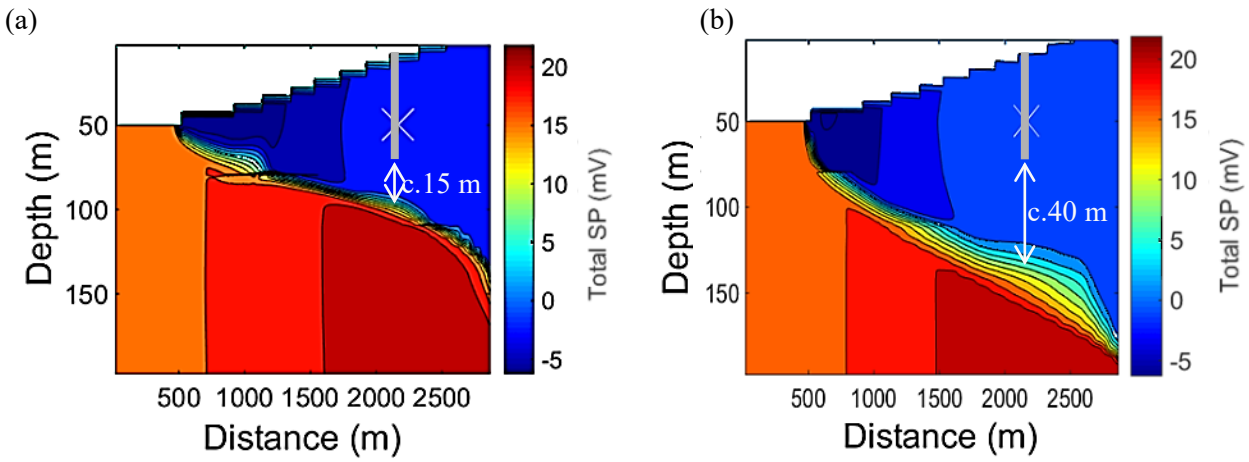

Figure 6.30 – TSP contours for models with different permeability structures at depth, the saline front can be distinguished by the grouping of SP contours around the source. (a) Model 1(b) with a linearly decreasing permeability at depth and a low inland head boundary condition resulted in a transition zone (TZ) of intermediate depth. (b) Model 2(b) also with a linearly decreasing permeability at depth, but this time with a high inland head boundary condition, resulted in the deepest TZ. Notice the impact the permeability structure at depth has on the distance (marked by the white arrows) from the base of the borehole (the grey line) to the mid-point of the TZ.

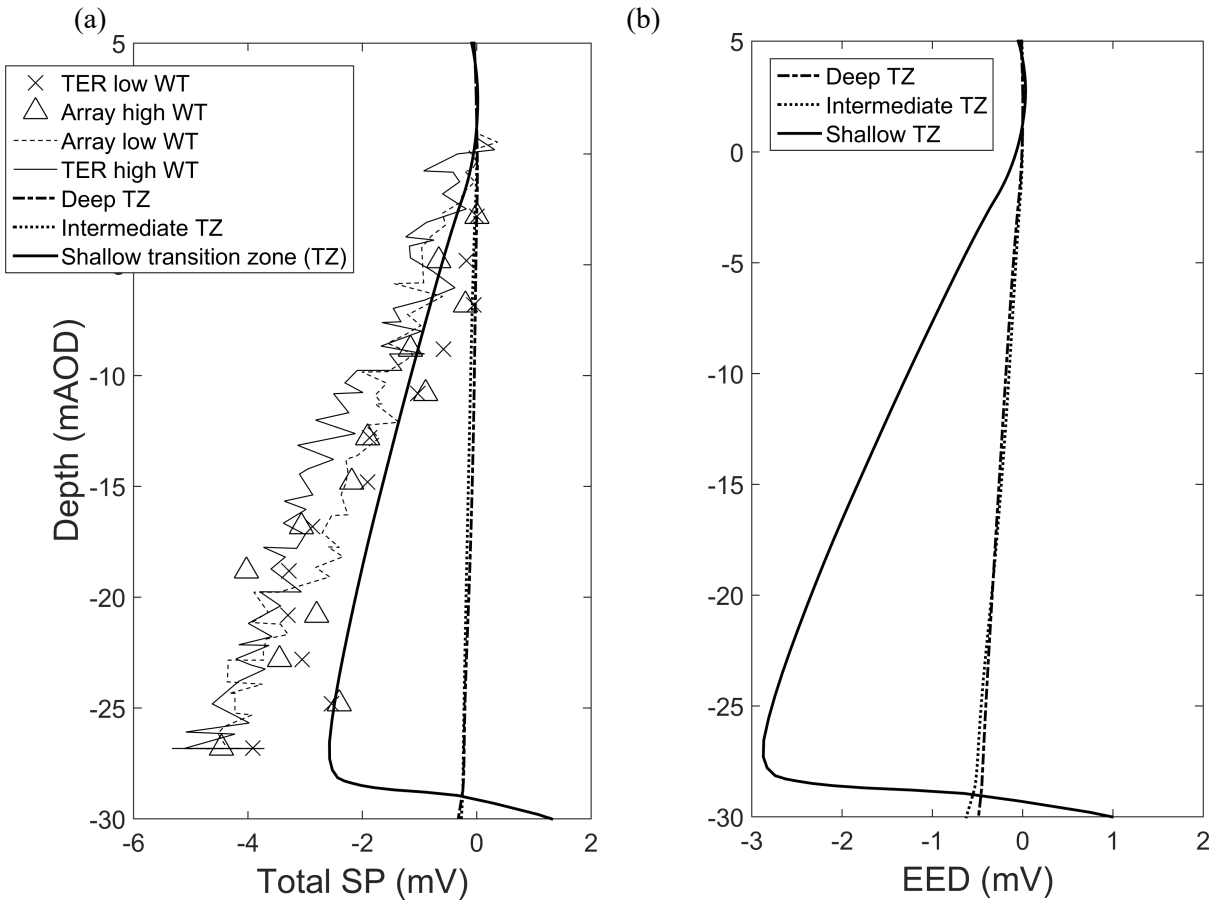

Figure 6.31 - (a) Change in gradient with increasing distance to the transition zone below the borehole. (b) The EED contribution to the voltage gradient for transition zones increasingly distant from the borehole. The EED component is the dominant contribution to the voltage gradient.

6.5 Discussion

Several authors have reported measurements of SP in coastal areas (Radhakrishna and Gangahara, 1990, Radhakrishna, 2001, Pezard et al., 2009, Kang et al., 2014); however, none have reported continuous and long-term SP measurements. Therefore, the results reported here provide the first evidence from field experiments of spatial and transient SP signals that appear to be indicative of the proximity of, and movement of a saline interface, some distance from a monitoring borehole in a coastal aquifer. However, several authors do report the use of SP for monitoring saline tracers in laboratory (Martinez-Pagan et al., 2010, Revil and Jardani, 2010, Ikard et al., 2012) and field experiments (Sandberg et al., 2002, Bolève et al., 2011, Ikard et al., 2012, Jougnot et al., 2015), and demonstrate that changes in SP appear to be detectable away from the source (see section 2.3.6.5).

There are two distinct features of the SP measurements reported in this chapter that appear to indicate the utility of SP as means of long-term monitoring and early warning of seawater intrusion. The first is the vertical SP gradient (c.0.22 mV/m) (Figure 6.16 – Figure 6.19), which modelling suggests indicates the close proximity of the saline front to the monitoring borehole (Figure 6.30 and Figure 6.31). The second is the observation of repeated systematic changes in SP that occurred just prior to saline breakthrough in late summer 2013 and 2014 (Figure 6.22 – Figure 6.26). The vertical SP gradient is discussed first followed by the SP precursor. However, before discussing these spatial and transient features of the SP data, the surface and borehole referencing configurations used for SP measurements are discussed.

6.5.1 Surface versus borehole referenced SP

Flow in the unsaturated zone is known to affect SP (Ernstson and Scherer, 1986, Thony et al., 1997, Perrier et al., 1997, Perrier, 2000, Darnet and Marquis, 2004) and it is possible that the increase in rainfall that started in mid-October 2013 (Figure 6.13) and continued through the rest of that winter led to saturation changes and/or vertical flow in the area around the reference electrode (Ref-C). These, in turn, resulted in the changes in voltage observed in Figure 6.13. Some authors suggest that SP measurements are useful in characterising flow processes in the unsaturated zone (Darnet and Marquis, 2004, Perrier, 2000, Ernstson and Scherer, 1986). In many cases such signals may be of interest; however, in others including for the purposes of the monitoring experiment reported here,

such signals are a source of noise and may mask the signals of interest. For example, the surface referenced SP (Figure 6.15) did not show any evidence of the SP precursor that appeared in the SP data when it was referenced against the shallowest borehole electrode (BH13-C) (Figure 6.21 - Figure 6.26). In the case of the diurnal and semi-diurnal SP (discussed in chapter 5) the periodicity of these signals meant that they would have appeared in the surface referenced data despite the effect of the transient signals generated in the unsaturated zone. However, the transient SP signals that occurred in the saturated zone (Figure 6.22 – Figure 6.26) may have been masked by these periodic and unsaturated zone transient processes. Unlike the precursor signal, the vertical gradient in SP was not masked by such complex processes at the surface reference electrode because; it was, and is, primarily a spatial feature of the SP data. Thus, the vertical SP gradient was present throughout the monitoring experiment regardless of the referencing scheme used (Figure 6.19 and Figure 6.24).

6.5.1 The vertical SP gradient

The vertical SP gradient, of c.0.22 mV/m, was a ubiquitous feature of the data from the Saltdean borehole (Figure 6.16 – Figure 6.19 and Figure 6.24). Furthermore, a vertical gradient was not observed at the inland site at Trumpletts Farm (Figure 4.1 and Figure 4.2) or, crucially, at the Balsdean OBH less than 1 km further inland (Figure 4.3). Therefore, the gradient appeared to be a result of the proximity of the saline front to the Saltdean borehole array. The proximity of the front was confirmed by the fact that saline breakthrough occurred at the Saltdean borehole (Figure 6.4). The lack of gradient at the Balsdean OBH and the lower baseline conductivity (Figure 6.6(b)) suggested that the saline front did not come close enough to cause any significant change in SP; which was true at least during the winter months when the SP data from this borehole was available.

The modelling suggests that the vertical gradient was primarily caused by the EED potential (Figure 6.28). Furthermore, the results from Model 1(b) and 2(b) (Table 4.3) suggested that as the salinity front became deeper (c.15 m and c.40 m respectively) with respect to the base of the borehole the gradient in SP disappeared (Figure 6.31). In model 3(b) the saline front was only c.4 m away from the base of the borehole (Figure 6.27). Therefore, it appears clear that the presence of the vertical gradient indicates the proximity of saline water to the borehole. The modelling results shown in Figure 6.29

also appeared to suggest that the gradient with depth, over a period of one month, changed systematically with time as the saline front moved through the aquifer towards the borehole. A similar observation was made in the field (Figure 6.19 and Figure 6.24). Therefore, observations of the change in gradient may be useful in determining whether the saline front is moving towards or away from the borehole.

Further evidence of the EED origin of the vertical gradient was provided by the fact that the polarity of the gradient remained constant throughout the monitoring period and across a tidal cycle. The conductivity profiles (Figure 6.7 - Figure 6.10) showed that there was vertical flow within the borehole. Therefore, there must also have been a vertical head gradient. As the head rose the water flowed up the borehole and as the head fell the water flowed back down; therefore, the vertical head gradient that led to this flow changed polarity when the head gradient reversed. Based on the laboratory measurements which showed that chalk has a negative EK coupling coefficient (Table 3.6) the vertical head gradient must lead to an EK potential of the opposite polarity. Since the vertical head gradient changed polarity across the tide, an EK source mechanism would also cause the polarity of the vertical voltage gradient to change, which was not observed (Figure 6.16 – Figure 6.19).

When the adit was included in the models (i.e. model 3(c) Table 4.3) a dynamic vertical head gradient was induced across the tidal cycle and the EK component did change polarity as predicted (Figure 6.32). Crucially, the EED component did not change polarity (Figure 6.33). Furthermore, EK, even with the adit included, could not explain the magnitude of the vertical gradient observed; the vertical change in EK was an order of magnitude too small. Therefore, the only possible source of the vertical gradient was the EED component of the SP, caused by the proximity of the saline front to the borehole. Note that because the borehole was not explicitly represented in the hydrodynamic model (section 4.3.1.2), flow was actually forced vertically through the bulk rock; thus, the head gradients in the model were likely to be overestimated yielding a higher EK component than was likely in reality.

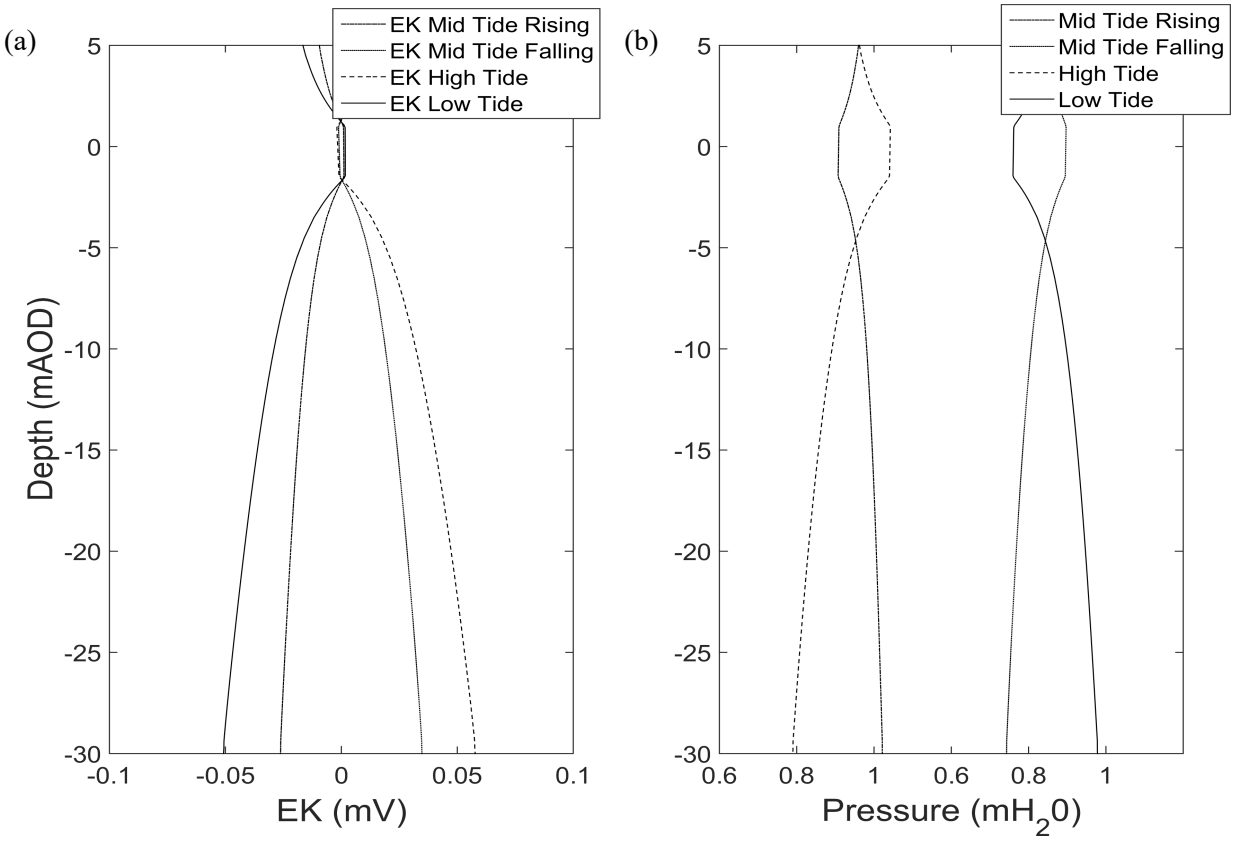

Figure 6.32 – (a) EK gradient across a tidal cycle with adit. (b) The head gradient across the same tidal cycle.

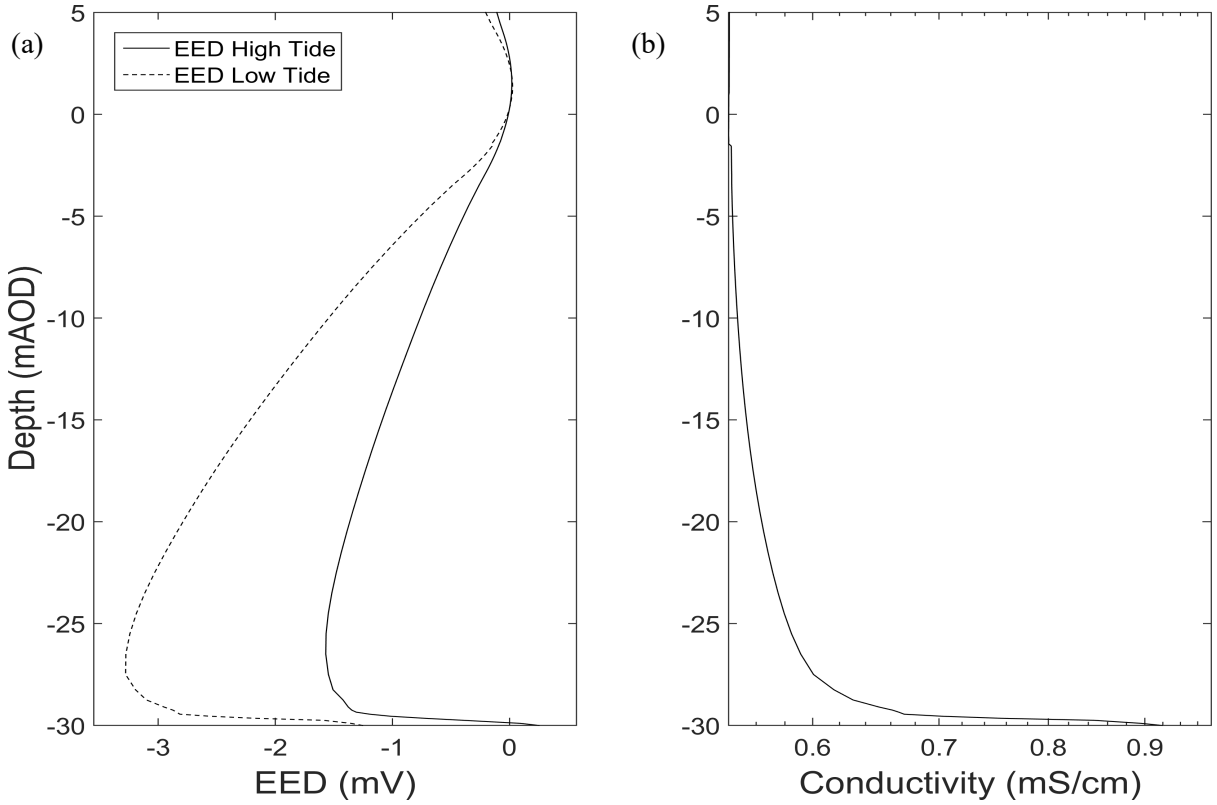

Figure 6.33 - (a) EED with depth across a tidal cycle with an adit included. (b) Conductivity with depth across the same tide cycle.

Vertical SP gradients have previously been reported in the literature (Ernstson and Scherer, 1986, Jougnot et al., 2015). However, both Ernstson and Scherer (1986) and Jougnot et al. (2015) reported SP gradients in the unsaturated zone. Ernstson and Scherer (1986) reported a positive SP gradient with depth, and it is likely that this was due to changes in the capillary head with depth. Jougnot et al. (2015) performed a saline tracer test in the unsaturated zone, and reported vertical distributions in SP after the tracer was injected. They suggested that the EED potential was likely to be the main source mechanism responsible for the vertical SP distribution observed in the top few metres of their monitoring array. However, their gradient appeared to be generated by the lateral movement of saline water towards their electrode array as opposed to the vertical distribution of saline water below the monitoring array (Figure 6.31). Also, Jougnot et al. (2015) only reported SP at three distinct times after injection of the tracer, and did not provide a continuous time series of the SP data as reported here. Finally, Pezard et al. (2009) reported vertically distributed SP from a coastal borehole in a limestone aquifer (Figure 2.17). Their borehole intersected the saline interface and their SP profiles appeared to show an increasingly negative SP with depth. Their gradient varied by approximately 50 mV over only 10 m, which is beyond the diffusion limit of the EED component (Table 3.7), and other factors must have contributed to the overall change of voltage with depth in their results. Thus, it appears that there is no previous evidence within the literature of a negative gradient of the type observed in the Saltdean monitoring borehole.

6.5.1.1 Impact of electrode effects on the vertical SP gradient

The SP profiles conducted using a single electrode demonstrates that the vertical SP gradient remains relatively constant throughout the monitoring period (c.0.22 mV/m, Figure 6.16 - Figure 6.18). Therefore, the significant change in the gradient recorded by the permanent array (Figure 6.18) after saline breakthrough in autumn 2013 was due to electrode effects caused by large changes in salinity at the electrodes (for further discussion see section 3.3.3.2). The effect was most significant at depth because the electrodes experienced the highest salinity at the base of the borehole (Table 6.1). Therefore, more diffusion of ions occurred across the electrode membrane at depth than it did higher in the borehole. The diffusion of different ionic species into the electrodes and the increase in chloride ions that occurred changed the intrinsic electrode potential. Maineult et al. (2005) demonstrated that

changes in SP were precisely correlated with the arrival of a concentration front at the electrodes, confirming that electrode performance is affected as soon as a salinity front reaches the electrodes. Jougnot and Linde (2013) demonstrated that when the concentration in the electrode chamber is much greater than the surrounding environment significant leakage of the chloride ions out of the electrode occurred. In the Saltdean borehole the opposite happened, the Silvion WE300 electrodes used in the borehole have a low chloride content (0.05M KCl) in the chamber (Silvion, 2015), which is most suitable for monitoring in the borehole pre-breakthrough. However, once the saline interface reached the borehole there was much higher chloride content in the surrounding environment than in the electrode chamber; thus, chloride and other ions diffused into the chamber changing the intrinsic potential and causing the drift visible after breakthrough in both 2013 and 2014. Once the salinity was entirely washed out of the borehole the effect was reversed, and the electrodes began to drift back to their equilibrium potential (i.e. March 2014 and December 2015 onwards).

6.5.2 The SP precursor

A precursor, of significant magnitude (c.300 μV), and of the type observed at the coastal site, has never previously been reported in the literature. However, the work of Martinez-Pagan et al. (2010) and Revil and Jardani (2010) is particularly relevant to this study, as they remotely monitored the progress of a descending 5.5 M NaCl plume in a sand tank experiment using SP. In their experiments the electrodes were placed at the bottom of the tank. They found that when the salt water reservoir, at the top of the tank, was opened all of the electrodes recorded a progressive change in the SP. The change was most significant (c.8 mV), and displayed a positive increase, consistent with this study (Figure 6.22- Figure 6.26), on the electrodes directly below the point at which the salt water entered the sand tank. They also pointed out, from numerical simulations of their experiments (Figure 2.16), that the SP signal decreased quickly outside the boundary of the plume which they argued explained the steady increase in the SP recorded in the electrode array. They attributed their measurements to the diffusion and EK potential associated with the pressure and chemical gradients in the sand tank, although they did not state which mechanism was dominant. However, it is likely, given the large concentration gradient introduced, that the EED potential contributed significantly. In addition, Bolève et al. (2011), observed an SP anomaly as a saline tracer moved through an embankment dam

which they attributed to the compression of the EDL and the resulting decrease in the EK coupling coefficient. However, Ikard et al. (2012) suggested the dominant component of the signal was the diffusion potential and suggested this would be consistent with the positive anomaly observed by Bolève et al. (2011). Bolève et al. (2011) did not comment on the timing of the transient SP signal in their array in relation to the position of the saline tracer, because they had no independent means of confirming its location. In contrast, the movement of the saline front towards the Saltdean borehole was confirmed by measurements of conductivity within the borehole.

The EED potential laboratory measurements (section 3.4.2) suggest that in chalk the voltage is positive in the seawater environment and negative in the groundwater. The conductivity profiles (Figure 6.7- Figure 6.10) suggested that the saline water entered the borehole at the base and Jones and Robins (1999) suggest that this was due to a fracture that provides a conduit for flow of saline water from the coast through the aquifer and into the borehole. The fracture aperture is significantly larger than the EDL (Table 3.8) so the diffusion potential is likely to be entirely dominant in the fracture, with a strong positive change in voltage occurring as the seawater front approaches the monitoring borehole through the fracture. However, the fact that the precursor is increasingly positive as the saline front approaches the borehole throughout summer but more negative at the high tide when the saline front is likely to be closest to the borehole during a tidal cycle, appears inconsistent (Figure 5.26). There are number possibilities as to why this apparent inconsistency may arise, including differential movement of the front at different timescales (e.g. tidal and seasonal), diffusion into and out of the matrix across the tide and with the seasons and its effect on the observed SP and differential rates of change in voltage measured at the electrodes within the array (see section 5.4.2.2). There is some evidence for the latter hypothesis, because SP changes were observed throughout the whole array (Figure 6.22 - Figure 6.26) and could have led to differential rates of change between different electrodes. However, at present there is not enough evidence to explain why the tidal SP and precursor are different and further work is required to investigate this.

It is also possible that the precursor consisted of a contribution from the change in head gradients as a result of the spring/neap cycle, resulting in an EK contribution to the precursor signal. However, the

spring/neap tides were apparent elsewhere in the head data, and at those times were not responsible for the same type of systematic increase in SP (see Figure 6.4 for demarcation of the spring/neap cycles), ruling out a dominant EK contribution. Thus, it is more likely that the EED component was dominant, with the current source (i.e. the saline interface) nearer the borehole during the spring tide. After breakthrough the decreases in conductivity in the borehole were clearly related to the neap tide (Figure 6.4). Thus, it appears reasonable to attribute the precursor signal to the fact that the saline interface was in closer proximity to the borehole due to the increased driving head at the coast during the spring tide and the decreased inland head in late summer, which led to breakthrough (Figure 6.4) and explains the shape of the SP precursor (Figure 6.22 - Figure 6.26).

Figure 6.23 shows a systematic change in SP, but of smaller magnitude (c.100 μV), prior to a subtle change in conductivity within the borehole. The change in SP was most likely due to changes in the salinity front some distance from the borehole, resulting in only small changes in conductivity within the borehole. Therefore, it appears that SP did provide a clear indication of the movement of saline water in the vicinity of the monitoring borehole. Crucially, saline breakthrough was not required in order for the precursor to be observed. Therefore, SP did provide early warning of imminent saline breakthrough. The SP response to the movement of the saline front towards the monitoring borehole was confirmed by the SP precursor observed prior to two consecutive saline breakthrough events in 2013 (Figure 6.22) and again in 2014 (Figure 6.25 and Figure 6.26). Crucially, and unlike previous studies (Bolève et al., 2011, Sandberg et al., 2002), the timing of the transient SP anomaly was tied to conductivity measurements which proved that saline water entered the borehole. The precursor began up to c.7 days before saline breakthrough, clearly indicating the possibility of using SP measurements as an early warning of imminent saline breakthrough at monitoring or abstraction boreholes. Early warning of this nature could provide the means for improved management of seawater intrusion in fractured coastal aquifers, possibly even allowing proactive management of abstraction regimes for coastal water supplies. Thus, SP monitoring may facilitate significant improvements in resource management in coastal aquifers. However, further work is required to fully understand the nature of the precursor. Furthermore, the signal was only observed in retrospect, after smoothing and filtering

was applied to the data. Therefore, further work is also required to determine whether the signal can be detected in real time and to develop a means of avoiding false positive SP warnings that may be caused by other effects within the SP data. Finally, the use of inversion algorithms has previously been shown to allow the position of the saline front to be determined from remote SP measurements (Martinez-Pagan et al., 2010). Such information would strengthen the use of SP monitoring in coastal aquifer management, and could be investigated in future work.

6.5.4 EED component SP solver tolerance

The field results demonstrate that SP monitoring has huge potential for resource management in coastal aquifers. However, although the EED model results also appear very promising, the sensitivity of this component to the solver tolerance leaves some questions over these particular results. In all models the MINRES method (Barrett et al., 1994, Van der Vorst, 2003) was used to solve the electrodynamic problem. However, it appeared that either the EED component could not reach an accurate solution before stagnating with a low tolerance (10^{-7}) or that it overshot the solution (Hoffman and Frankel, 2001, Szymkiewicz, 2012). Overshoot is a problem that is known to occur in some iterative methods (Hoffman and Frankel, 2001, Harbaugh, 2005, Szymkiewicz, 2012). The fact that the results from the higher tolerance (10^{-5}) produced a reasonable match to the field data suggest that overshot may have occurred using the lower tolerance (10^{-7}). When the tolerance was set larger than 10^{-7} the solver reported convergence. At tolerances smaller than this the solver stagnated, which may indicate breakdown of the method (Leyk, 1997). To reiterate, the same problem did not arise for the EK component of the model.

Before discussing possible solver issues, it is also important to acknowledge that the hydrodynamic model may not capture some of the processes occurring in the field. It is possible, for example, that the salinity distribution may not be accurately captured due to the lack of diffusion (section 4.3.1). Alternatively, there may be important three dimensional effects in operation at the field site that are not captured in the two dimensional models. However, the hydrodynamic models were rigorously developed based on the available evidence and any additions, with the exception of explicit inclusion of diffusion, would be based on speculation. However, it is worth noting that in their studies Maineult

et al. (2004) and Jougnot et al. (2015) went so far as to apply an arbitrary multiplier to their EED modelling results in order to match their SP observations, which might hint at problems with the present EED potential theory (Jougnot et al., 2015). Further work would be required to establish whether this is the case.

However, it is most likely that the issue is related to the solver. For example, Graham et al. (2016) found that the EED component, using the same solver, depended on model refinement. Unfortunately the model reported here already consisted of approximately 90,000 cells making further refinement very difficult. However, it is worth noting that the models were most highly refined around the borehole. In order to refine the model further, much more significant computational resources would be required. Therefore, it may be more computationally feasible to investigate the processes at a smaller scale. Another possibility is the use of local grid refinement in the area of the grid where the SP is generated (i.e. across the saline transition zone). Commonly local grid refinement uses the results from the global grid to provide the boundary conditions to the local grid, allowing a more highly refined grid in areas of the model that are of interest (Schlumberger, 2010). Another emerging method that could provide a solution is adaptive mesh technology (Jackson et al., 2015), where the grid automatically refines in the area around the current source (i.e. the salinity front). In principal adaptive mesh technology could be applied in future to solve the EED component problem. Such work is beyond the scope of this study. Despite the problems with the EED component, the arguments outlined above still provide strong evidence of the dominance of the EED component in the observed SP, both as the source mechanism for the vertical SP gradient and the pre-saline breakthrough SP precursor, making the SP of great interest to coastal water resources managers.

6.6 Conclusions

Saline breakthrough occurred in 2013 and 2014 at the Saltdean monitoring borehole. The breakthrough of saline water was due to a steady decline in the head over the summer months, in turn caused by a decline in recharge due to low rainfall. The highest conductivity values measured in the borehole were a result of the spring tide during late summer when the inland water levels were lowest. Conductivity profiling after saline breakthrough revealed vertical flow in the borehole, which

modelling suggested was caused by the presence of an adit at the top of the borehole. The salinity in the top few metres of the borehole remained relatively constant throughout the monitoring period suggesting inflow of fresh water controlled by the existence of the adit.

A ubiquitous vertical gradient in SP was only observed in the borehole nearest to the coast. There was no evidence of a similar gradient at a borehole many miles from the coast, or even at borehole only 1 km further inland. Therefore, the vertical gradient appears to be related to the presence of the saline front just below (c.4 m) the monitoring borehole. The gradient maintained a constant polarity, so could not have been caused by the EK potential. Further evidence, for this was provided by the numerical modelling results which suggested that as the saline front moved further from the borehole the vertical gradient disappeared. Thus, the main source mechanism for the gradient was the close proximity of the saline front to the base of the borehole caused by the EED potential that arose due to the concentration gradient between seawater and groundwater. Therefore, the change in gradient may, in fact, be the most interesting part of the SP data for improved management of the coastal aquifer. For example, continued monitoring of the gradient could be used to manage abstraction from coastal boreholes. Although the modelling results appear to support the EED origin of the vertical gradient, further work is required to understand the reason for the EED components sensitivity to tolerance.

An SP precursor was observed consistently prior to saline breakthrough. The precursor was caused by the movement of the saline front towards the monitoring borehole over the summer months. The SP systematically increased prior to increased conductivity within the borehole, with a maximum change in SP of c.300 μV. Saline breakthrough at the borehole was not required in order for the precursor to be observed, with SP signals of c.100 μV preceding even very subtle changes in the baseline conductivity in July 2013. The precursor began up to c.7 days before breakthrough. Therefore SP, does in fact, provide early warning of the movement of the saline front towards the monitoring borehole in the fractured Chalk aquifer, although further work is required to understand how the precursor signal could be utilised to improve management of the Chalk coastal aquifer.

Chapter 7

Conclusions

7.1 Summary and conclusions

Self-potential monitoring of seawater intrusion into a fractured coastal aquifer has been investigated using laboratory, field and numerical experiments. The results demonstrate that SP signals are of sufficient magnitude to be measured in coastal aquifers and yield useful spatial and temporal information on the movement of a saline front towards an observation borehole 1.7 km from the coast in the fractured Chalk aquifer on the South Coast of the UK.

7.1.1 Characterising SP in chalk

The relative contributions of the exclusion-diffusion (EED) and electrokinetic (EK) potential components of SP were investigated by conducting laboratory and numerical experiments. The laboratory experiments demonstrated that the EED potential in chalk is positive (with respect to a reference electrode in groundwater) and dominated by the diffusion potential. The relative contribution of exclusion and diffusion potentials to the EED component is influenced by the chalk surface charge, the thickness of the EDL and the ionic strength of groundwater. The EK coupling coefficient was negative so changes in pressure in the coastal aquifer yield a change in voltage of the opposite polarity. The measured values were used in a numerical model of the coastal aquifer to investigate the contribution of EED and EK to the SP observed in the field monitoring experiment.

7.1.2 The tidal SP

The SP at the coast contained a strong tidal signature. The M_2 principal lunar component was the dominant periodic component at the coastal site in both surface referenced and borehole referenced SP. However, the M_2 component also appeared in the surface array at an inland site in the Chalk aquifer, the origin of the M_2 signal appeared to be partly due to telluric currents caused by the geomagnetic ocean dynamo. However, Earth and atmospheric tides were also likely to contribute to the M_2 component at the inland site. The presence of the M_2 signal inland raises questions about the applicability of SP surface monitoring in coastal areas. However, careful selection of the reference

electrode location can mitigate the problem if long-term surface SP monitoring is necessary. Ideally though, surface referenced SP monitoring should be avoided in coastal aquifers due to the complications of geomagnetic, Earth and atmospheric tide processes that share many of the same periodic components as the ocean tide. Thus, the SP data reported were primarily referenced against the shallowest borehole reference electrode, which minimised the impact of these effects.

The M_2 component referenced in the borehole at the inland site was well below the 50% significance level from the PSD analysis, strongly suggesting that the much more significant M_2 component (c. 600 μV) referenced in the same way at the coastal site was primarily driven by hydrodynamic processes in the aquifer caused by the tides in the English Channel. Detailed analysis of the periodic signals at the coastal site suggested that the EK potential could not be solely responsible for the semi-diurnal SP observed, because the magnitudes of the coupling coefficients estimated over a tidal cycle were far larger than the maximum coupling coefficient measured in the laboratory. Therefore, the EED component must contribute significantly to the observed tidal SP. The dominance of the EED potential was supported by numerical modelling, which showed that that the EED component (c.0.6 – 1.2 mV) was an order of magnitude larger than the EK potential (c.0.02 – 0.1 mV). Therefore, the EED potential appears to be primarily responsible for the tidal SP, despite the issues encountered with the EED component of the SP solver. The numerical modelling suggested that the tidal SP was caused by the movement of saline water, some distance from the monitoring borehole (possibly up to c.200 m away), primarily through a fracture near the base of the borehole and superimposed on smaller tidal fluctuations within the matrix (c.4 m from the borehole). The dominance of the EED component in the tidal signature implies that the SP recorded in the borehole responded to the movement of a remote saline front long before saline breakthrough occurred at the borehole. Thus, the tidal SP provides evidence of the utility of SP measurements for remote monitoring of seawater intrusion.

7.1.3 The vertical SP gradient

Longer-term spatial, temporal and transient effects in the coastal SP time-series were also identified. The first of these observations was the consistent presence of a vertical SP gradient (c.0.22 mV/m) in the Saltdean borehole nearest the coast. The vertical gradient maintained a constant polarity

throughout the monitoring campaign. No such gradient was observed at the inland site in Berkshire, nor was it observed in the Balsedean OBH less than 1 km further inland. The absence of the gradient at the two sites further from the coast provided clear evidence that the gradient indicated the proximity of the saline front to the monitoring borehole. The numerical models confirmed that the close proximity of the saline front below the monitoring borehole was responsible for the vertical SP gradient, which disappeared as the distance from the base of the monitoring borehole to the saline front increased. In the models that yield a gradient the saline front was only a few metres (c.4 m) away. The EED origin of the vertical gradient was supported by numerical modelling, which clearly demonstrated that the EK component is insufficient to generate the observed SP gradient, even when vertical flow was accounted for due to the presence of an adit at the top of the borehole. The presence of the gradient is indicative of the saline front in close proximity to the monitoring borehole.

The gradient itself may provide sufficient evidence to alter pumping regimes to avoid saline breakthrough at an abstraction borehole. Furthermore, small changes observed in the vertical SP gradient appear to indicate the movement of saline water, towards or away from the monitoring borehole, and could allow proactive management of abstraction within the borehole. It is possible to envisage an SP tool installed in an abstraction borehole that allows daily automatic SP profiles to be conducted using a single travelling electrode referenced against a stationary electrode in the top of the borehole. The use of a single travelling electrode would avoid the electrode affects and differential electrode drift experienced by the permanent array in the Saltdean borehole after saline breakthrough. Decline in head within the borehole could then automatically trigger an increased SP profile sampling rate, which would allow small changes in the gradient to be observed. The polarity of the change would indicate whether the saline interface was moving towards or away from the abstraction borehole and abstraction rates could be adjusted accordingly.

7.1.4 The SP precursor

Finally, there was a systematic change in voltage just prior to saline breakthrough at the borehole that occurred in two consecutive years. In August 2013 and 2014, tidal processes coupled with a decline in inland head caused saline water to enter the monitoring borehole. Fluid electrical conductivity logging

over a tidal cycle showed that entry was via the fracture near the base of the borehole. Prior to each occurrence of saline breakthrough, an increase in the SP of c.300 μV was observed, commencing c.7 days before saline water was detected in the borehole. Furthermore, smaller precursor signals of c.100 μV were observed prior to subtle conductivity changes within the borehole, suggesting that saline breakthrough is not required for SP to respond to the movement of the saline front towards the borehole. However, it is not clear at present how this signal could be used in real time.

7.1.5 Summary

This study provides clear evidence for the utility of SP monitoring in a fractured coastal aquifer. The SP responds to the tidal processes within the aquifer primarily due to changes in the position of the saline front across the tidal cycle. Therefore, SP yields information on the approximate temporal behaviour of the saline front in relation to the monitoring borehole. Furthermore, significant transient features were identified in the SP time-series that began before any changes in conductivity within the borehole. These features strongly indicate that the SP can provide early warning days in advance of saline breakthrough at a monitoring borehole. Finally, the vertical SP gradient appears to indicate the proximity of the saline front to the monitoring borehole. The gradient is a ubiquitous feature of the SP within the coastal borehole and could be utilised immediately by water resource managers. Thus, this study suggests that SP monitoring can be used as a tool to improve seawater intrusion monitoring, allowing dense sampling in space and time, and improving management of highly exploited fractured coastal aquifers at significant risk of seawater intrusion. With the aims and key research questions, set out in section 1.2, in mind, this thesis shows that:

(i) SP can be used to monitor seawater intrusion into the coastal Chalk aquifer;

(ii) SP respond to tidal processes within the aquifer, which appear to be driven by changes in the position of the saline front;

(iii) SP appears to provide early warning of imminent saline breakthrough at a coastal monitoring borehole.

Furthermore, the thesis provides a number of original contributions to the study of SP and seawater intrusion monitoring; not least by reporting the first long-term field monitoring experiment of seawater intrusion using SP. The key contributions are:

(i) EED potential was measured for the first time in chalk and, more significantly, using natural electrolytes. A new method was developed for achieving repeatable and reliable experimental results.

(ii) Earth, atmospheric and geomagnetic tides were shown to be important when using surface referenced SP, but it was demonstrated that borehole referenced SP is less vulnerable to these effects and the SP measured in the costal borehole responded to tidal movement of the saline front.

(iii) A vertical SP gradient of the type observed in the coastal borehole has never previously been reported. The gradient appeared to be a result of the close proximity of the saline front to the monitoring borehole, and also responded to the movement of the saline front as the inland head declined over the summer.

(iv) Finally, this thesis demonstrates that the movement of a saline front can be remotely detected, providing the first independently confirmed SP early warning of imminent saline breakthrough at a monitoring borehole in a coastal aquifer.

7.2 Future work

Despite the progress that has been made in understanding the SP source mechanisms within the fractured coastal aquifer in the South Downs, and in demonstrating that SP can provide useful spatial and temporal information on the evolution of the salinity front with respect to an observation borehole, significant questions remain and further work is required to address them. For example, the work was only conducted in a highly fractured Chalk aquifer and it is not clear whether the observations made are unique to this system. Thus, further investigations are required at another site, preferably with a better characterised and more homogenous geology. It would also be useful to instrument a second borehole near the coast to determine whether the vertical SP gradient is observed in other parts of the coastal Chalk aquifer, where seawater intrusion is known to be a risk.

It was only possible to instrument an observation borehole in this study, for early warning purposes it would be preferable to instrument an abstraction borehole. However, it is not clear how easy this would be, given the likely additional levels of noise associated with instrumenting an abstraction borehole with electrodes. Further investigations are required to understand whether this is feasible.

The modelling work reported approximated the system as an equivalent porous medium; however a dual permeability approach would allow more rigorous investigation of diffusive exchange between the fractures and the matrix which may contribute towards the SP signals observed at the coast. For example, seasonal and tidal changes, including the possible inversion of the concentration gradient between the fractures and matrix may be important. Thus, further investigation of the relationship between the process that occurs in, and between, the fracture and matrix are required, and should be conducted by explicit inclusion of diffusion and dispersion within the hydrodynamic model.

There also remains some uncertainty over the EED potential results from the SP solver. Therefore, further work is required to understand why the EED component seems to be dependent on model tolerance. A detailed grid refinement study should be conducted and the application of local grid refinement or adaptive meshing methods should be investigated.

So far it has not been possible to simulate the systematic increase in voltage just prior to saline breakthrough at the observation borehole. Thus, further numerical modelling work is required to investigate the cause of the systematic change in voltage prior to saline breakthrough. Furthermore, although there is a clear precursor prior to each occurrence of saline breakthrough at the Saltdean borehole, it is not clear at present how this signal could be used to improve management of the coastal aquifer. The precursor was only observed in retrospect and methods allowing the SP precursor signals to be observed in real time would have to be developed for SP monitoring to be utilised for improved aquifer management. Furthermore, methods or criteria to determine the significance of a change in the background SP would have to be clearly developed and established in order to avoid false positive SP warnings. Only then could the SP precursor signal be used to proactively manage coastal abstraction. Finally, an inversion algorithm could be developed by which the distance of the saline front from the monitoring or abstraction borehole could be predicted using the measured SP signals.

References

Abarca, E., Carrera, J., Sanchez-Vila, X. & Dentz, M. 2007. Anisotropic dispersive Henry problem. *Advances in Water Resources,* 30**,** 913-926.

Ackerer, P., Younès, A. & Mancip, M. 2004. A new coupling algorithm for density-driven flow in porous media. *Geophysical Research Letters,* 31**,** L12506.

Ackerer, P., Younes, A. & Mose., R. 1999. Modelling variable density flow and solute transport in porous medium: 1. Numerical model and verification. *Transport in Porous Media,* 35**,** 345-373.

Adler, P. M., Thovert, J.-F., Jacquin, C., Morat, P. & Le Mouel, J.-L. 1997. Electrical signals induced by the atmospheric pressure variations in unsaturated media. *Comptes rendus de l'Académie des sciences. Série 2. Sciences de la terre et des planètes,* 324**,** 711-718.

Agnew, D. C. 2007. 3.06 - Earth tides. *In:* SCHUBERT, G. (ed.) *Treatise on geophysics.* Amsterdam: Elsevier.

Allen, D., Brewerton, L., Coleby, L., Gibbs, B., Lewis, M., Macdonald, A., Wagstaff, S. & Williams, A. 1997. The physical properties of major aquifers in England and Wales.

Alroudhan, A. 2015. *Wettability characterization using streaming potential measurements.* PhD, Imperial College London.

Alroudhan, A., Vinogradov, J. & Jackson, M. D. 2016. Zeta potential of intact natural limestone: Impact of potential-determining ions Ca, Mg and SO_4. *Colloids and Surfaces A: Physicochemical and Engineering Aspects*.

Andersen, M. S., Jakobsen, V. N. R. & Postma, D. 2005. Geochemical processes and solute transport at the seawater/freshwater interface of a sandy aquifer. *Geochimica et Cosmochimica Acta,* 69**,** 3979-3994.

Anderson, L. & Johnson, G. 1973. Application of self-potential method in search for geothermal energy. *Geophysics,* 38**,** 1190-1190.

Anderson, W. G. 1986. Wettability literature survey-part 3: The effects of wettability on the electrical properties of porous media. *Journal of Petroleum Technology,* 38**,** 1,371-1,378.

Angelis, M. D. 2005. Major ions in seawater. *Water encyclopedia.* John Wiley & Sons, Inc.

Apel, J. R. 1987. *Principles of ocean physics*, Elsevier Science.

Arora, T., Linde, N., Revil, A. & Castermant, J. 2007. Non-intrusive characterization of the redox potential of landfill leachate plumes from self-potential data. *Journal Contaminant Hydroogyl,* 92**,** 274-92.

Ataie-Ashtiani, B., Volker, R. E. & Lockington, D. A. 1999. Tidal effects on sea water intrusion in unconfined aquifers. *Journal of Hydrology,* 216**,** 17-31.

Banks, D., Davies, C. & Davies, W. 1995. The chalk as a karstic aquifer: Evidence from a tracer test at Stanford Dingley, Berkshire, UK. *Quarterly Journal of Engineering Geology and Hydrogeology,* 28**,** S31-S38.

Baptista, A. M., Westerink, J. J. & Turner, P. J. 1989. Tides in the English Channel and southern North Sea. A frequency domain analysis using model tide-nl. *Advances in Water Resources,* 12**,** 166-183.

Barker, J. A. & Foster, S. S. D. 1981. A diffusion exchange model for solute movement in fissured porous rock. *Quarterly Journal of Engineering Geology and Hydrogeology,* 14**,** 17-24.

Barlow, P. M. 2003. *Ground water in fresh water-salt water environments of the Atlantic*, Geological Survey (USGS).

Barrett, R., Berry, M. W., Chan, T. F., Demmel, J., Donato, J., Dongarra, J., Eijkhout, V., Pozo, R., Romine, C. & Van Der Vorst, H. 1994. *Templates for the solution of linear systems: Building blocks for iterative methods*, Siam.

Barry, P. H. & Diamond, J. M. 1970. Junction potentials, electrode standard potentials, and other problems in interpreting electrical properties of membranes. *The Journal of Membrane Biology,* 3**,** 93-122.

Båth, B. 2012. *Spectral analysis in geophysics*, Elsevier.

Bear, J., Cheng, A. H. D., Sorek, D. & Herrera, I. 1999. *Seawater intrusion in coastal aquifers - concepts, methods and practices,* Dordrecht, The Netherlands, Kluwer Academic Publishers.

Berkowitz, B. 2002. Characterising flow and transport in fractured geological media-a review. *Advances in Water Resources,* 25**,** 861-884.

Berkowitz, B., Bear, J. & Braester, C. 1988. Continuum models for contaminant transport in fractured porous formations. *Water Resources Research,* 24**,** 1225-1236.

Bindoff, N., Lilley, F. & Filloux, J. 1988. A separation of ionospheric and oceanic tidal components in magnetic fluctuation data. *Journal of Geomagnetism and Geoelectricity,* 40**,** 1445-1467.

Bitton, G. 1998. Formula handbook for environmental engineers and scientists. New York :: J. Wiley.

Bloomfield, J. 1996. Characterisation of hydrogeologically significant fracture distributions in the chalk: An example from the Upper Chalk of southern England. *Journal of Hydrology,* 184**,** 355-379.

Bloomfield, J. P., Brewerton, L. J. & Allen, D. J. 1995. Regional trends in matrix porosity and dry density of the chalk of England. *Quarterly Journal of Engineering Geology and Hydrogeology,* 28**,** S131-S142.

BODC, 2015. *UK tide gauge network* [Online]. British Oceanographic Data Centre. Available: https://www.bodc.ac.uk/data/online_delivery/ntslf/ [Accessed 13/08/205 2015].

Bolève, A., Janod, F., Revil, A., Lafon, A. & Fry, J. J. 2011. Localization and quantification of leakages in dams using time-lapse self-potential measurements associated with salt tracer injection. *Journal of Hydrology,* 403**,** 242-252.

Bolève, A., Vandemeulebrouck, J. & Grangeon, J. 2012. Dyke leakage localization and hydraulic permeability estimation through self-potential and hydro-acoustic measurements: Self-potential 'abacus' diagram for hydraulic permeability estimation and uncertainty computation. *Journal of Applied Geophysics,* 86**,** 17-28.

Bower, D. R. 1983. Bedrock fracture parameters from the interpretation of well tides. *Journal of Geophysical Research: Solid Earth,* 88**,** 5025-5035.

Braun, B. M. & Weingartner, H. 1985. Transference numbers of aqueous nacl and Na_2SO_4 at 25°c from emf measurements with sodium-selective glass electrodes. *Journal of Solution Chemistry,* 14**,** 675-686.

Bristow, R., Mortimore, R. & Wood, C. 1997. Lithostratigraphy for mapping the chalk of southern England. *Proceedings of the Geologists' Association,* 108**,** 293-315.

Brown, G. M. & Woods, W. G. 1971. Tidal influence on Earth currents at a coastal station. *Journal of Atmospheric and Terrestrial Physics,* 33**,** 289-293.

Bullard, E. 2011. *Physical properties of sea water* [Online]. Middlesex: Kaye and Labye National Physical Laboratory. Available: http://www.kayelaby.npl.co.uk/general_physics/2_7/2_7_9.html [Accessed 22 June 2012 2012].

Bumpus, P. B. & Kruse, S. E. 2014. Self-potential monitoring for hydrologic investigations in urban covered-karst terrain. *Geophysics,* 79**,** B231-B242.

Burbey, T. J. 2010. Fracture characterization using Earth tide analysis. *Journal of Hydrology,* 380**,** 237-246.

Butler, A., Hughes, A., Jackson, C., Ireson, A., Parker, S., Wheater, H. & Peach, D. 2012. Advances in modelling groundwater behaviour in chalk catchments. *Geological Society, London, Special Publications,* 364**,** 113-127.

Butler, A. P., Mathias, S. A., Gallagher, A. J., Peach, D. W. & Williams, A. T. 2009. Analysis of flow processes in fractured chalk under pumped and ambient conditions (uk). *Hydrogeology Journal,* 17**,** 1849-1858.

Byrdina, S., Friedel, S., Wassermann, J. & Zlotnicki, J. 2003. Self-potential variations associated with ultra-long-period seismic signals at merapi volcano. *Geophysical Research Letters,* 30.

Byrne, M. & Patey, I. Core sample preparation—an insight into new procedures. International symposium of the society of core analysts, Abu Dhabi, UAE, 2004.

Capaccioni, B., Didero, M., Paletta, C. & Didero, L. 2004. Saline intrusion and refreshing in a multilayer coastal aquifer in the catania plain (Sicily, southern Italy): Dynamics of degradation processes according to hydrochemical characteristics of groundwaters. *Journal of Hydrology,* 307**,** 1-16.

Carey, H., Lenkopane, M. K., Werner, A. D., Li, L. & Lockington, D. A. 2009. Tidal controls on coastal groundwater conditions: Field investigation of a macrotidal system. *Australian Journal of Earth Sciences,* 56**,** 1165-1179.

Castermant, J., Mendonça, C. A., Revil, A., Trolard, F., Bourrié, G. & Linde, N. 2008. Redox potential distribution inferred from self-potential measurements associated with the corrosion of a burden metallic body. *Geophysical Prospecting,* 56**,** 269-282.

Chae, G.-T., Yun, S.-T., Yun, S.-M., Kim, K.-H. & So, C.-S. 2012. Seawater–freshwater mixing and resulting calcite dissolution: An example from a coastal alluvial aquifer in eastern South Korea. *Hydrological Sciences Journal,* 57**,** 1672-1683.

Chapman, S. & Kendall, P. C. 1970. Sea tidal generation of electric currents and magnetic fields: Applications to five stations within the British Isles. *Planetary and Space Science,* 18**,** 1597-1605.

Chen, Y. J., Chen, G. Y., Yeh, H. D. & Jeng, D. S. 2011. Estimations of tidal characteristics and aquifer parameters via tide-induced head changes in coastal observation wells. *Hydrology and Earth System Sciences,* 15**,** 1473-1482.

Christensen, L., Fregerslev, S., Simonsen, A. & Thiede, J. 1973. Sedimentology and depositional environment of lower danian fish clay from stevns klint, denmark. Bulletin of the Geological Society of Denmark, 22, 193-212.

Cicerone, D. S., Regazzoni, A. E. & Blesa, M. A. 1992. Electrokinetics properties of calcite/water interface in the presence of magnesium and organic matter. *Journal of Colloid and Interface Science,* 154**,** 423-433.

Cochrane, N. A. & Srivastava, S. P. 1974. Tidal influence on electric and magnetic fields recorded at coastal sites in Nova Scotia, Canada. *Journal of Atmospheric and Terrestrial Physics,* 36**,** 49-59.

Comte, J.-C. & Banton, O. 2007. Cross-validation of geo-electrical and hydrogeological models to evaluate seawater intrusion in coastal aquifers. *Geophysical Research Letters,* 34.

Cook, S. Fri 11/05/2012 11:45 2012. *RE: Saltdean activities.* Type to MACALLISTER, D.

Cook, S. J., Fitzpatrick, C. M., Burgess, W. G., Lytton, L., Bishop, P. & Sage, R. 2012. Modelling the influence of solution-enhanced conduits on catchment-scale contaminant transport in the Hertfordshire Chalk aquifer. *Geological Society, London, Special Publications,* 364**,** 205-225.

Cooper, H. H., Kohout, F. A., Henry, H. R. & Glover, R. E. 1964. Sea water in coastal aquifers. *Relation of salt water to fresh groundwater.* USA: USGS.

Corwin, R. F. 1990. The self-potential method for environmental and engineering applications. *Geotechnical and Environmental Geophysics,* 1**,** 127 - 145.

Corwin, R. F. & Hoover, D. B. 1979. Self-potential method in geothermal-exploration. *Geophysics,* 44**,** 226-245.

Corwin, R. F. & Morrison, H. F. 1977. Self-potential variations preceding earthquakes in central California. *Transactions-American Geophysical Union,* 58**,** 560-561.

Cueto, M., Mcknight, D. & Herraiz, M. 2003. Daily geomagnetic variations on the Iberian Peninsula. *Geophysical Journal International,* 152**,** 113-123.

Cutillo, P. A. & Bredehoeft, J. D. 2011. Estimating aquifer properties from the water level response to Earth tides. *Ground Water,* 49**,** 600-610.

Dai, A. & Wang, J. 1999. Diurnal and semidiurnal tides in global surface pressure fields. *Journal of the Atmospheric Sciences,* 56**,** 3874-3891.

Damgaard, L. R., Risgaard-Petersen, N. & Nielsen, L. P. 2014. Electric potential microelectrode for studies of electrobiogeophysics. *Journal of Geophysical Research: Biogeosciences,* 119**,** 1906-1917.

Darnet, M. & Marquis, G. 2004. Modelling streaming potential (SP) signals induced by water movement in the vadose zone. *Journal of Hydrology,* 285**,** 114-124.

De Franco, R., Biella, G., Tosi, L., Teatini, P., Lozej, A., Chiozzotto, B., Giada, M., Rizzetto, F., Claude, C., Mayer, A., Bassan, V. & Gasparetto-Stori, G. 2009. Monitoring the saltwater intrusion by time lapse electrical resistivity tomography: The Chioggia test site (Venice lagoon, Italy). *Journal of Applied Geophysics,* 69**,** 117-130.

Dokou, Z. & Karatzas, G. P. 2012. Saltwater intrusion estimation in a karstified coastal system using density-dependent modelling and comparison with the sharp-interface approach. *Hydrological Sciences Journal-Journal Des Sciences Hydrologiques,* 57**,** 985-999.

Doodson, A. T. 1921. The harmonic development of the tide-generating potential. *Proceedings of the Royal Society of London. Series A, Containing Papers of a Mathematical and Physical Character***,** 305-329.

Eilers, P. H. C. 2003. A perfect smoother. *Analytical Chemistry,* 75**,** 3631-3636.

Eith, C., Kolb, M., Seubert, A. & Viehweger, K. H. 2001. Practical ion chromatography. *Metrohm Ltd., Herisau, Switzerland*.

Eriksson, R., Merta, J. & Rosenholm, J. B. 2007. The calcite/water interface i. Surface charge in indifferent electrolyte media and the influence of low-molecular-weight polyelectrolyte. *Journal of Colloid Interface Science,* 313**,** 184-93.

Eriksson, R., Merta, J. & Rosenholm, J. B. 2008. The calcite/water interface ii. Effect of added lattice ions on the charge properties and adsorption of sodium polyacrylate. *Journal of Colloid Interface Science,* 326**,** 396-402.

Ernstson, K. & Scherer, H. U. 1986. Self-potential variations with time and their relation to hydrogeologic and meteorological parameters. *Geophysics,* 51**,** 1967-1977.

FAO, 1997. *Seawater intrusion in coastal aquifers: Guidelines for study, monitoring and control,* Rome, Food and Agricultural Organisation of the United Nations.

Fenter, P., Geissbuhler, P., Dimasi, E., Srajer, G., Sorensen, L. B. & Sturchio, N. C. 2000. Surface speciation of calcite observed in situ by high-resolution x-ray reflectivity. *Geochimica et Cosmochimica Acta,* 64**,** 1221-1228.

Fetter, C. W. 1999. *Contaminant hydrogeology,* New Jersey, USA, Prentice Hall.

Fetter, C. W. 2001. *Applied hydrogeology,* New Jersey, USA, Prentice Hall.

Fleet, M., Brereton, N. R. & Howard, N. S. The investigation of saline intrusion into a fissured Chalk aquifer on the south coast of England. Proceedings of 5th Salt Water Intrusion Meeting, Medmenham, England, 1977. 137-157.

Forbes, J. M., Manson, A. H., Vincent, R. A., Fraser, G. J., Vial, F., Wand, R., Avery, S. K., Clark, R. R., Johnson, R., Roper, R., Schminder, R., Tsuda, T. & Kazimirovsky, E. S. 1994. Semidiurnal tide in the 80–150 km region: An assimilative data analysis. *Journal of Atmospheric and Terrestrial Physics,* 56**,** 1237-1249.

Franson, M. A. 1998. *Standard methods for the examination of water and wastewater 20th edition, ed,* Washington, DC, American Public Health Association, Standard Methods Committee.

Geller, M. A. 1970. An investigation of the lunar semidiurnal tide in the atmosphere. *Journal of the Atmospheric Sciences,* 27**,** 202-218.

Gokhberg, M. B., Kolosnitsyn, N. I. & Lapshin, V. M. 2009. Electrokinetic effect in the near-surface layers of the Earth. *Izvestiya, Physics of the Solid Earth,* 45**,** 633-639.

Goswami, R. R. & Clement, T. P. 2007. Laboratory-scale investigation of saltwater intrusion dynamics. *Water Resources Research,* 43.

Graf, T. & Therrien, R. 2005. Variable-density groundwater flow and solute transport in porous media containing nonuniform discrete fractures. *Advances in Water Resources,* 28**,** 1351-1367.

Graham, M., Butler, A. P., Jackson, V., Macallister, D. & Ijioma, A. A. Protecting coastal abstraction boreholes from seawater intrusion using self-potential data. European Geoscience Union, 2016 Vienna. EGU.

Guichet, X., Jouniaux, L. & Catel, N. 2006. Modification of streaming potential by precipitation of calcite in a sand-water system: Laboratory measurements in the pH range from 4 to 12. *Geophysical Journal International,* 166**,** 445-460.

Gulamali, M. Y., Leinov, E. & Jackson, M. D. 2011. Self-potential anomalies induced by water injection into hydrocarbon reservoirs. *Geophysics,* 76**,** F283-F292,doi:10.1190/1.3596010.

Halford, K. 2005. *Excel for hydrology* [Online]. USGS. Available: http://nevada.usgs.gov/tech/excelforhydrology/ [Accessed 26/08/2015 2015].

Hamilton, J. 1978. The quarter-diurnal tide in the English channel. *Geophysical Journal International,* 53**,** 541-552.

Hancock, J. M. 1975. Hancock petrology of the chalk. Proceedings of the Geologists Association, 1975, UK, 86(4), 499 - 535

Harbaugh, A. W. 2005. *Modflow-2005, the US geological survey modular ground-water model: The ground-water flow process*, US Department of the Interior, US Geological Survey Reston, VA, USA.

Hart, A. M., Honebon, C. D. & Rosser, W. G. V. 1983a. Local contributions to the M_2 lunar geomagnetic variations in the south west of England. *Physics of the Earth and Planetary Interiors,* 32**,** 60-64.

Hart, A. M., Krause, P. J. & Rosser, W. G. V. 1983b. Possible contribution of leakage currents from the Atlantic ocean to the magnetic-field variations observed in Devon. *Physics of the Earth and Planetary Interiors,* 32**,** 107-113.

Hayashi, M. 2004. Temperature-electrical conductivity relation of water for environmental monitoring and geophysical data inversion. *Environmental Monitoring and Assessment,* 96**,** 119-128.

Haynes, W. M. & Lide, D. R. 2012. *CRC handbook of chemistry and physics a ready-reference book of chemical and physical data : 2012-2013,* Boca Raton (Fla.); London; New York, CRC Press.

Healy, D. 11/01/2016 2016. *RE: Imperial college core analysis.* Type to MACALLISTER, D. & TAYLOR, C. W.

Heberling, F., Trainor, T. P., Lutzenkirchen, J., Eng, P., Denecke, M. A. & Bosbach, D. 2011. Structure and reactivity of the calcite-water interface. *Journal of Colloid Interface Science,* 354**,** 843-57.

Hewson-Browne, R. C. 1973. Magnetic effects of sea tides. *Physics of the Earth and Planetary Interiors,* 7**,** 167-186.

Hill, H. J. & Millburn, J. D. 1956. Effect of clay and water salinity on electrochemical behavior of reservoir rocks. *Petroleum Transactions, AIME,* 207**,** 65-72.

Hoffman, J. D. & Frankel, S. 2001. *Numerical methods for engineers and scientists*, CRC press.

Hounslow, A. 1995. *Water quality data: Analysis and interpretation*, CRC press.

Howell, S. R., Coulibaly, K., Vaughan, R., Ryan, D., Campbell, L., Guiton, S., De Verteuil, D. I. & Curum, N. The future of integrated groundwater and CSG simulation-modeling the Surat Basin, Queensland, Australia. SPE Unconventional Resources Conference and Exhibition-Asia Pacific, 2013. Society of Petroleum Engineers.

Hsieh, P. A., Bredehoeft, J. D. & Rojstaczer, S. A. 1988. Response of well aquifer systems to Earth tides: Problem revisited. *Water Resources Research,* 24**,** 468-472.

Hunt, C. W., And Worthington, M.H. 2000. Borehole electrokinetic responses in fracture dominated hydraulically conductive zones. *Geophysical Research Letters,* 27**,** 1315-1318.

Hunter, R. J. 1981. *Zeta potential in colloid science: Principles and applications,* London, Academic Press Limited.

Hunter, R. J. 2001. Foundations of colloid science. 2nd ed. Oxford: Oxford University Press.

Iglauer, S. & Muggeridge, A. 2013. The impact of tides on the capillary transition zone. *Transport in Porous Media,* 97**,** 87-103.

Ijioma, A. A. & Jackson, M. D. 2014. Closed-loop feedback control of smart wells for production optimisation using downhole measurements of self-potential. Society of Petroleum Engineers.

Ikard, S. J., Revil, A., Jardani, A., Woodruff, W. F., Parekh, M. & Mooney, M. 2012. Saline pulse test monitoring with the self-potential method to nonintrusively determine the velocity of the pore

water in leaking areas of earth dams and embankments. *Water Resources Research,* 48**,** W04201,doi:10.1029/2010WR010247.

Ireson, A. M., Mathias, S. A., Wheater, H. S., Butler, A. P. & Finch, J. 2009. A model for flow in the chalk unsaturated zone incorporating progressive weathering. *Journal of Hydrology,* 365**,** 244-260.

Jaafar, M. Z., Vinogradov, J. & Jackson, M. D. 2009. Measurement of streaming potential coupling coefficient in sandstones saturated with high salinity nacl brine. *Geophysical Research Letters,* 36**,** L21306,doi:10.1029/2009GL040549.

Jackson, D. & Rushton, K. R. 1987. Assessment of recharge components for a Chalk aquifer unit. *Journal of Hydrology,* 92**,** 1-15.

Jackson, M., Percival, J., Mostaghimi, P., Tollit, B., Pavlidis, D., Pain, C., Gomes, J., Elsheikh, A. H., Salinas, P., Muggeridge, A. & Blunt, M. 2015. Reservoir modeling for flow simulation by use of surfaces, adaptive unstructured meshes, and an overlapping-control-volume finite-element method. *SPE Reservoir Evaluation & Engineering*.

Jackson, M. D. 2010. Multiphase electrokinetic coupling: Insights into the impact of fluid and charge distribution at the pore scale from a bundle of capillary tubes model. *Journal of Geophysical Research-Solid Earth,* 115.

Jackson, M. D. 2015. 11.09 - Tools and techniques: Self-potential methods. *In:* SCHUBERT, G. (ed.) *Treatise on geophysics (second edition).* Oxford: Elsevier.

Jackson, M. D., Butler, A. P. & Vinogradov, J. 2012a. Measurements of spontaneous potential in chalk with application to aquifer characterisation in the southern UK *Quarterly Journal of Engineering Geology and Hydrogeology,* 45**,** 457-471.

Jackson, M. D., Gulamali, M. Y., Leinov, E., Saunders, J. H. & Vinogradov, J. 2012b. Spontaneous potentials in hydrocarbon reservoirs during waterflooding: Application to water-front monitoring. *SPE Journal,* 17**,** 53-69.

Jackson, M. D., Vinogradov, J., Saunders, J. H. & Jaafar, M. Z. 2011. Laboratory measurements and numerical modeling of streaming potential for downhole monitoring in intelligent wells. *SPE Journal,* 16**,** 625-636.

Jackson, P. E. 2000. Ion chromatography in environmental analysis. *Encyclopedia of analytical chemistry.* John Wiley & Sons, Ltd.

Jardani, A., Dupont, J. P. & Revil, A. 2006. Self-potential signals associated with preferential groundwater flow pathways in sinkholes. *Journal of Geophysical Research,* 111.

Jardani, A., Revil, A., Boleve, A. & Dupont, J. P. 2008. Three-dimensional inversion of self-potential data used to constrain the pattern of groundwater flow in geothermal fields. *Journal of Geophysical Research-Solid Earth,* 113.

Jardani, A., Revil, A. & Dupont, J. P. 2013. Stochastic joint inversion of hydrogeophysical data for salt tracer test monitoring and hydraulic conductivity imaging. *Advances in Water Resources,* 52**,** 62-77.

Johannsen, K., Kinzelbach, W., Oswald, S. & Wittum, G. 2002. The saltpool benchmark problem - numerical simulation of saltwater upconing in a porous medium. *Advances in Water Resources,* 25**,** 355-348.

Jones, H. K. & Robins, N. S. 1999. The Chalk aquifer of the South Downs. *British Geological Survey,* Keyworth, Nottingham.

Jougnot, D. & Linde, N. 2013. Self-potentials in partially saturated media: The importance of explicit modeling of electrode effects. *Vadose Zone Journal,* 12**,** NIL_274-NIL_294.

Jougnot, D., Linde, N., Haarder, E. B. & Looms, M. C. 2015. Monitoring of saline tracer movement with vertically distributed self-potential measurements at the hobe agricultural test site, Voulund, Denmark. *Journal of Hydrology,* 521**,** 314-327.

Jougnot, D., Linde, N., Revil, A. & Doussan, C. 2012. Derivation of soil-specific streaming potential electrical parameters from hydrodynamic characteristics of partially saturated soils. *Vadose Zone Journal,* 11**,** 15.

Jouniaux, L., Maineult, A., Naudet, V., Pessel, M. & Sailhac, P. 2009. Review of self-potential methods in hydrogeophysics. *Comptes Rendus Geoscience,* 341**,** 928-936.

Jouniaux, L. & Pozzi, J. P. 1995. Streaming potential and permeability of saturated sandstones under triaxial stress - consquences for electrotelluric anamalies prior to earthquakes *Journal of Geophysical Research-Solid Earth,* 100**,** 10197-10209.

Junge, A. 1990. A new telluric KCl probe using filloux's Ag/AgCl electrode. *Pure and Applied Geophysics,* 134**,** 589-598.

Kang, H. J., Cho, I. K., Kim, J. H., Yong, H. H., Song, S. H. & Park, Y. G. 2014. SP monitoring at a sea dike. *Near Surface Geophysics,* 12**,** 83-92.

Karl, J. H. 1989. 11 - Power spectral estimation. *In:* KARL, J. H. (ed.) *Introduction to digital signal processing.* San Diego: Academic Press.

Kendall, P. C. & Chapman, S. 1970. Model calculations on sea tidal generation of electric currents and magnetic fields. *The Quarterly Journal of Mechanics and Applied Mathematics,* 23**,** 535-547.

Kerrou, J. & Renard, P. 2010. A numerical analysis of dimensionality and heterogeneity effects on advective dispersive seawater intrusion processes. *Hydrogeology Journal,* 18**,** 55-72.

Kestin, J., Sokolov, M. & Wakeham, W. A. 1978. Viscosity of liquid water in the range− 8°C to 150°C. *Journal of Physical and Chemical Reference Data,* 7**,** 941-948.

Khan, A. E., Ireson, A., Kovats, S., Mojumder, S. K., Khusru, A., Rahman, A. & Vineis, P. 2011. Drinking water salinity and maternal health in coastal Bangladesh: Implications of climate change. *Environmental Health Perspectives*.

Kirsch, R. 2006. *Groundwater geophysics - a tool for hydrogeology,* Berlin, Springer.

Kosmulski, M., Maczka, E., Marczweska-Boczkowska, K. & Rosenholm, J. B. 2003. Electrokinetic potentials of mineral oxides and calcium carbonate in artificial sewater. *Marine Pollution Bulletin,* 46**,** 120-122.

Kuan, W. K., Jin, G., Xin, P., Robinson, C., Gibbes, B. & Li, L. 2012. Tidal influence on seawater intrusion in unconfined coastal aquifers. *Water Resources Research,* 48.

Kulessa, B. 2003. Cross-coupled flow modeling of coincident streaming and electrochemical potentials and application to subglacial self-potential data. *Journal of Geophysical Research,* 108.

Kulessa, B., Hubbard, B., Brown, G. H. & Becker, J. 2003. Earth tide forcing of glacier drainage. *Geophysical Research Letters,* 30.

Kumpel, H. J. 1997. Tides in water saturated rock. *In:* WILHELM, H., ZURN, W. & WENZEL, H. G. (eds.) *Tidal phenomena.* Berlin: Springer-Verlag Berlin.

Labregère, D., Delhomme, J. P. & Priestley, A. Mitigating salt water advance using horizontal wells: Risk based comparison of different approaches. 1st SWIM-SWICA Joint Saltwater Intrusion Conference, 2006 Cagliari, Italy. SWIM, 273 - 280.

Langmuir, D., Hall, P. & Drever, J. 1997. *Environmental geochemistry*, Prentice Hall, New Jersey.

Lanteri, Y., Szymczyk, A. & Fievet, P. 2009. Membrane potential in multi-ionic mixtures. *Journal of Physical Chemistry B,* 113**,** 9197-9204.

Leinov, E. & Jackson, M. D. 2014. Experimental measurements of the SP response to concentration and temperature gradients in sandstones with application to subsurface geophysical monitoring. *Journal of Geophysical Research: Solid Earth,* 119**,** 2014JB011249.

Leinov, E., Vinogradov, J. & Jackson, M. D. 2010. Salinity dependence of the thermoelectric coupling coefficient in brine-saturated sandstones. *Geophysical Research Letters,* 37**,** L23308,doi:10.1029/2010GL045379.

Levannier, A. Modeling of wellbore effects in managed aquifer recharge monitoring. Achieving groundwater supply sustainability and reliability through managed aquifer recharge., 2009 Abu Dhabi, United Arab Emirates. DINA-MAR, 85 - 90.

Leyk, Z. 1997. Breakdowns and stagnation in iterative methods. *BIT Numerical Mathematics,* 37**,** 377-403.

Li, Y. H. & Gregory, S. 1974. Diffusion of ions in water and deep sea sediments. *Geochemica et Cosmochimica Acta,* 38**,** 703 - 714.

Lilley, F. E. M. & Parker, R. L. 1976. Magnetic daily variations compared between the east and west coasts of Australia. *Geophysical Journal International,* 44**,** 719-724.

Lindzen, R. & Chapman, S. 1969. Atmospheric tides. *Space Science Reviews,* 10**,** 3-188.

Loaiciga, H. A., Pingel, T. J. & Garcia, E. S. 2012. Sea water intrusion by sea-level rise: Scenarios for the 21st century. *Ground Water,* 50**,** 37-47.

Lomb, N. R. 1976. Least-squares frequency analysis of unequally spaced data. *Astrophysics and Space Science,* 39**,** 447-462.

Long, J. C. S., Remer, J. S., Wilson, C. R. & Witherspoon, P. A. 1982. Porous media equivalents for networks of discontinuous fractures. *Water Resources Research,* 18**,** 645-658.

Lorne, B., Perrier, F. & J.P., A. 1999. Streaming potential measurements 1. Properties of the electrical double layer from crushed rock samples. *Journal of Geophysical Research,* 104**,** 17,857-17877.

Love, J. J. & Rigler, E. J. 2014. The magnetic tides of Honolulu. *Geophysical Journal International,* 197**,** 1335-1353.

Lowrie, W. 1997. *Fundamentals of geophysics,* Cambridge, Cambridge University Press.

Lu, C., Kitanidis, P. K. & Luo, J. 2009. Effects of kinetic mass transfer and transient flow conditions on widening mixing zones in coastal aquifers. *Water Resources Research,* 45.

MacDonald, A. M. & Allen, D. J. 2001. Aquifer properties of the chalk of England. *Quarterly Journal of Engineering Geology and Hydrogeology,* 34**,** 371-384.

Maineult, A., Bernabe, Y. & Ackerer, P. 2004. Electrical response of flow diffusion and advection in a laboratory sand box. *Vadose Zone Journal,* 3**,** 1180-1192.

Maineult, A., Bernabé, Y. & Ackerer, P. 2005. Detection of advected concentration and pH fronts from self-potential measurements. *Journal of Geophysical Research,* 110**,** B11205,doi:10.1029/2005JB003824.

Maineult, A., Strobach, E. & Renner, J. 2008. Self-potential signals induced by periodic pumping tests. *Journal of Geophysical Research,* 113.

Maineult, A., Thomas, B., Nussbaum, C., Wieczorek, K., Gibert, D., Lavielle, B., Kergosien, B., Nicollin, F., Mahiouz, K. & Lesparre, N. 2013. Anomalies of noble gases and self-potential associated with fractures and fluid dynamics in a horizontal borehole, Mont Terri underground rock laboratory. *Engineering Geology,* 156**,** 46-57.

Maliva, R. & Missimer, T. 2012. Groundwater flow and solute-transport modeling. *Arid Lands Water Evaluation and Management.* Springer.

Malmberg, C. & Maryott, A. 1956. Dielectric constant of water from 0 to 100°C. *Journal of Research of the National Bureau of Standards,* 56**,** 1-8.

Marshall, D. J. & Madden, T. R. 1959. Induced polarization, a study of its causes. *Geophysics,* 24**,** 790-816.

Martinez-Pagan, P., Jardani, A., Revil, A. & Haas, A. 2010. Self-potential monitoring of a salt plume. *Geophysics,* 75**,** WA17-WA25,doi:10.1190/1.3475533.

Mathias, S., Butler, A., Mcintyre, N. & Wheater, H. 2005. The significance of flow in the matrix of the chalk unsaturated zone. *Journal of Hydrology,* 310**,** 62-77.

Mathias, S. A. 2005. *Modelling flow and transport in the chalk unsaturated zone.* PhD, University of London.

Mathias, S. A., Butler, A. P., Jackson, B. M. & Wheater, H. S. 2006. Transient simulations of flow and transport in the chalk unsaturated zone. *Journal of Hydrology,* 330**,** 10-28.

Mathias, S. A., Butler, A. P., Peach, D. W. & Williams, A. T. 2007. Recovering tracer test input functions from fluid electrical conductivity logging in fractured porous rocks. *Water Resources Research,* 43.

Maurice, L. D., Atkinson, T. C., Barker, J. A., Bloomfield, J. P., Farrant, A. R. & Williams, A. T. 2006. Karstic behaviour of groundwater in the English chalk. *Journal of Hydrology,* 330**,** 63-70.

Maurice, L. D., Atkinson, T. C., Barker, J. A., Williams, A. T. & Gallagher, A. J. 2012. The nature and distribution of flowing features in a weakly karstified porous limestone aquifer. Journal of Hydrology, 438, 3-15.

Maus, S. & Kuvshinov, A. 2004. Ocean tidal signals in observatory and satellite magnetic measurements. *Geophysical Research Letters,* 31.

Mboh, C. M., Huisman, J. A., Zimmermann, E. & Vereecken, H. 2012. Coupled hydrogeophysical inversion of streaming potential signals for unsaturated soil hydraulic properties. *Vadose Zone Journal,* 11.

McConnel, C. L. 1983. Spontaneous potential corrections for groundwater salinity calculations - Carter County, Oklahoma, U.S.A. *Journal of Hydrology,* 65**,** 362-372.

McNaught, A. D. 2005. *IUPAC compendium of chemical terminology: The gold book*, International Union of Pure and Applied Chemistry.

Melloul, A. J. & Goldenberg, L. C. 1997. Monitoring of seawater intrusion in coastal aquifers: Basics and local concerns. *Journal of Environmental Management,* 51**,** 73-86.

MET, O, 2015. *Soil 30 cm temperature - annual average: 1981-2010* [Online]. MET Office. Available: http://www.metoffice.gov.uk/public/weather/climate/ [Accessed 12/08/2015 2015].

Michael, H. A., Mulligan, A. E. & Harvey, C. F. 2005. Seasonal oscillations in water exchange between aquifers and the coastal ocean. *Nature,* 436**,** 1145-1148.

Mondal, N. C., Singh, V. P., Singh, V. S. & Saxena, V. K. 2010. Determining the interaction between groundwater and saline water through groundwater major ions chemistry. *Journal of Hydrology,* 388**,** 100-111.

Monkhouse, R. A. & Fleet, M. 1975. A geophysical investigation of saline water in the chalk of the south coast of England. *Quarterly Journal of Engineering Geology,* 8**,** 291-302.

Muskat, M. & Wycokoff, R. 1935. An approximate theory of water-coning in oil production. *Transactions of the AIME,* 114**,** 144-163.

Nativ, R., And Fligelman, H. 1994. A field test of the modified SP log interpretation method for estimating groundwater salinity. *Journal of Hydrology,* 161**,** 133-144.

Nielsen, P. 1990. Tidal dynamics of the water-table in beaches. *Water Resources Research,* 26**,** 2127-2134.

Nourbehecht, B. 1963. *Irreversible thermodynamic effects in inhomogenous media and their application in certain geoeletric problems.* PhD, MIT.

NTSLF, 2015. *Highest recorded tide levels for Newhaven* [Online]. Available: http://www.ntslf.org/data/hilev?port=Newhaven [Accessed 24/11/2015 2015].

Nutbrown, D., Downing, R. & Monkhouse, R. 1975. The use of a digital model in the management of the Chalk aquifer in the South Downs, England. *Journal of Hydrology,* 27**,** 127-142.

Orihara, Y., Kamogawa, M., Nagao, T. & Uyeda, S. 2012. Variations of geoelectric potential differences associated with an anomalous volumetric strain change in the region of expected Tokai earthquake, Japan. *Natural Hazards and Earth Systems Sciences,* 12**,** 121-127.

Ortiz Jr., I., Von Goten, J. R. & Osoba, J. S. 1973. Relationship of the electrochemical potential of porous media with hydrocarbon saturation. *The Log Analyst***,** 25-32.

Osgood, C., Rosser, W. G. V. & Webber, N. J. W. 1970. Electric and magnetic fields associated with sea tides in the English channel. *Physics of the Earth and Planetary Interiors,* 4**,** 65-77.

Oswald, S. E. & Kinzelbach, W. 2004. Three-dimensional physical benchmark experiments to test variable-density flow models. *Journal of Hydrology,* 290**,** 22-42.

Palshin, N. A., Kaikkonen, P., Vanyan, L. L., Tiikkainen, J. & Rukol, V. H. 1997. On-land detecting a motionally induced electric field: Test measurements in northern Finland. *Journal of Geomagnetism and Geoelectricity,* 49**,** 1343-1350.

Palshin, N. A., Vanyan, L. L. & Kaikkonen, P. 1996. On-shore amplification of the electric field induced by a coastal sea current. *Physics of the Earth and Planetary Interiors,* 94**,** 269-273.

Panteleit, B., Hamer, K., Kringel, R., Kessels, W. & Schulz, H. D. 2011. Geochemical processes in the saltwater-freshwater transition zone: Comparing results of a sand tank experiment with field data. *Environmental Earth Sciences,* 62**,** 77-91.

Park, H.-Y., Jang, K., Ju, J. W. & Yeo, I. W. 2012. Hydrogeological characterization of seawater intrusion in tidally-forced coastal fractured bedrock aquifer. *Journal of Hydrology,* 446–447**,** 77-89.

Perrier, F. 2000. Characterization of electrical daily variations induced by capillary flow in the non-saturated zone. *Pure and Applied Geophysics,* 157**,** 785-810.

Perrier, F., Trique, M., Aupiais, J., Gautam, U. & Shrestha, P. 1999. Electric potential variations associated with periodic spring discharge in western Nepal. *Comptes Rendus De L Academie Des Sciences Serie Ii Fascicule a-Sciences De La Terre Et Des Planetes,* 328**,** 73-79.

Perrier, F. E., Petiau, G., Clerc, G., Bogorodsky, V., Erkul, E., Jouniaux, L., Lesmes, D., Macnae, J., Meunier, J. M., Morgan, D., Nascimento, D., Oettinger, G., Schwarz, G., Toh, H., Valiant, M. J., Vozoff, K. & Yazici-Cakin, O. 1997. A one-year systematic study of electrodes for long period measurements of the electric field in geophysical environments. *Journal of Geomagnetism and Geoelectricity,* 49**,** 1677-1696.

Petiau, G. 2000. Second generation of lead-lead chloride electrodes for geophysical applications. *Pure and Applied Geophysics,* 157**,** 357-382.

Petiau, G. & Dupis, A. 1980. Noise, temperature-coefficient, and long-time stability of electrodes for telluric observations. *Geophysical Prospecting,* 28**,** 792-804.

Pezard, P. A., Gautier, S., Le Borgne, T., Legros, B. & Deltombe, J. L. 2009. Muset: A multiparameter and high precision sensor for downhole spontaneous electrical potential measurements. *Comptes Rendus Geoscience,* 341**,** 957-964.

Pinettes, P., Bernard, P., Cornet, F., Hovhannissian, G., Jouneaux, L., Pozzi, J. P. & Barthes, V. 2001. Difficulty of detecting streaming potential generated at depth. *Pure and Applied Geophysics,* 159**,** 2629-2657.

Post, V. E. A. 2005. Fresh and saline groundwater interaction in coastal aquifers: Is our technology ready for the problems ahead? *Hydrogeology Journal,* 13**,** 120-123.

Power, T. Wed 09/05/2012 11:17 2012. *RE: Saltdean activities.* Type to MACALLISTER, D. J.

Press, W. H. & Teukolsky, S. A. 1990. Savitzky-Golay smoothing filters. *Computers in Physics,* 4**,** 669-672.

Price, M. 1987. Fluid flow in the chalk of England. *Geological Society, London, Special Publications,* 34**,** 141-156.

Price, M., Low, R. G. & Mccann, C. 2000. Mechanisms of water storage and flow in the unsaturated zone of the Chalk aquifer. *Journal of Hydrology,* 233**,** 54-71.

Pulido-Leboeuf, P., Pulido-Bosch, A., Calvache, M. L., Vallejos, Á. & Andreu, J. M. 2003. Strontium, SO_4^{2-}/Cl^- and Mg^{2+}/Ca^{2+} ratios as tracers for the evolution of seawater into coastal aquifers: The example of Castell de Ferro aquifer (SE Spain). *Comptes Rendus Geoscience,* 335**,** 1039-1048.

Radhakrishna, I. 2001. Saline fresh water interface structure in Mahanadi Delta region, Orissa, India. *Environmental Geology,* 40**,** 369-380.

Radhakrishna, I. & Gangahara, R. 1990. Evaluation of hydrogeochemical parameters with spontaneous potential logs. *Journal of Hydrology,* 114**,** 245-257.

Raynauld, J.-P. & Laviolette, J. R. 1987. The silver-silver chloride electrode: A possible generator of offset voltages and currents. *Journal of Neuroscience Methods,* 19**,** 249-255.

Recktenwald, G. 2012. The control-volume finite-difference approximation to the diffusion equation. [Online]. Available at: http://web.cecs.pdx.edu/~gerry/class/ME448/notes_2012/pdf/CVFDdiffusion2D.pdf [Accessed 12/12/2015].

Reilly, T. E., And Goodman, A.S. 1986. Analysis of saltwater upconing beneath a pumping well. *Journal of Hydrology,* 89**,** 169-204.

Reilly, T. E. & Goodman, A. S. 1985. Quantative-analysis of saltwater fresh-water relationships in groundwater systems - a historical perspective. *Journal of Hydrology,* 80**,** 125-160.

Revil, A. 1999a. Ionic diffusivity electrical conductivity membrane and thermoelectric potentials in colloids and granular porous media: A unified model. *Journal of Colloid and Interface Science,* 212**,** 503-522.

Revil, A. 2005. Self-potential signals associated with preferential ground water flow pathways in a buried paleo-channel. *Geophysical Research Letters,* 32.

Revil, A., And Pezard, P.A 1999b. Streaming potential in porous media 1. Theory of the zeta potential. *Journal of Geophysical Research,* 104**,** 20021-20031.

Revil, A. & Jardani, A. 2010. Stochastic inversion of permeability and dispersivities from time lapse self-potential measurements: A controlled sandbox study. *Geophysical Research Letters,* 37**,** L11404,doi:10.1029/2010GL043257.

Revil, A. & Jardani., A. 2013. *The self-potential method*, Cambridge University Press.

Revil, A., Leroy, P. & Titov, K. 2005. Characterization of transport properties of argillaceous sediments: Application to the Callovo-Oxfordian argillite. *Journal of Geophysical Research: Solid Earth,* 110**,** 1-18.

Revil, A. & Linde, N. 2011. Comment on 'streaming potential dependence on water-content in Fontainebleau sand' by V. Allegre, L. Jouniaux, F. Lehmann and P. Sailhac. *Geophysical Journal International,* 186**,** 113-114.

Revil, A., Mao, D., Haas, A. K., Karaoulis, M. & Frash, L. 2015. Passive electrical monitoring and localization of fluid leakages from wells. *Journal of Hydrology,* 521**,** 286-301.

Revil, A., Naudet, V. & Meunier, J. D. 2004. The hydroelectric problem of porous rocks: Inversion of the position of the water table from self-potential data. *Geophysical Journal International,* 159**,** 435-444.

Revil, A., Trolard, F., Bourrie, G., Castermant, J., Jardani, A. & Mendonca, C. A. 2009. Ionic contribution to the self-potential signals associated with a redox front. *Journal of Contaminat Hydrology,* 109**,** 27-39.

Rizzo, E., Suski, B. & Revil, A. 2004. Self-potential signals associated with pumping tests experiments. *Journal of Geophysical Research,* 109**,** B10203,doi:10.1029/2004JB003049.

Robert, T., Dassargues, A., Brouyere, S., Kaufmann, O., Hallet, V. & Nguyen, F. 2011a. Assessing the contribution of electrical resistivity tomography (ERT) and self-potential (SP) methods for

a water well drilling program in fractured/karstified limestones. *Journal of Applied Geophysics,* 75**,** 42-53.

Robins, N. S. & Dance, L. T. 2003. A new conceptual groundwater flow system for the central South Downs aquifer. *The Journal of chemical physics,* V17**,** 111 -116.

Robins, N. S., H.K. Jones & Ellis, J. 1999. An aquifer management case study - the chalk of the English South Downs. *Water Resources Management,* 13**,** 205-218.

Robinson, C., Li, L. & Prommer, H. 2007. Tide-induced recirculation across the aquifer-ocean interface. *Water Resources Research,* 43.

Rojstaczer, S. & Riley, F. S. 1990. Response of the water level in a well to Earth tides and atmospheric loading under unconfined conditions. *Water Resources Research,* 26**,** 1803-1817.

Rosser, W. G. V. & Schlapp, D. M. 1990. Geomagnetic lunar variations due to the ocean dynamo measured at European observatories. *Geophysical Journal International,* 103**,** 257-260.

Rushton, K. R. 2005. Estimating groundwater recharge for British aquifers. *Water and Environment Journal,* 19**,** 115-124.

Russak, A. & Sivan, O. 2010. Hydrogeochemical tool to identify salinization or freshening of coastal aquifers determined from combined field work, experiments, and modeling. *Environmental Science & Technology,* 44**,** 4096-4102.

Sandberg, S. K., Slater, L. D. & Versteeg, R. 2002. An integrated geophysical investigation of the hydrogeology of an anisotropic unconfined aquifer. *Journal of Hydrology,* 267**,** 227-243.

Saunders, J. H., Jackson, M. D., Gulamali, M. Y., Vinogradov, J. & Pain, C. C. 2012. Streaming potentials at hydrocarbon reservoir conditions. *Geophysics,* 77**,** E77-E90.

Saunders, J. H., Jackson, M. D. & Pain, C. C. 2008. Fluid flow monitoring in oilfields using downhole measurements of electrokinetic potential. *Geophysics,* 73**,** E165-E180.

Savitzky, A. & Golay, M. J. E. 1964. Smoothing and differentiation of data by simplified least squares procedures. *Analytical Chemistry,* 36**,** 1627-1639.

Scargle, J. D. 1982. Studies in astronomical time series analysis. Ii-statistical aspects of spectral analysis of unevenly spaced data. *The Astrophysical Journal,* 263**,** 835-853.

Schafer, R. W. 2011. What is a Savitzky-Golay filter?[lecture notes]. *Signal Processing Magazine, IEEE,* 28**,** 111-117.

Schlumberger 2010. Eclipse reservoir simulator, manual and technical description. ECLIPSE Technical Description, Version 10.

Schürch, M. & Buckley, D. 2002. Integrating geophysical and hydrochemical borehole-log measurements to characterize the Chalk aquifer, Berkshire, United Kingdom. *Hydrogeology Journal,* 10**,** 610-627.

Sedláček, M. Digital measurement of phase difference of lf signals-a comparison of DSP algorithms. Proceedings of IMEKO XVII World Congress (CD), Dubrovnik, Croatia, 2003. 639-644.

Sedlacek, M. & Krumpholc, M. 2005. Digital measurement of phase difference-a comparative study of DSP algorithms. *Metrology and Measurement Systems,* 12**,** 427-448.

Sheffer, M. R. & Oldenburg, D. W. 2007. Three-dimensional modelling of streaming potential. *Geophysical Journal International,* 169**,** 839-848.

Silvion 2013. Type WE200 reference electrode for permananet installation in soil. *In:* SILVION (ed.) *http://www.silvion.co.uk/pdf/1426002349WE200-R6.pdf.* http://www.silvion.co.uk/: Silvion.

Silvion 2015. Type WE300 low ion reference electrode for use in potable water. *In:* SILVION (ed.) *http://www.silvion.co.uk/pdf/1426002360WE300-R6.pdf.* http://www.silvion.co.uk/: Silvion.

Simmons, C. T., Bauer-Gottwein, P., Graf, T., Kinzelbach, W., Kooi, H., Li, L., Post, V., Prommer, H., Therrien, R., Voss, C. I., Ward, J. & Werner, A. D. 2010. *Variable density groundwater flow: From modelling to applications groundwater modelling in arid and semi-arid areas*, Cambridge University Press.

Singhal, B. B. S. & Gupta, R. P. 2010. *Applied hydrogeology of fractured rocks*, Springer Science & Business Media.

Smits, L. J. M. 1968. SP log intrepretation in shaly sands. *Society of Petroleum Engineers Journal,* 243**,** 123-136.

Snyder, K. V., Kriegstein, A. M. & Sachs, F. 1999. A convenient electrode holder for glass pipettes to stabilize electrode potentials. *Pflügers Archive,* 438**,** 405-411.

Somasundaran, P. & Agar, E. 1967. The zero point of charge of calcite. *Journal of Colloid and Interface Science,* 24**,** 433 - 440.

Sondi, I., Bišćan, J., Vdović, N. & Škapin, S. D. 2009. The electrokinetic properties of carbonates in aqueous media revisited. *Colloids and Surfaces A: Physicochemical and Engineering Aspects,* 342**,** 84-91.

Straface, S., Fallico, C., Troisi, S., Rizzo, E. & Revil, A. 2007. An inverse procedure to estimate transmissivity from heads and SP signals. *Ground Water,* 45**,** 420-8.

Strand, S., Høgnesen, E. J. & Austad, T. 2006. Wettability alteration of carbonates—effects of potential determining ions (Ca^{2+} and SO_4^{2-}) and temperature. *Colloids and Surfaces A: Physicochemical and Engineering Aspects,* 275**,** 1-10.

Surlyk, F., Damholt, T., Bjerager, M. & Forening, D. G. 2006. Stevns Klint, Denmark: Uppermost maastrichtian chalk, cretaceous-tertiary boundary, and lower danian bryozoan mound complex, Geological Society of Denmark.

Suski, B., Ladner, F., Baron, L., Vuataz, F. D., Philippossian, F. & Holliger, K. 2008. Detection and characterization of hydraulically active fractures in a carbonate aquifer: Results from self-potential, temperature and fluid electrical conductivity logging in the combioula hydrothermal system in the southwestern Swiss Alps. *Hydrogeology Journal,* 16**,** 1319-1328.

Szymkiewicz, A. 2012. *Modelling water flow in unsaturated porous media: Accounting for nonlinear permeability and material heterogeneity*, Springer Science & Business Media.

Tallgren, P., Vanhatalo, S., Kaila, K. & Voipio, J. 2005. Evaluation of commercially available electrodes and gels for recording of slow EEG potentials. *Clinical Neurophysiology,* 116**,** 799-806.

Tatro, M. E. & Amarasiriwardena, D. 2006. Optical emission inductively coupled plasma in environmental analysis. *Encyclopedia of analytical chemistry.* John Wiley & Sons, Ltd.

Telford, W. M., Geldart, L. P. & Sheriff, R. E. 1990. *Applied geophysics*, Cambridge university press.

Thatcher, K., Mackay, R. & Priestley, A. Modelling unsaturated flow through heterogeneous drift using Eclipse. Geophysical Research Abstracts, 2006. 06039.

Thomas, E. C. 1976. Determining Qv from membrane potential measurements on shaly sands. *Journal of Petroleum Technology***,** 1086-1096.

Thompson, D. W. & Pownall, P. G. 1988. Surface electrical properties of calcite. *Journal of Colloid and Interface Science,* 131**,** 74-82.

Thony, J.-L., Morat, P., Vachaud, G. & Le Mouël, J.-L. 1997. Field characterization of the relationship between electrical potential gradients and soil water flux. *Comptes Rendus de l'Académie des Sciences - Series IIA - Earth and Planetary Science,* 325**,** 317-321.

Tomaszkiewicz, M., Abou Najm, M. & El-Fadel, M. 2014. Development of a groundwater quality index for seawater intrusion in coastal aquifers. *Environmental Modelling & Software,* 57**,** 13-26.

Trauth, M. H. 2010. *Matlab® recipes for earth sciences: Third edition*. Springer

Trique, M., Perrier, F., Froidefond, T. & Avouac, J. P. 2002. Fluid flow near reservoir lakes inferred from the spatial and temporal analysis of the electric potential. *Journal of Geophysical Research,* 107**,** B102239,doi:10.1029/2001JB000482.

Van Cappellen, P., Charlet, L., Stumm, W. & Wersen, P. 1993. A surface complexation model of the carbonate mineral-aqueous solution interface. *Geochemica et Cosmochimica Acta,* 57**,** 3505-3518.

Van Der Vorst, H. A. 2003. *Iterative Krylov methods for large linear systems*, Cambridge University Press.

Van Weert, F., Van Der Gun, J. & Reckman, J. 2009. Global overview of saline groundwater occurence and genesis. *UNESCO and WMO, Utrectht, The Netherlands*.

Vdovic, N. 2001. Electrokinetic behaviour of calcite -the relationship with other calcite properties. *Chemical Geology,* 177**,** 241-248.

Vdovic, N. & Biscan, J. 1998. Electrokinetics of natural and synthetic calcite suspensions. *Colloids and Surfaces A: Physicochemical and Engineering Aspects,* 137**,** 7-14.

Vdovic, N. & Kralji, D. 2000. Electrokinetic properties of spontaneously preciptated calcium carbonate polymorphs: The influence of organic substances. *Colloids and Surfaces A: Physicochemical and Engineering Aspects,* 161**,** 499-505.

Vial, F. & Forbes, J. M. 1994. Monthly simulations of the lunar semi-diurnal tide. *Journal of Atmospheric and Terrestrial Physics,* 56**,** 1591-1607.

Vinogradov, J., Jaafar, M. Z. & Jackson, M. D. 2010. Measurement of streaming potential coupling coefficient in sandstones saturated with natural and artificial brines at high salinity. *Journal of Geophysical Research,* 115**,** B12204,doi:10.1029/2010JB007593.

Walters, R. A. 1987. A model for tides and currents in the English channel and southern North Sea. *Advances in Water Resources,* 10**,** 138-148.

Walton, N. 1989. Electrical conductivity and total dissolved solids—what is their precise relationship? *Desalination,* 72**,** 275-292.

Wang, F. C. 1965. Approximate theory for skimming well formulation in the Indus plain of west Pakistan. *Journal of Geophysical Research,* 70**,** 5055-5063.

Wang, J. & Tsay, T. K. 2001. Tidal effects on groundwater motions. *Transport in Porous Media,* 43**,** 159-178.

Wardle, C. 2011. *Sea-water intrusion* [Online]. UK Groundwater Forum: NERC/British Geological Survey. Available: http://www.groundwateruk.org/downloads/sea_water_intrusion.pdf [Accessed 15/01/2016 2016].

Warner, R. M. 1998. *Spectral analysis of time-series data*, Guilford Press.

Werner, A. D., Bakker, M., Post, V. E. A., Vandenbohede, A., Lu, C., Ataie-Ashtiani, B., Simmons, C. T. & Barry, D. A. 2013. Seawater intrusion processes, investigation and management: Recent advances and future challenges. *Advances in Water Resources,* 51**,** 3-26.

Werner, A. D., Jakovovic, D. & Simmons, C. T. 2009. Experimental observations of saltwater up-coning. *Journal of Hydrology,* 373**,** 230-241.

Westermann-Clark, G. B. & Christoforou, C. C. 1986. The exclusion diffusion potential in charged porous membranes. *Journal of Electroanalytical Chemistry,* 198**,** 213-231.

Wheater, H. S., Peach, D. & Binley, A. 2007. Characterising groundwater-dominated lowland catchments: The UK lowland catchment research programme (LOCAR). *Hydrology and Earth System Sciences Discussions,* 11**,** 108-124.

William, M. H. 2011. *CRC handbook of chemistry and physics : A ready-reference book of chemical and physical data,* Boca Raton, Fla. ; London, CRC.

Williams, A., Bloomfield, J., Griffiths, K. & Butler, A. 2006. Characterising the vertical variations in hydraulic conductivity within the Chalk aquifer. *Journal of Hydrology,* 330**,** 53-62.

Wilson, S. R., Ingham, M. & Mcconchie, J. A. 2006. The applicability of earth resistivity methods for saline interface definition. *Journal of Hydrology,* 316**,** 301-312.

Wishart, D. N., Slater, L. D. & Gates, A. E. 2008. Fracture anisotropy characterization in crystalline bedrock using field-scale azimuthal self potential gradient. *Journal of Hydrology,* 358**,** 35-45.

Wishart, D. N., Slater, L. D., Schnell, D. L. & Herman, G. C. 2009. Hydraulic anisotropy characterization of pneumatic-fractured sediments using azimuthal self potential gradient. *Journal of Contaminant Hydrology,* 103**,** 134-44.

Witthüser, K., Reichert, B. & Hotzl, H. 2003. Contaminant transport in fractured chalk: Laboratory and field experiments. *Ground Water,* 41**,** 806-815.

Wolthers, M., Charlet, L. & Van Cappellen, P. 2008. The surface chemistry of divalent metal carbonate minerals; a critical assessment of surface charge and potential data using the charge distribution multi-site ion complexation model. *American Journal of Science,* 308**,** 905-941.

Woodruff, W. F., Revil, A., Jardani, A., Nummedal, D. & Cumella, S. 2010. Stochastic bayesian inversion of borehole self-potential measurements. *Geophysical Journal International,* 183**,** 748-764.

Woods, M. A. 2006. UK chalk stratigraphy (Cenomanian - Santonian) determined from borehole geophysical logs. *Quarterly Journal of Engineering Geology and Hydrogeology,* 39**,** 83-96.

Worthington, A., Hedges, J. & Pallatt, N. 1990. SCA guidelines for sample preparation and porosity measurements of electrical resistivity samples. *The Log Analyst,* 31**,** 20-28.

Worthington, S. R. H. 2015. Characteristics of channel networks in unconfined carbonate aquifers. *Geological Society of America Bulletin,* 127**,** 759-769.

Worthington, S. R. H. & Ford, D. C. 2009. Self-organized permeability in carbonate aquifers. *Ground Water,* 47**,** 326-336.

Wylie, R. J. 1949. A quantative analysis of the electrochemical component of the SP curve. *Petroleum Transactions, AIME***,** 17-26.

Wylie, R. J. 1951. An investigation of the electrokinetic component of the self potential curve. *Petroleum Transactions, AIME,* 192**,** 1-18.

Xin, P., Robinson, C., Li, L., Barry, D. A. & Bakhtyar, R. 2010. Effects of wave forcing on a subterranean estuary. *Water Resources Research,* 46**,** 1-16.

Yi, Y., Matsumoto, K., Shum, C. K., Wang, Y. & Mautz, R. 2006. Advances in southern ocean tide modeling. *Journal of Geodynamics,* 41**,** 128-132.

Yuan, P.-Q., Cheng, Z.-M., Zhou, Z.-M., Yuan, W.-K. & Semiat, R. 2008. Zeta potential on the anti-scalant modified sub-micro calcite surface. *Colloids and Surfaces A: Physicochemical and Engineering Aspects,* 328**,** 60-66.

Zaporozec, A. 1972. Graphical interpretation of water-quality data. *Groundwater,* 10**,** 32-43.

Zeumann, S., Weise, A. & Jahr, T. 2009. Tidal and non-tidal signals in groundwater boreholes in the KTB area, Germany. *Journal of Geodynamics,* 48**,** 115-119.

Zhang, P. & Austad, T. 2006. Wettability and oil recovery from carbonates: Effects of temperature and potential determining ions. *Colloids and Surfaces A: Physicochemical and Engineering Aspects,* 279**,** 179-187.

Zhang, P., Tweheyo, M. T. & Austad, T. 2007. Wettability alteration and improved oil recovery by spontaneous imbibition of seawater into chalk: Impact of the potential determining ions Ca^{2+}, Mg^{2+}, and SO_4^{2-}. *Colloids and Surfaces A: Physicochemical and Engineering Aspects,* 301**,** 199-208.

Zhou, Q. L., Bear, J. & Bensabat, J. 2005. Saltwater upconing and decay beneath a well pumping above an interface zone. *Transport in Porous Media,* 61**,** 337-363.

Zhou, W. & Arthur, R. 1994. Environmental applications of Eclipse-a multiphase flow simulator used in the oil and gas industry. Arizona Univ., Tucson, AZ (United States). Coll. of Engineering and Mines; New Mexico State Univ., University Park, NM (United States); Waste-Management Education and Research Consortium (WERC), Las Cruces, NM (United States); USDOE, Washington, DC (United States).

Appendix 1
Diffusion Potential

In determining the diffusion potential for use in calculating the final value of the exclusion-diffusion potential in the laboratory experiments (section 3.2.3) the following expression was used (Lanteri et al., 2009):

$$\Delta V_D = -\frac{k_B T}{e}\left(\frac{\sum_i K_i D_i z_i (C_i^{\Delta x} - C_i^0)}{\sum_i K_i D_i z_i^2 (C_i^{\Delta x} - C_i^0)}\right) ln\left(\frac{\sum_i K_i D_i z_i^2 C_i^0}{\sum_i K_i D_i z_i^2 C_i^{\Delta x}}\right) \quad \textbf{Equation A1.1}$$

This equation is shown to be equivalent, in this case of a 1:1 electrolyte such as NaCl, to the expression used by Leinov and Jackson (2014). Here D_i is the diffusion coefficient, K_i is the hindrance diffusion coefficient and $C_i^{\Delta x}$ is the high salinity concentration of each ion and C_i^0 is the low salinity concentration of each ion. K_i takes account of the size of the hydrated ion relative to the pore throat radius and here is assumed to be 1, as the diffusion coefficient is calculated in an open reservoir configuration. It is assumed that only Na ions and Cl ions are present in solution, thus $z_{Na} = 1$ and $z_{Cl} = -1$. Therefor Equation A1.1 becomes:

$$\Delta V_D = -\frac{k_B T}{e}\left(\frac{(D_{Na} - D_{Cl})(C_{Na}^{\Delta x} - C_{Cl}^0)}{(D_{Na} + D_{Cl})(C_{Na}^{\Delta x} - C_{Cl}^0)}\right) ln\left(\frac{D_{Na} C_{Na}^{\Delta X} + D_{Cl} C_{Cl}^{\Delta X}}{D_{Na} C_{Na}^0 + D_{Cl} C_{Cl}^0}\right) \quad \textbf{Equation A1.2}$$

From the Einstein relation:

$$D_i = \frac{k_B T}{e}\beta_i \quad \textbf{Equation A1.3}$$

Here β_i are the ionic mobility's of the ion i.

For a 1:1 electrolyte $C_+^0 = C_-^0 = C^0$and $C_+^{\Delta x} = C_-^{\Delta x} = C^{\Delta x}$. Therefore:

$$\Delta V_D = -\frac{k_B T}{e}\left(\frac{\beta_{Na}}{\beta_{Na} + \beta_{Cl}} - \frac{\beta_{Cl}}{\beta_{Na} + \beta_{Cl}}\right) ln\left(\frac{C^{\Delta X}}{C^0}\right) \quad \textbf{Equation A14}$$

Here:

$$t_{\pm} = \frac{\beta_{\pm}}{\beta_{\pm} + \beta_{\pm}}$$ **Equation A1.5**

$$t_{Na} + t_{Cl} = 1$$ **Equation A1.6**

Here t_{Na} and t_{Cl} are the microscopic Hittorf transport numbers of the cations and anions. Therefore:

$$\Delta V_{ED} = -\frac{k_B T}{e}(2t_{Na} - 1) ln\left(\frac{C^{\Delta X}}{C^0}\right)$$ **Equation A1.7**

This is the same as the expression used by Leinov and Jackson (2014) in their experiments on sandstone core samples. For comparison the value of the diffusion potential for a NaCl solution of the same ionic strength as used in the GW/SW experiments is calculated, Equation A1.11 yields a value of 37.71 mV and Equation A1.7 yields a value of 35.48 mV. The difference can be explained by the slight approximation introduced by Equations A1.5 and A1.6. However this demonstrates the fact that Equation A1.1 can be safely employed for multi-ionic solutions.

Appendix 2
Water Quality Analysis Methods and Results

Water Quality Analysis

The IC method used is briefly outlined here, more details can be found in Eith et al. (2001). IC works by using an eluent to carry the sample ions to a separation column. The separation column slows the sample ions to an extent that is well characterised for each ion. The separated ions then arrive, either initially at a suppressor for anions, or at the conductivity detector directly for the cations. Once the ions arrive at the conductivity detector the electrical conductivity of the eluate is measured. Each conductivity peak represents an individual anion or cation. The IC unit used was the Metrohm 930 Compact IC Flex with a Metrosep A Supp 16 – 15/4.0 anion column and Metrosepp C4 250/4 cation column. Figure A1.1 shows the peak chart for the cation and anion columns used.

The eluent for the cations is Nitric/Dipicolinic acid with 1.7 mM/l of nitric acid and 0.7 mM/l of Dipicolinic acid. Temperature = 45. Eluent for the anions is a Carbonate/hydroxide eluent with 7.5 mM of Sodium carbonate and 0.75 mM/l of sodium hydroxide.

The results are calibrated against pre-prepared standards for anions and cations. The standards are initially manually diluted from stocks of 2000 mg/l to 200 mg/l. An auto dilution system then systematically dilutes the standards down to 2 mg/l, in the following increments; 100 mg/l, 50 mg/l, 20 mg/l, 10 mg/l and 5 mg/l. Any samples with constituent ionic concentration greater than 200 mg/l are diluted so that each sample ion is within the standard range. Therefore, seawater samples are diluted up to 100 times manually. Groundwater samples do not require any manual dilution. A calibration curve which relates the standard concentration to the measured conductivity of each ion was then constructed for each sample ion, an example of which is shown in Figure A2.2 for both anions and cations.

The details of the titration methods conducted by the University of Bangor used for carbonate and bicarbonate can be found in Franson (1998). The details of the ICP-AES methods used by the Natural History Museum can be found in Alroudhan (2015).

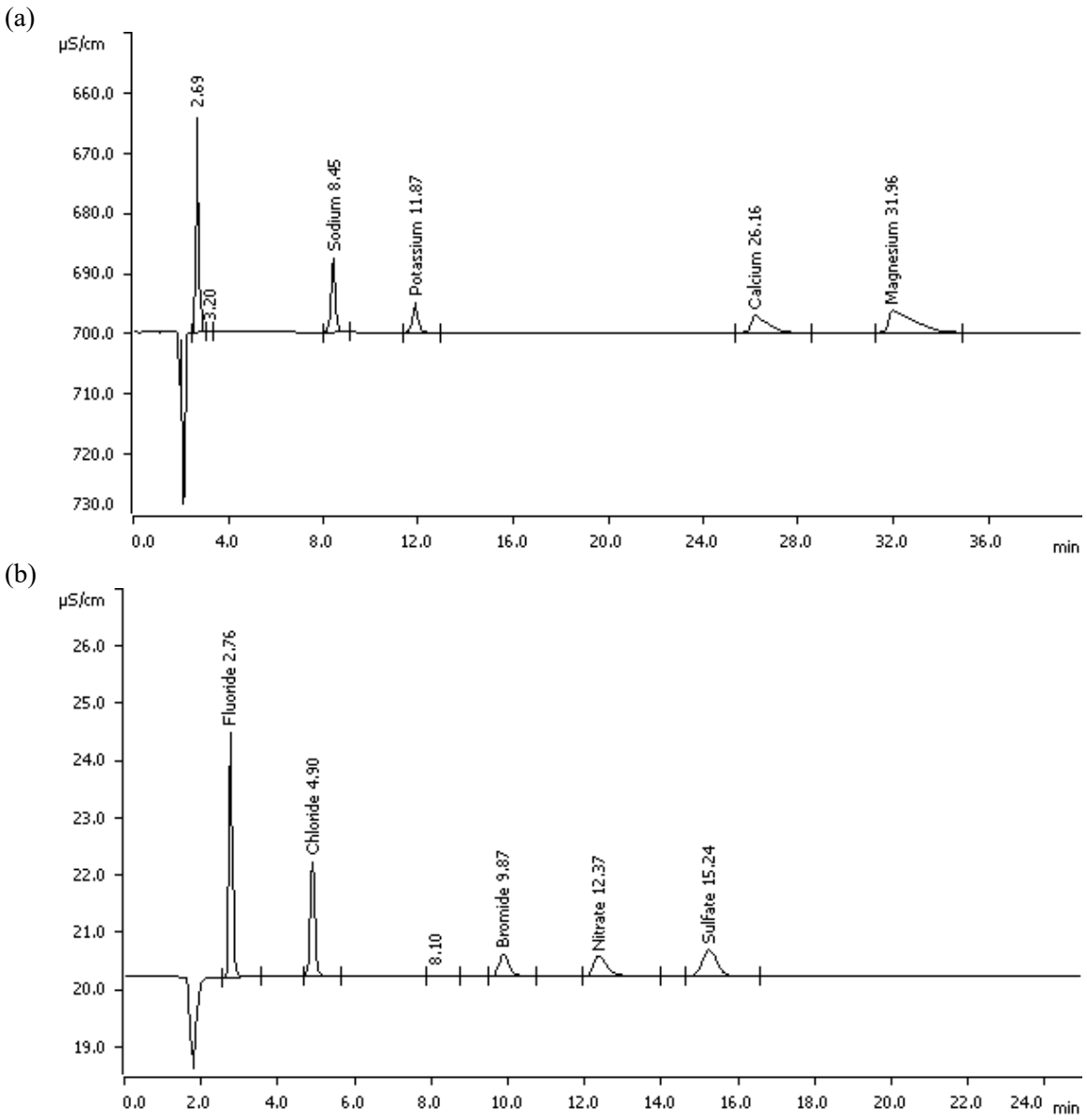

Figure A2.1 –(a) Cation peak conductivity and detection times for 10 mg/l standard. (b) Anion peak conductivity and detection time for 10 mg/l standard.

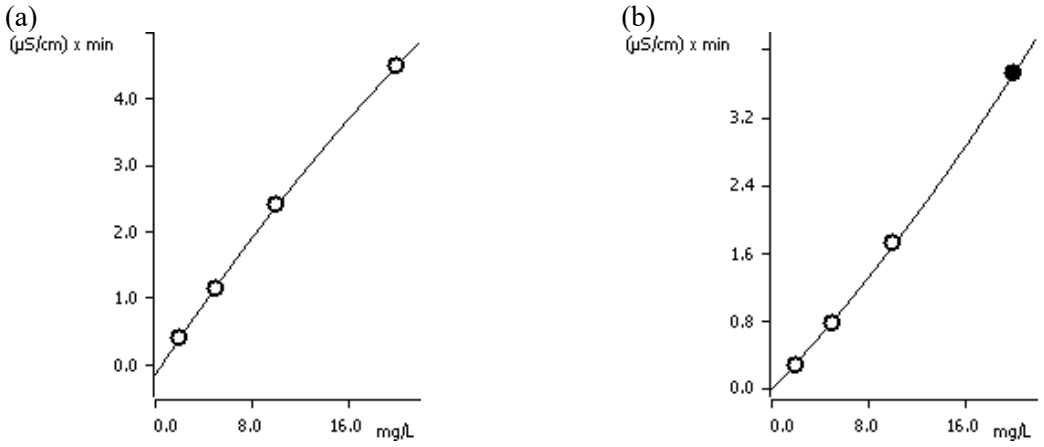

Figure A2.2 – (a) Calibration curve for sodium. (b) Calibration curve for chloride.

Ion Balance
The ionic balance for each sample is calculated using the following expression:

$$CBE = \frac{\sum C_+ - |\sum C_-|}{\sum C_+ + |\sum C_-|} X100$$

Here C_+ and C_- are the concentrations of the cations and anions respectively, concentrations are in milliequivalents per litre (mEq/l). To convert from mg/l to mEq/L the following expression is used:

$$C_{(mEq/l)} = \frac{C_{(mg/l)} \cdot z}{m}$$

Water Quality analysis results

SW #	Date	Na	K	Ca	Mg	F	Br	SO_4	Cl	Sr	HCO_3	CBE (%)
1	10/03/14	10003.2	401.00	394.1	1141.9	7.27	84.81	2312.2	17617.1	N/A	117	0.97
2	10/03/14	10013.1	630.50	475.2	1370.9	4.69	88.13	2987.8	18582.2	N/A	139	-0.13
3	17/03/14	10667.4	414.60	434.6	1283.2	7.48	88.89	2381.5	18862.7	N/A	N/A	1.41
4	11/09/14	10618.2	423.80	439.7	1315.6	5.11	92.21	2421.9	19466.4	N/A	122	0.01
5	29/09/14	10685.9	419.70	436.8	1304.6	7.39	91.15	2400.9	18968.6	N/A	N/A	1.35
6	26/09/14	9819.0	492.992	449.8	1203.1	7.54	91.29	2407.4	19166.7	N/A	N/A	-2.86
7	15/10/14	9995.3	423.00	425.7	1265.8	5.26	91.94	2418.0	19294.4	N/A	136	-2.32
8	31/10/14	9953.3	413.1.0	430.8	1287.2	5.19	89.73	2417.5	19294.4	N/A	N/A	-2.31
9	31/10/14	10145.4	428.8.0	430.8	1287.2	5.25	94.16	2409.8	19025.0	N/A	144	-0.92
10	09/06/14	10250.0	410.5.0	407.5	1180.0	N/A	62.50	2645.0	19750.0	7.85	N/A	-3.48
11	15/07/14	10350.0	410.5	448.5	1260.0	N/A	79.00	2610.0	20591.0	7.85	N/A	-4.21
12	27/11/13	10791.6	492.66	440.13	1168.0	N/A	162.63	2547.3	19174.5	7.90	N/A	0.16
13	19/08/13	9934.8	453.39	422.79	1030.0	N/A	161.35	2167.3	17060.2	8.24	N/A	1.75
14	06/08/13	10404.0	510	431.46	1168.0	N/A	165.59	2607.4	19417.4	9.43	N/A	-1.93
15	11/11/13	10302.0	476.34	414.12	1153.0	N/A	163.62	2542.1	18858.3	8.31	N/A	-1.14
Average		**10262.21**	**453.39**	**432.13**	**1227.9**	**6.13**	**107.00**	**2485.07**	**19008.53**	**8.27**	**131.6**	**-0.93**

Table A2.1 - Water quality data used to determine average concentration of SW used in EK and EED experiments. Also shown is the charge balance error (CBE), samples that did not meet the criteria of 5% are not shown, hence why there are fewer SW samples than GW samples.

GW #	Date	Na	K	Ca	Ba	Mg	F	Br	SO_4	Cl	Sr	NO_3	Si	HCO_3	CO_3	CBE (%)
1	29/07/13	24.38	1.14	49.47	0.01	5.81	0.14	0.605	14.76	43.62	0.196	23.76	4.02	140	24.66	-4.73
2	27/11/13	23.05	1.16	60.69	0.01	2.33	0.14	<0.1	13.98	44.06	0.200	24.19	4.23	165	23.41	-4.49
3	24/01/14	24.90	1.19	69.20	0.01	4.06	0.12	0.415	16.18	43.58	0.197	29.16	3.393	165	26.01	-2.14
4	05/03/14	27.30	1.29	62.30	0.01	3.34	0.13	0.422	16.60	47.69	0.196	28.41	3.486	152	24.71	-3.67
5	12/02/14	24.40	1.26	61.90	0.01	2.95	0.11	0.416	15.85	43.09	0.192	29.34	3.437	207	11.01	-077
6	10/03/14	24.30	1.21	68.10	0.01	2.97	0.13	0.414	16.95	43.90	0.195	25.76	3.408	177	24.76	-4.85
7	09/06/14	29.10	1.29	53.50	0.01	3.21	0.07	0.159	17.34	40.97	0.207	23.76	3.35	140	25.31	-3.52
8	10/03/14	47.68	2.71	63.93	N/A	4.74	0.06	0.287	18.40	68.43	N/A	26.48	N/A	N/A	N/A	3.47
9	10/03/14	24.03	1.45	54.00	N/A	3.42	0.12	0.158	16.76	40.64	N/A	26.12	N/A	152	24.28	-4.22
10	17/03/14	25.13	1.47	59.51	N/A	3.60	0.06	0.163	17.35	41.81	N/A	26.47	N/A	N/A	N/A	3.43
11	03/09/14	32.86	1.79	69.58	N/A	4.41	0.06	0.212	16.74	52.93	N/A	28.45	N/A	N/A	N/A	-1.88
12	11/09/14	26.82	1.58	70.17	N/A	3.68	0.06	0.177	15.67	42.57	N/A	29.13	N/A	N/A	N/A	4.03
13	26/09/14	27.45	1.56	73.26	N/A	3.63	0.06	0.17	16.02	41.70	N/A	29.41	N/A	161	28.84	-3.72
14	29/09/14	42.50	2.07	58.30	N/A	5.15	0.07	0.187	17.56	48.60	N/A	29.06	N/A	N/A	N/A	4.27
15	29/09/14	31.40	1.94	65.92	N/A	4.31	0.12	0.246	23.39	71.72	N/A	28.22	N/A	N/A	N/A	-4.77
16	15/10/14	34.65	1.77	70.94	N/A	4.45	0.06	0.215	16.92	51.87	N/A	29.35	N/A	N/A	N/A	5.53
17	31/10/14	N/A	8.64	55.97	N/A	9.16	0.07	0.147	15.99	40.17	N/A	28.20	N/A	N/A	N/A	5.20
18	19/11/14	25.16	1.60	59.57	N/A	3.71	0.06	0.17	15.74	41.05	N/A	28.81	N/A	162	25.12	-2.18
19	13/11/14	25.81	1.53	69.44	N/A	3.60	0.06	0.174	15.73	45.63	N/A	28.14	N/A	135	20.58	-0.49
20	13/03/15	28.99	1.57	61.89	N/A	3.75	0.09	0.159	15.57	44.06	N/A	27.00	N/A	N/A	N/A	0.87
21	05/03/15	27.77	1.60	55.74	N/A	3.79	0.07	0.143	14.00	38.00	N/A	28.94	N/A	141	24.71	-2.31
22	23/04/15	24.10	1.50	67.30	N/A	3.35	0.06	0.257	18.71	61.79	N/A	29.28	N/A	N/A	N/A	-4.85
23	02/04/15	31.03	1.38	58.76	N/A	3.06	0.08	N/A	22.63	46.85	N/A	27.41	N/A	N/A	N/A	-2.82
24	29/09/14	26.29	2.38	66.76	N/A	5.06	0.08	0.15	14.29	39.77	N/A	28.91	N/A	N/A	N/A	4.95
Average		**28.666**	**1.879**	**62.766**	**0.01**	**4.06**	**0.09**	**0.248**	**16.7798**	**46.87**	**0.198**	**27.870**	**3.62**	**158.18**	**24.71**	**-2.52**

Table A2.2 - Water quality data used to determine average concentration of GW used in EK and EED experiments. Also shown is the charge balance error (CBE) for each sample, samples that did not meet the criteria of 5% are not shown.

DI #	Date	Na	K	Ca	Mg	F	SO_4	Cl	NO_3	HCO_3	CBE (%)
1	07/01/15	3.55	7.774	27.2	5.42	0.13	35.71	6.23	14.03	54	2.84
2	27/01/15	3.49	12.01	39.89	6.43	0.11	37.89	12.47	37.72	N/A	7.36
3	11/02/15	3.24	6.64	23.44	4.58	0.11	29.90	11.75	27.10	N/A	-8.72
4	13/03/15	4.99	4.12	23.63	0.00	0.13	0.00	24.06	12.33	52	-7.25
5	02/04/15	4.73	3.91	9.66	2.08	0.10	11.93	3.19	1.98	41	-0.71
6	08/04/15	3.14	3.91	16.82	0.00	0.09	0.00	6.67	1.27	52	0.48
7	07/05/15	5.70	3.30	11.68	0.00	0.08	0.00	2.61	0.8	N/A	0.50
8	21/06/14	4.23	5.90	20.80	1.00	0.05	0.00	22.18	0.00	N/A	0.40
9	24/06/14	5.15	0.00	15.39	0.21	0.05	3.85	6.28	1.76	N/A	-4.46
Average		**4.25**	**5.95**	**20.96**	**2.08**	**0.096**	**11.93**	**10.60**	**10.78**	**49.75**	**0.06**

Table A2.3 - Water quality data used to determine average concentration of pre-equilibrated DI used in EED experiments. Also shown is the charge balance error (CBE), samples that did not meet the criteria of 10% are not shown.

5M #	Date	Na	K	Ca	Mg	SO_4	Cl	HCO_3	CBE (%)
1	07/01/15	145282.6	3.42	4.37	1.88	1857.78	185777.6	33	-0.39
2	27/01/15	160462.9	3.31	1.34	1.86	1808.96	180895.8	N/A	-0.37
3	11/02/15	136852.8	3.34	4.13	1.85	1768.18	176818.7	41	-0.37
4	13/03/15	147139.6	3.34	1.34	1.80	1768.19	169121.3	N/A	-0.37
5	02/04/15	131000.0	3.32	2.55	1.94	1691.21	168641.1	N/A	-0.35
6	08/04/15	148.436.1	3.31	1.68	1.85	1686.41	182321.5	50	-0.35
7	07/05/15	144270.9	3.31	4.17	1.82	1823.21	166801.4	N/A	-0.38
8	24/06/14	144500.0	5.95	1.31	1.87	1668.01	174413.5	60	-0.35
Average		**N/A**	**3.662**	**2.335**	**1.859**	**1755.989**	**N/A**	**46**	**-0.37**

Table A2.4 - Water quality data used to determine average concentration of pre-equilibrated 5M used in EED experiments. Note that the sodium and chloride concentrations for the 5M solutions are calculated, i.e. the Na and Cl concentrations are known, thus the values reported above for Na and Cl are not used in the EED calculations. The same applies for the calculation of the charge balance error. Samples that did not meet the criteria of 5% are not shown.

Appendix 3

Summary of EED results

An example of the results from the pre-eq(DI/5M) experiments presented first, followed by each of the individual EED experimental results from both the plug and column experiments for the GW/SW and pre-eq(DI/5M) experiments.

(a)

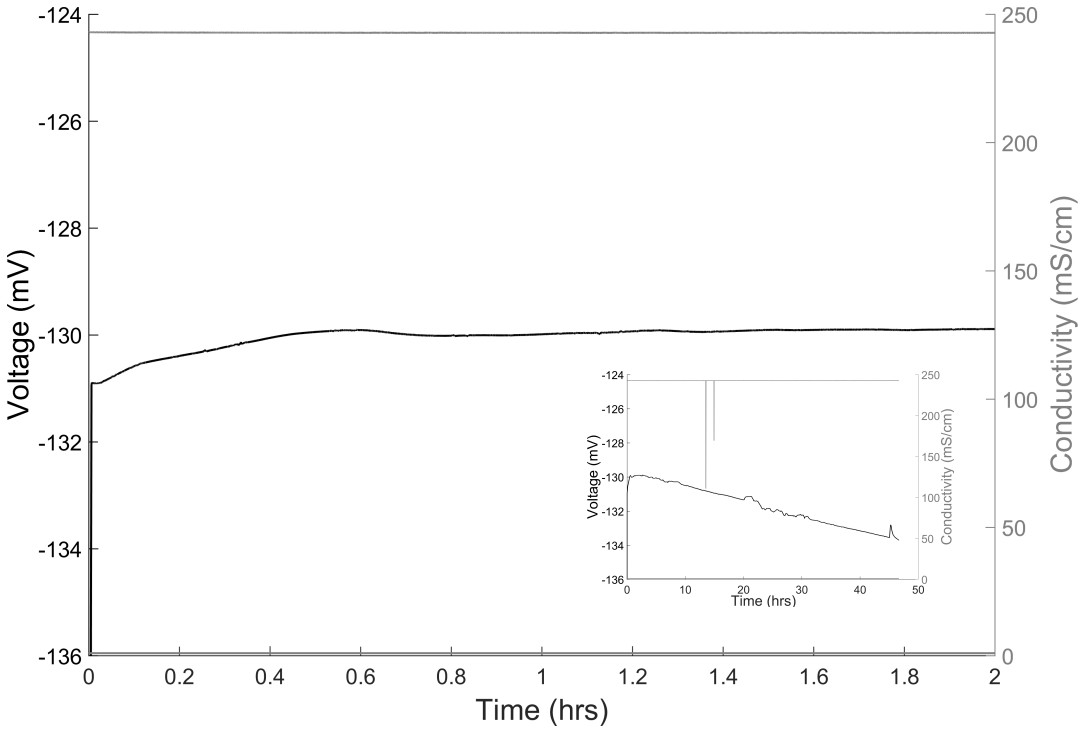

(b)

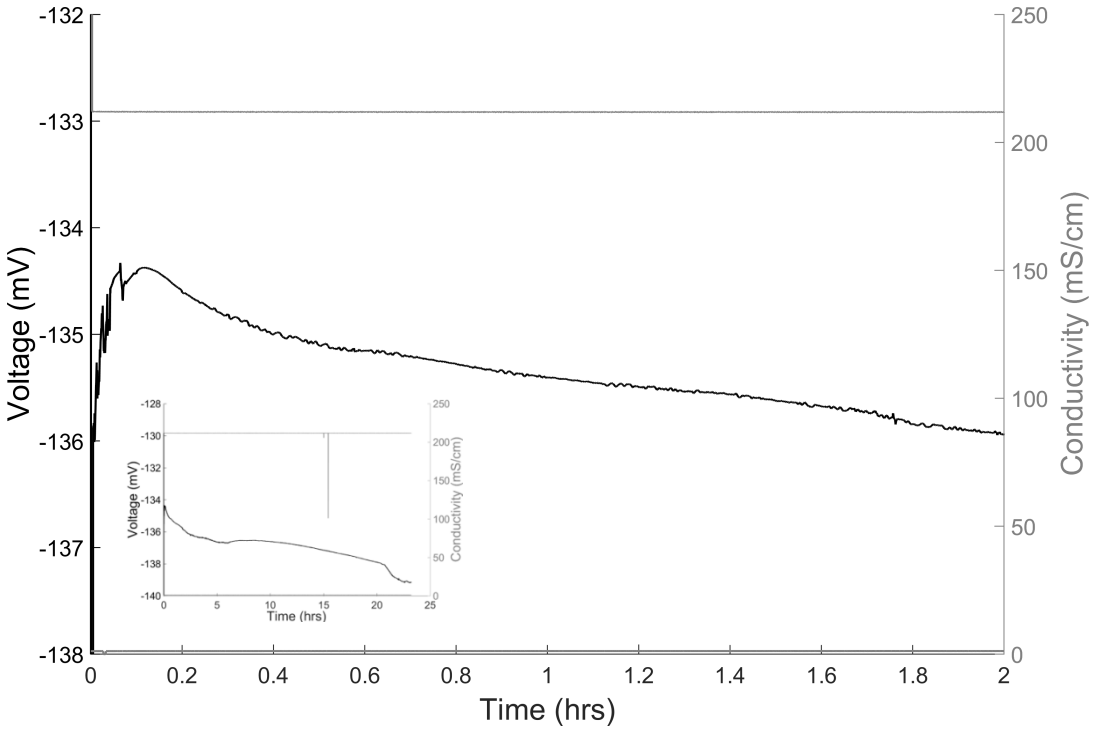

Figure A3.1 - EED potential results from pre-eq(DI/5M) experiments. (a) Column results. (b) Plug results (sample S2). The insets show the results from the longer time-series.

GW/SW Column Results				
Exp #	**Date**	**Column Voltage (mV)**	**Average ED Voltage (mV)**	**Electrode Potential (mV)**
1	01/10/2014	-78.84	27.89	-106.73
2	29/09/2014	-81.86		-109.75
3	26/09/2014	-82.85		-110.74
4	09/09/2014	-79.01		-106.90
5	05/09/2014	-82.9		-110.79
6	03/09/2014	-78.82		-106.71
7	01/09/2014	-81.01		-108.90
8	28/08/2014	-81.83		-109.72
9	22/08/2014	-81.81		-109.70
10	04/08/2014	-79.4		-107.29
11	17/03/2014	-80.22		-108.11
12	10/03/2014	-81.63		-109.52
13	05/03/2014	-83.52		-111.41
14	12/02/2014	-78.65		-106.54
15	23/01/2014	-81.57		-109.46
	Average	**-80.928**		**-108.82**

Table A3.1 – Summary of the column experiment results for the GW/SW experiments.

Pre-eq(DI/5M) Column Results				
Exp #	**Date**	**Column Voltage (mV)**	**Average ED Voltage (mV)**	**Electrode Potential (mV)**
1	25/02/2015	-129.99270	44.3	-174.29270
2	02/03/2015	-128.09585		-172.39585
3	13/03/2015	-128.53862		-172.83862
4	27/03/2015	-127.53049		-171.83049
5	02/04/2015	-128.22277		-172.52277
6	08/04/2015	-126.95620		-171.25620
	Average	**-128.22**		**-172.52277**

Table A3.2 – Summary of the column experiment results for the pre-eq(DI/5M) experiments.

GW/SW Plug Results					
Date	**Chalk Sample**	**Plug Voltage (mV)**	**Average Plug Volt (mV)**	**EED potential (mV)**	**Average EED potential (mV)**
S2					
05/09/14	S2	-94.75	-94.21	10.99	**14.61**
26/09/14	S2	-95.76		9.98	
17/03/14	S2	-93.02		12.72	
05/06/14	S2	-93.73		12.01	
01/10/14	S2	-93.81		11.93	
S3					
05/03/14	S3	-89.90	-87.44	15.84	**21.38**
13/06/14	S3	-88.20		17.54	
09/09/14	S3	-87.97		17.78	
29/09/14	S3	-88.12		17.62	
03/09/14	S3	-85.36		20.38	
23/09/14	S3	-85.08		20.66	
S4					
08/03/15	S4	-84.95	-86.23	20.79	**22.60**
02/03/15	S4	-87.11		18.63	
27/03/15	S4	-86.02		19.72	
13/03/15	S4	-86.82		18.92	
T1					
02/07/15	T1	-87.16	-86.60	18.58	**22.22**
09/07/15	T1	-86.04		19.70	

Table A3.3 – Summary of the plug experiment results for the GW/SW experiments.

Pre-eq(DI/5M) Plug Results					
Date	**Chalk Sample**	**Plug Voltage (mV)**	**Average Plug Volt (mV)**	**EC potential (mV)**	**Average EED potential (mV)**
S2					
14/04/15	S2	-153.82	-153.03	18.46	**17.45**
29/04/15	S2	-154.17		17.01	
05/05/15	S2	-151.10		20.08	
S3					
22/04/15	S3	-138.68	-138.71	32.50	**32.19**
05/05/15	S3	-138.74		32.44	
S4					
06/05/15	S4	-135.89	-136.08	35.29	**31.82**
12/05/15	S4	-137.88		34.40	
22/05/15	S4	-134.45		26.61	
Shale					
01/07/15	Shale	-189.20	-189.20	-14.22	**-14.22**

Table A3.4 – Summary of the plug experiment results for the pre-eq(DI/5M) experiments.

Appendix 4
Field Electrode Tests

The laboratory electrode dipole tests used to select the potable water and soil electrodes (Figure A4.1 and Figure A4.2 respectively) used in the SP monitoring experiments are presented here. The experiments were conducted in freshwater and bentonite respectively.

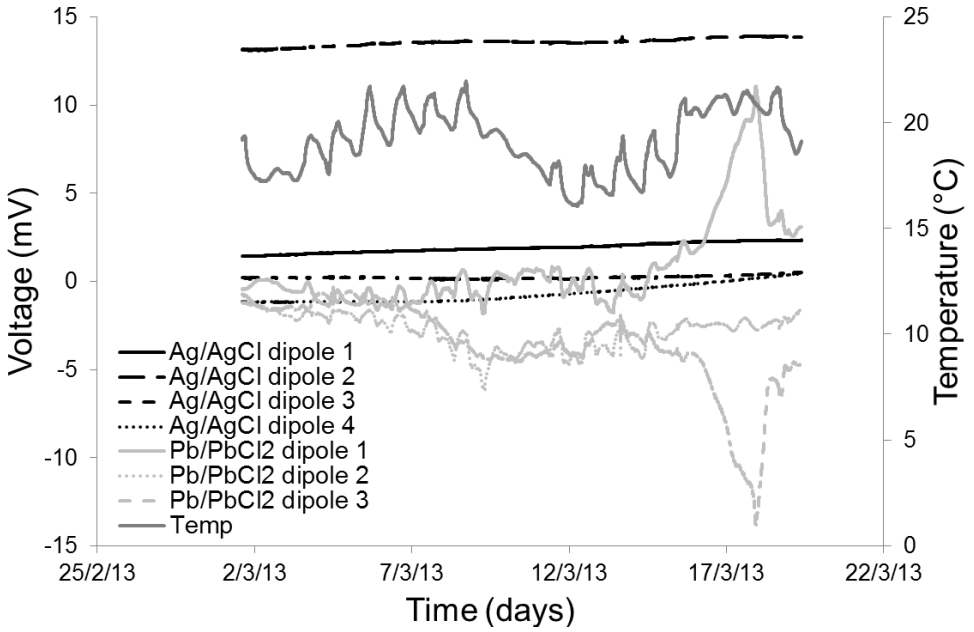

Figure A4.1 – Electrode test results from monitoring Ag/AgCl and Pb/$PbCl_2$ dipoles in tap water over a period of three weeks. It is clear from these results that the Ag/AgCl electrodes perform better in the fresh water. Pb/$PbCl_2$ electrodes appear to be more unstable and appear to have a larger temperature effect. The Ag/AgCl electrodes appear stable to within < 50 µV and display a drift < 400 µV over the three week monitoring period.

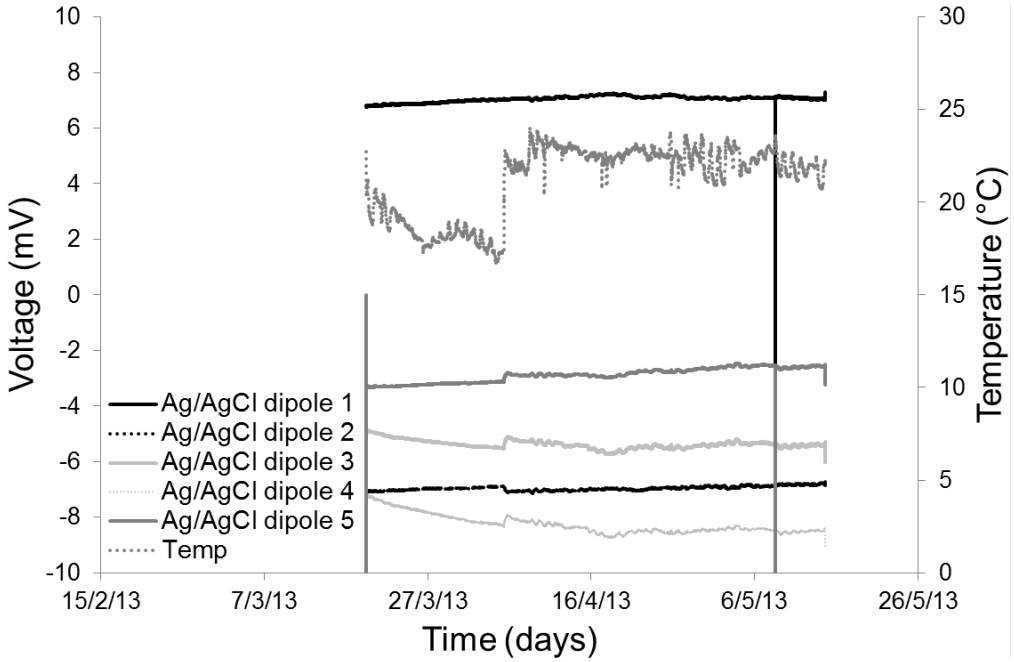

Figure A4.2 – Electrode test results from monitoring Ag/AgCl dipoles in bentonite saturated with tap water over a period of three weeks 8 weeks. The Ag/AgCl electrodes used in surface monitoring were chosen to be consistent with the choice of Ag/AgCl electrodes used in the borehole. The electrodes are stable to within < 100 µV and drift < 300 µV over the eight week monitoring period.

Appendix 5
1D Model Benchmark

The model results reported here show the 1D benchmark (i.e., the column experiment in section 3.2.3) test results for the two tolerance values used in the SP EED MINRES solver (10^{-5} and 10^{-7}, Figure A5.1 and Figure A5.2 respectively). The scaling factor used was $C\_scale = -0.2$ from Equation 4.10 in chapter 4. The results are identical for the two tolerance values. The potential difference across the front is c. 22 mV which is the EED measured in chalk sample S4. Sample S4 displayed the lowest exclusion efficiency. Note that the first 120 mm of this model represents the seawater reservoir in the column experiment and the last 120 mm from 240 mm onwards represents the groundwater reservoir. Both reservoirs have a porosity of 1. The chalk core has a porosity of 0.4 and sits between 120 mm and 240 mm. An EK benchmark test was also conducted using the same model and can be seen in Figure A5.3.

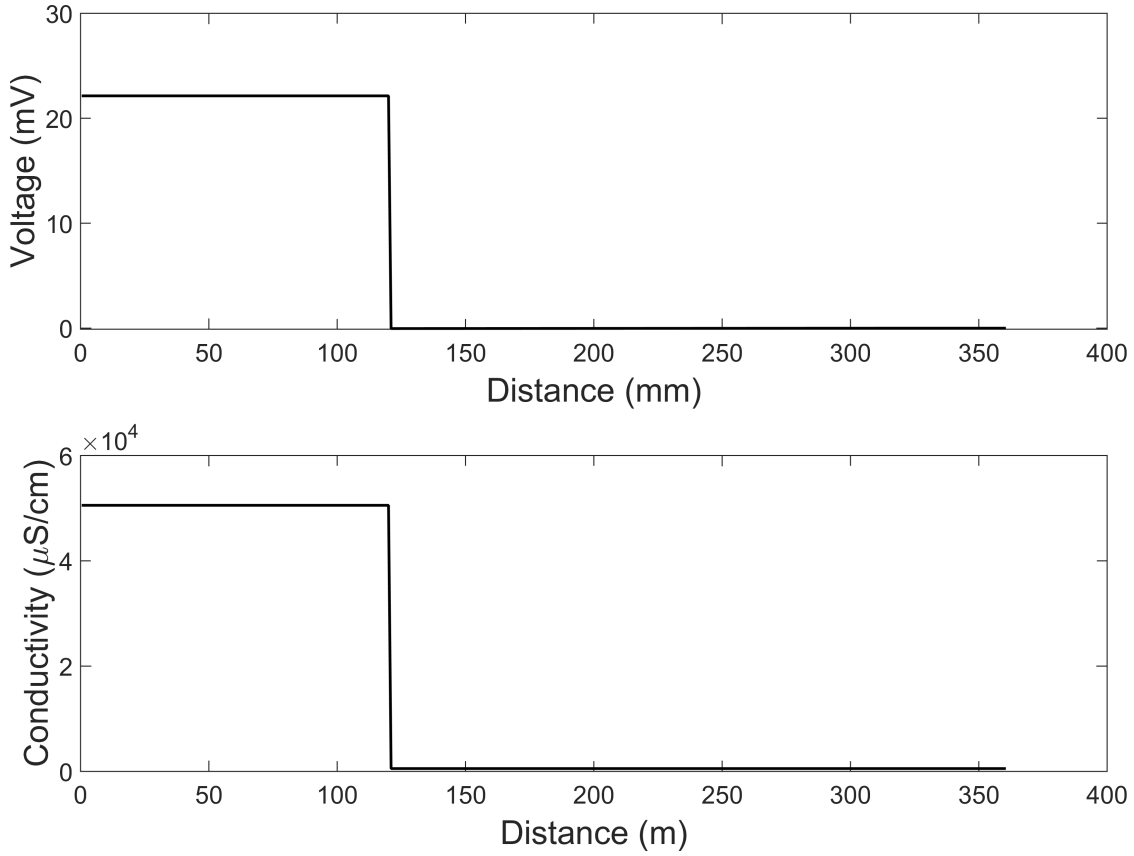

Figure A5.1 – EED potential from 1D model of plug experiment using a solver tolerance of 10^{-5}.

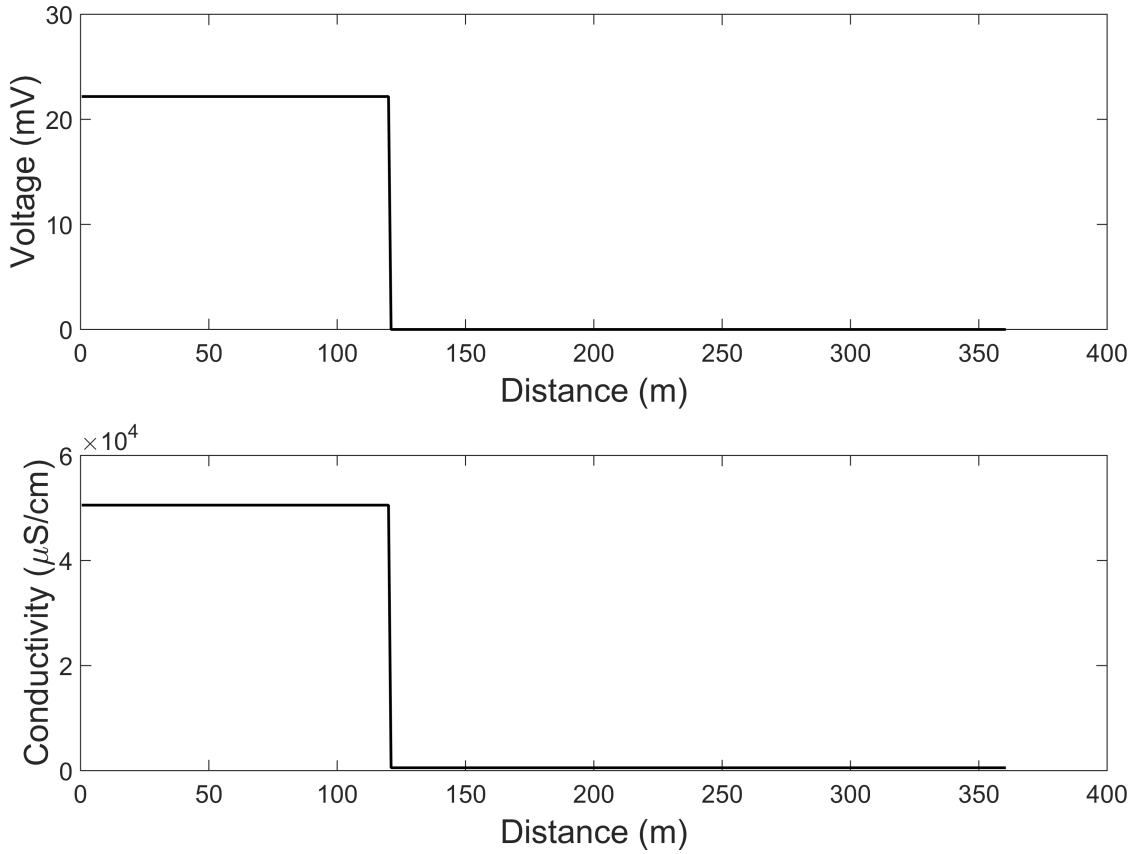

Figure A5.2 - EED potential from 1D model of plug experiment using a solver tolerance of 10^{-7}.

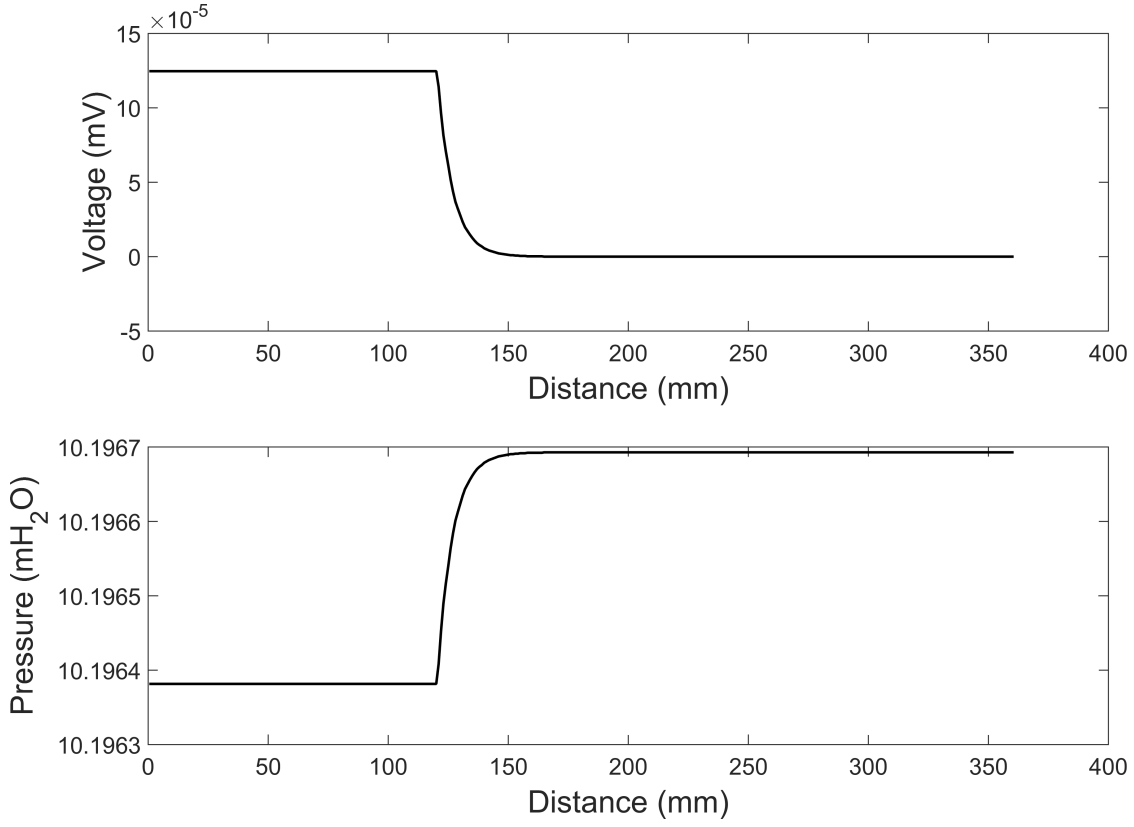

Figure A5.3 - EK test, the change in voltage is in the opposite sense to the change in pressure and the magnitude of change is consistent with the laboratory measured coupling coefficient. This was conducted using the same experimental setup as in Figure 7.5 and Figure 7.6.

Appendix 6
Coastal PSD analysis

The results from the PSD analysis of the hydrodynamic and SP data from the long-term monitoring experiment at the coastal site are presented here.

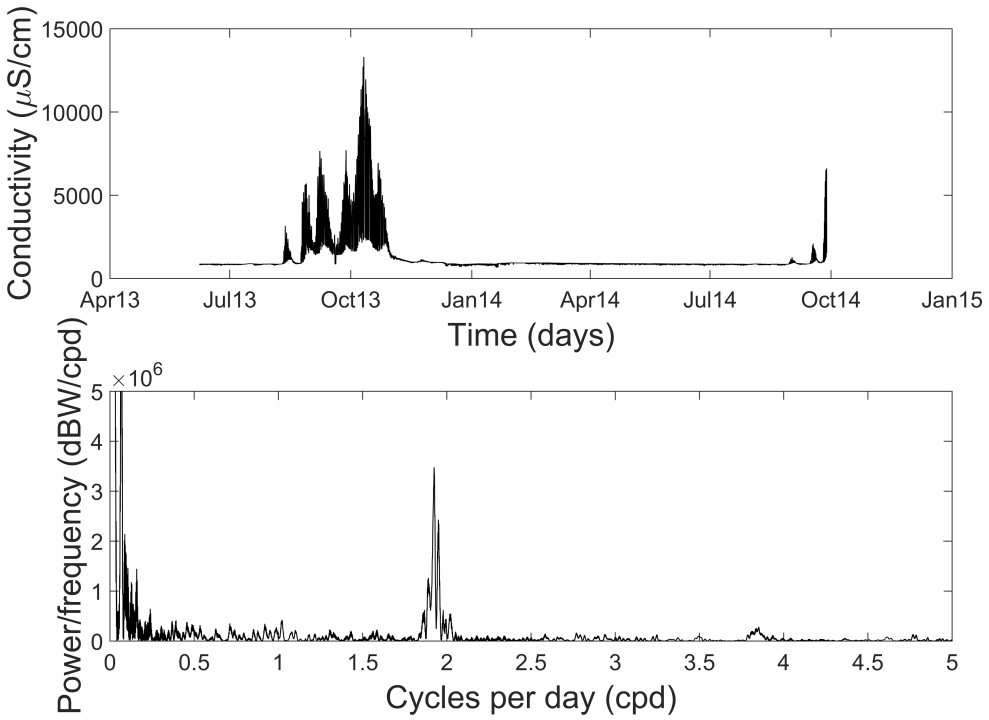

Figure A6.1 – PSD analysis of the coastal conductivity data for the full time-series.

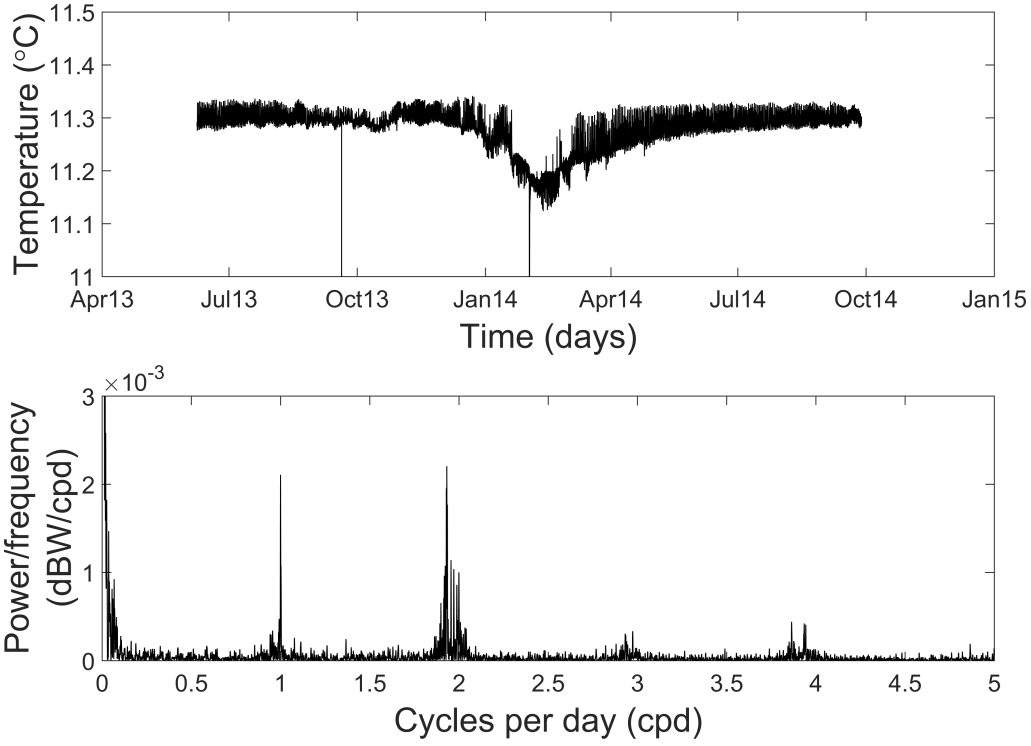

Figure A6.2 – PSD analysis of the coastal borehole temperature for the full time-series.

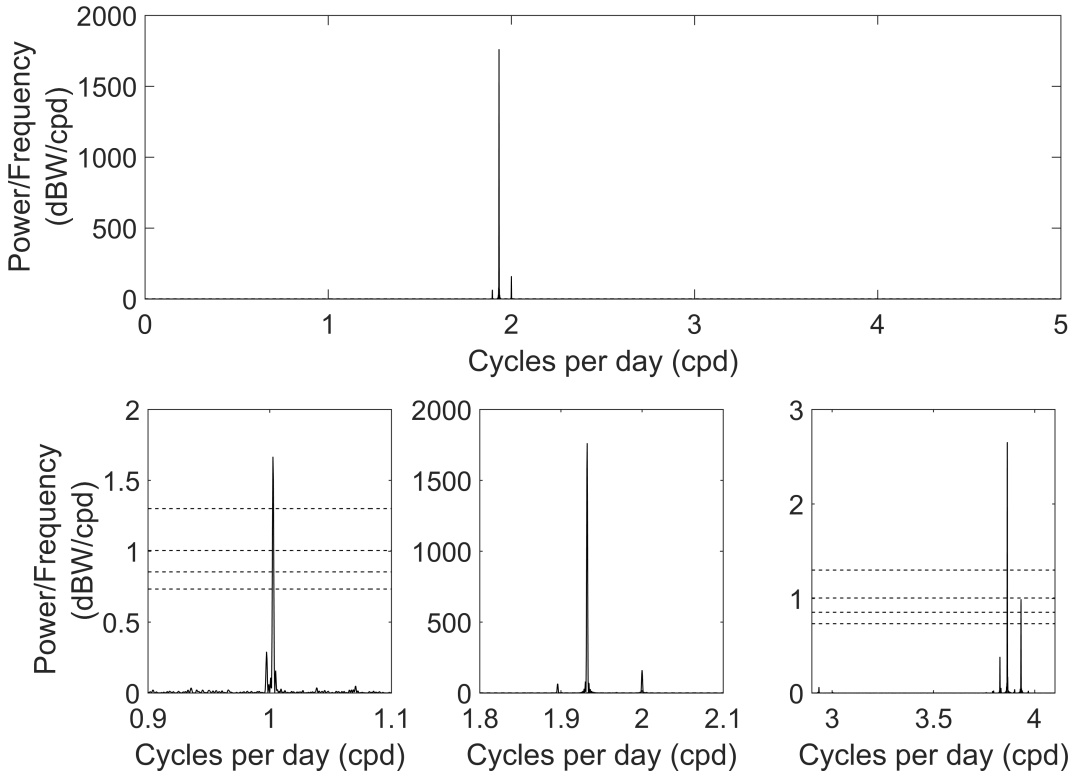

Figure A6.3 – PSD analysis of the Newhaven tidal data for the length of the monitoring experiment.

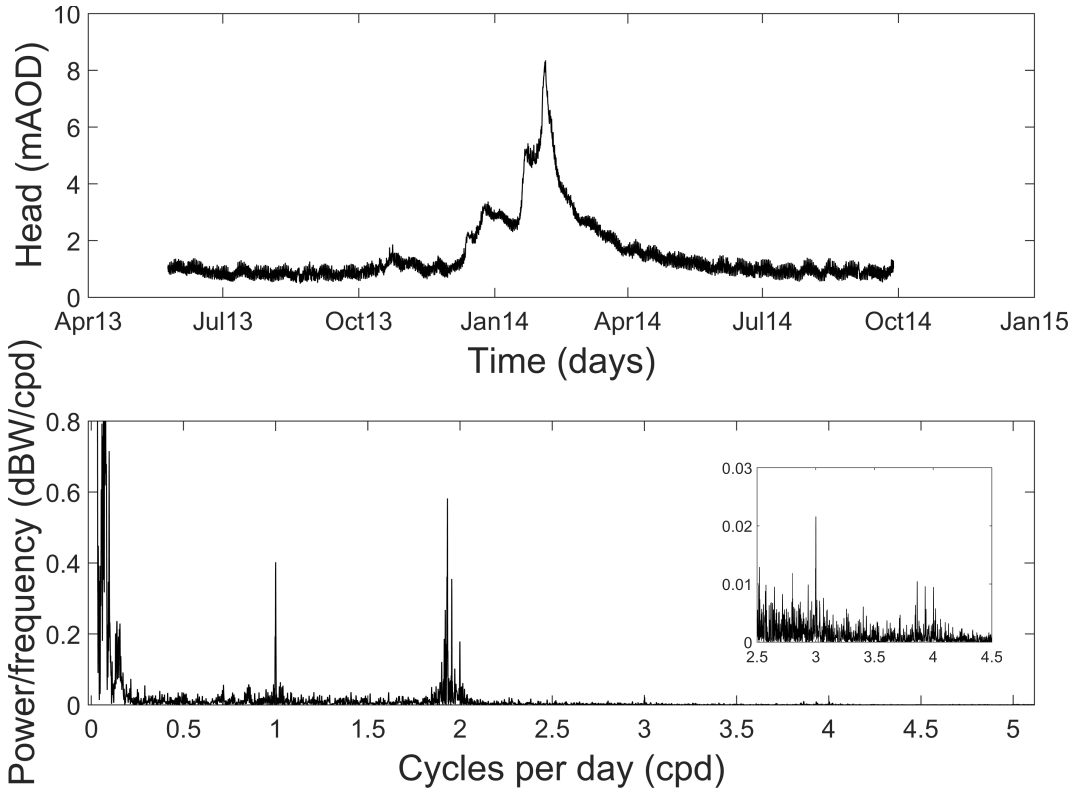

Figure A6.4 – PSD analysis for the coastal head data for the full time-series. The inset plot shows the frequency components with a periodicity of 3 -4 cycles per day.

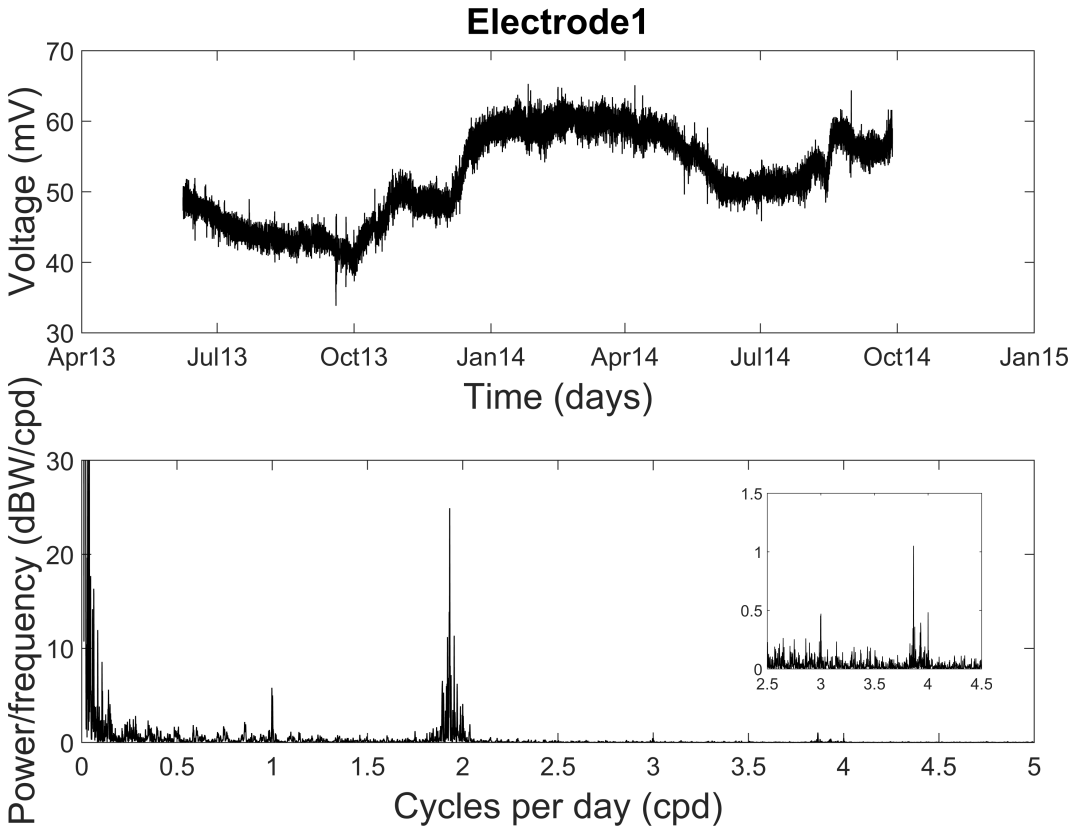

Figure A6.5 – PSD analysis of the surface referenced electrode data (BH1-C – Ref-C). The inset plot shows the frequency components with a periodicity of 3 -4 cycles per day.

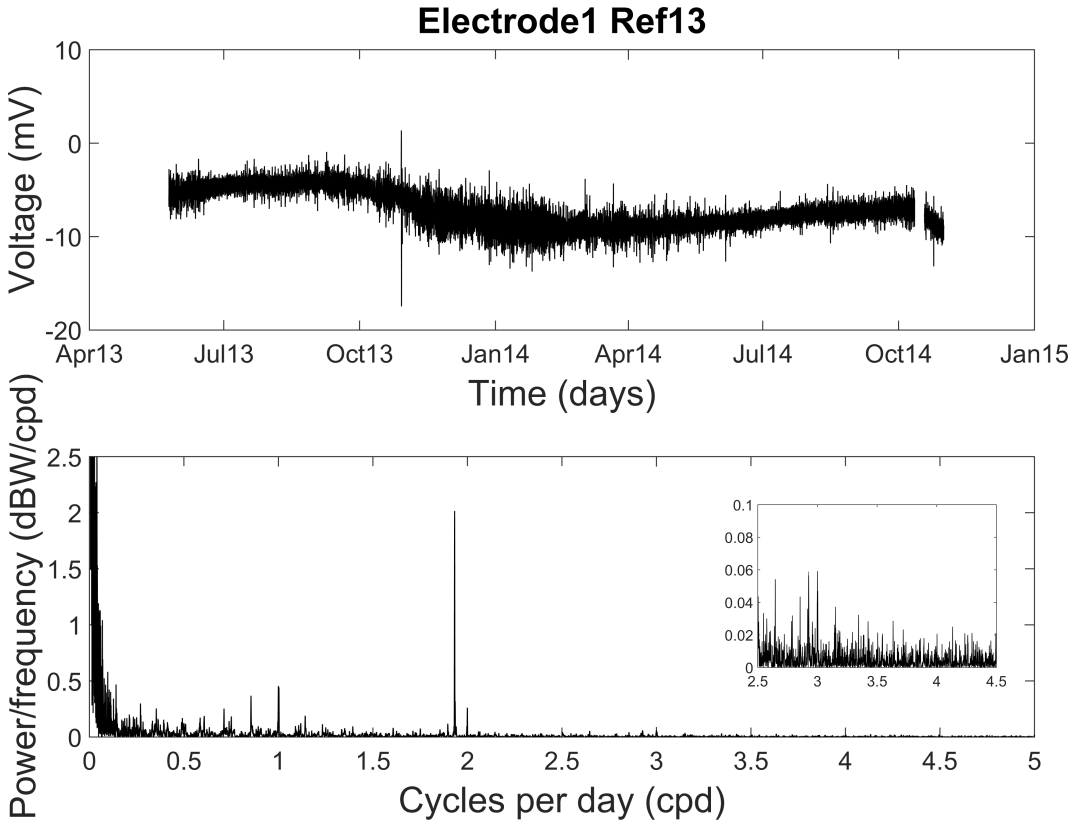

Figure A6.6 - PSD analysis of the surface referenced electrode data (BH1-C – BH13-C). The inset plot shows the frequency components with a periodicity of 3 -4 cycles per day.